Univerza v Ljubljani

Fakulteta za elektrotehniko

Lea Rems

Uporaba teoretičnih modelov elektroporacije lipidne membrane

DOKTORSKA DISERTACIJA

Mentor: prof. dr. Damijan Miklavčič

Somentor: dr. Mounir Tarek

Ljubljana, 2016

University of Ljubljana

Faculty of Electrical Engineering

Lea Rems

Applications of theoretical models of lipid membrane electroporation

DOCTORAL DISSERTATION

Mentor: Prof. Damijan Miklavčič, Ph.D.

Co-mentor: Mounir Tarek, Ph.D.

Ljubljana, 2016

PREFACE

The present PhD thesis is a result of numerical modeling, experimental investigations, and molecular dynamics simulations related to electroporation of lipid membranes. The work was carried out during the Ph.D. study period at the Laboratory of Biocybernetics, Faculty of Electrical Engineering, University of Ljubljana, Slovenia. Molecular dynamics simulations were performed at Équipe Théorie Simulations et Modélisation, Université de Lorraine, Nancy, France. The results of the research work are presented in papers, which were published or were submitted to international scientific journals:

Paper 1: Rems L, Miklavčič D. **Invited tutorial: Electroporation of cells in complex materials and tissue**. *J. App. Phys.* Submitted for review.

Paper 2: Retelj (Rems) L, Pucihar G, Miklavčič D. **Electroporation of intracellular liposomes using nanosecond electric pulses – A theoretical study**. *IEEE Trans. Biomed. Eng.* 60: 2624-2635, 2013.

Paper 3: Rems L, Ušaj M, Kandušer M, Reberšek M, Miklavčič D, Pucihar G. **Cell electrofusion using nanosecond electric pulses**. *Sci. Rep.* 3: 3382, 2013.

Paper 4: Dymek K, Rems L, Zorec B, Dejmek P, Gómez Galindo F, Miklavčič D. **Modeling electroporation of the non-treated and vacuum impregnated heterogeneous tissue of spinach leaves**. *Innov. Food Sci. Emerg. Technol.* 29: 55-64, 2015.

Paper 5: Casciola M, Kasimova MA, Rems L, Zullino S, Apollonio F, Tarek M. **Properties of lipid electropores I: Molecular dynamics simulations of stabilized pores by constant charge imbalance**. *Bioelectrochemistry*. Submitted for review.

Paper 6: Rems L, Tarek M, Casciola M, Miklavčič D. **Properties of lipid electropores II: Comparison of continuum-level modeling of pore conductance to molecular dynamics simulations**. *Bioelectrochemistry*. Submitted for review.

Acknowledgements

I have learned that dedicated work brings rewards. But I have also learned that some things in life simply come as a gift.

I am deeply grateful to my mentors, Prof. Dr. Damijan Miklavčič and Dr. Mounir Tarek, for sharing with me their knowledge, experience, and scientific curiosity. It has been a pleasure and a privilege to work under their guidance.

I would further like to thank my colleagues from the Laboratory of Biocybernetics (University of Ljubljana) and the group Théorie, Modélisation et Simulations (Université de Lorraine), as well as external collaborators, for providing a friendly working environment, and particularly for the vivid and helpful discussions we have had throughout our collaboration. I am especially in debt to Duša Hodžić, Marko Ušaj, Maša Kandušer, Tina Batista Napotnik, Tina Stepišnik, Janja Dermol, Suyashree Bhonsle, and Christoph Huber for discussions on biological aspects of electroporation, chemicals, experimental approaches and protocols; Peter Kramar for discussions on lipid bilayers; Matej Reberšek and Alojz Retelj for help with electronics and hardware equipment; Matej Kranjc, Bor Kos, Selma Čorović, and Kataryzna Dymek for discussions on numerical modeling; and Andraž Polak, Maura Casciola, Marina Kasimova, Marilyne Viano, and Pablo Campomanes for their indispensable help with molecular dynamics simulations.

I am also in debt to my family and friends for continuous support and understanding; above all to Tomaž for simply being whom he is.

Last but certainly not least I would like to thank Dr. Gorazd Pucihar for his guidance, as well as for transferring to me his research enthusiasm and experience on numerical modeling and experiments with cell cultures. We did this PhD together, nevertheless.

This research has been supported by Slovenian Research Agency (ARRS) under a Junior Researcher grant. Part of the work has been performed during the Short Term Scientific Mission (STSM-TD1104-270215-057439) granted by COST action TD1104 (www.electroporation.net). Research was conducted in the scope of the European Associated Laboratory for Pulsed Electric Field Applications in Biology and Medicine (LEA EBAM).

Dedicated to Dr. Gorazd Pucihar and Prof. Andrea Seljan Drofenik

Table of contents

Abstract

Electroporation, electropermeabilization, or pulsed-electric-field (PEF) treatment, are all terms naming the treatment of cells with short (ns–ms) electric pulses, which induce an increase in cell membrane permeability. This technique is widely used in various medical and biotechnological applications, e.g. for increasing the uptake of drugs and genetic material into cells and tissues, for nonthermal tissue ablation, extraction of different components from plant tissues, food preservation, as well as inactivation of bacteria in food processing and environmental applications. Electroporation is generally achieved by placing the target cells or tissue between electrodes, to which electric pulses are delivered. During pulse application, the resulting electric field induces a transmembrane voltage across the cell membranes, which, when sufficiently high, leads to membrane structural rearrangement. At least part of these rearrangements are attributed to formation of aqueous pores in the membrane lipid domains, since similar phenomenon can also be observed in model lipid membranes, such as planar lipid bilayers and lipid vesicles. The induced transmembrane voltage is determined by the pulse parameters, electric field strength, cell size, geometry, orientation, and the proximity of other structures, which perturb the local electric field, such as neighboring cells. The most complex is thereby electroporation in tissues, which can be highly heterogeneous.

In many applications of electroporation, the protocol of applying electric pulses needs to be carefully tailored as to ensure that the cells are not damaged by excessive electric field, allowing them to survive the exposure after being electroporated. For such purpose, theoretical models of electroporation can be of great help, as they provide the means to probe the effects of different pulse parameters and can guide the optimization of experimental protocols. The first aim of the present thesis was thereby to use theoretical (numerical) modeling to complement and guide *in vitro* experimental work. We performed three studies, each addressing a different application of electroporation. In the first study we investigated the possibility of using nanosecond electric pulses for electroporating intracellular liposomes. Liposomes are drug delivery vehicles which have the advantage to protect the drug from the hostile environment, particularly in the blood plasma, as well as the organism itself from the toxic effects of the drug. But once the liposomes reach the target cells, their content needs to be released into the cytosol. Nanosecond electric pulses, which are able to electroporate intracellular organelles, could provide a method to control the release of the liposomal content. Our numerical results predicted that that nanosecond pulses can efficiently be used for electroporating the liposomes without affecting the cell viability, provided that the pulses are not much longer than 10 ns, if liposomes are ~100 nm large.

Our second study was oriented towards cell electrofusion and demonstrated the potential advantage of using nanosecond electric pulses for electrofusing cells with different size. Cell cultures characterized by a larger size are generally electroporated at lower electric field strength. When simultaneously electroporating two cell cultures with different size, which is performed in cell electrofusion protocols, the larger cells may become damaged when exposed to an electric field required to electroporate the smaller cells, in particular when conventional tens or hundreds of microseconds long pulses are applied. This is known to be an issue in electrofusion of lymphocytes with myeloma cells in hybridoma technology for monoclonal antibody production.

Using numerical modeling, we demonstrated that when cells placed in a low conductive medium, typical for electrofusion protocols, are exposed to pulses with duration in the nanosecond range, the induced transmembrane voltage is the highest in the contact zone between cells, i.e., the target area for electrofusion. Amplification of the transmembrane voltage at the contact zone allows one to optimize the pulse parameters to specifically electroporate the contact zones and avoid problems due to cell size differences. We further developed an experimental protocol for fusing cells with nanosecond pulses, and confirmed our numerical predictions by experimental results.

The third study presents the development of an experimentally validated numerical model of a spinach leaf with resolved tissue structure in order to address the problems in cryopreservation of spinach leaves. In the latter, the cryoprotectant (e.g. trehalose) is first introduced into the extracellular space inside the leaf tissue by means of vacuum impregnation. Afterwards, the leaf is electroporated to allow the cryoprotectant to enter the cells, as the cryoprotectant needs to be present on both sides of the membrane in order to increase the freezing tolerance of the leaves. The leaf tissue is heterogeneous and it is difficult to achieve electroporation and survival of all cells in the tissue after exposure to electric pulses. In addition, the leaf is too thick to allow microscopic examination of all tissue layers. Consequently, the developed model allowed us to investigate electroporation of cells in different tissue layers and provided the possibility to further optimize the pulse parameters for reversible electroporation of all cells in the tissue.

Despite the general usefulness of numerical models of electroporation, the predictive power of the models relies on the proper description of the underlying electroporation process, which is not yet sufficiently well characterized on the molecular level. The possibility to progress towards improving the theoretical descriptions of electroporation, which are based on continuum theories, is offered by molecular dynamics simulations. The second aim of the thesis was thereby to compare the predictions arising from continuum electroporation models with results from molecular dynamics simulations. Our focus was the characterization of pore conductance, which is an important parameter in continuum electroporation models, and it can also be directly related to experimental measurements. We compared the results of pore conductance extracted from molecular dynamics simulations with the predictions of a continuum model based on the Poisson-Nernst-Planck theory. This theory is the origin of all theoretical descriptions of pore conductance, which are used in continuum electroporation models. Nevertheless, these descriptions contain many simplified assumptions. Our study demonstrated that the theory is able to describe the overall pore conductance to Na^+ and Cl^- ions very well, provided that we take into account the toroidal shape of the pore. In addition, we provided a continuum approach which allows to describe also the pore selectivity, i.e., higher conduction of Cl^- than Na^+ ions. We further compared our results to simplified theoretical expressions of pore conductance and demonstrated that the simplifications do indeed influence the overall predictions of continuum electroporation models.

In conclusion, theoretical models of electroporation provide a convenient way to complement experimental investigations by enhancing the understanding of the physics underlying the experimental data. Interconnections between molecular-scale, cell-scale, and tissue-scale models are feasible and important for progressing towards better understanding of the electroporation phenomenon and consequently developing more efficient therapies and technologies.

Razširjen povzetek v slovenskem jeziku

1 Uvod

1.1 Elektroporacija

Z izpostavitvijo bioloških celic električnemu polju lahko močno povečamo prevodnost in permeabilnost njihovih membran (Coster, 1965; Neumann in Rosenheck, 1972; Zimmermann *et al.*, 1974; Kinosita in Tsong, 1977a; Neumann *et al.*, 1982). V prisotnosti električnega polja se namreč na celičnih membranah vzpostavi transmembranska napetost, ki pri dovolj visoki vrednosti (reda 0,1 do 1 V) v membrani povzroči zaznavne strukturne spremembe. Te spremembe lahko eksperimentalno detektiramo, na primer, kot prehajanje različnih ionov in molekul prek membrane, za katere membrana v fizioloških pogojih predstavlja neprepustno oviro (Hibino *et al.*, 1991; Gabriel in Teissié, 1999; Pavlin *et al.*, 2007; Kotnik *et al.*, 2010).

Podobno dogajanje, kot ga zaznamo pri celičnih membranah, opazimo tudi pri modelnih lipidnih membranah, kot so ravninski lipidni dvosloji in lipidni vezikli (slika 1.1) (Benz in Zimmermann, 1980; Chernomordik *et al.*, 1987; Kakorin *et al.*, 1996). Raziskave torej kažejo, da se vsaj del strukturnih sprememb v celični membrani odvija v njenih lipidnih domenah. Čeprav natančno dogajanje na molekularnem nivoju celične membrane še ni povsem razloženo, številne teoretične in eksperimentalne študije ter simulacije molekularne dinamike kažejo, da lahko vsaj del strukturnih sprememb pripišemo majhnim vodnim poram v lipidnem dvosloju, katerih nastanek izzove električno polje oz. povišana transmembranska napetost (Weaver in Chizmadzhev, 1996; Neumann *et al.*, 1998; Tieleman, 2004). Skladno s to hipotezo pojav imenujemo elektroporacija (Neumann *et al.*, 1982).

Elektroporacija celic je lahko reverzibilna, kar pomeni, da se celične membrane po izpostavitvi pulzom zacelijo in povrnejo v prvotno stanje, ali ireverzibilna, kar vodi v smrt in razkroj celic. Reverzibilnost elektroporacije dosežemo s primerno izbrano jakostjo in dolžino izpostavitve električnemu polju (Maček-Lebar in Miklavčič, 2001). V praksi namreč elektroporacijo največkrat dosežemo tako, da na elektrode, med katerimi se nahajajo ciljne celice ali tkivo, dovedemo električne pulze določene oblike, dolžine, amplitude, števila in ponavljalne frekvence. V primeru celic in tkiv se za reverzibilno elektroporacijo pogosto uporablja zmerno število pravokotnih pulzov (1–10) pri ponavljalni frekvenci 1 Hz, z dolžino posameznega pulza v območju mikrosekund do milisekund in z amplitudo, ki zagotovi jakost električnega polja do nekaj 100 V/cm (Rols in Teissié, 1998; Marty *et al.*, 2006). Z višanjem števila, dolžine in/ali amplitude pulzov pa postane elektroporacija ireverzibilna (Rols in Teissié, 1990; Maček-Lebar in Miklavčič, 2001).

Tako reverzibilno kot ireverzibilno elektroporacijo celic in tkiv danes uporabljamo na številnih področjih v medicini in biotehnologiji. Reverzibilno elektroporacijo najpogosteje uporabljamo takrat, kadar želimo, da celične membrane postanejo prepustne za molekule, vendar celice postopek preživijo. Ireverzibilno elektroporacijo pa izkoriščamo za neposredno uničenje rakavih celic ali različnih mikroorganizmov (bakterij in kvasovk).

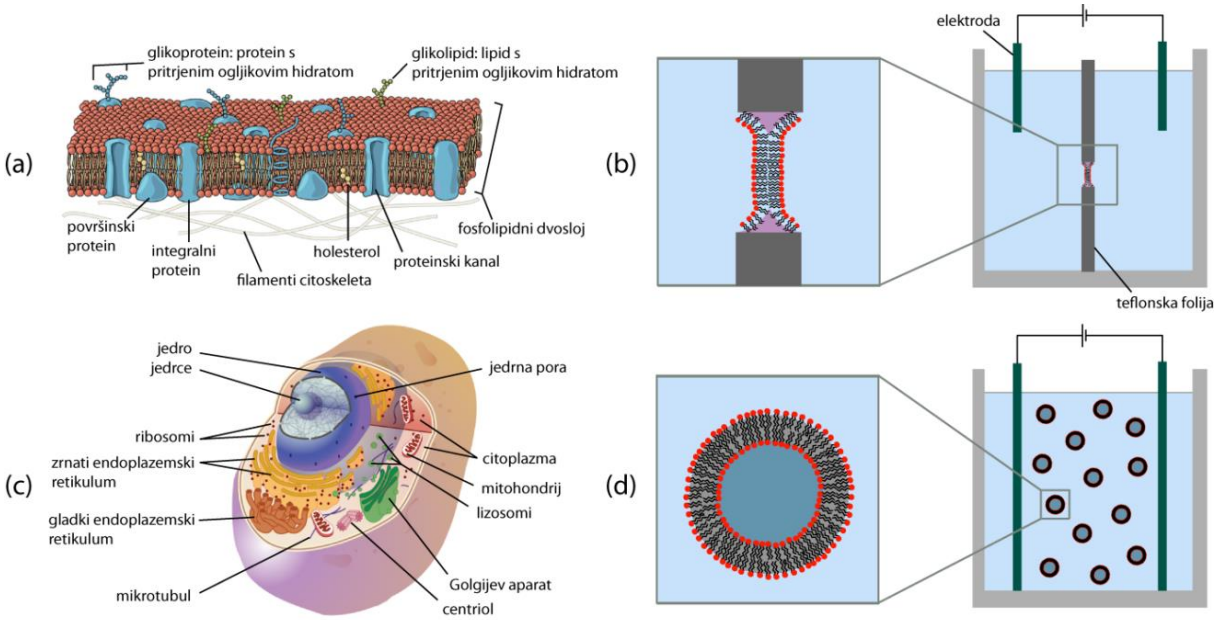

Slika 1.1: Celična membrana in modelne lipidne membrane. (a) Celična membrana, ki jo sestavlja lipidni dvosloj z vgrajenimi proteinskimi strukturami. (b) Ravninski lipidni dvosloj v luknjici teflonske folije. Pri študiji elektroporacije na vsako stran lipidnega dvosloja postavimo elektrode, na katere dovedemo električne pulze. (c) Celica s kompleksno strukturo znotrajceličnih organelov. (d) Lipidni vezikel – sferična struktura, obdana z membrano iz lipidnega dvosloja. Velikost lipidnih veziklov je lahko zelo različna; njihov premer obsega od nekaj 10 nm pa vse do približne velikosti celic, tj. več μm. Pri študiju elektroporacije suspenzijo lipidnih veziklov postavimo med elektrode, na katere dovedemo električne pulze. Na podoben način pogosto raziskujemo tudi elektroporacijo celic. Lipidni vezikli so enostaven model celične membrane v smislu vase sklenjenega lipidnega dvosloja, vendar ne vključujejo nobenih notranjih struktur.
Viri slik: (a) http://cnx.org/content/m45433/latest/?collection=col11487/latest; (b,d) http://en.wikipedia.org/wiki/Model_lipid_bilayer; (c) http://www.dmc.org/information-for-mitochondrial-medicine-center-patients.html (april 2014).

1.2 Uporaba elektroporacije v medicini in biotehnologiji

Elektroporacija je s terapevtskega stališča zelo zanimiva, saj omogoča kontroliran vnos različnih učinkovin v celice. Medtem ko je elektrokemoterapija – terapija, ki temelji na lokalno povečanem vnosu kemoterapevtikov v tumorsko tkivo z elektroporacijo – danes že uveljavljena v klinični praksi (Miklavčič *et al.*, 2012; Mali *et al.*, 2013; Di Monta *et al.*, 2014; Yarmush *et al.*, 2014; Cadossi *et al.*, 2014), sta vnos DNA cepiv in elektrotransfekcija genov z zapisom za različne terapevtske molekule trenutno v fazi kliničnih študij (Heller in Heller, 2010; Coosemans *et al.*, 2013; Kalams *et al.*, 2013; Hooper *et al.*, 2014). Obenem potekajo tudi klinične študije ablacije tumorjev z ireverzibilno elektroporacijo (Ben-David *et al.*, 2013; Cannon *et al.*, 2013; Rossmeisl *et al.*, 2013; Scheffer *et al.*, 2014). V zadnjih letih so številne raziskave usmerjene v transdermalni vnos učinkovin z elektroporacijo (Zorec *et al.*, 2013; Schoellhammer *et al.*, 2014), čedalje več pozornosti pa se posveča kombiniranju elektroporacije z različnimi nanostrukturami (Boukany *et al.*, 2011; Xie *et al.*, 2012; Huang *et al.*, 2014a; Liu *et al.*, 2013).

Z elektroporacijo dosežemo tudi zlivanje celic; če se elektroporirane celice nahajajo v stiku, se lahko zlijejo med sabo (Zimmermann, 1982). Metoda, ki jo imenujemo elektrozlivanje, se je izkazala kot učinkovita za pridobivanje celic, ki proizvajajo monoklonska protitelesa (proteine, ki jih uporabljamo v diagnostične in

terapevtske namene ter za detekcijo različnih molekul v raziskavah v biologiji, biotehnologiji, farmaciji in drugih sorodnih vedah) (Kemna *et al.*, 2011; Trontelj *et al.*, 2008; Yu *et al.*, 2008). Z elektrozlivanjem je mogoče pripraviti celična cepiva za stimulacijo imunskega odziva pri zdravljenju raka (Zheng *et al.*, 2008; Tan *et al.*, 2013) ter celice, ki proizvajajo inzulin in jih lahko uporabimo pri raziskavah in zdravljenju diabetesa (McCluskey *et al.*, 2011; Yanai *et al.*, 2013). Obenem je mogoče hibridizirati rastline, ki postanejo odporne na različne okoljske dejavnike (Greplová *et al.*, 2008). Raziskave nakazujejo še na možnost regeneracije živcev z uporabo elektrozlivanja (Sretavan *et al.*, 2005; Chang *et al.*, 2009).

Elektroporacija se je uveljavila tudi v prehrambni industriji. Z elektroporacijo sladkorne pese povečamo količino ekstrahiranega sladkorja in močno zmanjšamo potrebni energetski vložek v proizvodnji (Sack *et al.*, 2010). Ekstrakcija taninov in pigmentov iz grozdja z elektroporacijo je primerljiva kot pri termični ekstrakciji, pri čemer lahko postopek z elektroporacijo celo izboljša okus vina (Sack *et al.*, 2010). Nadalje, vakuumska impregnacija v kombinaciji z elektroporacijo izboljša toleranco zelenjave na zamrzovanje (Phoon *et al.*, 2008). Z dovajanjem električnih pulzov dosežemo inaktivacijo bakterij, kar predstavlja alternativo termični pasterizaciji tekoče hrane, hkrati pa metoda ohranja visoko hranilno vrednost hrane (Toepfl *et al.*, 2007). V podobnem smislu lahko z električnimi pulzi dosežemo tudi dekontaminacijo vode (Gusbeth *et al.*, 2009; Liu *et al.*, 2013). V proizvodnji biogoriv so ugotovili, da se elektroporirana biomasa suši hitreje od neelektroporirane, kar posledično pomeni prihranek energije (Sack *et al.*, 2010). Najnovejše raziskave pa so usmerjene v uporabo elektroporacije za pridobivanje lipidov (biogoriva) iz mikroalg (Zbinden *et al.*, 2013) in valorizacije odpadnega rastlinskega materiala (Brianceau *et al.*, 2015; Yu *et al.*, 2015).

Medtem, ko se za zgoraj opisane aplikacije elektroporacije običajno uporablja pravokotne pulze z dolžinami v območju mikrosekund in milisekund, je napredek v tehnologiji razvoja pulznih generatorjev v začetku prejšnjega desetletja omogočil raziskave s krajšimi nanosekundnimi pulzi (Schoenbach *et al.*, 2001). Izkazalo se je, da lahko nanosekundni pulzi izzovejo elektroporacijo celičnih organelov (Schoenbach *et al.*, 2001; Tekle *et al.*, 2005; Batista Napotnik *et al.*, 2010) in sprožijo programirano celično smrt – apoptozo (Beebe *et al.*, 2013). Slednje se ponuja kot obetavna metoda za ablacijo tumorjev, ki ne zahteva uporabe dodatnih kemičnih substanc (kot elektrokemoterapija) in ne povzroča nekrotične smrti celic (kot ireverzibilna elektroporacija) (Garon *et al.*, 2007; Chen *et al.*, 2014; Nuccitelli *et al.*, 2014). Teoretične študije med drugim kažejo, da je pri uporabi nanosekundnih pulzov elektroporacija tkiva bolj homogena kot pri uporabi običajnih mikrosekundnih pulzov (Gowrishankar in Weaver, 2006). Prednost uporabe nanosekundnih pulzov pa se je pokazala tudi pri elektrozlivanju celic različnih velikosti (Rems *et al.*, 2013).

Poleg širokega spektra uporabe v medicini, biotehnologiji in biologiji je elektroporacija pomembna tudi kot sam biološki proces. Zadnje raziskave namreč kažejo, da bi elektroporacija lahko imela pomembno vlogo v evoluciji pri omogočanju navzkrižnega prenosa genov med organizmi (Kotnik, 2013).

1.3 Vsiljena transmembranska napetost

Celična membrana je električno zelo slabo prevodna (prepustna za ione) in ima zaradi lipidnega dvosloja nizko relativno dielektričnost. Zato celično membrano s stališča električnih lastnosti obravnavamo kot kondenzator, ki je obdan s prevodno zunajcelično in znotrajcelično tekočino. Ko celico izpostavimo električnemu polju, se membrana začne elektriti zaradi elektroforetske migracije ionov v prevodnih tekočinah. Rezultat je povišana (vsiljena) transmembranska napetost (TMN), ki se prišteje mirovalni TMN (Hibino *et al.*, 1993; Kotnik in Pucihar, 2010). Za razliko od mirovalne TMN, ki je približno enaka povsod vzdolž membrane, se vsiljena TMN spreminja s položajem na membrani. Za osamljeno okroglo celico z radijem R v homogenem električnem polju E lahko analitično določimo potek vsiljene TMN z rešitvijo Laplaceove enačbe za električni potencial (Kotnik in Miklavčič, 2000):

$$\mathrm{TMN} = 1{,}5ER\cos\theta\left(1-\mathrm{e}^{-t/\tau_m}\right)+U_{mir} \tag{1}$$

Pri tem je θ kot med smerjo električnega polja in smerjo normale na membrano (slika 1.2, A1), U_{mir} je mirovalna TMN (običajno negativna in po velikosti reda 10 mV), τ_m pa časovna konstanta elektrenja membrane. Zgornja enačba je sicer poenostavljena oblika analitične rešitve, ki zanemari dielektrične lastnosti elektrolitskih tekočin in velja pri fizioloških pogojih, vendar lahko iz nje razberemo nekaj ključnih lastnosti TMN:

(i) TMN se ne vzpostavi na membrani takoj, ampak potrebuje določen čas, pogojen s časovno konstanto τ_m. Slednja je odvisna od električnih lastnosti membrane, zunaj- in znotrajceličnega medija, ter velikosti celice. Pri okrogli celici z radijem ~10 μm v zunajceličnem mediju s fiziološko prevodnostjo (~1 S/m) je časovna konstanta reda 100 ns; v nizkoprevodnem mediju, ki se pogosto uporablja *in vitro* z namenom zmanjšanja električnega segrevanja medija, se časovna konstanta bistveno poveča (Kotnik *et al.*, 1997).

(ii) TMN se spreminja vzdolž membrane in je po absolutni vrednosti najvišja na območjih membrane, kjer je normala na membrano poravnana s smerjo električnega polja (na "polih" celice). Ker se vsiljena TMN prišteje mirovalni TMN, ki je običajno negativna (U_{mir} < 0), je skupna absolutna |TMN| višja na strani pozitivne elektrode (anode) kot na strani negativne elektrode (katode). Zato je elektroporacijo membrane na anodni strani v splošnem mogoče zaznati pri nižji jakosti električnega polja v primerjavi s katodno stranjo (Gabriel in Teissié, 1997; Mehrle *et al.*, 1985; Tekle *et al.*, 1990).

(iii) TMN je proporcionalna celičnemu radiju R in jakosti električnega polja E, zaradi česar se vzpostavi višja TMN na večjih celicah in/ali ko uporabimo višjo jakost električnega polja; to omogoča selektivno elektroporacijo večjih celic v suspenziji celic dveh tipov, v primeru da se celice močno razlikujejo v velikosti (Sixou in Teissié, 1990).

(iv) Poleg zgoraj navedenega je TMN odvisna tudi od oblike in orientacije celic v električnem polju, ter bližine različnih struktur (na primer sosednjih celic), ki lokalno spremenijo porazdelitev električnega polja (Susil *et al.*, 1998; Valič *et al.*, 2003; Pucihar *et al.*, 2007; Huang *et al.*, 2014b).

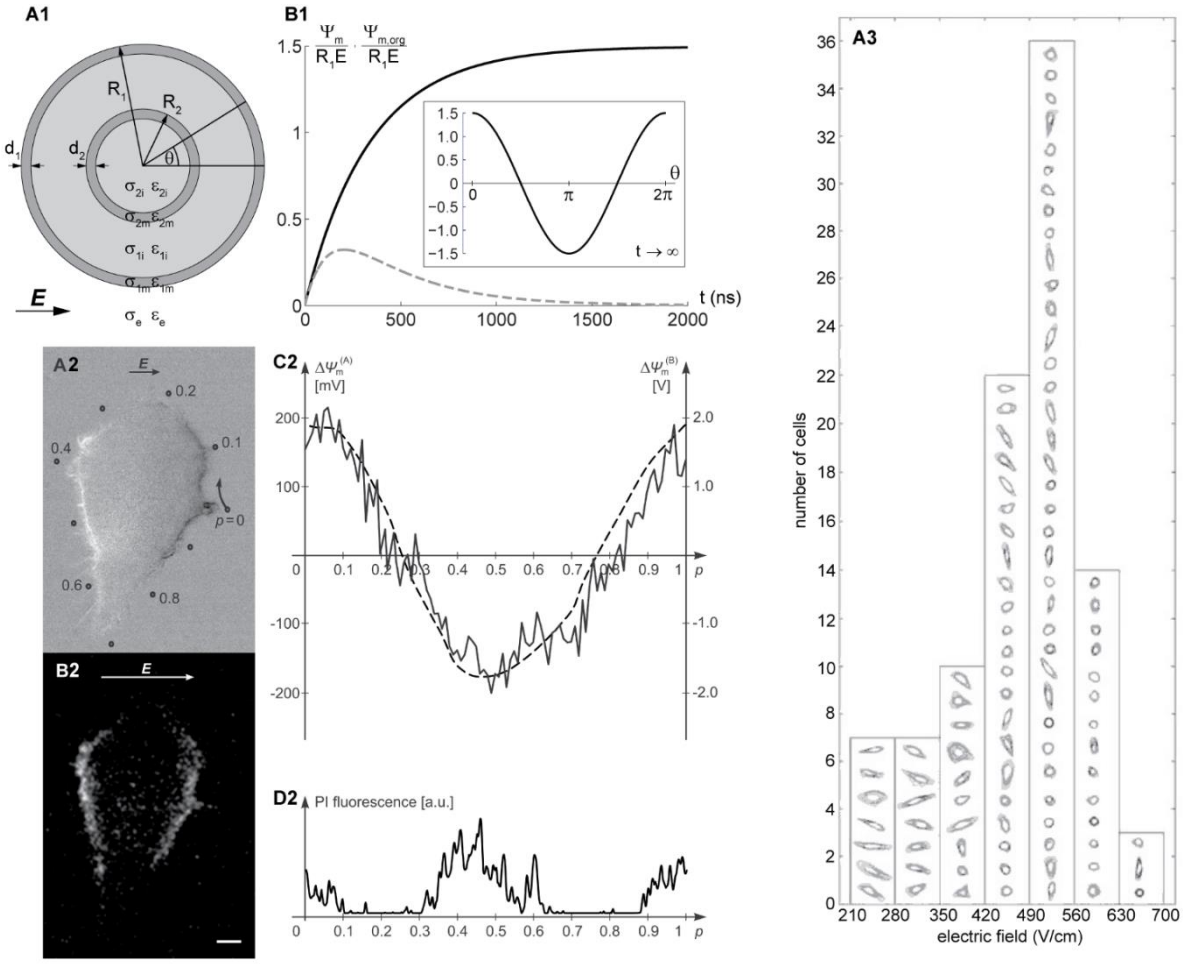

Slika 1.2 **(A1)** Model okrogle celice s koncentrično postavljenim okroglim organelom. Model sestavlja pet regij, pri čemer ima vsaka regija svojo prevodnost (σ_i, S/m) in dielektričnost (ε_i, F/m). Indeks "e" opisuje zunajcelični medij, indeks "1" opisuje celico in indeks "2" organel. **(B1)** Časovni potek vsiljene TMN pri $\theta = 0$ na celični membrani (Ψ_m, polna črta) in organelu ($\Psi_{m,org}$, prekinjena črta). TMN je normirana na jakost električnega polja E in celični radij R_1. Notranji graf prikazuje Ψ_m po obodu celične membrane v stacionarnem stanju. Povzeto po Kotniku in Miklavčiču (2006). **(A2)** Spremembe v fluorescenci napetostno-občutljivega barvila di-8-ANEPPS, ki odraža vsiljeno TMN na CHO celici. Temnejše regije sovpadajo z depolarizacijo membrane, svetlejše regije pa s hiperpolarizacijo membrane. **(B2)** Fluorescenca propidijevega jodida (PI), ki odraža transport PI prek elektroporirane membrane. **(C2)** Izmerjena (polna črta) in numerično določena (prekinjena črta) vsiljena TMN ($\Delta\Psi_m$) vzdolž poti, prikazane v (A2). **(D2)** Fluorescenca PI vzdolž poti, prikazane v (A2). Transport PI je mogoče detektirati na območjih membrane, ki sovpadajo s TMN, višjo od določene pragovne vrednosti. Povzeto po Kotniku *et al.* (2010) **(A3)** Najnižja jakost električnega polja, ki povzroči merljivo elektroporacijo pritrjenih CHO celic. Večje celice so elektroporirane pri nižjih jakostih električnega polja; vendar pa je kritična TMN za elektroporacijo nižja na manjših celicah (ni prikazano). Povzeto po Towhidi *et al.* (2008).

Elektroporacija membrane jasno izraža pragovni značaj, v smislu, da je elektroporacijo mogoče detektirati le na področjih membrane, kjer TMN preseže določeno kritično vrednost. To je na primer razvidno iz meritev transmembranskega transporta fluorescenčnega barvila propidijevega jodida v kratkem času po pulzu (slika 1.2, B2 in D2). Vendar pa je natančna vrednost kritične TMN za elektroporacijo precej slabo definirana, kar dokazuje tudi širok razpon vrednosti, ki se pojavljajo v literaturi (~0,2–1,0 V). Določitev "kritične" TMN je namreč odvisna od metode detekcije elektroporacije, pa tudi od metode, po kateri TMN izračunamo iz danih eksperimentalnih rezultatov. Elektroporacijo se običajno detektira preko močno povečanega transmembranskega

transporta molekul (npr. fluorescenčnih barvil), zato je detekcija seveda odvisna od občutljivosti detekcijskega sistema (Pakhomov *et al.*, 2015). Majhni ioni in molekule membrano prehajajo mnogo lažje kot večje molekule, iz česar sledi, da je potrebno za detekcijo večjih molekul dovesti daljše pulze, več pulzov in/ali pulze višje amplitude (Kinosita in Tsong, 1977b; Escande-Géraud *et al.*, 1988; Rols in Teissié, 1990, 1998; Nesin *et al.*, 2011). Poleg tega je "kritična" TMN odvisna od tipa celic (Čemažar *et al.*, 1998) in znatno variira že med celicami istega tipa, kljub enakim pogojem detekcije elektroporacije (Towhidi *et al.*, 2008). Študije celo kažejo, da je elektroporacijo manjših celic mogoče zaznati pri nižji TMN (Towhidi *et al.*, 2008; Henslee *et al.*, 2011). S tem lahko zaključimo, da je TMN pomembna, vendar ne edina veličina, ki določa elektroporacijo celične membrane.

Kljub temu, da "kritična" TMN ni univerzalna in dobro definirana, še vedno velja, da je za katero koli aplikacijo elektroporacije potrebno dovesti pulze, ki povzročijo dovolj visoko TMN za sprožitev elektroporacije. Pri tem ima pomembno vlogo tudi časovna konstanta elektrenja membrane. Na začetku procesa elektrenja je namreč v notranjosti celice prav tako prisotno električno polje, ki pa se postopoma zmanjšuje, ko TMN narašča proti svoji stacionarni vrednosti. Med elektrenjem so torej električnemu polju izpostavljeni tudi celični organeli. Tako lahko z uporabo nanosekundnih pulzov dovolj visoke amplitude (reda 10–100 kV/cm) elektroporiramo membrane celičnih organelov (poleg celične membrane) ter induciramo številne druge znotrajcelične procese (Kotnik in Miklavčič, 2006; Batista Napotnik *et al.*, 2010; Schoenbach in Joshi, 2010).

Kadar pa uporabimo pulze z dolžino v področju µs–ms (tj. pulze, daljše od časa elektrenja celične membrane), TMN doseže svojo maksimalno vrednost tekom pulza. Pri µs–ms pulzih zato lahko uporabimo nižje jakosti električnega polja (reda 0,1–1 kV/cm), pri čemer pulzi predvsem vplivajo na celično membrano. Celična notranjost kljub temu ni povsem zaščitena, saj se med pulzom zaradi elektroporacije poveča prevodnost celične membrane, kar omogoči, da električni tok teče tudi prek citoplazme. Izsledki teoretične študije so nakazali, da se kot posledica povečanja prevodnosti celične membrane lahko na membranah organelov vzpostavi dovolj visoka TMN za odprtje ionskih kanalov; pri določenih jakostih električnega polja pa bi lahko prišlo celo do elektroporacije organelov (Esser *et al.*, 2010).

Poudariti je še potrebno, da enačba (1) v splošnem velja samo dokler se membrana ne elektroporira. Ko namreč TMN doseže dovolj visoko vrednost za elektroporacijo membrane, se močno (lahko tudi za več velikostnih razredov) poveča električna prevodnost membrane (Kinosita in Tsong, 1979; Hibino *et al.*, 1993; Schmeer *et al.*, 2004; Pavlin *et al.*, 2005; Suzuki *et al.*, 2011). Zaradi povečane prevodnosti se membrana deloma razelektri prek prevodnih por, kar posledično zmanjša TMN na elektroporiranih območjih (Hibino *et al.*, 1993; DeBruin in Krassowska, 1999; Frey *et al.*, 2006). Visoko povečanje prevodnosti membrane pa je mogoče zaznati le tekom pulza in kratek čas po pulzu; prevodnost membrane se povrne praktično na svojo osnovno vrednost v času reda 1 µs po pulzu (Kinosita in Tsong, 1979; Hibino *et al.*, 1993; Pavlin *et al.*, 2005). Kljub temu, da se prevodnost membrane močno zmanjša, pa ostane celična membrana rahlo prepustna za ione in molekule tudi več minut po izpostavitvi električnim pulzom (Rols in Teissié, 1990; Saulis *et al.*, 1991; Shirakashi *et al.*, 2004; Pucihar *et al.*, 2008; Saulis in Saulė, 2012).

1.4 Transmembranski transport molekul

Povečanje transmembranskega transporta molekul je ena izmed najbolj izkoriščenih posledic elektroporacije. Ker se to podpoglavje nanaša predvsem na transport molekul, bomo namesto o elektroporaciji raje govorili o "permeabilizaciji", zato da ločimo transport molekul od visokega povečanja prevodnosti membrane (prehajanja majhnih ionov prek membrane) tekom aplikacije električnega pulza.

Detekcijo permeabilizacije celice pri elektroporaciji lahko izvedemo na več načinov. Prvi način je, da preštejemo delež celic, ki se je npr. obarval z barvilom (tripan modro, propidijev jodid, …), za katerega je celična membrana slabo prepustna pri fizioloških pogojih. Pri takšnem načinu detekcije ugotovimo, da se delež permeabiliziranih celic povečuje z jakostjo električnega polja *E*, dolžino pulza *T*, in številom pulzov *N*, dokler vse celice niso permeabilizirane (Teissié in Ramos, 1998; Maček-Lebar in Miklavčič, 2001). Glede oblike pulza so se pravokotni pulzi izkazali kot najbolj učinkoviti (Kotnik *et al.*, 2003). Hkrati pa se s povečevanjem *E*, *T* in *N* zmanjšuje delež preživelih celic, zato je potrebno ustrezno optimizirati parametre pulzov (Teissié in Ramos, 1998; Maček-Lebar in Miklavčič, 2001).

Druga možnost detekcije je, da merimo skupno količino molekul, ki so se transportirale prek celičnih membran pri populaciji celic (transport je lahko usmerjen iz zunajceličnega medija v celice ali iz celic v zunajcelični medij). Podobno kot prej ugotovimo, da se ta količina zvišuje z *E*, *T* in *N* in da so tudi v tem primeru pravokotni pulzi najbolj učinkoviti (Kotnik *et al.*, 2003; Rols in Teissié, 1990; Prausnitz *et al.*, 1993, 1995; Canatella *et al.*, 2001; Puc *et al.*, 2003; Pakhomov *et al.*, 2015). Pucihar in sodelavci so s takšnim pristopom detekcije merili kinetiko vnosa propidijevega jodida v celice med in po dovajanju enega 100–1000 μs dolgega pravokotnega pulza (Pucihar *et al.*, 2008). S pomočjo fotopomnoževalke so dosegli visoko časovno resolucijo meritev (200 ns–4 ms), ki so jih izvedli v širokem časovnem razponu (0–8 s po aplikaciji pulza). Na podlagi meritev so ugotovili, da poteka transport propidijevega jodida med pulzom elektroforetsko, po pulzu pa s pasivno difuzijo prek membrane. Po pulzu so pri transportu lahko razločili tri kinetične procese s časovnimi konstantami reda 10 ms, 100 ms in 10 s. Analiza njihovih rezultatov je še pokazala, da hitrost prehajanja molekul močno upade (približno za velikostni razred) v prvi kinetični fazi po pulzu; kljub temu pa ima dominantni prispevek k skupnemu transportu zadnja kinetična faza, saj traja najdlje. Neumann in sodelavci so opazili še en počasnejši kinetični proces s časovno konstanto reda 100 s (Neumann *et al.*, 1998).

Pomemben vpogled v mehanizme transporta predstavlja tudi časovno in prostorsko razločena vizualizacija transporta v osamljene celice med in po pulzu. Gabriel in Teissié sta s hitro video-mikroskopijo (300 slik/s) preučevala transport pozitivno nabitih kalcijevih ionov, propidijevega jodida in etidijevega bromida med aplikacijo električnih pulzov z dolžinami nekaj ms (Gabriel in Teissié, 1998a, 1999). Njuni rezultati so pokazali, da med pulzom transport ionov/molekul poteka le z anodne strani, kar je skladno z elektroforetskim transportom pozitivno nabitih delcev (Li in Lin, 2011). Po pulzu molekule vstopijo tudi s katodne strani, pod pogojem da je bila tudi katodna stran celične membrane elektroporirana. S primerno izbrano amplitudo pulzov je namreč mogoče zaznati transport samo prek anodne strani membrane (Mehrle *et al.*, 1985; Tekle *et al.*, 1990; Gabriel in Teissié, 1998b). Meritve s propidijevim jodidom in etidijevim bromidom so se izkazale tudi za zelo učinkovite

pri merjenju površine permeabilizirane regije, saj ti barvili povečata fluorescenco pri interakciji s permeabilizirano membrano. Velikost permeabilizirane regije je na anodni strani večja kot na katodni, kar je skladno s tem, da se na anodni strani vzpostavi višja napetost zaradi vpliva mirovalne TMN. S povečevanjem jakosti električnega polja (torej vsiljene TMN) se veča tudi površina permeabiliziranega območja membrane, kar je v skladu s pragovnim značajem elektroporacije (Gabriel in Teissié, 1997, 1998b, 1999).

Asimetrijo v transportu prek anodne in katodne strani celice so opazili tudi drugi raziskovalci (Mehrle *et al.*, 1985; Kinosita *et al.*, 1991; Tekle *et al.*, 1990, 1994). Nekatere študije so celo pokazale, da je smer asimetrije (večji transport bodisi z anodne bodisi s katodne strani) odvisna od parametrov pulza in od ionske koncentracije zunajceličnega medija (Kinosita *et al.*, 1991; Tekle *et al.*, 1994). Vendar pa te meritve niso bile opravljene tekom pulza, temveč nekaj deset milisekund po pulzu.

V nasprotju s pulzi dolžin v razponu µs–ms, ki povzročijo transport prek "polov" celic, naj bi nanosekundni pulzi povzročili t. i. supraelektroporacijo: nastanek majhnih, približno 1 nm velikih por, praktično vzdolž celotne celične membrane in membran celičnih organelov (Gowrishankar *et al.*, 2006; Vasilkoski *et al.*, 2006). Ker so nastale pore v membrani zelo majhne, naj bi molekule le s težavo prehajale "supraelektroporirano" membrano. Ta teoretična predpostavka je ponudila fizikalno razlago za množico eksperimentalnih študij, ki so poročale odsotnost detekcije transporta molekul, ki drugače brez težav prehajajo membrano pri elektroporaciji z µs–ms pulzi (Vernier *et al.*, 2006; Pakhomov *et al.*, 2007a; Bowman *et al.*, 2010; Nesin *et al.*, 2011). Selektiven transport povezan z velikostjo molekul pa je sicer mogoče opaziti tudi pri µs–ms pulzih, saj je potrebno povečati amplitudo, dolžino in/ali število pulzov za detekcijo transmembranskega transporta večjih molekul (Zimmermann *et al.*, 1976; Kinosita in Tsong, 1977b; Escande-Géraud *et al.*, 1988; Rols in Teissié, 1989).

Mnogo kompleksnejši od transporta majhnih molekul je transport makromolekul. Makromolekule, kot je npr. siRNA, za razliko od manjših molekul prehajajo celično membrano le tekom pulza (Rols in Teissié, 1998; Paganin-Gioanni *et al.*, 2011). Transport DNA je še posebej karakterističen. Zadnje študije nakazujejo, da transport DNA po elektroporaciji pretežno poteka preko endocitoze (Golzio *et al.*, 2002; Rosazza *et al.*, 2012; Markelc *et al.*, 2015). V splošnem je endocitoza, stimulirana s strani električnih pulzov, znan pojav, do katerega pride že pri amplitudah pulzov, ki so prenizke za elektroporacijo membrane (Lin *et al.*, 2011; Ben-Dov *et al.*, 2012).

1.5 Celjenje membrane po dovajanju električnih pulzov

V prejšnjem podpoglavju smo izključno govorili o transportu molekul prek membrane, ne pa tudi o povišanju električne prevodnosti membrane. Slednje je karakteristično zelo podobno kot pri modelnih lipidnih sistemih (Kinosita in Tsong, 1979; Benz in Zimmermann, 1980, 1981; Chernomordik *et al.*, 1987; Hibino *et al.*, 1993; Pavlin *et al.*, 2007). Podobno, kot velja pri detekciji transporta molekul: če TMN doseže določeno vrednost, se lahko prevodnost membrane poveča za več velikostnih razredov, v času krajšem od 1 µs, nato pa tekom pulza postopoma narašča. Ko je pulza konec, se prevodnost membrane povrne praktično na svojo osnovno vrednost, v času največ nekaj µs.

Določene spremembe pa ostanejo v membrani prisotne daljši čas po pulzu, kar je mogoče opaziti tako pri celičnih membranah kot tudi pri preprostih lipidnih dvoslojih. Te spremembe se odražajo v časovnem poteku povečanja prevodnosti membrane med dvema zaporednima pulzoma. V primeru, da sta pulza razmaknjena za manj kot nekaj 10 ms do sekund (odvisno od tipa membrane), je časovni potek povečanja prevodnosti membrane v drugem pulzu spremenjen glede na prvi pulz. V nasprotnem primeru pa je časovni potek povečanja prevodnosti med obema pulzoma enak. Ta "spomin" so pri lipidnih sistemih povezali s t. i. predporami (Maček-Lebar *et al.*, 2002; Melikov *et al.*, 2001; Kotulska *et al.*, 2010). Zanimivo je dodati, da časovni razpon 10 ms–1 s sovpada tudi s prvima dvema kinetičnima procesoma transporta propidijevega jodida po pulzu, kot so ju zaznali Pucihar in sodelavci (Pucihar *et al.*, 2008). Zdi se torej, da bi lahko procese, ki se dogajajo med pulzom in v kratkem času po pulzu, brez težav povezali z nastankom vodnih por v lipidnih domenah membrane.

Težje pa je razložiti dolgotrajno povečanje prepustnosti membrane po pulzu, ki lahko traja od nekaj deset sekund do nekaj minut, pri temperaturi 4 °C pa celo nekaj ur (Lopez *et al.*, 1988; Saulis *et al.*, 1991; Shirakashi *et al.*, 2004; Pucihar *et al.*, 2008; Saulis in Saulė, 2012). Poleg temperature je čas celjenja celične membrane odvisen tudi od drugih pogojev: med drugim od parametrov pulzov (Rols in Teissié, 1989, 1998), integritete citoskeleta (Rols in Teissié, 1992) in fluidnosti membrane (Kandušer *et al.*, 2006). Poleg tega je bilo pokazano, da celjenje membrane po elektroporaciji vključuje tudi intrinzične celične mehanizme popravljanja membrane (Huynh *et al.*, 2004).

Medtem, ko bi prvo, hitro fazo celjenja, lahko pripisali pasivnemu zapiranju por v lipidnem dvosloju, se med drugo, dolgo fazo celjenja, lahko odvijajo tudi drugačne strukturne spremembe (Wegner *et al.*, 2015). Molekularni mehanizem teh dolgoživih strukturnih sprememb sicer ni povsem pojasnjen. Lahko pa bi ga med drugim povezali s spremembami konformacije proteinov (Teissié *et al.*, 2005), peroksidacijo lipidov (Leguèbe *et al.*, 2014), stabilizacijo por zaradi anizotropnih inkluzij (Fošnarič *et al.*, 2003) in mehanskimi silami na membrano, ki nastanejo zaradi osmotskega neravnovesja med zunanjostjo in notranjostjo celice (Joshi in Hu, 2012).

1.6 Elektroporacija od celice do tkiva

Elektroporacija obsega širok spekter aplikacij, ki sega od elektroporacije posameznih celic pa vse do elektroporacije tkiva. Elektroporacija celic v tkivu je kompleksna, saj je tkivo heterogena struktura, s tem pa je tudi porazdelitev električnega polja v tkivu neenakomerna. Kljub temu pa je tudi elektroporacija tkiva pogojena z elektroporacijo individualnih celic v tkivu. Za učinkovito načrtovanje aplikacij, ki vključujejo elektroporacijo tkiv (različne terapije v medicini in tehnološki procesi na rastlinskih tkivih v industriji), moramo torej najprej razumeti elektroporacijo tam kjer se začne – pri celici. Osnovne karakteristike elektroporacije celice smo opisali že v podpoglavjih 1.3–1.5. Tukaj pa bomo nadaljevali z opisom elektroporacije celic v različnih skupkih, vse tja do tkiva.

Celica, izpostavljena električnemu polju lokalno spremeni porazdelitev polja v svoji okolici. Če so celice dovolj daleč narazen, se ne "čutijo"; če pa jih postavimo blizu skupaj, postane električno polje v njihovi okolici

spremenjeno. Najenostavnejša konfiguracija skupka celic, ki si jo lahko zamislimo, sta dve okrogli celici v homogenem električnem polju, poravnani v smeri električnega polja ali v smeri pravokotno na polje. Numerični izračun TMN napoveduje, da je v primerjavi z osamljeno celico maksimalna dosežena TMN manjša v paralelni konfiguraciji, ter večja v pravokotni konfiguraciji (Susil *et al.*, 1998). Henslee in sodelavci so to napoved postavili pod eksperimentalni test in ugotovili, da se jakost električnega polja, potrebnega za elektroporacijo para celic spremeni za ~5–10 % v primerjavi z osamljeno celico, kar se dobro sklada s teoretičnimi napovedmi (Henslee *et al.*, 2014). Vendar so avtorji poudarili tudi pomembnost dinamike spreminjanja prevodnosti celičnih membran, saj preprosti izračuni vsiljene TMN brez upoštevanja povečanja prevodnosti membrane niso mogli pojasniti vseh njihovih eksperimentalnih opažanj.

Naslednja kompleksnejša organizacija celic, ki se pogosto uporablja pri elektrozlivanju, so celice urejene v verigo in poravnane z električnim poljem. Podobno kot za dve celici postavljeni vzporedno z električnim poljem, numerični izračuni napovedujejo, da se TMN v okolici stika med celicami zmanjša (Susil *et al.*, 1998). Vendar se ta situacija spremeni, če so celice izpostavljene električnemu polju v nizkoprevodnem mediju. Na začetku prehodnega pojava (torej dokler se celične membrane še elektrijo) je TMN ravno na stiku med celicami najvišja, kar je posledica lokalnega povečanja električnega polja. To ugotovitev smo uporabili v študiji zlivanja celic z nanosekundnimi električnimi pulzi, kot bo opisano v podpoglavju 3.2 (Rems *et al.*, 2013).

Še korak dlje k kompleksnosti predstavljajo goste celične suspenzije. Lokalna porazdelitev električnega polja se zaradi bližine celic tudi v tem primeru spremeni (Susil *et al.*, 1998; Pavlin *et al.*, 2002). Po napovedih numeričnih izračunov se TMN "potlači" na polih posamezne celice v suspenziji, maksimalna TMN pa se v najbolj gostih suspenzijah zmanjša za faktor 1.5 v primerjavi s TMN na osamljeni celici. Skladno s to teoretično napovedjo poskusi pokažejo, da je potrebno goste celične suspenzije elektroporirati s pulzi višje amplitude (Canatella *et al.*, 2001; Pucihar *et al.*, 2007). Obenem se transport molekul v celice zmanjša, saj ozki medcelični prostori otežujejo prosto difuzijo molekul, hkrati pa medcelični prostori zagotavljajo le majhen rezervoar molekul. Omejena difuzija je predvsem izrazita, kadar se pojavi osmotsko nabrekanje celic po izpostavitvi pulzom (Pavlin *et al.*, 2005; Pucihar *et al.*, 2007)

Zanimivi so tudi poskusi na majhnih skupkih pritrjenih celic. Ko je skupek izpostavljen nizkemu električnemu polju, ki ne vodi do elektroporacije, se celice v skupku zaradi ionskih povezav med citoplazmami obnašajo kot ena sama velika celica. Ko pa je skupek izpostavljen elektroporacijskemu pulzu, je napetost na membranah tako visoka, da blokira ionske povezave, zaradi česar se med pulzom posamezne celice v skupku obnašajo kot individualne celice. To omogoča elektroporacijo in posledično prehajanje molekul prek območij membran, kjer so celice v stiku (Kotnik *et al.*, 2010, 2011).

Od majhnih celičnih skupkov lahko preidemo na površinski sloj celic. V takem sloju so celice nepravilnih oblik, njihova velikost in orientacija pa je močno heterogena. To ima vpliv na elektroporacijo posameznih celic v površinskem sloju, saj je pri postopnem povečevanju jakosti električnega polja moč opaziti, da imajo celice, ki so večje in orientirane v smeri električnega polja tendenco, da se elektroporirajo pri nižjih jakostih električnega polja (Valič *et al.*, 2003). Vnos molekul v posamezne celice površinskega sloja pa je manjši kot pri celicah v

suspenziji, delno zaradi zmanjšane difuzije molekul v medceličnih prostorih, delno pa zaradi manjše površine membrane, prek katere lahko molekule prehajajo (Pucihar *et al.*, 2008). Velik del površine celičnih membran je namreč pritrjen na podlago.

Površinski sloj celic lahko ponudi vpogled, kako heterogenost porazdelitve celic vpliva na elektroporacijo posameznih celic v sloju. Vendar pa je struktura površinskega sloja celic še vedno daleč od kompleksne strukture tkiva. Vmesno stopnjo kompleksnosti predstavljajo tridimenzionalni multicelični sferoidi, katerih struktura vsebuje tako celične povezave kot zunajcelični matriks (Sutherland, 1988; Santini *et al.*, 2000). Na podlagi rezultatov poskusov, ki so bili opravljeni na sferoidih, lahko ugotovimo naslednje. Po elektroporaciji je vnos molekul v celice sferoida močno zmanjšan v primerjavi z vnosom molekul v goste celične suspenzije (Canatella *et al.*, 2004; Chopinet *et al.*, 2012). Poleg tega je vnos v celice na periferiji sferoida večji kot v notranjosti sferoida (Canatella *et al.*, 2004; Gibot *et al.*, 2013). Razlog za to lahko vsaj delno pripišemo heterogeni strukturi celic v sferoidu, saj se velikost celic postopoma zmanjšuje proti notranjosti sferoida (Canatella *et al.*, 2004; Gibot in Rols, 2013). Heterogenost strukture je posledica drugačnega mikrookolja v notranjosti sferoida v primerjavi z njegovo periferijo. Vpliv na elektroporacijo celic v sferoidu pa ima lahko tudi "starost" sferoida in tip celic v sferoidu (Gibot in Rols, 2013; Marrero in Heller, 2012).

Naj povzamemo ugotovitve v zgoraj opisanih študijah. Celice v različnih skupinah se odzovejo na električne pulze na podoben način kot osamljene celice, vendar moramo upoštevati lokalne spremembe v električnem polju, ki so posledica bližine sosednjih celic ter sprememb v prevodnosti celičnih membran. S tem ugotovimo, da lahko znanje o celični elektroporaciji, ki ga pridobimo s poskusi na osamljenih celicah, prenesemo tudi na bolj kompleksne ureditve celic. Pri tem je potrebno upoštevati velikost, obliko in orientacijo posameznih celic v dani strukturi ter susceptibilnost posameznih celic na električne pulze. Pri molekularnem transportu prek membran pa je pomembno, da upoštevamo omejeno difuzijo molekul ter majhen rezervoar molekul v ozkih medceličnih prostorih.

V splošnem si torej lahko predstavljamo, da bi zgradili model tkiva s sestavljanjem posameznih celic. Kljub temu, da je v tej smeri dosežen že precejšnji napredek (Mezeme *et al.*, 2012a, 2012b), pa običajno še vedno modeliramo posamezna tkiva kot homogene strukture, ki jim pripišemo povprečne električne lastnosti, tj. prevodnost in dielektričnost (Gabriel *et al.*, 1996). Razloga za to sta vsaj dva. Prvi je ta, da je računska zahtevnost modelov, ki bi predstavljali vsako posamezno celico v tkivu visoka. Drugi razlog pa je žal povezan z našim pomanjkanjem znanja o tem, kako različne strukture v tkivu prispevajo k skupnim povprečnim lastnostim tkiva. Pomemben napredek v tej smeri so naredili Huclova in sodelavci z modelom različnih slojev kože, pri čemer so lastnosti vsakega sloja povezali s pripadajočo strukturo in obliko celic (Huclova *et al.*, 2010, 2011, 2012).

Pri obravnavi tkiva kot homogene celote je zelo enostavno izračunati povprečno porazdelitev električnega polja med elektrodami. Vendar pa pri elektroporaciji tkiva situacija ni tako enostavna, saj se zaradi povečanja prevodnosti celičnih membran poveča tudi prevodnost tkiva. V primeru, da električne pulze v tkivo dovedemo prek igelnih elektrod, je porazdelitev električnega polja med elektrodami nehomogena. Na območjih, kjer je

električno polje najvišje, se celice najprej elektroporirajo, kar poveča prevodnost tkiva na tistem območju. Lokalno povečanje prevodnosti pa povzroči, da se zviša električno polje na sosednjih neelektroporiranih območjih. Elektroporacija tako med pulzom "propagira", kar je potrebno upoštevati pri numeričnih izračunih načrtovanja terapij kot dinamično prevodnost odvisno od jakosti električnega polja $\sigma(E)$ (Šel *et al.*, 2005; Čorović *et al.*, 2013).

Pomembnost teoretičnega modeliranja elektroporacije se predvsem izkaže pri aplikacijah elektroporacije, kjer je preživetje celic ključnega pomena, na primer pri genski transfekciji, zlivanju celic, krioprezervaciji hrane ter elektroporaciji tkiva v bližini vitalnih struktur, kot so živci in glavne žile (Mir, 2009; Chopinet *et al.*, 2012; Yanai *et al.*, 2013; Gouaillier-Vulcain *et al.*, 2015; Shayanfar *et al.*, 2014; Phoon *et al.*, 2008; Kos *et al.*, 2015). Najtežjo nalogo predstavljajo heterogena tkiva, saj je porazdelitev električnega polja in s tem elektroporacija posameznih celic v tkivu odvisna od njihove razporeditve, oblike, velikosti, orientacije, ter drugih prevodnih poti, ki jih ne moremo videti s prostim očesom. Zato tudi ne moremo natančno predvideti električnega polja brez pomoči modeliranja. Zgoraj smo omenili tudi pomembnost dinamičnih sprememb prevodnosti v tkivu. Čeprav lahko fenomenološko opišemo odvisnost prevodnosti tkiva od jakosti električnega polja, je to v principu potrebno narediti za vsako tkivo posebej. Povečanje prevodnosti tkiva med pulzom je namreč v prvi vrsti posledica elektroporacije celic znotraj tkiva. Veliko bolj splošen pristop bi torej bil razvoj modelov, ki povezujejo makroskopske spremembe v prevodnosti tkiva s spremembami prevodnosti celičnih membran. K takšnemu razvoju numeričnega modela tkiva smo pristopili v študiji, ki bo predstavljena v podpoglavju 3.3. Za razumevanje strukturnih sprememb v celični membrani, ki povečajo samo prevodnost membrane, pa se je potrebno spustiti vse do molekularnega nivoja membrane, kar opisuje naslednje podpoglavje.

1.7 Teoretični modeli elektroporacije

V splošnem vsak namen uporabe elektroporacije zahteva prilagoditev eksperimentalnega protokola in parametrov električnih pulzov (dolžine, amplitude, števila in ponavljalne frekvence). Ker je izvajanje eksperimentov časovno, tehnično in finančno zahtevno, predstavljajo teoretični modeli elektroporacije nepogrešljivo alternativo za raziskovanje vpliva različnih parametrov pulzov na celično membrano in prednost pri iskanju primernega eksperimentalnega protokola. Obenem lahko teoretične izračune uporabimo kot pomoč pri razlagi eksperimentalnih rezultatov.

Danes sta za raziskovanje elektroporacije na ravni lipidne membrane na voljo dva teoretična pristopa. Na eni strani so t. i. zvezni modeli elektroporacije, ki membrano opisujejo na makroskopskem nivoju v smislu homogenega materiala z določenimi mehanskimi in električnimi lastnostmi. Zvezni modeli predstavljajo časovno in prostorsko povprečje dogajanja na molekularnem nivoju in se uporabljajo za modeliranje elektroporacije celic, celičnih skupkov in preprostih modelov tkiva (Neumann *et al.*, 1998; Weaver in Chizmadzhev, 1996; Gowrishankar in Weaver, 2006; Neu in Krassowska, 1999, 2003; Miklavčič in Towhidi, 2010; Joshi in Schoenbach, 2000; Li *et al.*, 2013; Mezeme *et al.*, 2012a). Na drugi strani pa so simulacije molekularne dinamike, ki obravnavajo elektroporacijo s stališča gibanja lipidnih molekul po zakonih klasične

mehanike (Gurtovenko *et al.*, 2010; Delemotte in Tarek, 2012; Leontiadou *et al.*, 2004; Tarek, 2005; Gurtovenko in Vattulainen, 2007; Marrink *et al.*, 2001; Vernier *et al.*, 2013). Pri tem ločimo simulacije, ki opisujejo gibanje vsakega atoma posebej (angl. *all atom*), simulacije pri katerih so CH_2 skupine v lipidnih repih obravnavane kot en delec (angl. *united atom*) in simulacije, pri katerih je združevanje posameznih atomov še bolj grobo (angl. *coarse grain*) (Gurtovenko *et al.*, 2010).

1.7.1 Zvezni modeli elektroporacije

Teoretična obravnava pojava elektroporacije izhaja iz eksperimentalnih opažanj, da se pod vplivom električne napetosti ravninski lipidni dvosloj ireverzibilno mehansko poruši (Crowley, 1973; Abidor *et al.*, 1979). Ena od prvih hipotez o mehanizmu porušitve je temeljila na predpostavki, da lahko lipidno membrano obravnavamo kot tanek sloj dielektričnega in elastičnega materiala, na katerega električna TMN deluje s kompresijsko silo. Ko TMN preseže kritično vrednost, postane pritisk na membrano zaradi električne sile večji, kot mu membrana lahko nasprotuje s svojo elastičnostjo. Rezultat je mehanska porušitev dvosloja (Crowley, 1973).

Kasneje je bila zgornja hipoteza ovržena. V skladu s takrat novejšimi podatki o modulu elastičnosti lipidnega dvosloja je teoretična obravnava na podlagi zgornje hipoteze namreč predvidela znatno višjo kritično vrednost TMN za porušitev dvosloja od tistih, izmerjenih eksperimentalno (Abidor *et al.*, 1979). Abidor in sodelavci so pokazali tudi, da je porušitev lipidnega dvosloja stohastičen (in ne deterministčen) proces ter da je čas, v katerem se zgodi porušitev, odvisen od velikosti TMN. Njihove meritve so nadalje pokazale, da je porušitev dvosloja (v smislu povečanja membranske prevodnosti za več velikostnih razredov) v določenih primerih lahko reverzibilna, če je TMN na lipidnem dvosloju prisotna dovolj kratek čas. Kot mehanizem porušitve so predlagali nastanek majhnih vodnih por v lipidnem dvosloju, ki se pod vplivom TMN začnejo širiti. Ko ena od por doseže kritično velikost, postane njeno širjenje neomejeno, kar vodi v mehansko porušitev dvosloja.

Teoretični opis procesa so zasnovali na obstoječi teoriji porušitve tankih filmov milnice (angl. *black soap films*) (Abidor *et al.*, 1979). Za opis časovne dinamike širjenja in krčenja por v lipidnem dvosloju, so uporabili enačbo Smoluchowskega:

$$\frac{\partial n}{\partial t} = D_p \frac{\partial}{\partial r}\left(\frac{\partial n}{\partial r} + \frac{n}{kT}\frac{\partial \Delta W}{\partial r}\right) \tag{2}$$

pri čemer $n(r,t)$ predstavlja porazdelitveno funkcijo števila por v membrani glede na njihov radij r ob času t (Pastushenko *et al.*, 1979). Tako je $n\mathrm{d}r$ enako številu por v membrani z radijem med r in $r + \mathrm{d}r$. Parametra D_p in $\Delta W(r)$ sta difuzijska konstanta por v prostoru njihovih radijev in sprememba energije lipidnega dvosloja, ki je posledica nastanka pore, k je Boltzmannova konstanta, T pa temperatura. Enačba (1) v splošnem pravi, da se populacija por s časom spreminja zaradi termičnih fluktuacij molekul in zaradi delovanja posplošene sile $-\partial\Delta W/\partial r$, ki sili sistem k energetskemu minimum (Powell in Weaver, 1986).

Pri teoriji por ima sprememba energije ΔW ključno vlogo, saj določa časovno dinamiko por v prostoru njihovih radijev, hkrati pa naj bi bila z njo pogojena hitrost nastajanja in zapiranja por (Glaser *et al.*, 1988; Neu in Krassowska, 1999; Vasilkoski *et al.*, 2006; Weaver in Chizmadzhev, 1996; Weaver in Mintzer, 1981).

Sprememba energije je bila ocenjena na podlagi naslednje predpostavke. Predstavljajmo si, da iz membrane izrežemo majhen krog (poro) z radijem *r*. Na tem mestu se zmanjša mehanska površinska napetost membrane Γ, hkrati pa se pojavi nova mehanska površinska napetost vzdolž notranje stene pore, t. i. robna napetost (angl. *edge tension*) γ (Abidor *et al.*, 1979; Litster, 1975; Taupin *et al.*, 1975). Ob prisotnosti transmembranske (električne) napetosti U_m se z nastankom pore spremeni tudi kapacitivna energija membrane, saj je pora napolnjena z vodo, ki ima višjo dielektrično konstanto kot lipidi. Če predpostavimo, da je pora neprevodna in ima obliko valja, lahko skupno spremembo energije zapišemo kot:

$$\Delta W = 2\pi r\gamma - \pi r^2 \Gamma - \pi r^2 \frac{(\varepsilon_w - \varepsilon_l)\varepsilon_0}{2d_m} U_m^{\ 2} \tag{3}$$

pri čemer je d_m debelina membrane, ε_w in ε_l relativni dielektrični konstanti vode in lipidov, ε_0 pa dielektričnost vakuuma (Abidor *et al.*, 1979). Ker so Abidor in sodelavci pri teoretični analizi svojih meritev ugotovili, da je nastajanje in zapiranje por relativno počasen proces, so sklepali da verjetno obstajata dva tipa por, in sicer hidrofobne ter hidrofilne (Abidor *et al.*, 1979). Na začetku naj bi v membrani nastala hidrofobna pora, pri kateri so lipidni repi neposredno izpostavljeni vodnim molekulam. Hidrofobna pora pa naj bi se pri določeni velikosti pretvorila v hidrofilno poro, pri kateri se lipidne glave reorientirajo v notranjost pore in zaščitijo lipidne repe pred izpostavitvijo vodi. Ta reorientacija lipidov pa naj bi zahtevala dodaten vložek energije.

Pomemben prispevek k razvoju modelov elektroporacije v zadnjih 15 letih sta prispevala Neu in Krassowska (Neu in Krassowska, 1999, 2003). Ker je enačba Smoluchowskega numerično zahtevna za reševanje, poleg tega pa vsebuje veliko število parametrov, katerih vrednosti so znane le na velikostni red natančno, sta predlagala asimptotično redukcijo parcialne diferencialne enačbe Smoluchowskega v navadno diferencialno enačbo (DeBruin in Krassowska, 1999; Neu in Krassowska, 1999). Ta je povzemala hitrost nastajanja in zapiranja por, vendar je temeljila na predpostavki, da so vse pore v membrani enako velike. Zaradi te omejitve sta kasneje svoj asimptotični model razširila s še eno navadno diferencialno enačbo, ki opisuje širjenje in krčenje vsake posamezne pore (Neu in Krassowska, 2003; Smith *et al.*, 2004). Pomembna prednost njunih izpeljav je, da so navadne diferencialne enačbe načeloma numerično lažje rešljive in zahtevajo manj računalniškega časa.

1.7.2 Simulacije molekularne dinamike

Leta 2001 so Marrink in sodelavci (Marrink *et al.*, 2001) opazili nastanek razmeroma stabilne pore pri simulacijah spontanega sestavljanja lipidov v lipidni dvosloj. Pora je imela podobno strukturo, kot so jo predpostavljali že zvezni modeli elektroporacije – toroidna oblika pore z okoliškimi lipidnimi glavami v steni pore. Omenjena študija je povzročila razmah nadaljnjih študij nastanka in širjenja por v lipidnem dvosloju pod vplivom različnih zunanjih delavnikov: električnega polja (Tarek, 2005; Tieleman, 2004; Vernier in Ziegler, 2007; Ziegler in Vernier, 2008), neravnovesja ionov na obeh straneh dvosloja (torej vsiljene TMN) (Delemotte in Tarek, 2012; Gurtovenko in Vattulainen, 2007) in mehanske površinske napetosti membrane (Leontiadou *et al.*, 2004). S stališča zveznih modelov elektroporacije je eden od pomembnejših prispevkov omenjenih simulacij ravno potrditev nastanka in širjenja por v lipidnem dvosloju pod vplivom električnega polja ter sposobnost prevajanja ionov skozi pore.

Vse več nadaljnjih simulacij je bilo usmerjenih v pridobivanje rezultatov, ki jih lahko primerjamo s predpostavkami zveznih modelov elektroporacije. Raziskovalci so izračunali kritično vrednost mehanske površinske napetosti membrane za porušitev dvosloja (Leontiadou *et al.*, 2004) in mehansko robno napetost lipidnega dvosloja (Jiang *et al.*, 2004), določili so energijo por v odvisnosti od velikosti por v odsotnosti TMN (Wohlert *et al.*, 2006), identificirali so posamezne faze pri nastanku in zapiranju pore in kako so le-te odvisne od električnega polja (Levine in Vernier, 2010, 2012). Preučevali so odvisnost časa, ki je potreben za nastanek por, od jakosti električnega polja, kateremu je izpostavljen lipidni dvosloj (Kandasamy in Larson, 2006; Bockmann *et al.*, 2008; Ziegler in Vernier, 2008; Levine in Vernier, 2012; Gurtovenko in Lyulina, 2014). Ugotovili so, da lahko opazujemo pore stabilne velikosti, če po nastanku pore ustrezno zmanjšamo jakost električnega polja (Fernández *et al.*, 2012). Velikost pore je potem pogojena z jakostjo znižanega električnega polja. Na ta način stabilizirane pore omogočajo podrobnejšo analizo strukture pore in preučevanje prevodnosti por za različne ione (Ho *et al.*, 2013). V nasprotnem primeru (pri konstantnem električnem polju) ni mogoče opazovati stabilnih por, saj pore zelo hitro narastejo na velikost simulacijskega območja. Ne nazadnje pa so se v nekaj raziskavah dotaknili tudi vprašanja, kako na elektroporacijo vplivajo v dvosloj vgrajeni proteini in kako poteka transport DNA in RNA molekul prek por (Breton *et al.*, 2012; Siu in Böckmann, 2007; Tarek, 2005).

Čeprav danes prevladuje mnenje, da se med elektroporacijo v membrani ustvarijo majhne, za ione in molekule prepustne pore, razvoj eksperimentalnih metod, ki bi omogočale njihovo vizualizacijo le počasi napreduje (Szabo in Wallace, 2015). Večina mikroskopskih tehnik namreč ne omogoča ustreznega kontrasta, časovne in prostorske ločljivosti, ki bi omogočale opazovanje teh kratkoživih in dinamičnih nanometrskih struktur v lipidnem dvosloju. Razvoj zveznih modelov elektroporacije je zato temeljil na posrednih eksperimentalnih podatkih, ki obsegajo merjenje toka in porušitvene napetosti ravninskih lipidnih dvoslojev (Abidor *et al.*, 1979; Glaser *et al.*, 1988; Kramar *et al.*, 2007), elektro-optična merjenja na lipidnih veziklih (Kakorin *et al.*, 1996), merjenje toka prek celične membrane z metodo vpete krpice membrane (angl. *patch clamp*) (Melikov *et al.*, 2001; Pakhomov *et al.*, 2007a), merjenja prevodnosti celičnih suspenzij (Pavlin *et al.*, 2005), merjenja vsiljene TMN s fluorescentnimi barvili (Frey *et al.*, 2006; Hibino *et al.*, 1991) in opazovanja transporta molekul prek celičnih membran ali membran lipidnih veziklov (Gabriel in Teissié, 1999; Kotnik *et al.*, 2010; Neumann *et al.*, 1998).

Ker se je razvoj zveznih modelov, ki opisujejo elektroporacijo s stališča nastanka por, začel približno dve desetletji preden so postale računsko zahtevne simulacije molekularne dinamike na voljo, so morali raziskovalci podatke o obliki por, njihovi prevodnosti za ione in prepustnosti za molekule "ugibati". Čeprav simulacije molekularne dinamike danes ponujajo nepogrešljiv vpogled v elektroporacijo na molekularni ravni, pa imajo tudi te svoje omejitve. Zaradi računske zahtevnosti simulacij lahko opazujemo le majhen košček lipidnega dvosloja z nekaj 100 lipidi, v časovnem oknu, ki obsega do nekaj 100 ns. Obenem so rezultati simulacij lahko odvisni od izbire sklopa parametrov, ki opisujejo interakcije med posameznimi atomi (angl. *force field*) (Fernández *et al.*, 2010).

Za ovrednotenje veljavnosti predpostavk zveznih modelov elektroporacije je torej potrebna njihova primerjava z izsledki, ki jih lahko ponudijo simulacije molekularne dinamike. Velja tudi obratno. Primerjava rezultatov

simulacij molekularne dinamike z napovedmi zveznih modelov ter primerjavo slednjih z eksperimentalnimi rezultati na ravninskih lipidnih dvoslojih ali celicah lahko prispeva k ovrednotenju rezultatov simulacij molekularne dinamike. Pogosto je namreč enostavneje primerjati eksperimentalne rezultate z napovedmi zveznih modelov kot neposredno z molekularno dinamiko (npr. meritev toka prek ravninskega lipidnega dvosloja ali celične membrane, kvantitativna ocena števila transportiranih molekul prek membrane) (Kramar *et al.*, 2007; Dehez *et al.*, 2014; Polak *et al.*, 2015).

2 Namen disertacije

Numerično modeliranje elektroporacije kot komplementarna metoda eksperimentom *in vitro*

Glavni namen gradnje in razvoja modelov elektroporacije je preverjanje popolnosti našega znanja o pojavu in njihova uporaba za načrtovanje z elektroporacijo povezanih tehnologij in terapij. Pri načrtovanju eksperimentalnih protokolov si namreč želimo v čim večji meri izkoristiti karakteristike samega pojava elektroporacije. Modeli elektroporacije nam lahko dajo teoretični vpogled v učinkovitost določenega eksperimentalnega protokola in možnost, da ta protokol ustrezno optimiziramo. V doktorski disertaciji sem uporabila numerično modeliranje elektroporacije kot komplementarno metodo eksperimentalnim študijam pri naslednjih aplikacijah elektroporacije: (i) uporabi nanosekundnih električnih pulzov za kontrolo izlitja učinkovin iz liposomov, ko so ti dostavljeni v tarčne celice; (ii) uporabi nanosekundnih pulzov za zlivanje celic, predvsem v protokolih, kjer se celice močno razlikujejo v velikosti; (iii) elektroporaciji špinačnega lista pri krioprezervaciji špinače.

Primerjava predpostavk modelov elektroporacije z izsledki simulacij molekularne dinamike

Razvoj zveznih modelov elektroporacije je temeljil na meritvah toka, transmembranske napetosti in transporta molekul prek membrane, pri čemer natančno dogajanje na molekularnem nivoju membrane ni bilo znano. V zadnjem desetletju naše znanje dopolnjujejo številni rezultati simulacij molekularne dinamike, ki jih lahko primerjamo s predpostavkami zveznih modelov elektroporacije. Te rezultate je potrebno sistematično analizirati in identificirati manjkajoče podatke, ki bi pripomogli k validaciji zveznih modelov na podlagi simulacij molekularne dinamike. Možna razhajanja med predpostavkami zveznih modelov in izsledki simulacij molekularne dinamike lahko postanejo osnova za nadgradnjo zveznih modelov. Eden od pomembnejših parametrov modelov elektroporacije je prevodnost pore in njena odvisnost od velikosti pore. V doktorski disertaciji sem zato zgradila numerični model prevajanja ionov skozi lipidno poro in primerjala rezultate numeričnega modela z rezultati simulacij molekularne dinamike.

3 Rezultati in diskusija

Spodaj so opisane posamezne študije, ki sem jih v okviru doktorske disertacije opravila v sodelovanju s soavtorji. Pri vsaki študiji so na kratko opisane tudi metode dela.

3.1 Elektroporacija znotrajceličnih liposomov z nanosekundnimi pulzi

Liposomi so fosfolipidni vezikli, ki so bili predstavljeni kot potenciali prenašalci učinkovin v 70-ih letih prejšnjega stoletja (Gregoriadis in Ryman, 1971). Liposomi imajo tako hidrofilno kot hidrofobno domeno (notranjost liposoma in membrano), zato lahko prenašajo hidrofilne, hidrofobne, in amfifilne molekule. Njihova primarna vloga je, da ščitijo učinkovino pred "sovražnim" okoljem, v katerem bi učinkovina lahko izgubila svojo funkcijo (npr. v krvi), ter da ščitijo organizem pred toksičnimi posledicami učinkovine (Hillaireau in Couvreur, 2009). Vendar je njihova največja omejitev, da niso stabilni in lahko razpadejo preden pridejo do tarčnih celic v telesu (Benvegnu *et al.*, 2009). Zaradi potrebe po večji stabilnosti so tako začeli izdelovati liposome iz naravnih ali sintetičnih arhaealnih lipidov (arheosomov) ter drugih sintetičnih polimerov (Benvegnu *et al.*, 2009; Hillaireau in Couvreur, 2009). Slabost takih veziklov pa je, da ko pridejo v tarčno celico, spustijo učinkovino šele več ur po tem, ko so vstopili.

Ker nanosekundni električni pulzi omogočajo elektroporacijo znotrajceličnih organelov, smo želeli preverili, če bi jih lahko potencialno uporabili kot metodo za kontrolirano izlitje učinkovine iz liposomov, ko ti enkrat vstopijo v tarčno celico (Retelj *et al.*, 2013). V ta namen smo zgradili numerični model celice z znotrajceličnim jedrom in majhnimi liposomi, postavljenimi na različnih mestih znotraj celice, ter modelirali izpostavitev celice nanosekundnemu električnemu pulzu (slika 3.1).

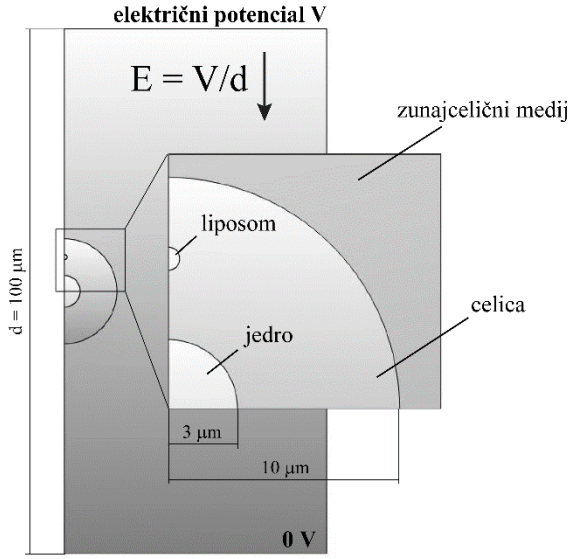

Slika 3.1: Model liposoma znotraj celice z jedrom. Geometrija modela je aksisimetrična, pri čemer predstavlja os simetrije leva stranica. Celica je postavljena v zunajcelični medij, ki ga predstavlja pravokotnik, katerega zgornja in spodnja stranica modelirata elektrodi. Zgornji stranici je pripisan izbrani potek električnega potenciala, ki modelira električni pulz, spodnji stranici pa je pripisan električni potencial 0 V. Na sredini celice se nahaja koncentrično postavljeno okroglo celično jedro; na sredini med jedrno in celično membrano pa se nahaja liposom. Vzeto iz Retelj *et al.* (2013).

Pri gradnji modela smo uporabili metodo končnih elementov, ki je na voljo v programskem okolju Comsol Multiphysics. Porazdelitev električnega polja v posameznih domenah modela (zunajcelični medij, citoplazma, notranjost jedra, notranjost liposoma) smo določili z rešitvijo Laplaceove enačbe za električni potencial V

$$-\nabla\left(\sigma_i \nabla V\right) - \nabla \frac{\partial\left(\varepsilon_i \nabla V\right)}{\partial t} = 0 \tag{9}$$

kjer σ_i in ε_i določata prevodnost in dielektričnost posamezne domene. Membrane celice, jedra in liposoma smo modelirali z robnim pogojem

$$\boldsymbol{n} \cdot \boldsymbol{J} = \frac{\sigma_m}{d_m} U_m + \frac{\varepsilon_m}{d_m} \frac{\partial U_m}{\partial t} \tag{10}$$

kjer je $\boldsymbol{n}$ enotski vektor v smeri normale na površino membrane, $\boldsymbol{J}$ gostota električnega toka, U_m transmembranska napetost, določena kot razlika električnih potencialov na notranji in zunanji strani membrane, σ_m, ε_m, in d_m, pa so prevodnost, dielektričnost in debelina membrane. Spremembo prevodnosti celične membrane kot posledico elektroporacije smo vgradili v model s teoretičnim pristopom, ki sta ga predlagali DeBruin in Krassowska (1999).

Model smo predvsem želeli uporabili za teoretični vpogled, ali lahko dosežemo elektroporacijo liposomov, ne da bi pri tem prekomerno poškodovali celico. Hkrati pa smo želeli ugotoviti, pri kakšnih eksperimentalnih pogojih bi bila elektroporacija liposomov najbolj učinkovita. Tako smo naredili parametrično študijo, kjer smo preverili, kako vplivajo različni parametri modela na elektroporacijo celice, jedra in liposomov, ko naš model izpostavimo nanosekundnemu električnemu pulzu. V parametrični študiji smo najprej določili sklop osnovnih parametrov modela, nato pa smo izbrali enega od parametrov in ga spreminjali v eksperimentalno relevantnem območju. Osnovni parametri in razpon, v katerem smo jih spreminjali, so prikazani v Tabeli I.

Tabela I: Parametri modela

Parameter	Simbol	Osnovna vrednost	Razpon vrednosti
Radij celice	R_c (µm)	10	
Radij celičnega jedra	R_n (µm)	3	
Radij liposoma	R_{lip} (nm)		50–500
Debelina celične membrane	d_{pm} (nm)	5	
Debelina membrane jedra	d_{ne} (nm)	10	
Debelina membrane liposoma	d_{lm} (nm)	5	
Prevodnost zunajceličnega medija	σ_e (S·m^{-1})	1.2	0.01–1.6
Dielektričnost zunajceličnega medija	ε_e	72.3	
Prevodnost citoplazme	σ_{cp} (S·m^{-1})	0.5	0.1–1.3
Dielektričnost citoplazme	ε_{cp}	72.3	
Prevodnost celične membrane	σ_{pm} (S·m^{-1})	$3\cdot10^{-7}$	10^{-10}–10^{-4}
Prevodnost celične membrane	ε_{pm}	5	
Prevodnost nukleoplazme	σ_{np} (S·m^{-1})	1	$2\cdot \sigma_{cp}$
Dielektričnost nukleoplazme	ε_{np}	72.3	
Prevodnost jedrne membrane	σ_{ne} (S·m^{-1})	$1\cdot10^{-4}$	
Dielektričnost jedrne membrane	ε_{ne}	10	
Prevodnost notranjosti liposoma	σ_{lip} (S·m^{-1})	0.5	0.01–2
Dielektričnost notranjosti liposoma	ε_{lip}	72.3	
Prevodnost membrane liposoma	σ_{lm} (S·m^{-1})	$3\cdot10^{-7}$	
Dielektričnost membrane liposoma	ε_{lm}	2.1	2–5

Parametrična študija je pokazala, da na elektroporacijo liposomov vplivajo vsi parametri, razen osnovna prevodnost (neelektroporirane) celične membrane. To je smiselno, saj se po elektroporaciji znatno poviša prevodnost celične membrane, kar smo upoštevali v modelu. Najvplivnejši parameter med vsemi pa je velikost liposoma. Ker so liposomi majhni, je prehodni pojav naraščanja transmembranske napetosti na membrani liposoma zgolj ~10 ns ali krajši. Zato podaljševanje pulza preko 10 ns ne bi bistveno prispevalo k lažji elektroporaciji liposoma. Nasprotno pa bi daljši pulzi lahko bistveno bolj poškodovali celico, saj je iz številnih eksperimentalnih študij na temo elektroporacije celic z nanosekundnimi pulzi jasno razvidno, da imajo daljši nanosekundni pulzi večje citotoksične učinke (Ibey *et al.*, 2010a, 2011; Pakhomov *et al.*, 2004, 2007b; Stacey *et al.*, 2011). Ker pa je maksimalna napetost, ki se vzpostavi na membrani liposoma, močno pogojena z velikostjo liposoma (slika 3.2), lahko večje liposome elektroporiramo pri bistveno nižjih amplitudah nanosekundnega pulza. Ker se citotoksičnost nanosekundnih pulzov veča z amplitudo nanosekundnega pulza, je torej najugodnejše za dani protokol, da so liposomi čim večji. Parametra, ki ugodno prispevata k lažji elektroporaciji membrane liposoma (pri pulzu dolžine 10 ns) sta tudi višja prevodnost notranjosti liposoma ter višja prevodnost zunajceličnega medija, pri čemer sta oba parametra eksperimentalno enostavno dosegljiva. Preverili smo tudi vpliv položaja liposoma znotraj celice na njegovo elektroporacijo, vendar se je izkazal za nepomembnega v primerjavi z vplivom velikosti liposoma. V splošnem smo v študiji ugotovili, da je pri amplitudah pulza, kjer nekatere celice še niso podvržene citotoksičnim učinkov nanosekundnih pulzov (Pakhomov *et al.*, 2004; Ibey *et al.*, 2011), mogoče doseči elektroporacijo tudi majhnih liposomov z radijem 50 nm. Vendar to velja le pod pogojem, da elektroporacijski pulzi niso bistveno daljši od ~10 ns.

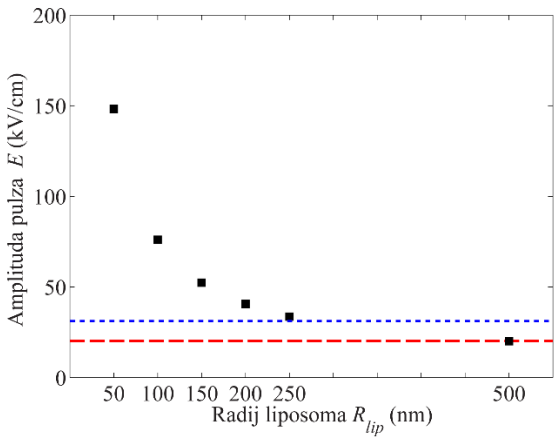

Slika 3.2: Amplituda pulza dolžine 10 ns, ki je potrebna za elektroporacijo liposomov različnih velikosti. Rdeča in modra vodoravna črta predstavljata amplitudo pulza, pri katerem model napove elektroporacijo celice in jedra. Vzeto iz Retelj *et al.* (2013).

Potrebno pa je poudariti, da smo pri naši študiji predpostavili, da se liposomi elektroporirajo pri TMN ~1 V. Bolj natančno, maksimalna TMN, ki se je vzpostavila na liposomu pri amplitudi pulza, za katerega smo predvideli, da pride do elektroporacije, je bila ~1.4 V. To predpostavko lahko primerjamo z eksperimentalnimi rezultati elektroporacije suspenzije liposomov z nanosekundnimi pulzi (Tekle *et al.*, 2005). Tekle in sodelavci so namreč

elektroporirali liposome zgrajene iz fosfolipidov DOPC, napolnjene z medijema dveh različnih prevodnosti (napolnjene z raztopino NaCl ali raztopino saharoze), tako da so jih izpostavili enemu pulzu dolžine 10 ns ter amplitude 80, 160 ali 240 kV/cm. Ugotovili so, da se noben tip liposomov ni elektroporiral pri 80 kV/cm, liposomi napolnjeni s slano raztopino so se elektroporirali pri 160 kV/cm, liposomi napolnjeni z raztopino saharoze pa šele pri 240 kV/cm. Da bi ugotovila, kakšna napetost se je vzpostavila na teh liposomih pri elektroporaciji, sem teoretično replicirala njihov eksperiment. Izračunala sem maksimalno TMN, ki bi se vzpostavila na osamljenem liposomu pri upoštevanju parametrov pulzov in prevodnosti raztopin uporabljenih v poskusu (Tekle *et al.*, 2005). Na ta način sem ocenila, da je bila maksimalna dosežena napetost na liposomu ~0.9 V (Rems in Miklavčič, 2015). S tem lahko ugotovimo, da so predvidene amplitude pulzov, potrebne za elektroporacijo liposomov, v naši študiji lahko celo rahlo pretirane. Kasneje so Polak in sodelavci objavil tudi rezultate študije simulacij molekularne dinamike, ki so pokazali, da se arhealni lipidi elektroporirajo pri približno 2–2.5 krat višji napetosti kot fosfolipidi DPPC (Polak *et al.*, 2014). Za elektroporacijo liposomov zgrajenih iz arhealnih lipidov (arheosomov), bi torej potrebovali višje amplitude pulzov za njihovo elektroporacijo. Poleg tega arheosomi vstopijo v celico z endocitozo (Batista Napotnik *et al.*, 2013), kar pomeni, da imajo arheosomi dodatno membrano, ko vstopijo v celico, kar bi še dodatno povišalo amplitudo pulzov, potrebno za njihovo elektroporacijo.

Pri poskusih elektroporacije znotrajceličnih arheosomov, ki so bili narejeni v našem laboratoriju, elektroporacija arheosomov ni bila nikoli detektirana. Vendar je bila amplituda pulzov pri poskusih omejena z zmogljivostjo pulznega generatorja. Na podlagi parametrov pulzov, ki so bili uporabljeni pri poskusih, ter ostalih eksperimentalnih pogojev (T. Batista Napotnik, zasebni pogovor) ocenjujem, da so bile dosežene amplitude pulzov prenizke za elektroporacijo arheosomov. Druga možna razlaga pa je tudi, da elektroporacija ni bila nikoli detektirana, ker se pore v teh arhealnih lipidih prehitro zaprejo, da bi se lahko za detekcijo ustrezna količina fluorescenčnega barvila izlila iz njih v časovnem razponu nanosekund. Simulacije molekularne dinamike so namreč pokazale, da se v arhaealnih lipidih tvorijo nestabilne hidrofobne pore (Polak *et al.*, 2014).

3.2 Zlivanje celic z nanosekundnimi pulzi

Elektrozlivanje ali elektrofuzija je metoda pri kateri z elektroporacijo dosežemo, da se različne celice lahko zlijejo med sabo. Elektroporacija namreč povzroči, da celična membrana postane fuzogena, tj. sposobna zlivanja z drugo celično membrano. Če se torej dve celici z elektroporiranima membranama nahajata v stiku, se lahko zlijeta v eno celico (Teissié in Ramos, 1998).

Z zlivanjem običajno pridobivamo hibridne celice, ki združujejo lastnosti starševskih celic, iz katerih so nastale. Na tak način je mogoče hibridizirati rastline, ki postanejo odporne na različne okoljske dejavnike (Greplová *et al.*, 2008), pripraviti celična cepiva za stimulacijo imunskega odziva pri zdravljenju raka (Tan *et al.*, 2013) ter celice, ki proizvajajo inzulin in jih lahko uporabimo pri raziskavah in zdravljenju diabetesa (McCluskey *et al.*, 2011). Najbolj razširjen primer zlivanja, pa je zlivanje limfocitov B in mielomskih celic v t. i. hibridome, ki proizvajajo monoklonska protitelesa (Trontelj *et al.*, 2008).

Konvencionalna metoda zlivanja v hibridomni tehnologiji je sicer uporaba polietilen glikola, vendar se je elektrozlivanje izkazalo za učinkovitejše v smislu števila pridobljenih hibridomov (Yu *et al.*, 2008). Žal pa ima tudi elektrozlivanje svoje omejitve, saj je obsežnost elektroporacije celične membrane sorazmerna z velikostjo celic. Limfociti B so približno dvakrat manjši od mielomskih celic. Če torej hkrati izpostavimo limfocite B in mielomske celice električnim pulzom, ki zagotovijo elektroporacijo limfocitov B, lahko ti pulzi ireverzibilno elektroporirajo mielomske celice (Trontelj *et al.*, 2008). Tako je tudi število preživelih hibridomov zelo majhno. V najboljšem primeru dosežemo največ ~1 % hibridomov na število uporabljenih limfocitov B (Kemna *et al.*, 2011; Yu *et al.*, 2008).

Običajno se za elektrozlivanje uporabljajo električni pulzi z dolžinami v področju od 10–100 μs. Z uporabo numeričnega modeliranja pa smo ugotovili, da lahko s skrajšanjem dolžine pulzov v področje nanosekund omejimo elektroporacijo le na področje stika med celicami, torej le tam, kjer je to potrebno za elektrozlivanje (slika 3.3) (Rems *et al.*, 2013). Načeloma pri tem ne poškodujemo nobene od celic, ne glede na njihovo velikost, s tem pa lahko izboljšamo število pridobljenih hibridomov.

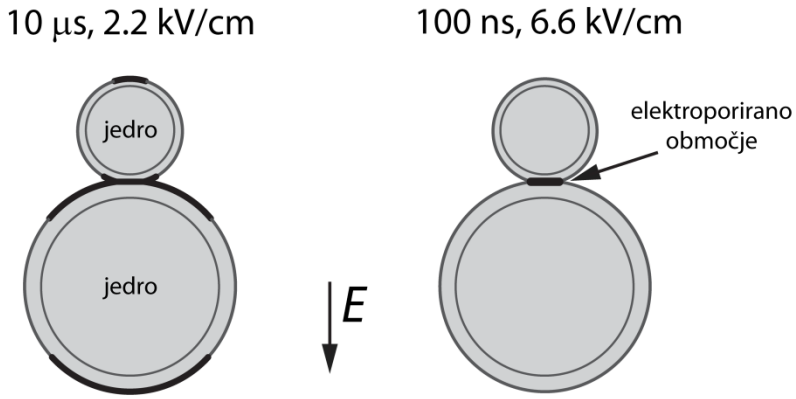

Slika 3.3: Primerjava elektroporacije dveh različnih celic v stiku z 10 μs in 100 ns pravokotnim pulzom. Znotraj celic se nahajajo še celična jedra. Elektroporirano območje membran je označeno odebeljeno. 10 μs pulz povzroči obsežno elektroporacijo velike celice, kar celico lahko poškoduje do te mere, da ne preživi. 100 ns pulz nasprotno povzroči samo elektroporacijo stika med celicami. Teoretično lahko torej z nanosekundnim pulzom dosežemo elektrozlivanje, ne da bi poškodovali katerokoli od celic. Prirejeno po Rems *et al.* (2013).

Model, s katerim smo prišli do opisanih ugotovitev, je temeljil na podobnem modelu elektroporacije, kot smo ga uporabili pri študiji elektroporacije znotrajceličnih liposomov. Ker vemo, da je predpogoj za elektrozlivanje elektroporacija celičnih membran na področju stika med celicami (Teissié in Ramos, 1998), je ta model zadostoval za raziskovanje možnosti elektrozlivanja celic z različnimi parametri električnih pulzov.

Napovedi modela smo nato preverili s poskusi na celični kulturi B16-F1. Celice smo najprej inkubirali v nizkoprevodnem hipotoničnem mediju, za katerega je bilo pokazano, da je ugoden za elektrozlivanje (Ušaj in Kandušer, 2012). Stik med celicami smo vzpostavili z 30 sekund trajajočim dielektroforetskim sinusnim

električnim poljem, pod vplivom katerega so se celice postavile v verige. Celice smo nato izpostavili nanosekundnim pulzom, ter jih ponovno za 30 sekund z dielektroforetskim signalom zadržali v verigah, da se stiki med celicami niso prehitro porušili, kar bi preprečilo njihovo zlivanje (Ušaj *et al.*, 2013).

Za elektrozlivanje smo pri poskusih uporabili 20 električnih pulzov različnih dolžin (50, 100, 150 ns) in amplitud (6, 9, 12 kV/cm). Rezultati so pokazali, da se delež zlitih celic s povečanjem dolžine in/ali amplitude pulzov do neke mere viša, nato začne upadati, znatno pa se poveča delež mrtvih celic. Mrtve celice so kazale značilne spremembe v morfologiji. Skrčile so se, njihova jedra pa so na slikah svetlobnega polja potemnela (slika 3.4). Največji delež zlitih celic (8 %) smo dobili pri parametrih pulzov 100 ns, 9 kV/cm, pri čemer je delež mrtvih celic znašal 20 %. Največji delež mrtvih celic (75 %) pa smo opazili pri najintenzivnejših pulzih, ki smo jih preučevali (150 ns, 12 kV/cm), pri čemer je bil delež zlitih celic le 1 %.

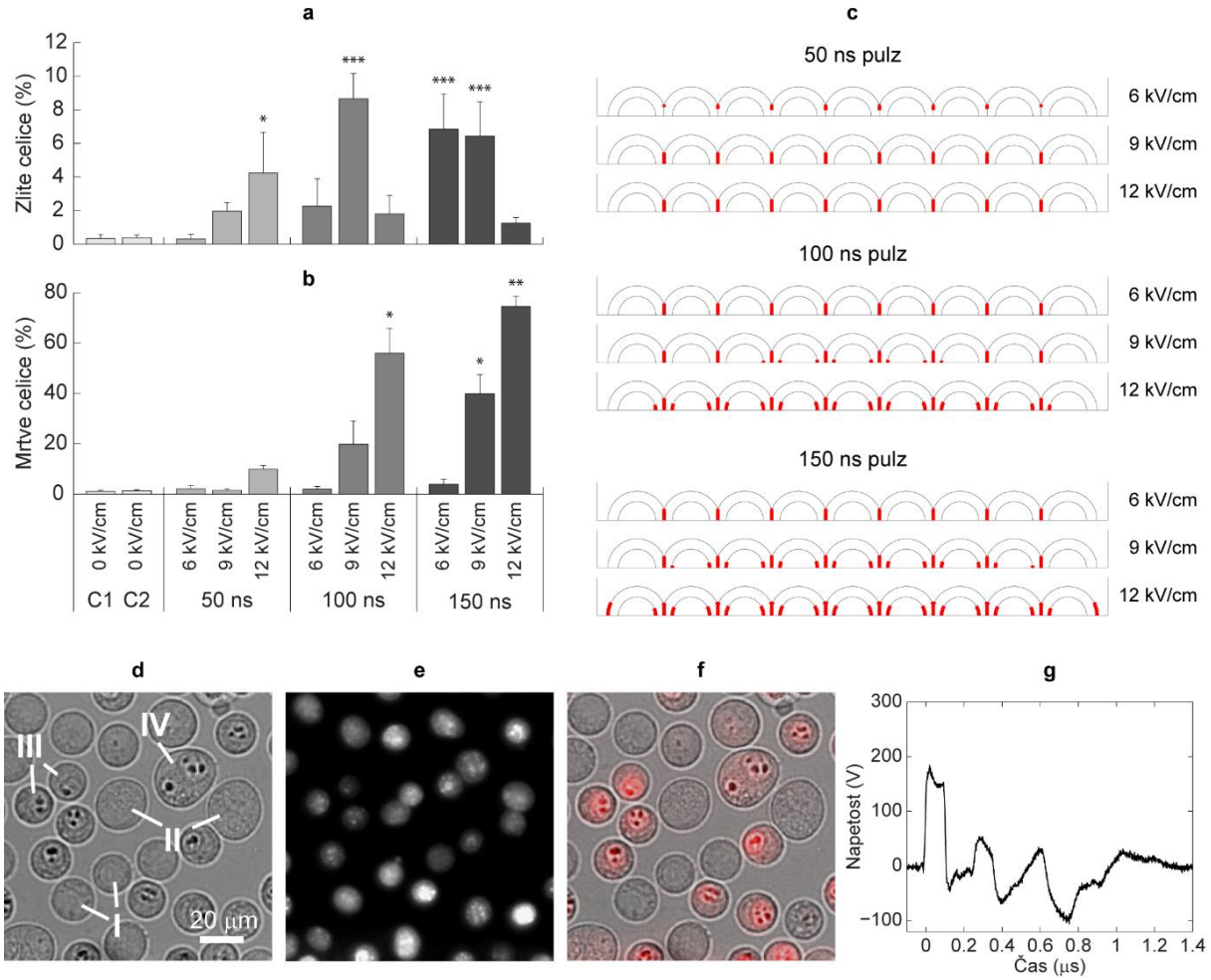

Slika 3.4: (a) Delež zlitih celic in (b) delež celic obarvanih s propidijevim jodidom (PI), ki predstavljajo mrtve celice. Rezultati so prikazani za različne parametre nanosekundnih pulzov, ki so bili uporabljeni pri poskusih. C1–kontrolna skupina brez izpostavitve električnemu signalu. C2–kontrolna skupina izpostavljena samo dielektroforetskemu signalu. (c) Pripadajoči rezultati numeričnega modela celic urejenih v verige, kar predstavlja konfiguracijo celic med izpostavitvijo nanosekundnim pulzom. Smer električnega polja je od leve proti desni. Z rdečo barvo so prikazana elektroporirana območja membran. (d) Morfološke spremembe celic po zlivanju. I–celici z normalno morfologijo, II–zliti celici z normalno morfologijo, III–celici s spremenjeno morfologijo, IV–zlita celica s spremenjeno morfologijo. (e) Jedra celic, obravana s fluorescenčnim barvilom Hoechst. (f) Celice s spremenjeno morfologijo so se obarvale s propidijevim jodidom (označeno rdeče), kar je nakazovalo na njihovo smrt. (g) Primer signala nanosekundnega pulza. Vzeto iz Rems *et al.* (2013).

Vzporedno s poskusi na celicah smo zgradili tudi numerično replikacijo (model) poskusov, pri kateri smo upoštevali geometrijske lastnosti celic in njihove postavitve med elektrozlivanjem ter električne lastnosti elektrofuzijskega medija. Električne lastnosti celic so bile vzete iz študij, ki so preučevale vpliv nizkoprevodnih hipotoničnih medijev, podobnih temu v naših poskusih, na električne lastnosti celic. Ugotovili smo, da se napovedi modela relativno dobro ujemajo z rezultati poskusov. Pri vseh parametrih pulzov, kjer smo zaznali povečanje števila zlitih celic, je model napovedal veliko število por na področjih stika med membranami. Število por se je povečevalo z amplitudo pulza, kar je bilo skladno z višjim deležem zlitih celic. Pri parametrih pulzov, kjer je model pokazal tudi večje območje elektroporiranosti jedrnih ovojnic, pa smo pri poskusih opazili znatno povečanje deleža mrtvih celic. V zadnjem delu raziskave smo opravili še poskuse zlivanja med celicami B16-F1 in CHO in pokazali, da je z nanosekundnimi pulzi mogoče zlivati tudi različno velike celice različnih tipov.

Na podlagi rezultatov zaključujemo, da so nanosekundni pulzi primerni za elektrozlivanje celic. Skladno z rezultati numeričnega modela predvidevamo, da bi nanosekundni pulzi lahko bistveno izboljšali preživetje celic pri elektrozlivanju celic različnih velikosti.

3.3 Model elektroporacije celic v heterogeni strukturi špinačnega lista

Zamrzovanje hrane je ena od dobro vzpostavljenih metod prezervacije hrane, vključno sadja in zelenjave. Vendar pa lahko zamrzovanje spremeni kvaliteto hrane, tako da na primer zelenjavi spremeni teksturo in okus, kar posledično ogrozi njen tržni potencial (Gómez Galindo in Sjöholm, 2004). Za izboljšanje kvalitete zamrznjene hrane se uporablja več metod, med katerimi je tudi vakuumska impregnacija v prisotnosti raztopine krioprotektanta, kot je sladkor trehaloza (Dymek *et al.*, 2015a). Sladkorji namreč stabilizirajo celične membrane s tem, da se z vodikovimi vezmi vežejo na sladkorne in polarne skupine v glavah fosfolipidov, kar zmanjša negativne posledice dehidracije membrane, ki je prisotna pri zamrzovanju (Danyluk *et al.*, 1998; Gómez Galindo in Sjöholm, 2004).

Pri vakuumski impregnaciji se zaradi poroznosti tkivne strukture zrak, ki je ujet v tkivu, zamenja s tekočino, v katero je tkivo potopljeno (Panarese *et al.*, 2013). Sladkor (krioprotektant) tako doseže medcelične prostore v tkivu. Zaradi neprepustnosti celičnih membran za sladkorje, pa ta ne vstopi v citoplazmo. Ena od možnosti povečanja koncentracije sladkorja v celicah je uporaba elektroporacije. Phoon in sodelavci so pokazali, da kombinacija vakuumske impregnacije s trehalozo in elektroporacije močno poveča toleranco špinače na zmrzovanje; v nasprotju z neelektroporiranimi listi, lahko elektroporirani špinačni listi po odmrznitvi ostanejo čvrsti, celice v listu pa ostanejo žive in ohranijo integriteto membran (slika 3.5) (Phoon *et al.*, 2008).

Pri zamrzovanju špinače je pomembno, da preživi čim več celic v listu (v idealu vse), saj je glavni cilj, da list po odmrznitvi ohrani čim več lastnosti svežega lista. Električni pulzi morajo torej zagotoviti elektroporacijo vseh celic in s tem omogočen vstop sladkorju v citoplazmo, kar celice varuje med zamrzovanjem; obenem pa električni pulzi ne smejo povzročiti ireverzibilne elektroporacije in s tem celično smrt še pred zamrzovanjem. Ena od težav pri optimizaciji krioprezervacije špinače je, da je špinačno tkivo heterogeno. Obsežnost elektroporacije je namreč odvisna od velikosti celic, njihove orientacije in organizacije (Valič *et al.*, 2003;

Towhidi *et al.*, 2008; Canatella *et al.*, 2004). Ker pa je obsežnost elektroporacije (povečanja permeabilnosti celičnih membran) povezana tudi z zmožnostjo preživetja celic, je v heterogeni strukturi težko hkrati zagotoviti elektroporacijo in preživetje vseh celic v tkivu (Canatella *et al.*, 2004; Chopinet *et al.*, 2012). Poleg tega pa optimizacijo otežkoča tudi debelina lista, saj je pod mikroskopom mogoče optično pregledati le zgornje plasti tkiva.

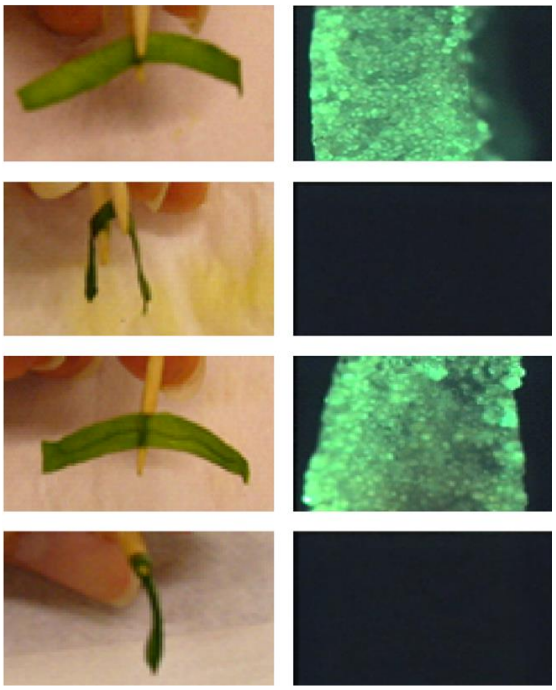

Slika 3.5: Levo: Test čvrstosti špinačnega lista. Desno: Fluorescenca barvila *fluorescein diacetate*, ki obarva žive celice. Od zgoraj navzdol so predstavljeni špinačni listi, ki so bili pred zamrzovanjem izpostavljeni različnim pogojem: svež list, ki ni bil zamrznjen; zamrznjen in odmrznjen list; vakuumsko impregniran in elektroporiran list po odmrznitvi; vakuumsko impregniran list po odmrznitvi. Vzeto iz Phoon *et al.* (2008).

Vpogled v porazdelitev električnega polja in elektroporacije celic v notranjosti lista lahko ponudi numerični model. Hkrati je z modelom mogoče iskati parametre električnih pulzov, ki bi bili najustreznejši za elektroporacijo špinačnega lista, kot smo pokazali že pri zgornjih dveh študijah. Gradnja modela tkiva pa je precej bolj kompleksna, kot je gradnja modela elektroporacije posameznih celic. Potrebno je namreč identificirati, katere strukture najbolj prispevajo k električnim lastnostim lista in s tem porazdelitvi električnega polja znotraj lista. Pristop mora torej biti postopen in voden z meritvami električnih lastnostih lista. Struktura špinačnega lista in geometrija pripadajočega numeričnega modela, ki smo ga zgradili v naši študiji, sta prikazana na sliki 3.6.

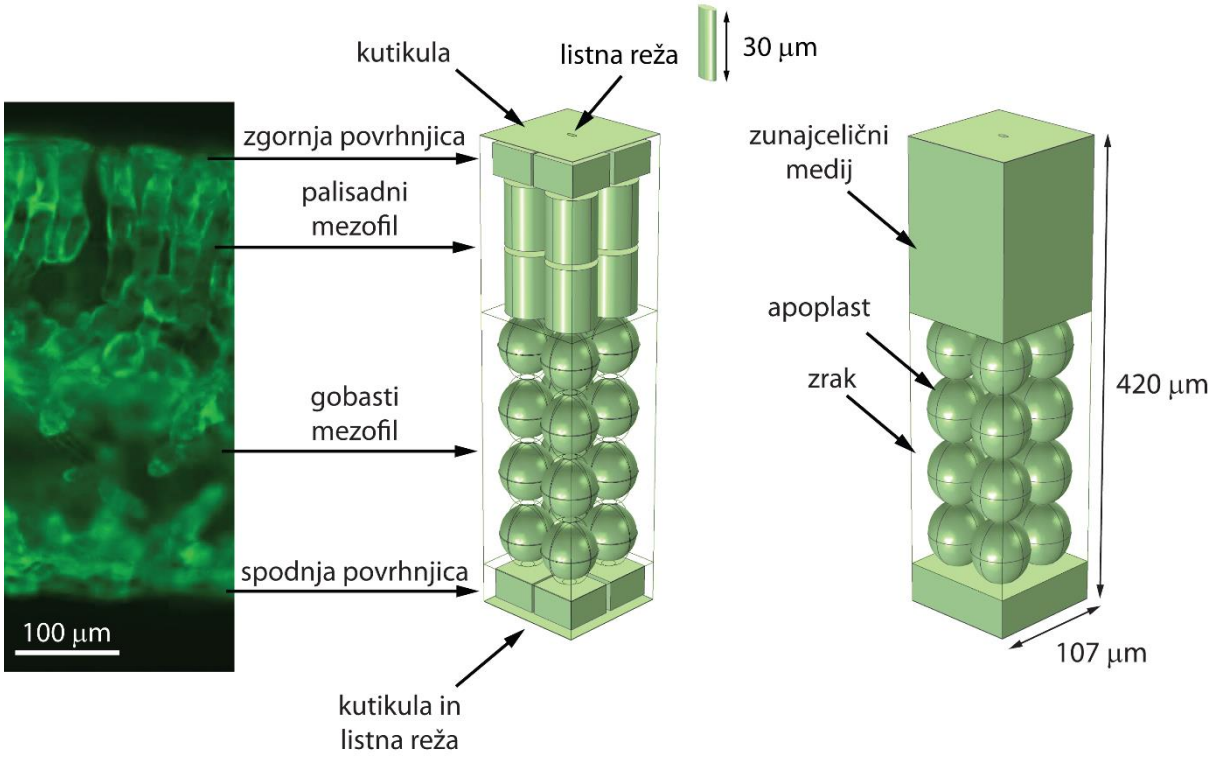

Slika 3.6: Mikroskopska slika prereza lista špinače (levo) in geometrija pripadajočega numeričnega modela (sredina in desno). Zaradi boljše preglednosti, je geometrija modela prikazana na dva načina, pri čemer so pri vsakem od obeh prikazov označene druge strukture modela špinačnega lista. Prirejeno po Dymek et al. (2015b).

V prvem koraku smo naredili meritve električne prevodnosti špinačnega lista. Meritve so bile opravljene tako, da smo iz vsakega lista izrezali 1 cm × 1 cm velik vzorec, ga potopili v fosfatni pufer ter nato položili med dve elektrodi iz nerjavečega jekla s površino 64 mm^2 (površina elektrod je bila manjša od površine lista). Električno prevodnost lista smo izmerili z impedančnim analizatorjem v frekvenčnem razponu od 20 Hz do 1 MHz. Nato smo zgradili več variant numeričnega modela, pri čemer smo preverili vpliv strukture in porazdelitve celic gobastega mezofila, vpliv kutikule ter listnih rež na električno prevodnost modela lista. S primerjavo izračunov in meritev smo ugotovili, da k električnim lastnostim lista predvsem prispeva kutikula (hidrofobna plast, ki prekriva list).

Meritve so smo nato ponovili še na listih, vakuumsko impregniranih z fosfatnim pufrom znane prevodnosti (0.25 S/m). Pri neobdelanem listu se predvsem v gobastem mezofilu nahaja približno 30 % zraka, ki ga po vakuumski impregnaciji zamenja zunanja raztopina. Ponovno smo primerjali meritve z izračuni modela, pri čemer smo v modelu neprevodni zrak zamenjali s prevodno tekočino. Ker v literaturi nismo našli nobenih meritev električnih lastnosti špinačne kutikule, smo naredili izračune za različne vrednosti prevodnosti in dielektričnosti kutikule, pri čemer smo izhajali iz objavljenih meritev električnih lastnosti kutikule paradižnika (Ramos-Barrado *et al.*, 1993). Za nadaljnjo validacijo modela smo nato uporabili vrednosti električnih lastnosti kutikule, ki so najbolje opisale meritve.

Nato smo naredili še meritve električnega toka skozi list med aplikacijo enega elektroporacijskega pulza dolžine 250 µs in različnih napetosti od 50 do 500 V. Meritve smo ponovno primerjali z izračuni, pri čemer smo v model vgradili še model elektroporacije, podobno kot pri prejšnjih dveh študijah. Pri izračunih smo postavili še dve hipotezi: (i) listne reže so med elektroporacijo napolnjene z zrakom ali (ii) listne reže so med elektroporacijo napolnjene s citoplazemsko tekočino, ki je iztekla iz elektroporiranih celic zapiralk (par celic, ki odpira in zapira listno režo). Hipotezi smo v modelu realizirali tako, da smo celični reži na vrhu in dnu lista "napolnili" z zrakom ali prevodno tekočino in primerjali izračunani tok. Ugotovili smo, da prva hipoteza bolje opiše električni tok skozi list pri pulzu najnižje amplitude (50 V), medtem ko druga hipoteza bolje opiše električni tok skozi list pri vseh pulzih z amplitudo ≤ 200 V. Pri amplitudi 100 V je bila eksperimentalna meritev električnega toka vmes med napovedni modela pri vpoštevanju prve ali druge hipoteze. Hipotezi smo nato preverili še preko detekcije vnosa fluorescenčnega barvila propidijevega jodida v celice zapiralke po elektroporaciji. Skladno z izračuni toka, pri pulzu amplitude 50 V v celicah zapiralkah nismo detektirali vnosa barvila, nakazujoč odsotnost elektroporacije, pri amplitudi 100 V je bilo le nekaj celic zapiralk elektroporiranih, medtem ko so bile pri pulzih z amplitudami višjimi od 100 V vse celice zapiralke elektroporirane (pri vseh celicah smo zaznali vnos barvila) (slika 3.7).

S primerjavo izračunov in eksperimentalnih meritev smo tako validirali model, ki ga lahko uporabimo pri nadalnjih študija in optimizaciji krioprezervacije špinače. Pomemben prispevek pa ima že sama gradnja modela, saj smo identificirali ključne strukture, ki prispevajo k električnim lastnostim lista, električnemu toku skozi list ter s tem porazdelitvi električnega polja v listu med elektroporacijo.

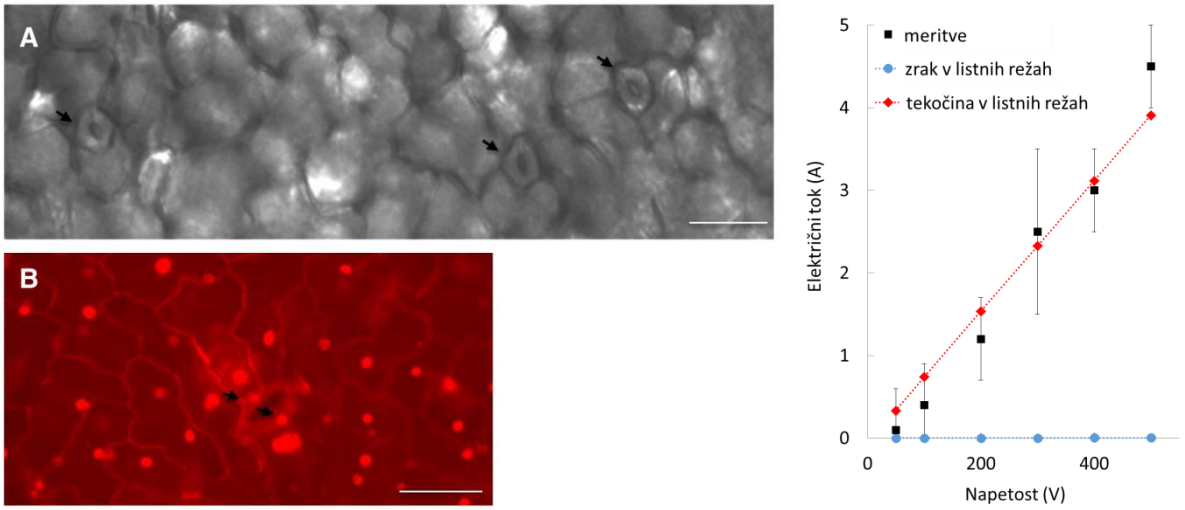

Slika 3.7: Levo: Reprezentativne mikroskopske slike, ki prikazujejo: (A) odprte listne reže po vakuumski impregnaciji (označene s puščicami). (B) Elektroporacija celic zapiralk, ki so se obarvale z barvilom propidijev jodid. List je bil izpostavljen enemu pravokotnemu pulzu dolžine 250 µs in amplitude 200 V. Desno: Meritve toka skozi list med elektroporacijo s pulzom dolžine 250 µs različnih amplitud. Prikazani so tudi rezultati numeričnega modela pri dveh hipotezah: prva hipoteza je, da so listne reže so napolnjene z zrakom, druga hipoteza je, da so listne reže napolnjene s celično tekočino, ki je pritekla iz elektroporiranih celic zapiralk. Prirejeno po Dymek et al. (2015b).

3.4 Karakterizacija lipidnih por s simulacijami molekularne dinamike

3.4.1 Razvoj metode konstantnega neravnovesja naboja

Simulacije molekularne dinamike ponujajo nepogrešljiv vpogled v molekularne mehanizme elektroporacije lipidnega dvosloja. Ena od metod, s katero lahko dosežemo elektroporacijo, je neravnovesje električnega naboja med dvema stranema lipidnega dvosloja (Gurtovenko in Vattulainen, 2005; Kandasamy in Larson, 2006; Delemotte in Tarek, 2012). Neravnovesje, ki ga npr. dosežemo tako, da postavimo presežek kationov nad dvosloj in presežek anionov pod dvosloj, povzroči TMN prek dvosloja. Pri dovolj visokem neravnovesju naboja in s tem dovolj visoki TMN se v dvosloju ustvari pora, prek katere nato stečejo ioni. Ker tok ionov razelektri membrano (zmanjša se neravnovesje naboja), TMN pade pod nivo, ki je potreben za vzdrževanje pore in pora se skrči ter postane neprevodna za ione (Gurtovenko in Vattulainen, 2007). To otežuje karakterizacijo por, saj se TMN, tok ionov in velikost pore tekom simulacije nenehno spreminjajo.

Pri metodi, kjer namesto neravnovesja naboja elektroporacijo dvosloja dosežemo z električnim poljem, je mogoče z zmanjšanjem električnega polja po elektroporaciji stabilizirati velikost pore (Fernández *et al.*, 2012). V prisotnosti ionov v sistemu lahko tako določimo prevodnost por v odvisnosti od njihove velikosti (Ho *et al.*, 2013). Metoda električnega polja se smatra za reprezentativno pri pogojih nanosekundnih električnih pulzov, ki ne povzročijo znatnega kapacitivnega elektrenja membrane, temveč se na membrani ustvari električna napetost zaradi polarizacije vodnih dipolov v bližini lipidnih glav ter polarizacije lipidnih dvopolov, ki sledi polarizaciji vode (Ziegler in Vernier, 2008). Karakterizacijo transporta ionov pri takšnih pogojih težko povežemo z eksperimentalnimi pogoji. Pred kratkim pa so Kutzner in sodelavci razvili algoritem, ki v sistemu z ionskim kanalom vzdržuje neravnovesje ionov prek kanala kljub konstantnemu prehajanju ionov skozi kanal (Kutzner *et al.*, 2011). Algoritem temelji na tem, da pogosto šteje ione, ki se nahajajo na dveh straneh kanala. Če se število kationov in anionov spremeni v primerjavi z začetno konfiguracijo (kar pomeni, da je nek ion prešel kanal), algoritem vzpostavi nazaj začetno konfiguracijo, tako da ion istega tipa zamenja z vodno molekulo iz regije na drugi strani kanala. Njihov algoritem ponuja možnost za vzdrževanje neravnovesja naboja tudi pri simulacijah lipidnega dvosloja z vodno poro, s čimer lahko preprečimo krčenje pore kot posledico toka ionov skozi poro.

Vendar pa je imajo simulacije po metodi neravnovesja naboja še eno pomankljivost povezano z lateralno površinsko napetostjo na membrani. Pri simulacijah takšnega tipa je zaradi periodičnih robnih pogojev namreč potrebno zagotoviti, da ioni, ki so v presežku, ne preidejo na drugo stran dvosloja prek periodične meje simulacijske celice. To lahko dosežemo tako, da v sistem implementiramo sloj vakuuma, ki loči vodno regijo na dva ločena dela (Delemotte *et al.*, 2008; Delemotte in Tarek, 2012). Takšno simulacijo pa je potrebno izvajati pri konstantnem volumnu (konstantni velikosti simulacijske celice), kar vnaša artefakt v simulacijo po tem, ko se v dvosloju ustvari pora. Zaradi pore imajo lipidi namreč manj prostora, kar posledično zmanjša povprečno površino, ki jo ima posamezna lipidna molekula na voljo. S tem se ustvari lateralna napetost na membrani, ki nasprotuje širjenju pore (Tarek, 2005; Tolpekina *et al.*, 2004; Wohlert *et al.*, 2006; den Otter, 2009).

Da bi odpravili pomanjkljivosti simulacij z neravnovesjem naboja, smo implementirali algoritem Kutznerja in sodelavcev ter s posebnim postopkom zagotovili, da je lateralna napetost na membrani konstanta in enaka

~0 N/m ne glede na spreminjanje velikosti pore. Najprej smo izvedli simulacije dvosloja pri konstantnem pritisku, pri čemer se je površina dvosloja adaptirala na energetsko najbolj ugodno. Ko je površina dvosloja v ravnovesju, na membrano namreč ne deluje lateralna napetost. Nato smo v sistem implementirali sloj vakuuma in simulacije izvedli pri konstantni lateralni napetosti. Kontrola lateralne napetosti v simulaciji omogoča, da dvosloj lahko poljubno spreminja svojo površino na račun konstantne dolžine simulacijske celice v smeri pravokotno na površino dvosloja. Veljavnost protokola smo preverili tako, da smo izračunali lateralno napetost v sistemu z vakuumom. Ta je znašala ~100 mN/m, kar lahko pripišemo dvema prehodnima območjema med vodo in vakuumom v sistemu. Lateralna napetost, ki jo izračunamo iz simulacije, je enaka seštevku vseh lateralnih napetosti v sistemu; tipična vrednost lateralne napetosti na prehodu med vodo in vakuumom pa je ~50 mN/m. S tem lahko tudi ugotovimo, da je lateralna napetost na dvosloju, kot želeno, enaka ~0 N/m.

Z vzpostavljenim protokolom smo lipidni dvosloj, zgrajen iz 1024 fosfolipidov POPC in obdan z ~1 M raztopino NaCl, najprej izpostavili dovolj velikemu neravnovesju naboja, da se je ustvarila pora. Nato smo neravnovesje zmanjšali na različne izbrane vrednosti, in za vsako izbrano neravnovesje izvedli 80 ns dolge simulacije. Metoda je pokazala, da se po kratkem prehodnem času (~20 ns) pore stabilizirajo in nihajo okrog povprečne velikosti, ki je pogojena z vrednostjo neravnovesja naboja. Večje neravnovesje hkrati povzroči višjo TMN in večji tok skozi poro (slika 3.8).

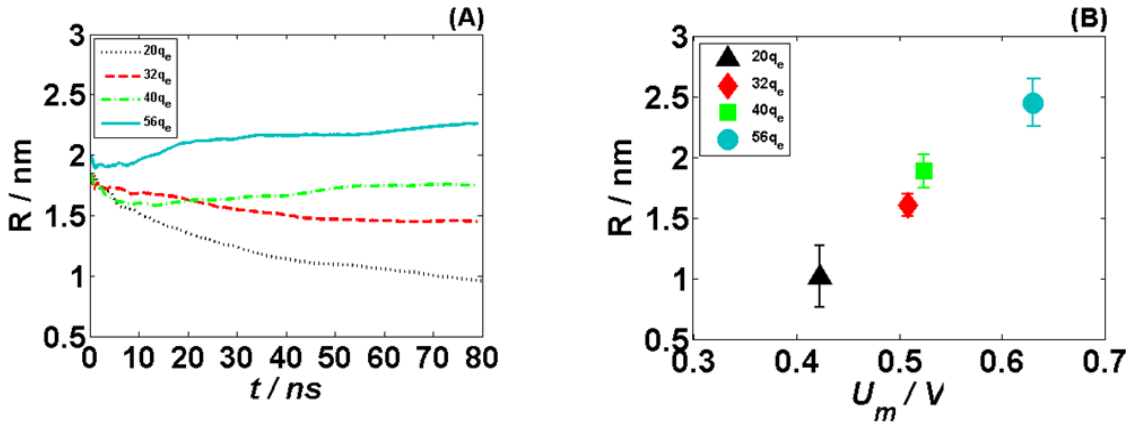

Slika 3.8: (A) Kumulativno povprečje radija pore *R* pri različnih vrednostih neravnovesja naboja (prikazano v legendi, pri čemer je q_e elementarni naboj). Po približno 20 ns se pore stabilizirajo. (B) Relacija med transmembransko napetostjo U_m in radijem pore pri različnih vrednostih neravnovesja naboja.

Da bi preverili vpliv velikosti lipidnega dvosloja na rezultate simulacij, smo simulacije ponovili še na manjšem sistemu, zgrajenem iz 256 lipidnih molekul. Velikost por v manjšem sistemu je bila bistveno manjša kot pri večjem sistemu, kljub podobni TMN pri obeh sistemih. Pri manjšem sistemu je namreč pora vplivala na skoraj vse lipide v sistemu (slika 3.9). Nasprotno je bil večji sistem dovolj velik, da lipidi na robu sistema niso več "čutili" pore.

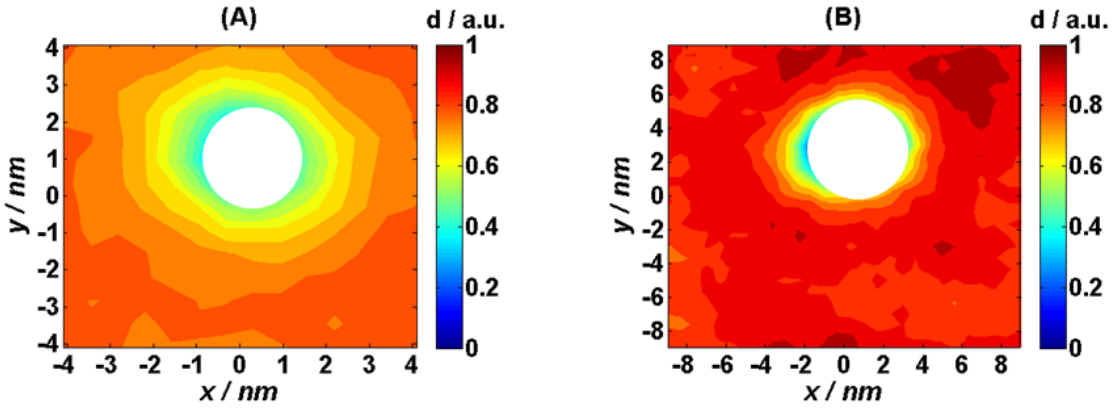

Slika 3.9: Profil gostote lipidov pri sistemu z 256 lipidnimi molekulami (A) in 1024 lipidnimi molekulami (B). Bel krog na sredini predstavlja poro. Pri manjšem sistemu se gostota lipidov spreminja od pore vse do roba sistema, medtem ko pri večjem sistemu gostota doseže konstantno vrednost zunaj pore, kar pomeni da lipidi na robu sistema ne čutijo več pore.

3.4.2 Primerjava numeričnega modela prevodnosti pore z rezultati simulacij molekularne dinamike

Teoretični opis prevodnosti pore v odvisnosti od njenega radija je eden od pomembnejših parametrov pri zveznih modelih elektroporacije. Skupna prevodnost elektroporirane membrane je namreč enaka seštevku prevodnoti vseh por v membrani. Prevodnost celotne membrane pa določa TMN, ki nadalje določa dinamiko nastajanja, širjenja in krčenja por v membrani (Barnett in Weaver, 1991; Freeman *et al.*, 1994; DeBruin in Krassowska, 1999; Krassowska in Filev, 2007). Poleg tega je teoretični opis prevodnosti pore pomemben pri določanju velikosti por iz eksperimentalnih meritev prevodnosti ravninskih lipidnih dvoslojev. Pri določenih eksperimentalnih pogojih lahko namreč merimo prevodnost (najverjetneje) osamljenih por v lipidnem dvosloju; kadar vsilimo zmeren električni tok skozi dvosloj, ali kadar na dvosloj vsilimo majhno napetost, ki je ravno dovolj velika, da se v dvosloju začnejo odpirati in zapirati posameze pore (Kalinowski *et al.*, 1998; Melikov *et al.*, 2001; Koronkiewicz *et al.*, 2002; Kotulska, 2007; Kramar *et al.*, 2012).

Obstoječi teoretični izrazi, ki opisujejo prevodost lipidnih por, originalno izvirajo iz kombinacije Nernst-Planckovih enačb in Poissonove enačbe (Glaser *et al.*, 1988; Barnett, 1990; Kakorin in Neumann, 2002; Li in Lin, 2010). Nernst-Planckove enačbe opisujejo difuzno in elektroforetsko gibanje ionov, pri čemer ione obravnavajo s stališča prostorske porazdelitve ionske koncentracije. Vsak tip ionov v sistemu je opisan s svojo Nernst-Planckovo enačbo. Poissonova enačba pa opisuje porazdelitev električnega polja v prisotnosti presežka prostorske gostote naboja, ki je povezan s porazdelitvijo koncentracije vseh tipov ionov po prostoru. Pri obravnavi velikega števila tipov ionov postane sistem enačb velik in računsko zahteven (Zheng in Wei, 2011). Poleg tega so enačbe analitično rešljive le za preprosto geometrijo por. Zato so teoretični opisi prevodnosti por v splošnem poenostavljeni in temeljijo na predpostavki, da se v elektrolitu, ki obdaja cilindrično poro, nahaja ena vrsta pozitivnih in ena vrsta negativnih monovalentnih ionov (Glaser *et al.*, 1988; Barnett, 1990; Kakorin in Neumann, 2002; Li in Lin, 2010).

Poisson-Nernst-Planckova (PNP) teorija je sicer splošen in dobro uveljaven teoretični pristop k opisovanju časovno in prostorsko povprečenega toka ionov na številnih znanstvenih področjih, vključno pri raziskovanju ionskih kanalov in nanokanalov (Bhattacharyya in Nayak, 2009; Daiguji *et al.*, 2004; Im in Roux, 2002; Roux *et al.*, 2004; Zheng in Wei, 2011). Vendar ima teorija znane omejitve pri teoretični obravnavi sistemov na molekularni ravni, saj ne upošteva velikosti ionov in korelacij med ioni. V primeru ionskih kanalov te omejitve predvsem pridejo do izraza pri ozkih kanalih z radijem manjšim od 2–3 Debyejevih dolžin (Moy *et al.*, 2000; Corry *et al.*, 2000).

Rezultati simulacij molekularne dinamike, ki so bili pridobljeni z metodo konstantnega neravnovesja naboja, so ponudili priložnost, da preverimo, kako dobro lahko PNP teorija opiše prevodnost lipidne pore. V ta namen smo zgradili numerični model lipidnega dvosloja s toroidno poro, soroden tistemu, ki sta ga predlagala Li in Lin (2010), le da smo numerični model priredili sistemu v simulacijah molekularne dinamike. Eden glavnih vodil v študiji je namreč bil, da ne uporabimo nobene nepotrebne predpostavke, in vse parametre numeričnega modela pridobimo s samih simulacij.

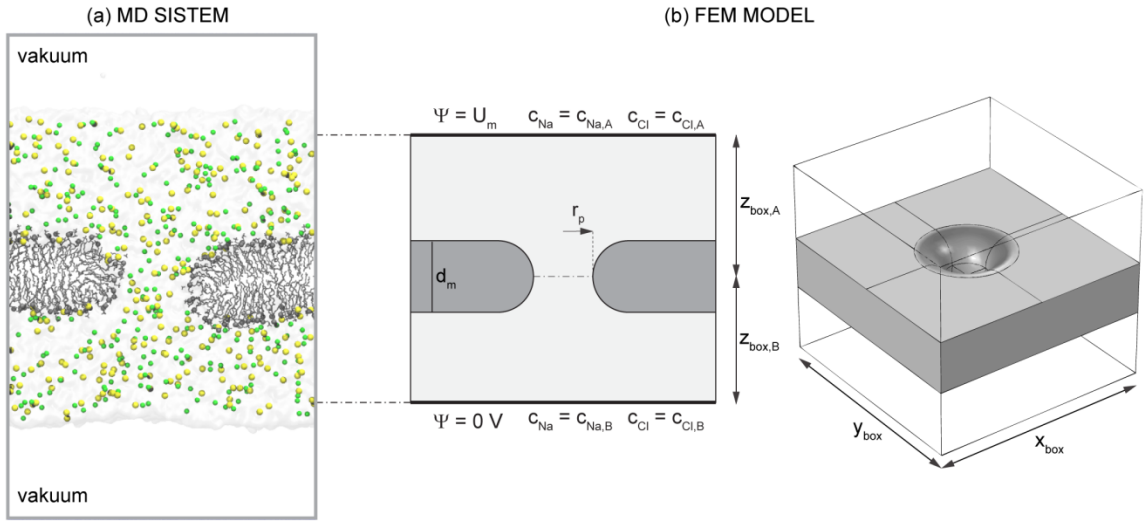

Slika 3.10: (a) Prerez sistema iz simulacij molekularne dinamike. Velikost simulacijske celice je označena s sivim pravokotnikom. S sivo bravo je označen lipidni dvosloj, rumene krogle predstavljajo natrijeve ione, zelene krogle kloridne ione, sivo ozadje pa predstavljajo vodne molecule. Zgoraj in spodaj je sloj vakuuma. (b) Na levi strani je prikazan prerez, na desni strani pa 3D prikaz numeričnega modela pore v lipidnem dvosloju. S temno sivo barvo je označen lipidni dvosloj, s svetlo barvo pa elektrolitska raztopina.

Pri podrobni analizi rezultatov simulacij smo ugotovili, da se zaradi vezave Na^+ ionov na glave lipidov ustvari električni dvosloj okrog lipidnih glav, tako na planarnem delu dvosloja, kot znotraj pore. Kljub temu, da Na^+ ioni niso trajno vezani in lahko prispevajo k toku ionov skozi poro, se v povprečju na steni pore ustvari efektivni površinski naboj, kar ustvarja elektrostatično bolj ugodno okolje za Cl^- ione. Poleg tega so Cl^- ioni tudi bolj mobilni od Na^+ ionov. Skupna posledica je znaten elektroosmotski tok vode v smeri toka Cl^- ionov, ki še dodatno inhibira prehajanje nasprotno usmerjenih Na^+ ionov.

Da bi sistematično preverili vpliv električnega dvosloja in elektroosmotskega toka, smo zgradili tri variacije numeričnega modela. V prvi smo zanemarili tako električni dvosloj kot elektroosmotski tok. V drugi smo modelirali električni dvosloj kot površinski naboj. Reprezentacija vezanih Na^+ ionov s površinskim nabojem je groba aproksimacija, saj ima molekularni sistem mehak (zvezen) prehod med vodo in hidrofobno lipidno sredino. Nasprotno pa v modelu predpostavimo grob (nezvezen) prehod. Zato smo se odločili, da opravimo izračune za dve vrednosti površinskega naboja (0.20 in 0.27 q_e/nm^2, pri čemer je q_e elementarni naboj), ki smo ju z analizo podatkov iz simulacij lahko ocenili kot fizikalno smiselni. V tretji variaciji modela pa smo poleg površinskega naboja upoštevali še elektroosmotski tok.

Rezultati tretje variacije modela pri treh vrednostih površinskega naboja (0.00, 0.20 in 0.27 q_e/nm^2) so prikazani na sliki 3.11. Znaki predstavljajo rezultate simulacij, črte pa rezultate numeričnega modela. Iz rezultatov je razvidno, da je skupna prevodnost pore, torej prevodnost za Na^+ in Cl^- ione, zelo podobna pri vseh vrednostih površinskega naboja in se tudi odlično ujema z rezultati simulacij (slika 3.11a). Zelo podobne rezultate dobimo tudi s prvo variacijo modela (rezultati niso prikazani), kar pomeni, da pri obravnavi skupne prevodnosti pore, električni dvosloj in elektroosmotski tok ne izkazujeta posebnega vpliva. Pomembnejši vpliv pa se pokaže, ko primerjamo posebej prevodnost pore za Na^+ ione in Cl^- ione (slika 3.11b). Model, ki upošteva tako površinski naboj kot elektroosmotski tok bistveno bolje opiše tako prevodnost za Na^+ kot za Cl^- ione, hkrati pa dobro opiše tudi razmerje njune prevodnosti (slika 3.11c). Pri tem ima sama izbrana vrednost površinskega naboja (0.20 in 0.27 q_e/nm^2) manjši vpliv. Iz slike 3.11c pa je še razvidno, da model, ki upošteva samo elektroosmotski tok, ne pa površinskega naboja (ravna črta), ni ustrezen. To pomeni, da ima površinski naboj pomemben vpliv na prevodnost pore za Na^+ ione in Cl^- ione.

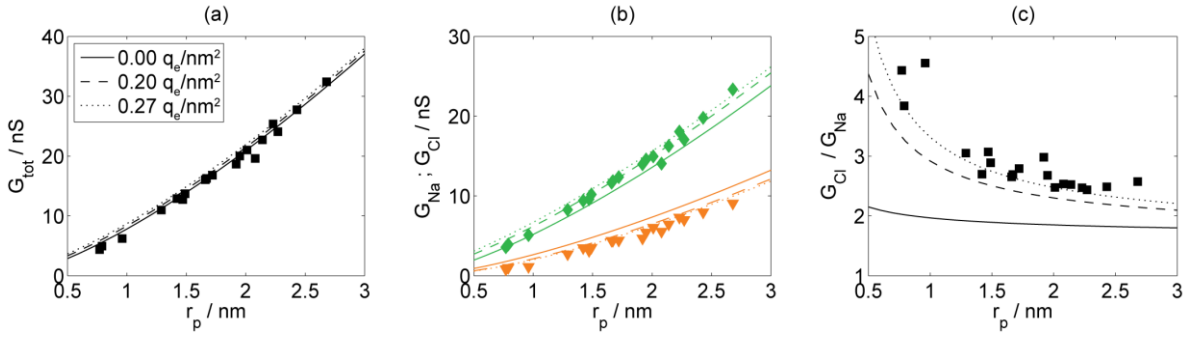

Slika 3.11: (a) Prevodnost pore določena s simulacijami molekularne dinamike (kvadrati) in z numeričnim modelom, ki upošteva elektroosmotski tok. V legendi je prikazana vrednost površinskega naboja, ki je bil uporabljen pri izračunih. (b) Prevodnost pore za kloridne ione (zelena) in natrijeve ione (oranžna). Podobno kot pri (a) znaki predstavljajo rezultate simulacij molekularne dinamike, črte pa rezultate numeričnega modela. (c) Razmerje med prevodnostjo pore za kloridne in natrijeve ione.

Kljub razliki v prevodnosti za posamezne ione je skupna prevodnost pore vedno približno enaka. Kadar nas torej zanima le skupna prevodnost, zadostuje že prva variacija modela. Rezultate te variacije smo zato nadalje primerjali s preprostejšo analitično rešitvijo za cilindrično poro in poenostavljenim izrazom, ki opiše prevodnost

pore zgolj kot prevodnost valja napolnjenega s prevodno tekočino (ta se pogosto uporablja v literaturi) (Kalinowski *et al.*, 1998; Koronkiewicz *et al.*, 2002; Kotulska, 2007). Iz slike 3.12 je razvidno, da rezultate molekularne dinamike najbolje opiše prevodnost določena za toroidno poro. Vendar je analitična rešitev za cilindrično poro tudi dober približek; pri večjih porah ne opazimo več nobene razlike med prevodnostjo cilindrične in toroidne pore. Nasprotno pa poenostavitev prevodnosti pore s prevodnostjo valja povsem napačno opiše funkcijsko odvisnost prevodnosti pore od njenega radija.

Na podlagi rezultatov lahko zaključimo, da PNP teorija ustrezno opiše prevajanje ionov skozi poro. Poudariti pa je še potrebno, da so bile simulacije narejene pri koncentraciji ~1 M NaCl, zaradi česar se je v pori vedno nahajalo večje število ionov. Večje število ioniv omogoča, da se ioni elektrostatsko ščitijo med sabo. Če pa bi bila koncetracija ionov tako nizka, da bi se ob danem tranutku nahajal v pori en sam ion, bi se v pori ustvarila znatna energijska bariera, ki bi zmanjšala celotno prevodnost pore (Corry *et al.*, 2003). Vredno bi bilo torej narediti nadaljnje simulacije in primerjavo s še pri nižji koncentraciji NaCl ter pri drugih vrstah elektrolita.

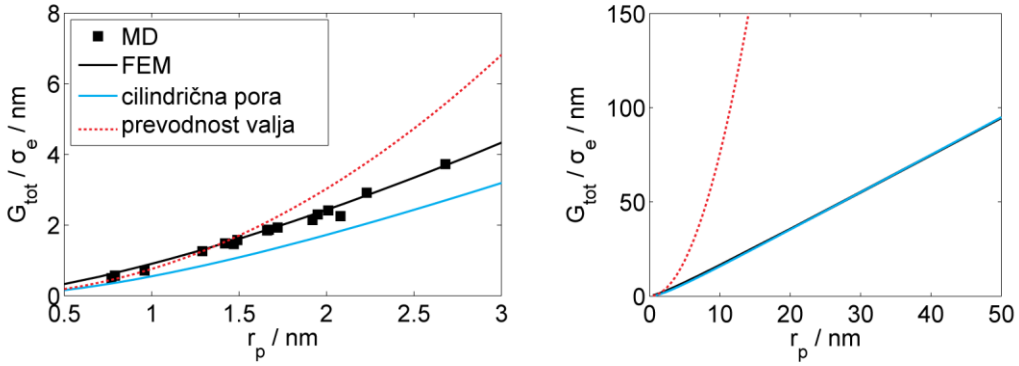

Slika 3.12: Primerjava analitičnih izrazov za prevodnost pore. Prevodnost pore je bila normirana na specifično prevodnost elektrolita σ_e. Levi graf prikazuje normirano prevodnost majhnih por, desni graf pa velikih por. MD–rezultati simulacij molekularne dinamike, FEM–rezultat numeričnega modela. Prikazani sta še analitična rešitev za cilindrično poro, in izraz, ki opisuje prevodnost valja.

4 Zaključki

V doktorski disertaciji smo pokazali, da lahko z numeričnimi modeli učinkovito prispevamo k eksperimentalnim raziskavam. Numerični modeli sicer ne morejo nadomestiti eksperimentov, lahko pa vodijo začetni razvoj eksperimentalnega protokola in njegovo nadaljnjo optimizacijo, ter pripomorejo k interpretaciji eksperimentalnih rezultatov. Povezave med modeli na molekularni ravni, ravni celice in ravni tkiva so dosegljive in pomembne za napredovanje v razumevanju elektroporacije, s tem pa posledično razvoju učinkovitejših terapij in tehnologij.

Izvirni prispevki k znanosti

Eksperimentalni protokol za zlivanje različno velikih bioloških celic z električnimi pulzi trajanja največ nekaj sto nanosekund

Elektrozlivanje je vzpostavljena metoda za proizvodnjo hibridnih celic. Za razliko od kemičnih in virusnih metod, je elektrozlivanje fizikalna metoda, zato jo lahko varno uporabljamo tudi v kliniki. Pri elektrozlivanju je pomembno, da celice preživijo izpostavitev električnim pulzom, saj lahko le tako pridobimo žive zlite celice. Pri večini aplikacij si želimo doseči zlivanje med celicami različnega tipa. Če se celice močno razlikujejo v velikosti, lahko to predstavlja težavo pri elektrozlivanju, saj lahko večje celice postanejo poškodovane pri parametrih električnih pulzov, ki so potrebni za elektroporacijo manjših celic. Večje celice se namreč običajno elektroporirajo pri nižjih jakostih električnega polja kot manjše celice, posebej kadar dovajamo običajne pulze z dolžino nekaj 10 μs in več. Z uporabo numeričnega modeliranja smo pokazali, da lahko s pulzi dolžine v področju nanosekund dosežemo selektivno elektroporacijo stikov med celicami, ne glede na velikost celic. Nanosekundni pulzi tako lahko omogočijo elektrozlivanje celic različnih velikosti, ne da bi pri tem poškodovali celice. Na podlagi predpostavk numeričnih izračunov smo razvili uspešen eksperimentalni protokol za elektrozlivanje celic z nanosekundnimi pulzi. Rezultati eksperimentov pa so potrdili napovedi numeričnega modela.

Numerični model biološkega tkiva z razločeno celično strukturo, ki omogoča načrtovanje elektroporacije tega tkiva

Numerični modeli elektroporacije tkiva običajno obravnavajo tkivo kot homogeno strukturo s povprečnimi električnimi lastnostmi. Pri heterogenih tkivih je takšna obravnava preveč poenostavljena, saj heterogenost celične strukture povzroči nemohogeno porazdelitev električnega polja v tkivu. Modeliranje heterogenih tkiv kot homogeno strukturo tako lahko vodi do nepravilne interpretacije numeričnih rezultatov. Pri protokolih elektroporacije, kjer je preživetje celic ključnega pomena, je hkrati tudi pomembno, da pri načrtovanju protokolov upoštevamo heterogenost tkivne strukture. Napredek v razvoju modelov tkiv z razločeno celično strukturo ima torej visok pomen. Krioprezervacija predstavlja primer aplikacije, kjer morajo električni pulzi zagotoviti elektroporacijo vseh celic v tkivu, kar omogoči da krioprotektant vstopi v vse celice in jih ščiti med zamrzovanjem. Hkrati pa električni pulzi tudi ne smejo poškodovati celic. V namen optimizacije krioprezervacije špinače smo razvili numerični model z razločeno celično strukturo špinačnega lista. Model je bil validiran na podlagi meritev električnih lastnosti špinačnih listov v frekvenčni domeni in z meritvami električnega toka skozi list med dovajanjem elektroporacijskih pulzov. Ta model je prvi numerični model elektroporacije tkiva, ki upošteva celotno celično strukturo tkiva. Postopek, po katerem smo razvili model, pa lahko vodi nadaljnji razvoj podobnih modelov za druge tipe tkiva.

Numerični model prevodnosti vodne pore v lipidnem dvosloju, validiran s simulacijami molekularne dinamike

Prevodnost pore je eden najpomebnejših parametrov, ki premošča teoretične in eksperimentalne študije vodnih por, ki nastanejo v lipidnem dvosloju pod vplivom vsiljene transmembranske napetosti (tj. elektroporacije). Simulacije molekularne dinamike namreč ponujajo možnost študije por na molekularnem nivoju, pri eksperimentih na ravninskih lipidnih dvoslojih pa raziskovanje por poteka preko meritev njihove prevodnosti. Most med eksperimentalnimi študijami in simulacijami molekularne dinamike ponujajo modeli, ki sistem opisujejo s strani zveznih teorij. V namen učinkovite premostitve smo razvili numerični Poisson-Nernst-Planckov model ionskega toka prek lipidne pore. Model je bil zgrajen neposredno po molekularnem sistemu, s katerim smo izmerili prevodnost por s pomočjo simulacij molekularne dinamike. S kvantitativno primerjavo med napovedmi modela in rezultati, ki smo jih pridobili z analizo simulacij, smo numerični model validirali. Ta model predstavlja prvo direktno replikacijo molekularnega sistema z numeričnim modelom v smislu ionske prevodnosti lipidne pore. Pričakujemo lahko, da bo ta model prispeval k učinkovitejši karakterizaciji lipidnih por v eksperimentalnih študijah, hkrati pa lahko pričakujemo, da bo izboljšal tudi napovedi modelov, ki opisujejo elektroporacijo celičnih membran.

Introduction

Electroporation is known as the phenomenon, whereby application of electric pulses induces reversible or irreversible structural changes in the membranes of biological cells and other lipid systems, leading to an increase in the membrane conductivity as well as permeability for molecules otherwise deprived of transmembrane transport mechanisms (Tsong, 1991; Weaver and Chizmadzhev, 1996; Kotnik *et al.*, 2012). As electroporation provides a simple biophysical approach to perturb the barrier function of cell membranes, it has a high applicative potential in diverse biomedical and biotechnological fields. Indeed, electroporation is already successfully and routinely utilized in cancer treatment, food processing, and biomedical research, with many other applications being rapidly developed (Yarmush *et al.*, 2014; Mahnič-Kalamiza *et al.*, 2014; Kotnik *et al.*, 2015).

The phenomenon itself, however, is not entirely understood. As the name "electro*poration*" already implies, the structural changes in the membrane are attributed to aqueous pores in the membrane, which form under the influence of the applied electric pulses. Electric pulses namely induce a transmembrane voltage (electric potential difference) across the cell membranes, which according to theoretical predictions, molecular dynamics simulations, as well as experimental investigations on model lipid systems, increases the probability for formation of aqueous pores specifically in the lipid domains of the membrane (Hibino *et al.*, 1993; DeBruin and Krassowska, 1999; Melikov *et al.*, 2001; Szabo and Wallace, 2015). Although such pores indeed most probably present at least part of the structural changes, cells membranes are nevertheless much more complex structures than lipid bilayers and there is enough experimental evidence demonstrating that cell electroporation cannot be viewed as simply as electroporation of a lipid vesicle (Huynh *et al.*, 2004; Teissié *et al.*, 2005; Wegner *et al.*, 2015).

Unfortunately, there are no experimental methods yet developed that would allow to directly observe the changes in the molecular structure of the cell membrane during and after application of typical (ns–ms) electroporative electric pulses in a temporally and spatially resolved manner. The experimental evidence is thereby indirect, measured by means of changes in membrane conductance, transmembrane voltage, transmembrane molecular transport and leakage of cytosolic ions, as well as consequences like cell swelling, cell death, and structural changes that can be detected by techniques such as electron microscopy, nuclear magnetic resonance, and atomic force microscopy (Kinosita and Tsong, 1979; Escande-Géraud *et al.*, 1988; Lopez *et al.*, 1988; Rols and Teissié, 1990; Hibino *et al.*, 1993; Gabriel and Teissié, 1999; Canatella *et al.*, 2001; Kandušer *et al.*, 2006; Pakhomov *et al.*, 2007a; Pavlin *et al.*, 2007; Kotnik *et al.*, 2010; Nesin *et al.*, 2011; Chopinet *et al.*, 2013). In addition, electroporation is highly dynamic, with structural changes being characteristically different during as compared to after application of an electric pulse (Pavlin and Miklavčič, 2008; Wegner *et al.*, 2015). For example, the conductance of the membrane can increase by orders of magnitude during the pulse, yet returns nearly to its baseline value within microseconds after the pulse, whereas most of the transmembrane molecular transport generally occurs within minutes after the pulse (Hibino *et al.*, 1993; Pucihar *et al.*, 2008). Apart from

the *wide range of temporal scales* involved in electroporation, there is also a *wide range of spatial scales*. We know that a small pore in the lipid bilayer should have a diameter on the order of a nanometer. A typical cell is, though, three to four orders of magnitude larger than the assumed pore. Furthermore, in medical treatments, electroporation is performed on cells in centimeters-large portions of tissue, whereas the demands of industrial-scale applications require that tens or hundreds of tons of plant tissue are treated per hour (Zimmermann *et al.*, 1974; Melikov *et al.*, 2001; Tarek, 2005; Sack *et al.*, 2010; Mali *et al.*, 2013; Pakhomov *et al.*, 2015).

If we go back to a single cell or a model lipid membrane, the difficulties of experimental research are imposed also by the limited sensitivity of the detection systems. The conductance of a single lipid pore with radius of 1 nm in typical physiological solutions with conductivity of about 1 S/m should have a conductance of roughly 0.5 nS (Li and Lin, 2010). When applying a measuring voltage of 0.1 V, the measuring system needs to resolve an electric current of 0.05 nA in order to detect a change in the membrane conductance due to a single pore. Not all systems are capable of such resolution. For comparison, the measurement system for planar lipid bilayers in our laboratory can resolve electric currents of 0.02 μA (Polak *et al.*, 2012). Such small changes in membrane conductance are indeed physiologically important. For example, Pakhomov *et al.* used the whole cell patch-clamp technique to measure minutes-long changes in membrane conductance after exposure to a single 60 ns, 12 kV/cm pulse. They detected a maximum increase in the conductance from about 0.2 nS in control cells (5 GΩ in their report) to 1 nS (1 GΩ) in electroporated cells about 100 s after pulse application. This measured increase would correspond to at most few very small pores or a single slightly larger pore (Pakhomov *et al.*, 2007a). Nevertheless, a similar pulse could induce measurable uptake of fluorescent thallium ions into the cell (Ibey *et al.*, 2010b). On the other hand, ^{31}P NMR studies performed by Lopez *et al.*, although using much longer 100 μs pulses, suggested that practically all phospholipids within the membrane area, where the transmembrane voltage was elevated above a certain value during the pulse, are in an altered state during the resealing phase of the membrane (Lopez *et al.*, 1988). Eruption of microvilli localized to the regions of the elevated transmembrane voltage were also observed in the resealing phase (Escande-Géraud *et al.*, 1988). A recent atomic force microscopy study further suggested that the elasticity of the entire cell membrane is altered in the resealing phase after the pulses (Chopinet *et al.*, 2013). This challenges the idea of local aqueous pores as being the only structural changes in the membrane. Finally, Wegner *et al.* reported that the transient electroporation during the pulse and persistent permeabilization after pulse application are two distinct processes, which can be separated at appropriate pulse parameters (Wegner *et al.*, 2015).

Due to the wide range of temporal and spatial scales as well as limitations imposed by experimental systems, we need to resort to combined experimental and theoretical investigations in order to better understand the electroporation phenomenon (or perhaps more adequately, electroporation phenomena). The theoretical modeling of electroporation is nevertheless also highly challenging. The wide span of spatial and temporal scales as well as the structural and geometrical complexity of the cell membranes necessarily requires a multi-scale approach, as explained below.

At the present stage, it is possible to model the increase in the transmembrane voltage induced by a non-electroporative electric pulse very well by treating the cell membrane as a leaky dielectric surrounded by

conductive electrolyte solutions and solving the Laplace equation for the electric potential. Using this approach, good agreement between theoretical predictions and experimental measurements can indeed be obtained for single cells as well as cells in cell assemblies, such as cell clusters (Lojewska *et al.*, 1989; Hibino *et al.*, 1993; Kotnik *et al.*, 2010). However, there is a long way from small groups of cells to cells in the heterogeneous structure of tissues. One of the key difficulties in characterizing electroporation of cells in tissues is that the tissue thickness often precludes the possibility to visually examine individual cells in different tissue layers (Chopinet *et al.*, 2012; Dymek *et al.*, 2015b). Electroporation in such case is thus performed "blindly" without having a physical understanding of the electric field distribution to which different cells are exposed. However, progress has been made also in this direction by magnetic resonance electric impedance tomography (MREIT) (Kranjc *et al.*, 2014). Yet, modeling the tissue by resolving the underlying cellular structure can contribute to this understanding, which is particularly important if we need to optimize the pulse parameters such that all cells in the tissue are preserved and not damaged by excessively high electric field. Progress towards bridging the gap between modeling of individual cells and modeling of tissue as a homogeneous structure (characterized by its bulk properties) is therefore highly beneficial if not utterly necessary.

There are also other advantages of numerical modeling, not restricted only to cells in tissue, but related to practically any *in vitro* experiment. Numerical calculations are generally less time consuming and much less expensive than *in vitro* experimental work. Speaking from personal experience, combining numerical modeling with experiments gives one also a much deeper understanding of experimental protocols and insights into which experimental parameters need to be carefully controlled. Though numerical modeling cannot completely replace experimental work, it can contribute to the initial design of the protocol and can guide its further optimization. In addition, theoretical models can help understand unexpected or unclear experimental results (Šemrov and Miklavčič, 1998; Gowrishankar *et al.*, 2006; Li *et al.*, 2013).

As noted above, we know well how to model the exposure of cells to *non*-electroporative electric pulses. However, during an electroporated pulse, the conductivity of the cell membrane can increase by orders of magnitude, which in turn perturbs the electric field distribution around as well as inside the cell (Smith and Weaver, 2008). Hence, when modelling cells in cell assemblies or investigating electroporation of intracellular organelles, it is important to take this increase in conductivity into account in order to approach more closely to the realistic situation.

The increase in cell membrane conductivity is driven by the increase in the transmembrane voltage in a nonlinear way (Kinosita and Tsong, 1979; Hibino *et al.*, 1993; Pavlin *et al.*, 2007; Suzuki *et al.*, 2011). To model this increase, generally, the Laplace equation for the electric potential needs to be coupled with a model of membrane electroporation. According to the limited available experimental data (Kinosita *et al.*, 1988; Hibino *et al.*, 1991, 1993), existing electroporation models, which arise from theories describing irreversible and reversible electrical breakdown of planar lipid bilayers, are able to predict the increase in the cell membrane conductance rather well (at least qualitatively) (DeBruin and Krassowska, 1999; Krassowska and Filev, 2007; Smith and Weaver, 2008).

Nevertheless, continuum electroporation models describe the nature of lipid pores in terms of continuum theories, which are well applicable to large systems, but may not be fully applicable to the molecular scale. Some of the assumptions embedded in these models were already compared to results from molecular dynamics simulations, however, there are still essential components of the models, which were not yet systematically validated with models describing the lipid bilayer with atomistic detail (Wohlert *et al.*, 2006; Bockmann *et al.*, 2008; Levine and Vernier, 2010). Thereby it is reasonable to maintain some doubt in the simplified assumptions embedded in continuum electroporation models. Looking from another point of view, the computational cost of the simulations allows one to study only small bilayer patches with areas of the order of 100 nm^2 over times reaching hundreds of nanoseconds. In order to relate the simulation results to typical experimental systems, models arising from continuum theories may sometimes be a necessary intermediate step. Bridging the gap between continuum models of electroporation and molecular dynamics simulations thereby emerges as important, if we are to develop robust continuum models and efficiently relate the knowledge gained from simulations to experimental systems.

In the present thesis, I followed two main objectives: (i) to use numerical modeling of electroporation to complement and guide *in vitro* experimental work; and (ii) to compare the predictions arising from continuum electroporation models with results from molecular dynamics simulations. All results of the work are presented in the form of papers, which were published or were submitted to scientific journals.

Paper 1 entitled **Invited tutorial: Electroporation of cells in complex materials and tissue** is a tutorial paper which gives the introductory overview on electroporation and developed theoretical/numerical approaches of scaling the knowledge of electroporation from single cells to cells in more complex environment up to the tissue level.

Papers 2–4 present the realization of the first objective of the thesis and are related to the ongoing development of numerical models of electroporation from single cells, through cell assemblies, towards cells in tissue. Each of the papers considers a different application of electroporation.

Paper 2 entitled **Electroporation of intracellular liposomes using nanosecond electric pulses – A theoretical study** addresses the possibility to electroporate intracellular liposomes using nanosecond electric pulses for the purpose of drug delivery. Liposomes are namely drug delivery vehicles which have the advantage to protect the drug from the hostile environment, particularly in the blood plasma, as well as the organism itself from the toxic effects of the drug. But once the liposomes reach the target cells, they need to release their content into the cytosol. In the paper we studied whether nanoseconds pulses, which are able to electroporate intracellular organelles, could provide the means to release the liposome content in a controlled manner without perturbing cell viability.

Paper 3 entitled **Cell electrofusion using nanosecond electric pulses** demonstrates the potential advantage of using nanosecond pulses for electrofusing cells of different size and corroborates the feasibility of this approach

experimentally. Cell cultures characterized by a larger size are generally, though not always, electroporated at lower electric field strength. When simultaneously electroporating two cells cultures of different size, which is performed in cell electrofusion protocols, the larger cells may become damaged when exposed to an electric field required to electroporate the smaller cells, in particular when conventional microseconds-long pulses are applied. This is known to be an issue in electrofusion of lymphocytes with myeloma cells in hybridoma technology for monoclonal antibody production. In the study, we numerically investigated the induced transmembrane voltage on cells in close contact, mimicking the cells right before electrofusion. We showed that when cells placed in a low conductive medium, typical for electrofusion protocols, are exposed to pulses of durations in the nanosecond range, the highest transmembrane voltage induced is in the contact zone between cells, i.e., the target area for electrofusion. Amplification of the transmembrane voltage at the contact zone allows one to optimize the pulse parameters to specifically electroporate the contact zones and avoid problems due to cell size differences.

Paper 4 entitled **Modeling electroporation of the non-treated and vacuum impregnated heterogeneous tissue of spinach leaves** presents the development of a numerical model of a spinach leaf with resolved tissue structure in order to address the problems in cryopreservation of spinach leaves. In the latter, the cryoprotectant (e.g. trehalose) is first introduced into the extracellular space inside the leaf tissue by means of vacuum impregnation. Afterwards, the leaf is electroporated to allow the cryoprotectant to enter the cells, as the cryoprotectant needs to be present on both sides of the membrane, i.e., both from the extracellular and intracellular side, in order to increase the freezing tolerance of the leafs. The tissue of the leaf is heterogeneous and it is difficult to achieve electroporation and survival of all cells in the tissue after exposure to electric pulses. In addition, the leaf is too thick to allow microscopic examination of all tissue layers. Consequently the developed model allowed us to investigate how different cells are electroporated and provided the possibility to further optimize the pulse parameters for reversible electroporation of all cells in the tissue. The model was validated based on measurements of the leaf properties in a non-electroporative alternating electric field, by measurements of the electric current through the leaf during electroporation, as well as by available microscopic examinations of the leaf.

Papers 5 and 6 are linked and present the realization of the second objective of the thesis.

Paper 5 entitled **Properties of lipid electropores I: Molecular dynamics simulations of stabilized pores by constant charge imbalance** describes a novel method, which allows thorough characterization of rather stable conductive pores in the lipid bilayer. The method is based on imposing a specific “swapping” algorithm that is able to return ions which passed through the pore back to their original position below or above the bilayer. This allows one to maintain a constant charge imbalance across the bilayer which permits the transmembrane voltage, ionic current through the pore, and the pore size to adapt to its energetically favorable configuration. Once the system reaches its equilibrium, it is possible to thoroughly characterize the size and ionic conductance of a pore, and transmembrane voltage at a given charge imbalance. The method further addresses the problems of finite-size effects and relaxation of the surface tension in simulations.

In Paper 6 entitled **Properties of lipid electropores II: Comparison of continuum-level modeling of pore conductance to molecular dynamics simulations** we compared the results of pore conductance obtained in Paper 5 with the predictions of a continuum model based on the Poisson-Nernst-Planck theory. This theory is the origin of all theoretical descriptions of pore conductance which are used in the continuum electroporation models. Nevertheless, these descriptions contain many simplified assumptions. In the paper, we demonstrate that the theory is able to describe the overall pore conductance to Na^+ and Cl^- ions very well provided that we take into account the toroidal shape of the pore. Moreover, we numerically investigated the influence of the binding of Na^+ ions to lipid headgroups and electroosmotic flow across the pore on the pore selectivity, i.e., higher conduction of Cl^- than Na^+ ions. We further compared our results to simplified theoretical expressions of pore conductance and demonstrated that the simplifications do indeed influence the overall predictions of continuum electroporation models.

As the results are already thoroughly discussed in the respective papers, the final chapter of the thesis is entitled *Conclusions*.

Paper 1

Title: **Invited tutorial: Electroporation of cells in complex materials and tissue**

Authors: Lea Rems and Damijan Miklavčič

Publication: J. Appl. Phys. Submitted for review.

Journal information

JOURNAL OF APPLIED PHYSICS		
Publisher	AMER INST PHYSICS, 1305 WALT WHITMAN RD, STE 300, MELVILLE, NY 11747-4501 USA	
ISSN eISSN	0021-8979 1089-7550	
Research domain	Physics	
Impact factor	2.183 (2014) 2.276 (5 year)	
JCR® category	Rank in category	Quartile in category
PHYSICS, APPLIED	42 of 144	Q2

Source: Web of Science™ (December 2015)

Author contributions of L. Rems

L. Rems gathered most of the literature and wrote most of the manuscript.

Invited tutorial: Electroporation of cells in complex materials and tissue

L. Rems and D. Miklavčič[a)]

University of Ljubljana, Faculty of Electrical Engineering, Tržaška 25, SI-1000 Ljubljana, Slovenia

[a)] Author to whom correspondence should be addressed. Electronic mail: damijan.miklavcic@fe.uni-lj.si

Electroporation is being successfully used in biology, medicine, food processing, and biotechnology, and in some environmental applications. Recent applications include in addition to classical electroporation, where cells either in suspension or in tissue are exposed to micro- to milliseconds pulses, also applications of extremely short nanosecond pulses, i.e. high-frequency electroporation. Electric pulses are applied to cells in tissues which represent complex environment. Understanding of cell membrane electroporation in tissues and other complex environments is key to its successful use and optimization in various application; thus it will be explained theoretically/numerically and related to experimental observations.

I. INTRODUCTION

Application of electric pulses as means of increasing cell membrane conductivity and permeability has been discovered already at the end of 1950s[1–3]. Later on, the phenomenon was attributed to transient aqueous pores in the membrane, formed under the influence of the electric field[4–6], and was hence termed electroporation[7]. Throughout the past decades, this intriguing phenomenon was honored by extensive research, which revealed many other fascinating features: electroporation can be used to nonselectively increase the uptake of drugs or genetic material into cells[7–10], extract molecules from cells[11,12], insert proteins into the cell membrane[13,14], induce cell-cell or cell-vesicle fusion resulting in viable hybrids[15–17], fuse individual cells with tissue[18], initiate targeted necrotic or apoptotic cell death[19–23], induce intracellular effects such as release of intracellular calcium[24–26], and to modify the texture and viscoelastic properties of plant tissues[12,27].

The most appealing feature of electroporation is that it is universal: it is general to all cell types (eukaryotic cells, bacteria and archaea[28,29]) in any cell arrangement (in suspension, adhered to surface, in clusters, or in tissue); and apart from cells, it can also be observed in any other bilayered membrane system such as planar lipid bilayers[30], lipid vesicles[31], and polymeric vesicles[32]. This universality lead to the development of numerous applications in diverse fields[33] including medicine, biotechnology, food processing, and environmental applications, some of which already reached the patient/consumer[12,34]. Currently the most developed medical applications include electrochemotherapy[10,35], gene electrotransfer[36,37], tissue ablation by means of irreversible electroporation[38], and cardiac muscle ablation for treatment of arrhythmias[39–41]. In food processing (where electroporation is generally referred to as pulsed electric field or PEF treatment) the industrial applications range from pasteurization of liquid food[12], extraction of sugar from sugar beet[42–44], treatment of grapes in wine production[45], to valorization of waste material such as extraction of polyphenols from grape pomace[46,47].

In many of the above applications, electroporation is performed on cells in tissues. New emerging technologies utilize electroporation in synergy with different forms of nanostructured material. Understanding the mechanisms by which electric pulses act on cells in such complex environments requires a multi-scale approach, where we seek information from molecular models and simple lipid systems up to *in vitro* and *in vivo* experiments. Therefore we will dedicate the first part of this tutorial to the knowledge gained primarily from *in vitro* experiments on cell cultures, but also from insights provided by experiments on planar lipid bilayers, lipid vesicles, and molecular dynamics simulations. Note that the *in vitro* data comes primarily from mammalian cell cultures, for which the literature is most abundant. Studying electroporation in such "simple" environment is inevitable as it allows basic research on different aspects of electroporation. Our understanding of electroporation in simple systems is then transferrable to electroporation of cells in more complex systems, which we will discuss in the second part of the tutorial. We will review the aspects of electroporation in increasingly complex cell assemblies up to the tissue level, followed by a brief overview of sophisticated nanoscale technologies, which are paving the path to use electroporation in a wide range of new and interesting ways. Finally, we will point out the questions which remain to be answered in order to better understand electroporation-related processes allowing us to improve the designs of current as well as future technologies and treatments.

II. ELECTROPORATION ON SINGLE CELL AND SUBCELLULAR LEVEL

In order to study the mechanisms of cell electroporation, we first need to understand how electric pulses act on biological materials. When, for example, a dilute suspension of cells is exposed to electric pulses such as by placing the suspension between plate electrodes in cuvettes, an electric field is established between the electrodes during each pulse. The electric field directly generates forces that tend to move the charged ions and molecules as well as orient the permanent and induced electric dipoles in the sample. Depending on specific conditions, the consequences of these forces can be various, including electric current flowing between the electrodes causing Joule heating[48,49], electrophoretic, dielectrophoretic and electrodeformation forces acting on suspended cells[15,50,51], structural modification of biomolecules[52,53], and chemical reactions at the electrode-electrolyte interface[54–56].

However, the most important consequence of the electric field, which is present under all conditions and was shown to drive the structural rearrangements of the cell membrane components, resulting in increased membrane permeability, is the voltage which is induced across the membranes[4] (Section II.A). Other phenomena may have a contributing effect, though further research is necessary to clearly elucidate the extent of their contribution. Despite decades of investigation, the exact molecular mechanism(s) that lead to membrane alterations allowing passage of otherwise impermeable solutes are still unclear (Section II.C). Theoretical considerations and insights from molecular dynamics simulations suggest that at least during the pulse application, aqueous pores are formed in the lipid bilayer, which is currently considered as the most probable mechanism of initial membrane perturbation (Section II.B). However, the leakiness of the cell membranes persists for tens of seconds to several minutes or even hours following pulse application, which can hardly be attributed to highly dynamic lipid pores

(Section II.D). For this reason we need to remain conservative and understand the term electro*poration* in a broader sense, where a "pore" could present any local and highly permeable membrane defect, as already proposed in the earliest studies of electroporation[5,57].

Although the initiation of the membrane structural rearrangements is a purely biophysical response, we must be aware that the resulting loss of membrane barrier function perturbs the physiological state of cells and induces a cellular response following pulse application (Section 2D). Extensive *in vitro* experiments using electric pulses with duration in the range of μs–ms revealed five consecutive steps, which are present in cell electroporation[58], and are given in Table I. Next to each electroporation step we also indicate its time scale.

TABLE I. Steps in electroporation (adapted from Teissié et al.[58])

Electroporation steps	*Time scale*	*Refs.*
Trigger (initiation): Structural changes in the membrane are induced when the transmembrane voltage reaches sufficiently high, i.e. "critical" value.	ns–μs	59–65
Expansion: As long as the transmembrane voltage is maintained above the "critical" value, the size and/or number of permeable membrane defects (pores) increases.	pulse duration (ns–ms)	59–61,64
Stabilization (**recovery**): When the transmembrane voltage reduces below the "critical" value, the membrane conductivity and highly permeable state rapidly recovers; however, slightly increased membrane permeability is stabilized and persists for considerable time after application of electric pulses, which allows transmembrane diffusion of ions and molecules in the resealing step.	ms–s	59–61,64–67
Resealing: The permeable membrane is slowly resealed and the cell recovers its original impermeability unless the cell was irreversibly damaged.	s–min (~20–37°C) hours (4°C)	59,65,68–79
Memory: Some effects of the electric pulses persist on longer time scale, even after the membrane resealed. Unless the cells undergo long term death, they will finally return to their normal state.	hours	21,80–82

A. The induced transmembrane voltage

In their physiological state, practically all cells have a small resting transmembrane voltage (TMV), which is maintained by a system of ion pumps and channels in the membrane. The magnitude of the resting TMV varies from cell to cell type, but it generally reaches few tens of millivolts with the cell interior being more negative than the exterior. Aside from the highly selective transport of ions which is controlled by membrane proteins, the cell membrane is practically non-conductive in the electrical sense. When exposed to an external electric field, the membrane hence behaves similarly as a capacitor, where the redistribution of electrophoretically driven charged ions in the electrolytes surrounding the membrane, i.e. electric current, leads to an induced TMV. The induced TMV superimposes to the resting TMV, but unlike the latter, it varies with the position on the membrane[60,61,83,84]. Knowing the time course and spatial distribution of the induced TMV is very important from the standpoint of electroporation, since only the membrane areas, where the absolute value of the TMV exceeds certain value for sufficiently long time, become permeabilized[5,60,61,67,85,86].

The general approach to calculate the induced TMV is to solve the Laplace equation for the electric potential in the space between the electrodes. The validity of this theoretical approach was confirmed experimentally by measurements of the induced TMV with voltage-sensitive dyes[83,86,87]. For isolated cells with simple shapes, the induced TMV can be derived analytically[88–90], whereas for irregularly shaped cells and/or cells which are in close proximity, the solution can only be obtained numerically[84,91].

For an isolated spherical cell in homogeneous direct current (DC) electric field, the simplified expression (assuming physiological conditions and disregarding the dielectric permittivity of electrolytes) describing the time course of the TMV after the onset of a step increase in electric field is given by[89]

$$\mathrm{TMV} = 1.5ER\cos\theta\left(1-\mathrm{e}^{-t/\tau_m}\right)+U_{rest} \tag{1}$$

where E is the electric field strength, R is the cell radius, θ the angle between the direction of the electric field and the vector normal to the membrane surface, τ_m the charging time of the membrane, and U_{rest} the resting TMV (Fig. 1, A1–B1). Note that equation (1) corresponds to the total TMV, which is the sum of the induced TMV and the resting TMV. This equation shows several important features of the TMV:

(i) The induced TMV does not establish immediately, but requires certain charging time τ_m, which depends on the electric properties of membrane, extra- and intracellular solutions, and cell size; for spherical cells with radius of ~10 μm in extracellular medium with physiological conductivity (~150 mM salt, ~1 S/m), this charging time is on the order of 100 ns; low conductive medium, which is often used in experiments *in vitro* in order to reduce Joule heating, extends it considerably[88]. Nevertheless, for any electric pulse with duration longer than about five membrane charging times, the TMV is able to reach its steady state and equation (1) can be simplified into $\mathrm{TMV} = 1.5RE\cos\theta + U_{rest}$.

(ii) The induced TMV varies locally with the position on the membrane with the highest absolute |TMV| established at the "poles" of the cell (membrane areas, which are facing the electrodes), and minimal |TMV| established around the "equator", so only the "poles" get electroporated. In addition, as the induced TMV superimposes onto the resting TMV, which is for most cell types negative ($U_{rest} < 0$), the |TMV| on the side of the positive electrode (anode) is higher than on the side of the negative electrode (cathode). Indeed, it is possible to observe electroporation at the anodic side of the cell at lower electric field strength compared to the cathodic side[85,92–94].

(iii) The induced TMV is proportional to the cell radius R and the electric field strength E meaning that higher TMV will be established on larger cells and when applying pulses with higher amplitude; this enables targeted electroporation of larger cells in a population of cells which considerably differ in size[95].

(iv) Apart from the above, the induced TMV depends also on the shape and orientation of the cell in the electric field, as well as the proximity of other structures such as neighboring cells, which can perturb the local electric field distribution[96,97].

Although the occurrence of membrane electroporation clearly expresses a threshold behavior which is correlated with the TMV[60,85,86] (Fig. 1, A2–D2), there is some controversy on the actual magnitude of TMV required to trigger electroporation. This critical TMV was estimated to be on the order of few 100 mV to about

1000 mV[2,5,98,99,85]; however, the estimates unfortunately greatly depend on the calculation as well as the detection method. Since electroporation is usually assessed by monitoring the abrupt increase in transmembrane transport of a certain solute (e.g. fluorescent dye), the detection of electroporation of course depends on the sensitivity of the detection system[100]. Moreover, it was shown that small ions and molecules pass the electroporated membrane much easier than larger molecules, meaning that higher electric field and/or pulse duration and/or number of pulses will be required to detect electroporation when using larger solutes[68,69,71,73,101,102] (see also Section II.C). Furthermore, it was demonstrated that the critical TMV for observable electroporation slightly reduces with increasing the duration of the pulse[5,61–63,103,104] and temperature[28,59,78,98]. It moreover depends on the cell type[105], and can also vary considerably between cells of the same type with an apparent tendency than smaller cells require lower TMV for electroporation[106–108,94]. These data suggest that the cell size and consequently the induced TMV are important[5,109–111], though not the only factors determining cell electroporation[94,105,112–114] (Fig. 1, A3).

Regardless of the fact that the "critical" TMV is not universal and well-defined, for any application of electroporation, the amplitude of the electric pulses needs to be appropriately adjusted, such that the pulses result in an electric field capable of inducing sufficiently high TMV. The time dependence of the TMV results here in another important feature. During the charging process of the membrane, high electric field is present also in the cell interior, but its magnitude gradually reduces with time as the TMV approaches its steady state, effectively shielding the cell interior from the external electric field. During the charging time thus, the TMV is induced also on the membranes of the intracellular organelles[115] (Fig. 1, B1). Hence, by using pulses with duration in the nanosecond range, and amplitudes resulting in an electric field of ~10–100 kV/cm, the pulses can also electroporate intracellular organelles (in addition to the plasma membrane) and initiate numerous intracellular effects[116–118].

On the contrary, if pulses with duration in the μs–ms range are used (i.e. longer than the charging time of the membrane), electroporation occurs primarily on the cell plasma membrane. As the TMV is allowed to reach its maximum (steady state) value, the amplitude of the pulses can be considerably lower than when using ns pulses; generally, pulses resulting in electric field strength on the order of 0.1–1 kV/cm are sufficient. The cell interior is, however, not completely shielded even when applying μs–ms pulses. The membrane conductance can increase by several orders of magnitude during the pulse[2,59,64,98,119], which consequently increases the electric current flowing through the cytoplasm and somewhat increases the voltage across the organelles. A theoretical study predicted that this voltage can be large enough to gate organelle channels, and at some field strengths even sufficient for electroporation of organelle membranes[120].

We must also stress that the induced TMV obeys equation (1) only as long as one can assume that the membrane conductance is virtually null. When the conductance increases due to electroporation, the membrane partially discharges through the conductive pathways. This consequently reduces the TMV at the regions where electroporation occurred, as was demonstrated by measuring the TMV during electroporative pulses with voltage-sensitive dyes[60–63]. The experimental observations could be well described by a theoretical model which considered that the TMV drives the formation of aqueous pores in the membrane lipid bilayer[121].

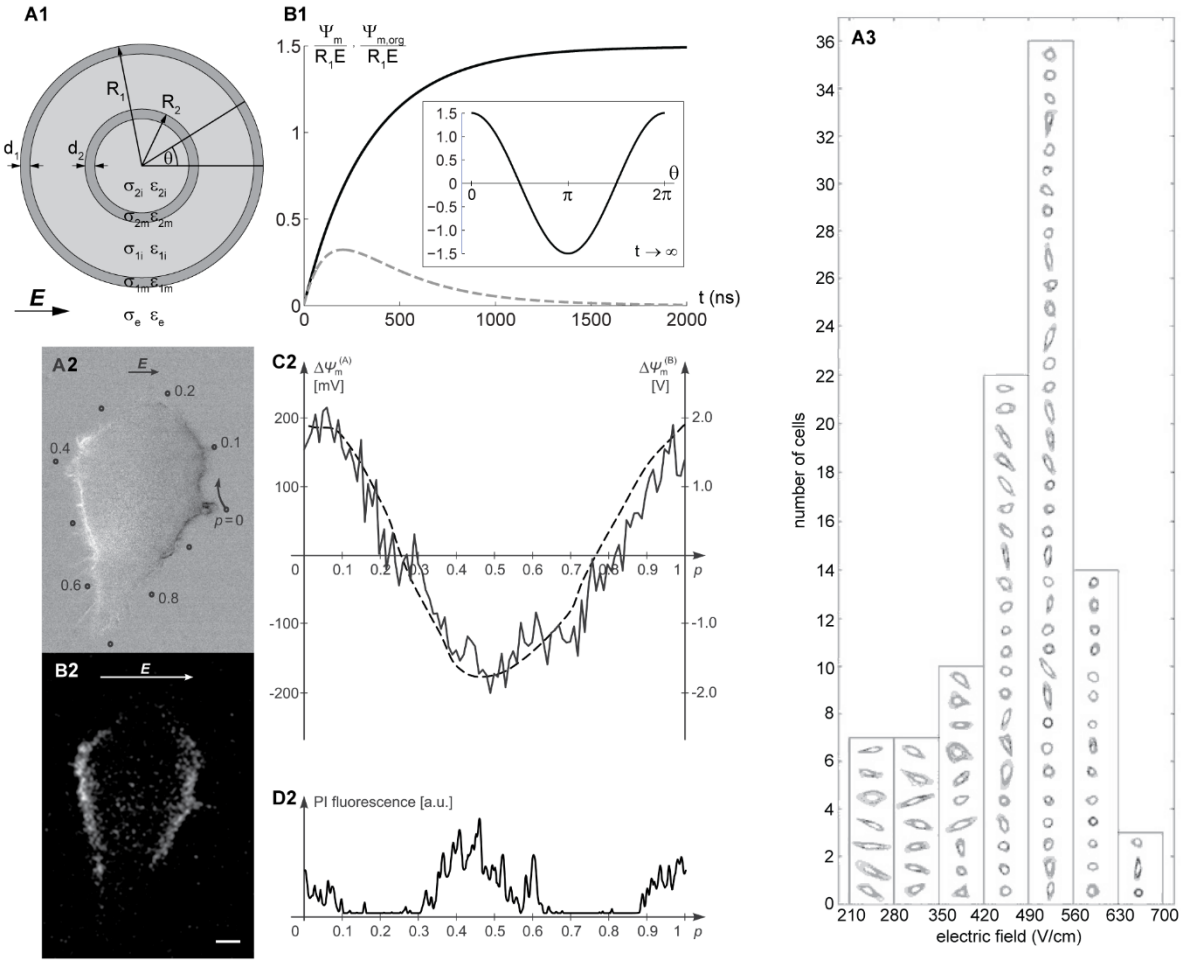

FIG. 1 **(A1)** Model of a spherical cell with a concentric spherical organelle. The model consists of five regions, each characterized by an electric conductivity (σ, in S/m) and a dielectric permittivity (ε, in As/Vm). Subscript index "e" corresponds to the extracellular solution, "m" to the membrane, "i" to the internal solution, index "1" to the cell and index "2" to the organelle. **(B1)** The time course of the induced TMV on the cell membrane (Ψ_m, solid) and organelle membrane ($\Psi_{m,org}$, dashed), normalized by the electric field strength *E* and the cell radius R_1, at $\theta = 0$. Inset shows steady state Ψ_m along the cell circumference. Adapted from Kotnik and Miklavčič[115]. **(A2)** Changes in fluorescence of a voltage-sensitive dye di-8-ANEPPS reflecting the induced TMV in a CHO cell. Dark regions correspond to membrane depolarization and bright regions correspond to membrane hyperpolarization. **(B2)** Propidium iodide (PI) fluorescence, reflecting transport of PI across the electroporated membrane. **(C2)** TMV ($\Delta\Psi_m$) along the path shown in (A2) as measured (solid) and as predicted by numerical computation (dashed). **(D2)** Fluorescence of PI along the path shown in (A2). The transport of PI can be detected at the areas, which correspond to TMV above a certain threshold. Adapted from Kotnik et al.[86] **(A3)** The lowest electric field leading to detectable electroporation of attached CHO cells when applying a 100 μs pulse. Larger cells are electroporated at lower pulse amplitudes; however, the critical TMV for electroporation is smaller for smaller cells (not shown). Adapted from Towhidi et al.[108]

As a final remark in this section we note that in most current protocols the increase in the TMV resulting in membrane electroporation is achieved by establishing an electric field between electrodes, which are in direct contact with the treated biological material. This has some unfavorable consequences, such as electrolytic effects and mechanical injury when using needle electrodes to treat tissues. The electrolytic effects can be diminished by using bipolar instead of monopolar pulses[122]; however, the mechanical injury cannot be avoided, specifically when treating deep seated tumors or large cutaneous tumors. For this reason, ongoing research efforts are

addressing the possibility of inducing electroporation by means of magnetic fields[123–126] or delivering electromagnetic pulses using antennas[127,128].

Most biological materials are paramagnetic or diamagnetic, which means that they are practically "transparent" to magnetic field. A time-varying magnetic field can therefore induce a corresponding time varying electric field rather deep inside the biological material (cell suspension/tissue). The induced electric field can then induce TMV leading to increased cell membrane permeability[123–126]. Nevertheless, such "magnetoporation" has not yet been developed to the extent that would enable as efficient membrane permeabilization as conventional electroporation techniques.

The delivery of electromagnetic pulses using antennas is a feasible approach, but at the moment only from a theoretical point of view[128]. Such approach can be useful only if the pulse duration is in the subnanosecond range (~100–200 ps), as this enables to focus the radiation on a local tissue target with a spatial resolution of about 1 cm[127,128]. Picosecond pulses are too short to allow redistribution of ions in the electrolyte and corresponding membrane charging, yet the increase in the TMV can still be observed due to polarization of water and lipid dipoles. The increase in the TMV is therefore a purely dielectric response. Indeed, *in vitro* studies using subnanosecond pulses demonstrated that these pulses are able to induce action potentials and calcium transients in excitable cells[129], can perturb cell membrane integrity, and reduce cell viability[127,130,131], provided that the electric field intensity is of the order of ~100 kV/cm and sufficiently high number of pulses is applied. Corresponding molecular dynamics simulations suggested that formation of pores in the lipid bilayer, similar to the ones induced by longer pulses, can be accounted as possible mechanism of increased membrane permeability[129]. Local temperature increases resulting from the power dissipation inside the membrane may also have a contributing effect that is yet to be confirmed[132].

B. Formation of aqueous pores in the lipid bilayer

The theory describing formation of aqueous pores in the lipid bilayer under the influence of increased TMV has been proposed already in the late 1970s[6,133] and was indirectly corroborated by a number of experiments on simple lipid bilayers[6,134–138] and lipid vesicles[139,140]. The theory is able to explain the increase in the membrane conductance in the orders of magnitude observed during the pulse application without significant change in the membrane capacitance; the fact that certain types of planar lipid bilayers are able to electroporate reversibly or rupture irreversibly depending on the pulse parameters; and the stochastic nature of lipid bilayer rupture[141,142]. Furthermore, similar characteristics with respect to the increase in the membrane conductance were also observed in cell membranes: rapid (< μs) increase in conductance after the TMV reaches a certain critical value, gradual increase in conductance during the pulse, rapid decrease in the conductance to nearly its baseline value in few microseconds after the pulse, reduction of the critical TMV with pulse duration, and dependence of the critical TMV on the temperature[59,98,119,60,61,64].

However, a direct visual support for the theory has only been suggested recently by visualizing the dynamics of conductive pores in droplet-interface bilayers in real time using total internal reflection fluorescence

microscopy[138]. The pulses which were applied (~10 s, ≤ 350 mV) are though still very far from the ones used in cell electroporation. Although pores have also been visualized by rapid-freezing electron microscopy in electroporated erythrocytes[143], it was argued that the observed pores were experimental artefacts reflecting the creation of hemolysis pores induced by cell swelling[58].

Another support for the theory comes from atomistic molecular dynamics (MD) simulations, which have been in the past decade intensively used to study the molecular mechanisms of electroporation in lipid bilayers[144–146]. MD is an *in silico* method for simulating the movement of atoms and molecules by solving Newton's equations of motion, where the forces acting between the particles are derived from a potential energy of interatomic interactions described in different force fields[147]. Although very insightful, MD simulations are computationally highly demanding: in order to obtain the results in reasonable time, the simulations are generally carried out for small bilayer patches comprising up to ~100–1000 lipid molecules and over time scales reaching hundreds of nanoseconds[148].

In MD simulations there are two approaches to mimic electroporation conditions[147]. The first approach is to impose an electric field $\boldsymbol{E}$ which acts on all charged atoms in the system with the force $\boldsymbol{F_e} = q_i\boldsymbol{E}$, where q_i is the charge of the i-th atom (this electric field should not be confused with the one reported in experimental studies[146,149]). The imposed electric field leads to reorientation of water dipoles (and to a much lesser extent lipid dipoles) particularly at the water-lipid interface, which increases the electric field inside the bilayer correspondingly increasing the voltage across the bilayer[146,149,150]. The second approach to increase the TMV is to impose a charge imbalance, e.g., by placing an excess number of monovalent cations above the bilayer and corresponding excess number of monovalent anions below the bilayer[151]. The first approach is usually carried out in the absence of ions and models a purely dielectric response; this can be considered representative of nanosecond pulses, as they are too short to allow considerable charging of the membrane. The second approach is considered to be more representative of μs–ms pulses, which allow full charging of the membrane.

Regardless of the method used, the sequence of events describing pore formation and annihilation is similar in both approaches[151]. If the imposed electric field or charge imbalance is high enough, a conical structure of water molecules (a "water finger") starts to protrude into the bilayer hydrophobic core. When water from one side of the bilayer connects with water from the other side of the bilayer, a water-spanning column is formed across the bilayer[152]. Since the hydrophobic lipid tails are directly exposed to water, this configuration is often termed a hydrophobic pore[6]. In bilayers composed of specific lipids, such as negatively charged phosphatidylserine, or lipids with large headgroups, such as archaeal lipids, where the energetic barrier for reorientation of headgroups is very high, the hydrophobic pore simply expands allowing ions to pass through[28,153]. However, in the case of typical zwitterionic phospholipids, the lipid headgroups begin to migrate along the water column forming a so-called hydrophilic pore[149,152]. The pore then further increases in size and starts to conduct ions[154,155]. Once the external source (imposed electric field or charge imbalance) is removed, the pore follows the reverse sequence of events and closes within tens to hundreds of nanoseconds[149,152,156,157].

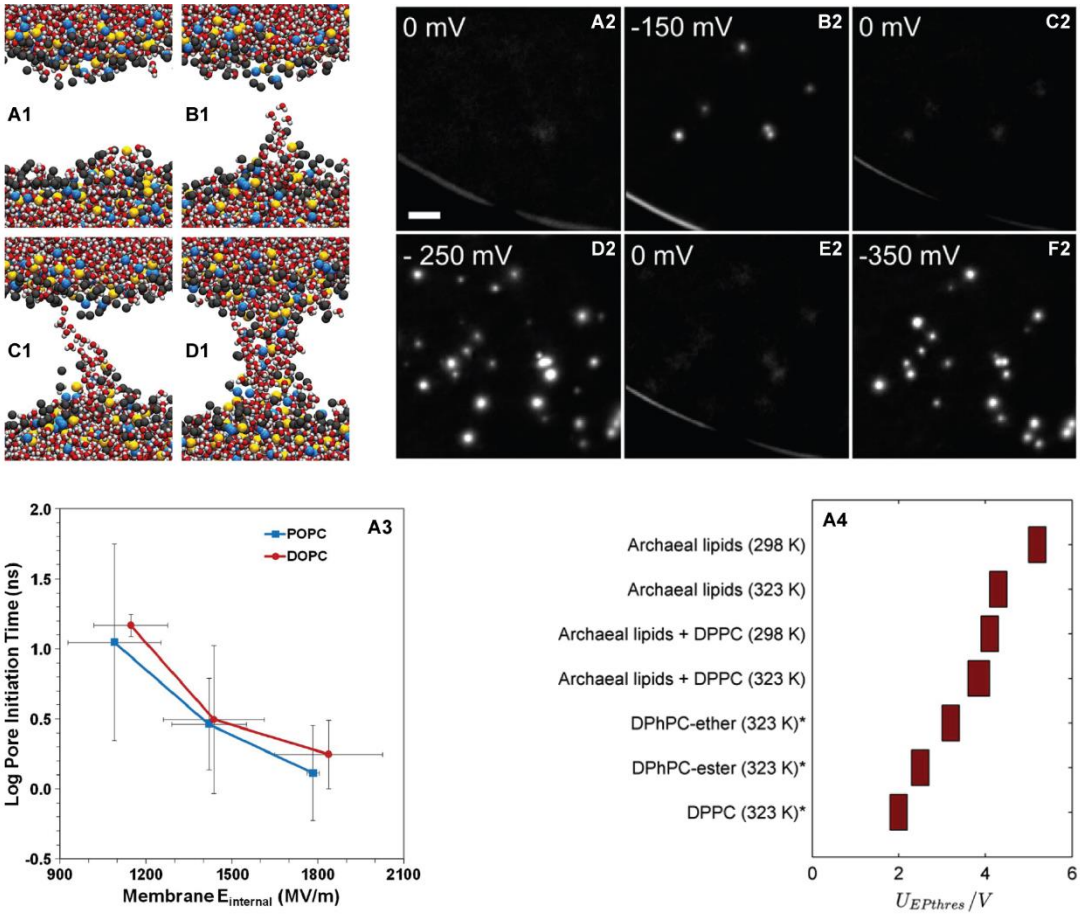

FIG. 2. **(A1–D1)** MD representation of a pore formation sequence in a palmitoyloleoylphosphatidylcholine (POPC) bilayer system. Small red and white spheres are water molecules, gold and blue spheres are head group phosphorus and nitrogen, respectively, and large gray spheres are phospholipid acyl oxygens. Hydrocarbon chains in the interior of the bilayer are not shown for clarity. In the presence of a porating electric field (B1) a water intrusion appears, and (C1) extends across the bilayer. (D1) Head groups follow the water to form a hydrophilic pore. The pore formation sequence, from the initiation of the water bridge to the formation of the head-group-lined pore takes less than 5 ns. Taken from Vernier et al.[146] **(A2–F2)** Image series showing the appearance of multiple pores in droplet interface bilayers as the applied potential is decreased. The ionic flux through the pores is visualized by means of potassium sensitive fluorophore APG-4 using total internal reflection fluorescence microscopy. Each image is an average of 100 frames (20 Hz acquisition). Scale bar 5 μm. Taken from Szabo and Wallace[138]. **(A3)** Pore formation time (time required to form the water bridge shown in (C1) is exponentially dependent on the applied electric field, expressed here as the electric field observed in the lipid bilayer interior. Error bars are standard error of the mean from at least three independent simulations. Taken from Vernier et al.[146] **(A4)** Threshold TMV ($U_{EPthres}$) required to form a pore within ~60 ns of an MD simulation when applying a charge imbalance across bilayers made from the following lipids: dipalmitoylphosphatidylcholine (DPPC), diphytanoylphosphatidylcholine (DPhPC) with ester of ether linkages, archaeal lipids and their mixtures with DPPC. The temperature, at which a given simulation was thermostated, are given in brackets.

An important aspect of the initiation of pore formation is that it is driven primarily by the interfacial water molecules[158,159]. The water can namely perforate and form a pore even in a vacuum slab[158] or an octane layer[144]. The initiation of a water protrusion is, however, a stochastic event which cannot be exactly predicted in advance[152]. Therefore we can only speak about the *probability* of forming a pore. Nevertheless, the probability of pore formation increases substantially with increasing electric field or charge imbalance[152,160], meaning that a pore can be formed in a shorter period of time[152]. The magnitude of the electric field or charge imbalance

required to observe electroporation on a given time scale, though, depends significantly on the type of lipid[28,149,161,162]. This magnitude was shown to be correlated with the lateral pressure in the hydrophilic headgroup as well as in the hydrophobic core region, which may cause reduced water mobility inside the bilayer[28,161,162].

As MD simulations provide the temporal and spatial resolution which cannot be achieved by any other experimental technique, they are indispensable for characterization of the properties of lipid pores[155], probing the mechanisms of transport of ions and macromolecules across lipid pores[148,154,163], for providing molecular mechanisms of the influence of protein structures[53,145] and cholesterol[164,165] on pore formation, for assessing the influence of different lipid mixtures[28,166,167], asymmetry in the lipid composition[166,162], and heterogeneous membranes with liquid-ordered and liquid-disordered lipid phases[168]. We will not go into details on all of these findings, but we encourage the reader to see the cited references.

Finally we need to give a comment on the magnitude of the imposed electric field or the induced TMV resulting from charge imbalance required to observe a pore in MD simulations, as they appear at first sight considerably higher than the ones reported in experiments. This issue was nicely explained by Vernier et al.[146,149] The electric field imposed in MD simulations corresponds to the electric field that would exist in vacuum in the absence of any electric dipoles. In order to make a comparison with electric fields reported in experiments, we need to take into account that the water dipoles in the MD system on average reorient due to the imposed electric field. Because of this orientation, they effectively decrease the field by a factor of ~80 (relative dielectric permittivity of water). This effective (net) electric field experienced by the system is consequently almost two orders of magnitude smaller than the one actually imposed. This effective electric field is indeed well within the range of electric fields used when experimentally applying nanosecond pulses, i.e., pulses with duration directly corresponding to the time scale of the simulations. Another reason arises from the stochastic nature of the pore formation. If one wants to observe a pore on a time scale applicable for atomistic simulations (nanoseconds), it is necessary to increase the electric field or the charge imbalance in order to increase the probability for its formation (Fig. 2, A3).

C. Induced transmembrane molecular transport

Electric-pulse-induced increase in the transmembrane molecular transport is one of the most exploited features of electroporation. The passage of otherwise impremeant molecules can be observed across the membrane areas which were brought to the permeable state already during the pulse application[65,67]. As already discussed above, these regions are correlated with the areas where the TMV exceeds the "critical" value[67,86]. Since we will primarily be discussing molecular transport in this section, we will rather use the term "permeabilization" instead of electroporation, in order to delineate it from the increase in the membrane conductance (increased transmembrane transport of small ions during the pulse).

Whether cells were permeabilized or not by electric pulses can be assessed in different ways. One possibility is to count the percentage of cells which were stained with a marker, e.g. trypan blue or propidium iodide, for

which the membrane is otherwise poorly permeable. When using such approach the percentage of permeabilized cells increases with electric field strength *E*, pulse duration *T*, and number of pulses *N* until all cells are permeabilized[103,169]. With respect to the pulse shape, square pulses were found to be most efficient[170]. The percentage of viable cells, on the contrary decreases with *E*, *T*, and *N*, therefore the parameters of the pulses need to be appropriately adjusted if the protocol requires that cells remain viable[103,169]. Such assessment of permeabilization and viability clearly reflects statistical variability in the cell population. In a study done by Puc et al.[109], this variability could, however, mostly be attributed to the distribution of the cell size.

Another way to assess permeabilization is to quantify the amount of molecules loaded into or leaked from a population of cells. Similarly as when counting the percentage of permeabilized cells, the amount of loading/extraction increases with *E*, *T*, and *N*[71,171–174,109,100], again with square pulses being the most efficient[170]. Pucihar et al.[65] used such approach to monitor the kinetics of propidium iodide uptake during and after a single 100–1000 μs square pulse by means of a photomultiplier tube with a high temporal resolution (200 ns–4 ms) and on a wide range of time scales (0–8 s after the onset of the pulse). They found that the transport during the pulse is primarily electrophoretic, whereas after the pulse it proceeds by diffusion. In this recovery/resealing phase after the pulse they could resolve three kinetic stages with time constants in the range of tens of milliseconds, hundreds of milliseconds, and tens of seconds. Their analysis demonstrated that the flux of molecules significantly decreases after the first kinetic stage (by about an order of magnitude), however the dominant transport occurs in the last stage, since it is two orders of magnitude longer than the first two stages. When observing the transport on even longer time scale, Neumann et al.[7] observed another kinetic stage with time constant on the order of 100 seconds.

Highly insightful is also the temporally and spatially resolved monitoring of molecular transport in single cells during and after the pulse. Gabriel and Teissié[67,175] used a rapid videoimaging system (300 frames/s) to monitor the transport of positively charged calcium, propidium iodide, and ethidium bromide into single cells. Their experiments demonstrated that *during* the application of a milliseconds-long electric pulse, the transport occurs only from the anodic side, whereas *after* the pulse, the transport is observed also from the cathodic side provided that both sides of the cell were permeabilized (Fig. 3). Such observation is quite expected, since the dominant transport mechanism for charged species during the pulse is generally electrophoresis (and/or electroosmosis), which is for positively charges species directed from anodic towards cathodic side[65,66,176–178]. Propidium iodide and ethidium bromide were also found to be particularly suited for measuring the size of the permeabilized membrane area. Although they are primarily used as nucleic acid stains, their fluorescence increases also when interacting with the permeabilized membrane[85]. Permeabilization was found to be asymmetric with respect to the two sides of the cell, with larger permeabilized area at the anodic side corroborating the influence of the resting TMV on electroporation. The size of the permeablized area on either side of the membrane increased with the electric field strength, but was independent of the pulse duration. This is consistent with the prediction that only the membrane areas where TMV exceeds the critical value become permeabilized.

Asymmetric uptake pattern could also be observed by Tekle et al.[179], however they used an imaging system with lower time resolution (30 frames/s) and hence monitored transport after the pulse. They observed that in high salt

medium the preferential uptake of calcium and ethidium bromide occurred from the anodic side, whereas in low salt medium all tested molecules (calcium, ethidium bromide, propidium iodide, and ethidium homodimer) entered preferentially (though not necessarily exclusively) from the cathodic side. Notably, the general uptake pattern was consistent on three different cell lines and remained the same if they added the molecules 1–2 s after the pulse. They attributed this observation to asymmetric electroporation, with larger pore size and slower resealing kinetics at the cathodic side. Similar was suggested also by Kinosita et al.[180] in order to explain the asymmetry in calcium transport into sea urchin eggs.

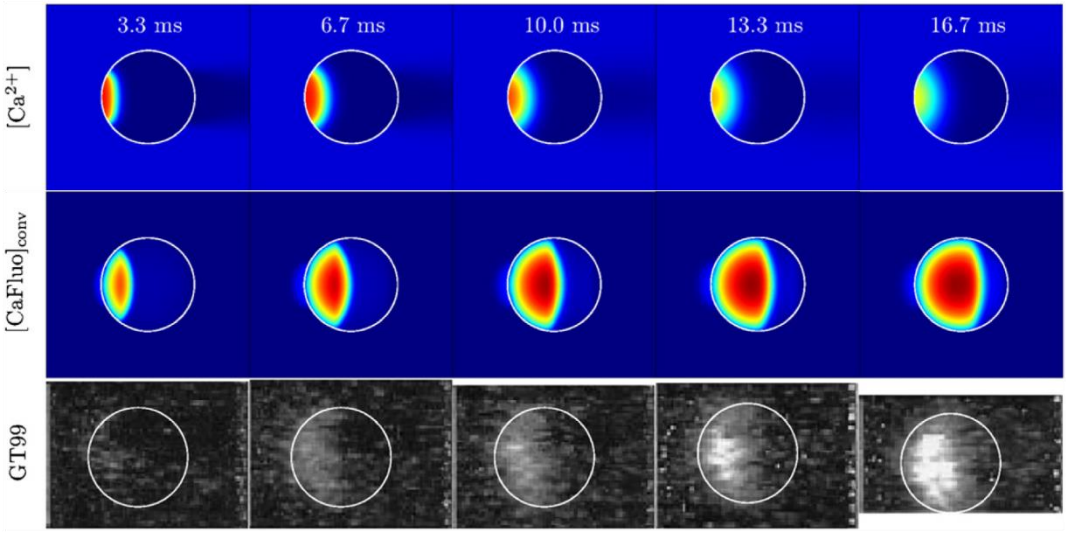

FIG. 3. Numerical calculations on the time course of calcium transport into a CHO cell during and after a single 6 ms, 1 kV/cm square pulse. The cell has a radius of 8 μm and its position is indicated by a white circle. Numerical model was constructed based on experimental results of Gabriel and Teissié[67]. (*Top row*) Calcium electrophoretically enters the cell from the anodic side and becomes "stacked" close to the membrane. This phenomenon, known as field-amplified sample stacking is caused by to deceleration of calcium when it crosses the membrane. The deceleration is caused by lower calcium mobility and lower electric field on the cytoplasmic side of the membrane as compared to the exterior side of the membrane[177]. After the pulse, calcium starts to diffuse throughout the cytoplasm. (*Middle row*) Calculations of calcium–Fluo-3 fluorescence as would be seen under the microscope. (*Bottom row*) Experimental results of Gabriel and Teissié[67]. Adapted from Li and Lin[177].

In contrast to μs–ms pulses, which induce molecular transport only at the poles of the cell, nanosecond pulses appear to electroporate practically the entire membrane area[181]. This was predicted by a theoretical model of pore creation driven by TMV, suggesting that the pores formed by a nanosecond pulse, with electric field strength considerably higher than used with conventional μs–ms pulses, results is so-called supraelectroporation: formation of a large number of small pores over most of the cell membrane and membranes of the organelles[104,182]. This model was also able to give a rationale for the numerous experimental observations reporting the lack of transport of larger solutes (e.g. propidium iodide) after electroporating the cells with ns pulses; opposed to the transport of small ions and molecules which was readily detected across the "supraelectroporated" membrane[183,75,101,102].

Selective transport with respect to the size of the solute can also be observed for longer pulses. In order to detect the transport of solutes with increasing size, pulses resulting in increasingly higher electric field strength and/or pulses with longer duration and/or number need to be applied[106,68,69,184,73,103]. Moreover, larger molecules are able to pass the membrane after the pulses for a shorter period of time than smaller ions/molecules[72,79]. This shows that the increase in membrane permeability with respect to the solute size can be controlled by pulse parameters.

Apart from pulse parameters, molecular uptake was also observed to increase in medium with decreasing conductivity[68,76,185]. Two mechanisms were proposed to explain this phenomenon. The first suggestion is that the increase in membrane permeability can be attributed to the deformation of cells in low conductive medium, associated increase in membrane tension, and increase in the permeabilized membrane area[185]. The second suggestion is related to the local enhancement of the electric field around a cell in medium with decreasing conductivity[186]. Note that the latter mechanism is valid only if electrophoresis can be considered as the dominant mechanism of molecular loading.

In contrast to small or medium-size molecules and ions, the transmembrane transport of macromolecules is more complex. Macromolecules can be loaded into the cell only if they are present in the pulsing buffer surrounding the cells during the pulse application; when added in the buffer after application of electric pulses, no transport occurs[73,187]. Furthermore, longer pulses were found to be much more efficient for inducing the transport of macromolecules while maintaining cell viability[73]. This clearly points to the importance of electrophoresis, which was further demonstrated in the case of siRNA[187]. The negatively charged siRNA accumulates at the cathodic side of the cell membrane by electrophoretic migration, where it can translocate to the cytoplasmic size during the pulse. According to MD simulations and experiments on giant lipid vesicles, the translocation of siRNA through a pore in the lipid bilayer is a fast process driven by the electric field acting on this charged molecule, and can occur in less than 10 ns[163].

The transmembrane transport of DNA is an even more complicated process[188,189]. Similarly as siRNA, the DNA is electrophoretically dragged to the cathodic side of the permeabilized membrane. Electrophoretic forces may even push the DNA towards the permeabilized membrane leading to its insertion[9]. In order to enhance the contribution of electrophoresis and improve transfection, a combination of a high voltage and a low voltage pulse was proposed, first causing electroporation and the second providing the electrophoretic force to bring the DNA to the cell surface[190,191]. However, the DNA does not enter the cell immediately, but interacts with the membrane resulting in formation of local aggregates[188]. The actual translocation takes place several minutes after pulse delivery. The mechanisms of translocation are not well understood, but recent experimental evidence suggests that endocytosis could be the dominant pathway by which DNA enters the cells both *in vitro* and *in vivo*[192–195]. Interestingly, nanoparticles (e.g quantum dots[196] and silica-based nanoparticles[197]) with diameters of few tens of nanometers appear to enter electroporated cells without being endocytosed.

Implication of electrically stimulated endocytotic-like process has also been demonstrated for other macromolecules, such as β-galactosidase and bovine serum albumin resulting in enhanced delivery of macromolecules into the cells for more than 1 hour after electroporation[80,82,198]. It is well known that electric

treatment can alter the cell surface leading to elevated adsorption of macromolecules and stimulation of electroendocyosis even when using pulses with amplitudes far below the electroporation threshold[199,200,82,201]. Recent findings suggest that this process could be initiated by electrochemical production of protons at the anode interface and corresponding acidification of the extracellular media[202].

In the text above we summarized the general experimental observations on the induced transmembrane transport. However, the exact molecular forms of the pathways, through which the molecules pass the membrane, is not completely clear. As discussed in Section II.B, the initial membrane perturbation, which occurs during the pulse is very similar for planar lipid bilayer and cells including the kinetic rates of the processes, and can be rather well described by the theory considering creation and further expansion of conductive aqueous pores in the lipid bilayer[61,121,203]. This theory is also consistent with results from MD simulations. Such pores present direct aqueous pathways for ions and other solutes across the membrane and could also account for the mechanism of translocation of macromolecules such as siRNA[163]. Most of the pores though need to quickly collapse or at least shrink to a very small negligibly conducting size after the pulse in order to account for the rapid decrease in membrane conductance in few μs, which is reasonably consistent with the time scales of pore closure observed in MD simulations. Nevertheless, experiments on simple unmodified lipid bilayers demonstrated that bilayers are able to "remember" the previous pulse on a time scale from milliseconds to seconds[137,204,205] (this time probably depends on the type of lipid and experimental conditions), the "memory" being attributed to metastable "prepores". Similar memory effect can also be observed in measurements of cell membrane conductance. If one applies two equal consecutive pulses delayed by less than tens of milliseconds to seconds[48,59–61] (again probably depending on the cell type and experimental conditions), the measured increase in conductance during the second pulse will be different as compared to the first pulse. On the contrary, if the pulses are further apart, the increase in conductance is the same for the two pulses. Interestingly, this time scale also corresponds to the rapid kinetic decays in propidium iodide transport immediately after the pulse observed by Pucihar et al.[65] and Gabriel and Teissié[67] (tens of milliseconds to hundreds of milliseconds). This seems to further corroborate that the transmembrane transport in the initial stage of electroporation occurs in the lipid domains of the cell membrane.

The intriguing part is though the transport that persists over tens of seconds or even hundreds of seconds after the pulse application, which is observed for numerous ions and small molecules (charged and neutral) in different cell lines and under different experimental conditions[65,71,72,74,75,77,101]. This transport contributes largely to the overall transport as it lasts much longer than the transport during and immediately after the pulse. Perhaps even more intriguing is that each subsequent pulse can increase the flux of molecules, meaning that number (or size) of the leaks responsible for the long lived transport accumulates with subsequent pulses[64,71], despite the fact that, at the same time, the increase in membrane conductance during each pulse can remain approximately the same[64].

Pavlin et al.[64,206] following Neumann et al.[74,207] attributed this observation to two types of pores: short-lived small ones, which are responsible for the orders of magnitude increase in the membrane conductance during the pulse, but close rapidly after the pulse; and long-lived permeable ones, which are responsible for the molecular transport after the pulse. This distinction between two types of pores can be understood in the sense that some of the pores created during the pulse became stabilized due to, e.g., pore coalescence[208–210], by anisotropic

inclusions[211], release in the membrane surface tension caused by pore formation[203,212], or due to osmotic flows, cell-size modulation, and resulting membrane stresses[213]. This may indeed be the case, since the estimates on the number of long-lived pores, which were derived from the measurements of post-pulse efflux of ions from the cytoplasm, reached a number of about one hundred pores with radius ~1 nm per cell[59,206].

Generally speaking, though, the long-lived "pores" could (at least in part) be caused by mechanisms other than aqueous pores in the lipid bilayer. Apart from the electrically induced endocytotic-like transport, one possible mechanism of a leaky membrane involves a change in the conformation of membrane proteins[58,214], and another one involves lipid peroxidation[215].

In the cell membrane, the lipids are in strong interaction with membrane proteins and cytoskeletal proteins. The involvement of cytoskeleton in the membrane resealing process has been clearly demonstrated experimentally[214,216]. Thereby Teissié et al.[58,214] suggested that electric pulses first trigger a conformational change in the lipids which shifts the lipid-protein complex from its energetic minimum. However, metastable states are then attained by a conformational change of the proteins. These metastable states are long-lived because the system must follow the reverse set of events in order to recover its initial stable configuration. The energy for the backward transition can be given by thermal motion, but it may also involve enzymatic process as suggested by the dependence of the resealing process on temperature and the fact that starved cells cannot fully recover after electroporation[216]. Only limited data is available on the conformational changes of proteins caused by electroporation[52]. However, it was shown by ^{31}P NMR studies that a reversible change in the conformation of phospholipid polar head groups is present during the resealing phase of the membrane[70].

Lipid peroxidation on the contrary results from chemical modifications of the lipid structure, which is mediated by reactive oxygen species (ROS)[217,218]. Particularly prone to oxidation are unsaturated lipids with double bonds in their tails; namely the hydrogen atoms on the methylene groups immediately adjacent to double bonds have low carbon–hydrogen (C—H) bond energies. For this reason, they can be readily abstracted by radical species. Once a radical comes close to the lipid tail and abstracts the hydrogen, a lipid peroxyl radical forms in the presence of molecular oxygen. The peroxyl radical can then undergo subsequent intermediate peroxidation products, which are responsible for propagating the radical damage, as they can abstract hydrogen atoms from neighboring molecules. Lipid oxidation is thereby a nucleation process, where a single initial free radical attack generates damage to multiple lipid molecules. Eventually, the initially attacked lipid attains a hydrogen and converts to a non-reactive lipid hydroperoxide. The entire process of peroxidation is terminated when: (i) the concentration of initiating radicals is sufficiently high to support radical–radical reactions resulting in the formation of non-radical phospholipids products, or (ii) termination may occur by the intervention of lipophilic chain-breaking antioxidants[218].

Due to the modified structure, peroxidized lipid bilayers have altered properties. Insights from fluorescence, EPR and MD studies suggest that the presence of peroxidized lipids in lipid bilayers decreases the lipid order, lowers the phase transition temperature, leads to lateral expansion and thinning of the bilayer, alteration of bilayer hydration profiles, increased lipid mobility, and augmented flip-flop; influences lateral phase organization,

promotes formation of water defects, and under extreme conditions leads to disintegration of the bilayer[219–221]. In other words, oxidized bilayers are leaky and prone to spontaneous pore formation, which enables enhanced passage of ions and molecules across the membrane[222,223].

Importantly, ROS generation and lipid peroxidation is present also in electroporation. Firstly, electroporation studies with microsecond and millisecond pulses demonstrated, that electric pulses induce ROS generation. This was shown by using chemiluminescent probe lucigenin to detect superoxide anion radicals[224], and by analyzing photooxidation reaction of 5-(*N*-hexadecanoyl)-aminofluorescein incorporated into the cell membrane[225]. Moreover, generation of ROS was found to be specific to the permeabilized part of the membrane[225]. Secondly, the studies also showed oxidative damage of unsaturated lipids, both in model and cell membranes, as confirmed by measuring the concentration of conjugated dienes, malondialdehyde[226], and hydrogen peroxide[227,228]. Results further demonstrated that ROS concentration and extent of lipid peroxidation increases with electric field intensity[224–228], pulse duration, and number of pulses[224], and is correlated with cell membrane permeability[224,227,228], membrane resealing time[224], and cell damage[224,226].

Similarly as with longer pulses, ROS generation appears to have important contributions in effects, observed after exposure of cells to nanosecond pulses. ROS, including hydrogen peroxide and possibly other species, were found to be generated both intracellularly and extracellularly[229]. When cells were exposed to electric pulses in oxygen-deprived medium, the cytotoxic effects of nanosecond pulses were reduced[230]. Furthermore, experimental study coupled with molecular dynamics simulation showed that oxidation of membrane components enhances the membrane susceptibility to electroporation when either nanosecond or microsecond pulses are applied[231].

Nevertheless, the involvement of membrane proteins and lipid peroxidation in membrane electroporation requires further systematic research to quantify its contribution to the experimentally observed long-lived cell membrane permeability.

D. Membrane resealing

As discussed in the previous section, the rapid decrease in membrane conductance and transmembrane transport after the pulse can be linked to a passive process, such as shrinkage and collapse of lipid pores. The long-term resealing of the slightly permeable membrane with concomitant transmembrane transport of molecules, which follows the rapid recovery, is more puzzling. The resealing kinetics were shown to depend on a number of conditions. The membrane reseals faster at higher temperature[68,69,214], with viable cells being able to remain permeable even for 6 hours at 4°C [70]. The resealing also involves cytoskeleton. When disrupting the microtubules in CHO cells with colchicine, and actin-spectrin network in erythrocytes with thermal shock, the resealing of the membrane became faster[214,216]. The ATP content of cells does not influence the rate of resealing, however many of ATP-depleted cells undergo subsequent death, even though they started to reseal[232]. The resealing time was further observed to be faster in medium with high ionic strength[184] and in hypoosmolar medium[114,233]. The resealing time is also dependent on the membrane fluidity. The resealing time was shown to

be faster in cells pretreated with nonlethal amount of lysolecithin, which increases the membrane order (decreases fluidity) and longer in cells pretreated with nonlethal concentration of ethanol, which decreases the membrane order (increases fluidity)[234]. Correspondingly, the resealing time was found to be the faster in B16-F1 cells than V-79, the former having an overall less fluid membrane[78]. As mentioned above, the resealing time is also correlated with the amount of generated ROS and the extent of oxidative lipid damage. The resealing can moreover be accompanied by colloid-osmotic cell swelling or cell shrinkage[102], and structural modification of the membrane, such as transient blebbing[235] and eruption of microvilli[69].

The pulse parameters also affect the resealing kinetics, particularly pulse duration and pulse number were both shown to increase the time required for a cell to reseal[71,73,184]. The electric field strength was shown not to have an effect on the resealing time in the range of pulse parameters tested[71,74,207]. An interesting effect was though observed for the pulse repetition frequency: when the delay between pulses is increased and consequently the total treatment time is prolonged (particularly beyond 10–100 s, though the effect depends on the pulse parameters and cell/tissue type), the cells apparently become more susceptible to the pulses. Such "electrosensitization" can be achieved with nanosecond or microsecond pulses and results in increased membrane permeability as well as lower number of cells surviving the exposure[236–240]. The exact mechanism for electrosensitization has yet to be established, but it may be related to modifications in cell physiology due to prolonged leakage of the cytosolic content and increased Ca^{2+} levels inside the cell, osmotic swelling, and chemical modifications of the membrane such as oxidative lipid damage[236]. In contrast to these reports, Demiryurek et al.[241] showed that when using a double pulse exposure with a high voltage electroporative AC pulse and a low voltage DC pulse, by itself not able to electroporate the cells, the delivery of molecules is reduced when *increasing* the delay between pulses, suggesting that the second pulse reopens the pores created by the first one.

Particularly intriguing is the fact that the resealing kinetics after electroporation proceed on the same time scale as the kinetics of membrane repair after being mechanically punctured, e.g. by a microneedle, or a laser beam[242,243]. Indeed Hyunth et al.[244] used electroporation as means of membrane wounding to study lysosomal exocytosis in the process of membrane repair. They showed that electroporation triggers lysosomal exocytosis in NRK cells and human fibroblasts, which is enhanced with longer pulses. They also showed that exocytosis was reduced and viability decreased in fibroblasts with abnormal lysosome size, which have a defective exocytotic response.

The processes of membrane repair by means of exocytosis require the presence of calcium in the extracellular medium[242,243]. This is though generally not required for cells to reseal after electroporation. Recent data however point to different mechanisms of membrane repair, depending on the size of the wound[243,245]. Cells are able to reseal after moderate mechanical injury also in the absence of calcium, albeit at a slower rate[246]. Although high concentration of calcium in the extracellular buffer can lead to cell lysis after electroporation[247], some authors nevertheless reported that the resealing was faster in the presence of calcium ions[61,76]. Note also that even in a simple phosphate buffered saline without calcium chelating agents, calcium concentration higher that the cytoplasmic can be found[85].

To conclude, whatever mechanisms of cell membrane resealing (and the corresponding transmembrane transport) take place after exposure to electric pulses, they are certainly more complex than just a passive pore closure.

III. ELECTROPORATION IN COMPLEX ENVIRONMENT

A. From multiple cells to tissue

In the previous sections we provided an overview on the general characteristics of cell electroporation. Here we will focus on cell electroporation in multicellular environment, particularly from the viewpoint of the electric field distribution and consequently the induced TMV, which is affected by the proximity of other (cell) structures. Namely, when a cell is charged by an electric pulse, the redistribution of ions around the membrane perturbs the electric field around the cell. Hence, if cells are in close proximity, they "feel" the electric field perturbation arising from the neighboring cells in addition to the externally applied electric field.

The first and most simple situation that we can consider are two spherical cells that are positioned next to each other either parallel or perpendicular to the applied electric field. Theoretical predictions from calculating the induced TMV in the steady state predicted that in the first configuration the maximum TMV established on the cell membrane decreases whereas in the second configuration, it increases[97]. Henslee et al.[248] tested these predictions by monitoring the transport of propidium iodide into two cells in close proximity after applying a 1 ms pulse. They found that the TMV required for electroporation of a cell pair changes by ~5–10% of that required for a single isolated cell, in rather good agreement with the calculated relative decrease/increase in the TMV. However, their data suggested that the dynamics of the cell membrane discharging due to the increase in membrane conductance would need to be taken into account in order to explain all of their experimental observations.

The next more complex configuration are spherical cells arranged into pearl chains by means of dielectrophoresis. Such approach is often used to bring the cells into contact for electrofusion[15]. Namely, when cell membranes are electroporated, they are also fusogenic, which provides the possibility to fuse different types of cells into viable hybrids possessing the combined properties of the parental cells lines[249–251]. For pulses in the range of μs–ms, for which the TMV reaches its steady state, the maximum induced TMV on each cell in such configuration decreases and the TMV distorts from the cosine shape observed for isolated cells; namely, it flattens at the poles of the cell[97]. This behavior of the TMV however changes during the membrane charging provided that the cells are exposed to electric pulses in a medium with conductivity considerably lower than the conductivity of the cell cytoplasms. Under such conditions, the electric field is locally amplified at the poles of the cells and reaches the highest value at the contact area between cells (Fig. 4, A1–B1). This phenomenon was also observed experimentally; when plant protoplasts were pulsed in sorbitol solution as isolated cells, only the anodic side was electroporated, whereas when pulsed in chain arrangement, both the anodic and cathodic sides were electroporated using the same pulse parameters[252,253]. This feature may be useful particularly when fusing cells of different size[254]. As we have thoroughly discussed above, when pulses are long enough for the induced

TMV to reach the steady state, the maximum TMV scales proportionally with the cell radius, hence larger cells tend to be electroporated at lower electric field strength. This can though cause problems when fusing cells which differ considerably in size, such as lymphocytes and myeloma cells in hybridoma production. The pulses can namely be damaging to myeloma cells and hence the fused cells cannot survive[255]. Yet, if the electric field is too low, the lymphocytes are not electroporated and no fusion occurs. An approach was proposed to overcome this problem by exposing cells to electric pulses in typical low conductive electrofusion medium using nanosecond pulses, where the cell membranes are still in the charging phase and the amplification of TMV at the contact area can be observed (Fig. 4, C1–D1). Accompanying experiments corroborated the theoretical predictions and proved the feasibility of such approach[254].

Further complexity can be achieved by considering a cell suspension of increasing density. When cells are in dilute suspension, they are sufficiently far apart, so on average they do not sense the perturbation of the electric field caused by neighboring cells. However, when the density of cells in the suspension increases, the induced TMV on each cell is more and more influenced by the proximity of other cells. If spherical cells are packed together such that they are in contact, the maximum induced TMV will become equal to the product of the cell radius and the electric field strength (TMV = *RE*), which correspond to a factor of 1.5 reduction with respect to TMV on isolated cells[97,256]. Due to the reduction of the induced TMV, cells in dense suspensions need to be electroporated at higher electric field strength than cells in dilute suspension as corroborated by numerical calculations[257] and experiments[174,258]. In addition, the amount of molecules loaded into densely packed cells was found to be reduced due to limited dye availability in the extracellular medium. This was further potentiated by cell swelling after their exposure to electric pulses in low conductive medium[48,258].

Electroporation of cells is also accompanied by leakage of cytosolic solutes into the extracellular medium. Particularly in dense suspensions, where the volume fraction of cells is comparable to the volume of the extracellular medium, the leakage results in an increase in the suspension conductivity. The dynamics of such conductivity changes was extensively studied by Pavlin et al.[48,64,206] during application of a train of eight 100 μs pulses applied to dense suspension of B16-F1 cells. They found that the increase in suspension conductivity can be separated into two parts: large increase during the pulse due to increase in the conductance of the cell membranes, and gradual increase between the pulses caused by efflux of ions from the cells. The contribution arising from the increase is conductance of the cell membranes vanishes very rapidly after the pulse, due to fast membrane recovery. But as the cells are electroporated in a vectorial way (only the part of the membranes facing the electrodes), this affects the suspension conductivity in an anisotropic way. More specifically, during the pulse, the suspension has a higher conductivity in the direction parallel than in direction perpendicular to the electric field[259]. Similar anisotropic increase of conductivity can also be observed in tissues[259].

The limiting density of a cell suspension can be obtained by forming cell pellets by means of centrifugation. Stronger packing of pellets is achieved by increasing the centripetal acceleration, which then results in an increase in the pellet resistance (which depends on the pellet porosity and geometry)[260]. The cell pellet behaves as a parallel set of resistance and capacitance, the former reflecting mostly the conductivity of extracellular pathways (porosity and gap conductivity), and the latter the capacitance of cell membranes[261]. When applying a

voltage across the pellet sufficient to cause membrane electroporation, the pellet resistance considerably decreases (i.e., pellet conductance increases). The larger the pellet (more layers of cells are stacked one above the other) the higher the voltage required for electroporation, as the voltage drops over cell membranes in the sense of a voltage divider. Experiments by Abidor et al.[260,261] demonstrated that the recovery of the pellet conductance proceeds in three kinetic stages: with time constants of 0.5–1 ms, ~10 s, and time on the order of minutes. After moderate electric treatment, which mostly allowed only the passage of small ions across the membrane, the conductance after the pulse decreased. This was due to cell swelling which could be inhibited by addition of sucrose or bovine serum albumin.

As described above, cells in suspension can be brought into contact by certain manipulation. However, the quality of the contact is not the same as between cells, which are grown in clusters or in monolayers. Neighboring cells in adherent cell cultures form spontaneous contacts by connecting themselves with membrane structures. Such spontaneous contacts are formed in short time after plating the cells (within 20 minutes)[262]. As the quality of the contact is better, this improves the yield of fused cells as compared to cells simply put together by dielectrophoresis[262]. If cells in confluent monolayers are exposed to electric pulses, this can even result in fusion of large groups of cells, yielding fused cells with more than a hundred nuclei[184]. Indeed cell electrofusion was also documented *in vivo*, albeit not in all types of tissues[263]. Fusion was observed in tumors with reduced extracellular matrix, which pointed to the role of the extracellular matrix in preventing the mixing of membranes between neighboring cells[263].

The effect of cell connections on the induced TMV was studied by Kotnik et al.[86,264] on an *in vitro* model of CHO cells in clusters. Cells in clusters are connected by gap junctions, which form conductive pathways between the cytoplasms. Hence, when a nonelectroporative pulse is applied, the clustered cells will act as a single large cell possessing one single cytoplasm. However, if an electroporative pulse is applied, which results in much higher induced TMV across the membranes, the gap junctions become blocked and the cells in clusters start to behave as individual cells. This allows transport of molecules even at membrane areas, where the cells are connected (Fig. 4, A2–D2).

Although cells in clusters act as single entities during electroporation, the shape and orientation of individual plated cells varies considerably. The cells are namely irregularly shaped and spread over the surface, which effectively increases their size with respect to suspended cells. Electroporation can consequently be detected at lower field strength then with cells in suspension[184]. But as one gradually increases the electric field, it can be observed that cells which are larger and oriented with their longer axis parallel to the electric field, tend to be electroporated at lower electric field[96]. Nevertheless, the amount of molecules transported into cells in monolayers is lower than in suspension[65]. Partially this can be attributed to the effective reduction of the electric field by the neighboring cells and partially to the hindered diffusion of the molecules between the cell-cell contacts and the cell-surface contacts.

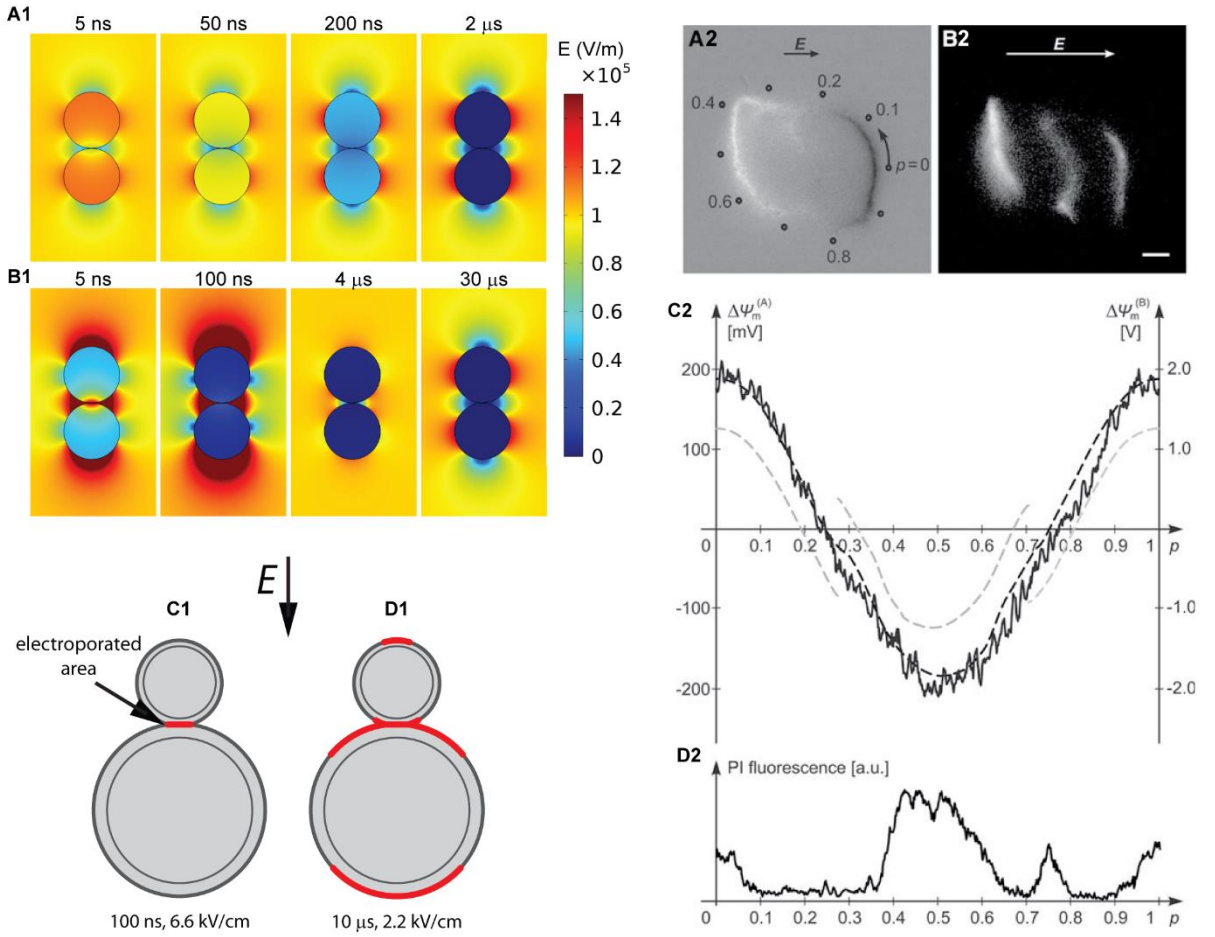

FIG. 4. **(A1–D1)** Time course of the electric field distribution after the onset of a square pulse in a pair of cells in contact. Extracellular medium conductivity is 1 S/m (A1) or 0.01 S/m (B1). In low conductive medium and at the beginning of the pulse, the electric field is amplified at the poles of the cells. Example is shown for two cells with equal size, however similar can also be observed for cells with different size. Hence, if one uses a 100 ns pulse to electroporate the cell pair, one is able to electroporated only the contact zones (C1). On the contrary, if the pulse is longer, the larger cell is considerably more electroporated then compared to the smaller cell in the pair (D1). Partially adapted from Rems et al.[254] **(A2–D2)** Induced TMV and electroporation of a clustered pair of CHO cells. (A2) Changes in fluorescence of voltage-sensitive dye di-8-ANEPPS caused by a nonporating 50 ms, 100 V/cm pulse. Dark regions correspond to membrane depolarization and bright regions correspond to membrane hyperpolarization. (B2) Transport of PI into the same two cells caused by a porating 200 μs, 1000 V/cm pulse, as visualized 200 ms after exposure. Scale bar 5 μm. (C2) Steady-state TMV measured along the path shown in (A2) (*solid*) and as computed numerically for electrically interconnected (*dashed black*) and electrically insulated (*dashed gray*) cells. The left y scale corresponds to the 100 V/cm pulse amplitude used in (A2) and the right y scale, to the 1000 V/cm used in (B2). (D2) PI fluorescence measured along the path shown in (A2). Taken from Kotnik et al.[86]

Another step towards a tissue-like structure are three-dimensional multicellular spheroids, which are characterized by cell interconnections as well as the extracellular matrix, and can be used as models of microregions of larger tumors[265,266]. Canatella et al.[173,267] compared the electroporation behavior and molecular uptake into DU145 prostate cancer cells in suspension and in spheroids. They observed that the overall amount of calcein loaded into spheroids was considerably lower than in suspended cells. Moreover, molecular loading into spheroid cells progressively decreased from the periphery to the spheroid interior. This could (at least in part) be attributed to the reduction of the TMV in densely packed environment, limited extracellular solute

reservoir within the spheroid (both are similar as for cells in dense suspensions), and progressively smaller size of the cells in the interior of the spheroid (caused by different microenvironment inside the spheroid than on the periphery). Inhomogeneous labelling with peripheral cells being more permeabilized was also observed by Gibot et al.[268] in spheroids of HTC-166 cells. They further showed that smaller and "younger" spheroids are more sensitive to electric pulses, corroborating the importance of the cell heterogeneity in the spheroid, but also suggesting a role of spheroid maturation[269].

Chopinet et al.[270], compared the electrotransfer of plasmid DNA in suspended cells and in spheroids of HTC-166 cells, similarly as Canatella et al. compared the uptake of small molecules representative of "drugs". However, the results of transfection efficiency demonstrated even more striking difference. Whereas about 24% of cells could be transfected when in suspension, only few cells (less than 1%) in spheroids expressed the transfected gene. The first major obstacle was the inability of DNA to diffuse into the core of the spheroid, where it could interact with the permeabilized cells, thereby only the cells at the periphery on the cathodic side of the spheroid could be transfected[271]. The second obstacle was the decrease in cell viability with increasing the electric field strength. Marrero and Heller[272] also obtained low transfection efficiency in spheroids from human HaCaT keratinocytes. But when they injected the gene into the spheroid together with B16-F10 mouse melanoma cells, the latter could be more easily transfected. This demonstrated that the transfection efficiency depends also on the type of cells in the spheroid. Comparative studies with an *in vivo* tumor model showed that the information gained from the spheroid model was indeed largely transferable to the *in vivo* situation[272].

Overall the studies discussed in the present section demonstrated that cells in a cell assembly respond to electric pulses similarly as single cells provided that we take into account the local electric field distribution to which an individual cell in the assembly is actually exposed, as the external electric field is modified in the presence of neighboring cells. Thereby the knowledge on the basic characteristics of membrane electroporation gained from experiments on individual cells is transferable to electroporation of assembled cells. However, the studies also demonstrated the importance of the heterogeneity of the cell assembly (size, shape, orientation, sensitivity of cells to electric pulses), cell clustering resulting in limited diffusion of molecules between cells, and possible implication of other structures, such as extracellular matrix, which is completely absent in suspended cells. For this reason, multicellular spheroids are a better *in vitro* tissue model than cells in dense suspensions or cells grown in monolayers. Yet, even multicellular spheroids cannot directly represent all of the properties of an *in vivo* tissue[265,266]. Hence, theoretical analysis of the electric field distribution in a tissue and its correlation with reversible and irreversible electroporation is indispensable. For example, numerical analysis of tumor tissue electroporation demonstrated that endothelial cells lining the tumor blood vessels are exposed to ~40% higher electric field than the surrounding tumor cells, and are therefore easily electroporated. This leads to endothelial cell swelling and apoptosis, which disrupts the blood flow to the tumor cells and participates in tumor necrosis after electrochemotherapy[273].

When theoretically modeling a tissue, we nevertheless usually assume that the tissue is a homogeneous structure with "bulk" electrical properties, i.e. conductivity and permittivity, which can be directly measured experimentally. In such treatment, the cellular structure of the tissue is of course completely neglected. There are

at least two reasons for this neglect: the first arises from the computational cost of representing each cell in a large tissue volume; the second unfortunately from our lack of knowledge on how exactly different structures in the tissue contribute to the bulk tissue properties. An excellent work to relate the bulk properties of the skin tissue with underlying cellular arrangement was done by Huclova et al.[274–276]. This approach shows great promise, but as for now, the empirically determined properties are more reliable as compared to simplified tissue representations. In the "bulk" treatment, the actual heterogeneity of the tissue structure is reflected in the dependency of the bulk properties on the frequency of the applied electric field[277], and by that also on the duration of the pulses applied to the tissue. This frequency-dependency is specific for each type of tissue, as the tissues differ in their microscopic structure, including size, shape, orientation, and density of the constituting cells. Moreover, certain tissues express anisotropic properties due to preferential orientation of the cells in one direction. A good example is the skeletal muscle, where the long muscle fibers are able to conduct the electric current more readily in the direction parallel than perpendicular to the fibers[277].

By knowing the bulk properties of a tissue, we can easily calculate the macroscopic electric field distribution for different electrode configurations (note that the size, shape and position of the electrodes inside the tissue significantly affect the distribution of the electric field). As the tissues also express a threshold behavior for electroporation with respect to the electric field strength, we can compare numerically determined electric field distribution with experimentally determined regions where reversible and where irreversible tissue electroporation occurred. Using such approach Miklavčič et al.[278] determined the thresholds for reversible and irreversible electroporation in the rabbit liver tissue. They applied eight 100 μs electric pulses to the tissue using needle electrodes with different diameters, which consequently affected the distribution of the electric field inside the tissue between the electrodes. By comparing the calculated electric field distribution with the histological analyses of the treated tissues, they found that the threshold electric field for reversible electroporation was 362 ± 21 V/cm and for irreversible electroporation 637 ± 43 V/cm.

The more difficult part is then how to relate the macroscopic threshold electric field back to the local electric field "felt" by an individual cell in the tissue. The simplest approach is to consider a simplified average shape of the cells and treat the local electric field as though the cells are in a dense suspension. By doing so, Miklavčič et al.[278] estimated the threshold TMV for reversible electroporation to be 372 ± 75 mV and for irreversible electroporation 694 ± 136 mV. The estimated TMVs are on the lower side of the ones reported from *in vitro* experiments, but still in very good agreement with the range of the reported values (few hundred mV to ~1000 mV). This clearly shows that the behavior of cells in a tissue is not so far from the behavior of cells in dense suspensions (at least with respect to the electroporation threshold). When estimating the "critical" TMVs for other tissues, they found that they vary between different tissue types, which is also something what is observed *in vitro* for different cell types.

The simplified treatment above however does not take into account the changes in local tissue conductivity caused by electroporation. When a square pulse is applied via needle electrodes inserted into tissue, the electric field distribution is inhomogeneous. In the regions, where the electric field is above the threshold for electroporation, the conductivity of the tissue increases due to the increase in the conductivities of the cell

membranes. Local changes in tissue conductivity in turn change the electric field distribution – the electric field becomes higher at regions which have not yet considerably electroporated and are therefore less conductive. This consequently results in gradual propagation of electroporated tissue area. Tissue electroporation is dynamic and is manifested in an electric-field-dependent tissue conductivity $\sigma(E)$. Šel et al.[279] assumed a sigmoidal dependence $\sigma(E)$ and performed a numerical analysis, probing the spatial changes in the electric field distribution in distinct sequential steps during pulse application. Together with measurements of electric current flowing between the electrodes, the method allowed them to reestimate the electric field thresholds for reversible and irreversible electroporation in rabbit liver tissue yielding 460 V/cm and 700 V/cm, respectively. Corresponding new estimates of the threshold TMV were 500 mV and 760 mV for reversible and irreversible electroporation, respectively. The importance of taking into account the tissue conductivity changes in numerical analyses of tissue electroporation and corresponding treatment planning was later signified by Čorović et al.[280] by comparing results from three different modeling approaches to *in vivo* measurements. One of the difficulties in estimating the tissue conductivity changes is that they are inhomogeneous and cannot be directly resolved spatially by measuring the electric current between the electrodes. Considerable progress in this direction has though been achieved by monitoring local tissue conductivity during electroporation with magnetic resonance electric impedance tomography (MREIT)[281].

B. Cells and structured nanomaterial

The experimental and theoretical insights described up to now considered setups, where the electrodes used to deliver electric pulses are far away from an average individual cell, thereby the cells "feel" the electric field over their entire membranes. New emerging nanoscale technologies nevertheless enable focal enhancement of the electric field only at a certain part of the membrane, leaving the remaining parts of the cell intact. The source of such local electric field can be very different, as presented below on few interesting examples.

When conductive entities in electrolytic medium are subject to an external electric field, they locally enhance the field. Thereby metal particles such as gold nanoparticles can potentiate electroporation. Indeed, such enhancement was successfully confirmed on a chronic myeloid leukemia cell line, NIH 3T3 and K562 cells; gold nanoparticles enhanced the transfection efficiency and reduced the cytotoxic effects of the pulses[282,283].

The magnitude of the electric field is directly proportional to the local electric current density. By concentrating the electric current over a small area, one can thus enhance the local electric field. This can be done by means of a microchannel-nanochannel-microchannel configuration[284–286] (Fig. 5, A). The idea consists of positioning a cell in one of the microchannels next to the entrance of the nanochannel, e.g., by using optical tweezers. A voltage pulse is then applied between the microchannels, with the voltage drop being mostly concentrated over the nanochannel. This results in an enormous electric field inside the nanochannel (e.g. 700 kV/cm for a 200 V pulse), with fringing field being also able to reach the cell. The enhanced electric field inside the nanochannel is particularly suited for delivery of different molecules. When a charged agent (e.g. siRNA, quantum dots, plasmid DNA, lipoplex nanoparticles with encapsulated agent) is placed into the microchannel opposite to the one which

contains the cell, the agent is electrophoretically accelerated through the nanochannel and injected into the cell. The delivery bypasses endocytotic pathways, for which it can considerably speed up the process of gene transfection (few hours) with respect to conventional "bulk" electroporation (about one day). Moreover, the delivered dose of the agent can be controlled by adjusting the duration and number of pulses.

A related approach for molecular delivery was proposed based on a system of alumina nanostraws (typically 250 nm in diameter, 1.5 μm in height, 0.2 straws/μm^2) extending from a track-etched membrane, which forms an array of hollow nanowires connected to an underlying microfluidic channel (Fig. 5, B). On top of the nanostraw membrane, cells can spread and proliferate in similar fashion as in routine culture on flat surface. The cells engulf the nanostraws, but without perturbing their membranes. To achieve access to the cytosol, voltage pulses are applied between the microfluidic channel beneath the nanostraw membrane and the cell culture well, which electroporate the membranes above the nanostraws. The transport of the agent to be delivered, is driven from the microfluidic channel by electrophoresis during the pulse and diffusion after the electroporative pulse. The cell membranes are able to reseal in less than 10 minutes, preventing leakage of cytosolic compounds, which ensures that cell viability is preserved[287].

Similarly as on nanostraws, cells can be grown on platinum nanopillar electrode arrays, which can be used to measure action potentials in excitable cells[288] (Fig. 5, C). The electrodes are tightly coupled to the cell membrane and allow extracellular recording of the action potential signal. Transient electroporation with the same electrodes reduces the impedance between the electrode and the cell interior which drastically improves the quality of the signal; the recorded signal amplitude increases from 100–200 μV to 11.8 mV immediately after electroporation, whereas the noise level (30 μVpp) remains similar to that of extracellular recordings. The intracellular recordings after electroporation can be followed for few minutes before the cell membrane reseals. In contrast to patch clamping, the nanopillar electrodes are minimally invasive (tip radius of < 100 nm) and allow repetitive recordings on multiple cells in parallel over several consecutive days. Moreover, electroporation provides the possibility to repeatedly switch between intracellular and extracellular recordings.

In contrast to the systems above, where one needs to bring a cells next to the nanostructure in order to electroporate it, magneto-electric nanoparticles can be brought to cells[290]. These nanoparticles are being studied as potential drug delivery systems, where their insertion into the target cells would be controlled remotely via an external magnetic field. Magneto-electric nanoparticles namely act as localized magnetic-to-electric-field nano-converters; when exposed to a magnetic field, they locally start to emit a strong electric field. The idea is therefore to bring the magneto-electric nanoparticles close to the target cells, and then excite them with a magnetic field, such that they would locally electroporate the cell membrane and let themselves into the cytoplasm. Once inside, somewhat higher magnetic field would be used to release the drug, which they are carrying. Furthermore, when cells have different electroporation thresholds, careful adjustment of the magnetic field would allow to specifically target only particular cells, such as cancer cells. The proof of concept of such promising approach was successfully shown on an *in vitro* model of human ovarian carcinoma cell (SKOV-3) and healthy cell (HOMEC) lines, whereby magneto-electric nanoparticles were able to specifically enter the tumor cells and decrease their viability to 10% after 36 hours of treatment.

Apart from drug delivery, nanoscale technologies can also be used in environmental applications. Cui et al.[289,291,292] proposed different designs for a filter for water sterilization based on silver nanowires or copper oxide nanowires (Fig. 5, D). A low voltage (e.g. 20 V) is applied between the filter and the water flowing through the filter, which results in a highly amplified electric field of >100 kV/cm along the edges of the nanowires. When bacteria and viruses approach the electric field emitted by the nanowires, they become inactivated by means of electroporation. Such approach can result in more than 6 log (99.9999%) removal. The most important benefits of the proposed system are low cost, low energy consumption and fast treatment speed. When building the system with copper oxide nanowires[292] they additionally showed that sufficiently high electric field can be achieved simply by static electricity which can be generated by an individual person's motion. Thereby the system is readily applicable to regions of the developing world with poor access to electricity, or for other catastrophic situations accompanied by lack of drinkable water and loss of electricity.

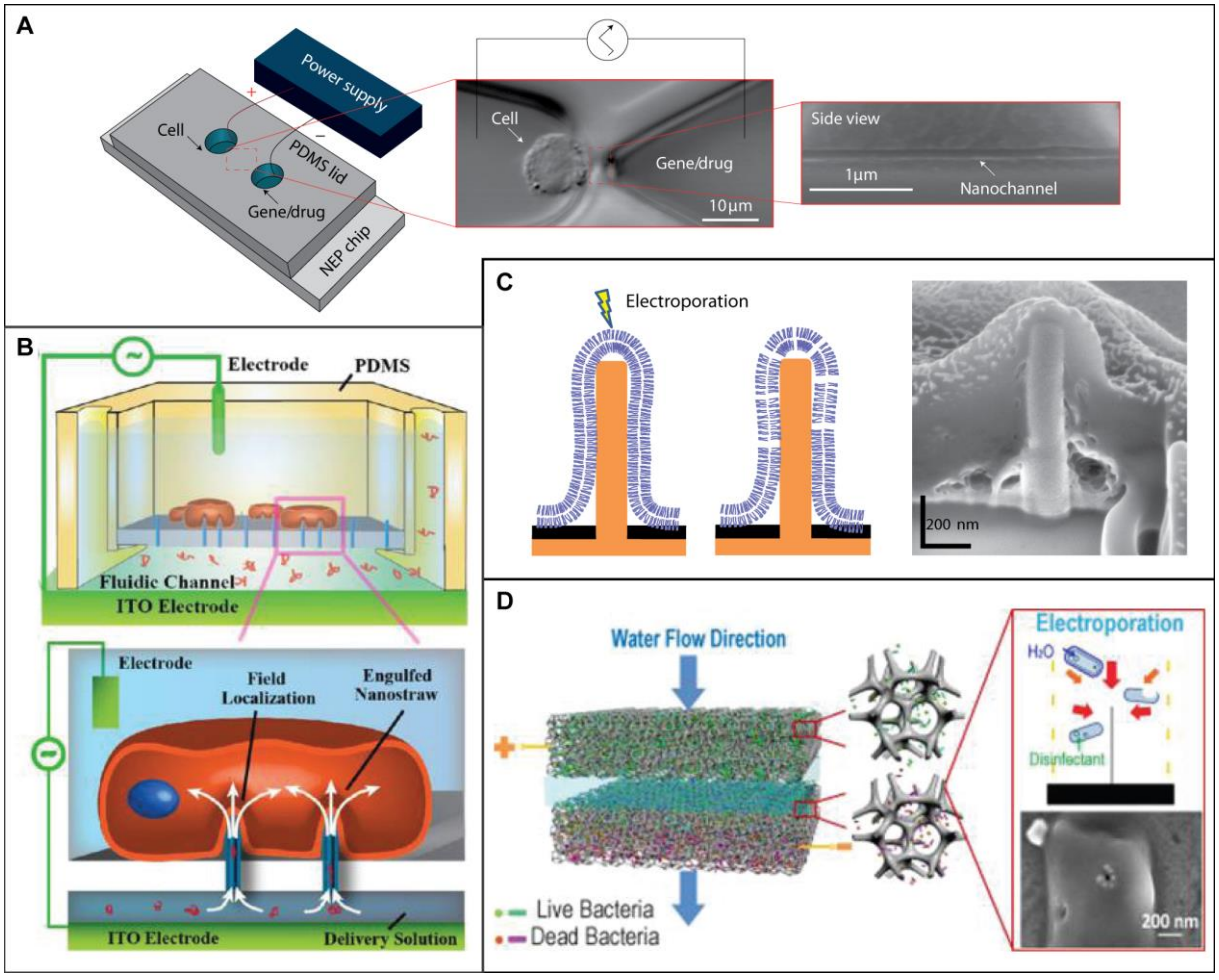

FIG. 5. **(A)** *Left:* Schematic of the nanoelectroporation chip. *Middle:* Optical micrograph of a Jurkat cell in the left microchannel, which is positioned at the tip of the nanochannel using optical tweezers. *Right:* Scanning electron microscope image of the nanochannel (~90 nm in diameter and ~3 mm long). Adapted from Boukany et al.[284] **(B)** Schematic of the nanostraw-electroporation system. Taken from Xie et al.[287] **(C)** The cell–nanopillar electrode interface. *Left:* Schematic of the interface before and after electroporation. *Right:* Interface exposed by focused ion beam milling shows that the nanopillar electrode is fully engulfed by the cell. Adapted from Xie et al.[288] **(D)** Schematic of the water sterilization filter. Bacteria are inactivated as they approach the tip of the nanowire. High-magnification scanning electron microscope image demonstrating pores formed on E. coli surface after filtration under 20 V. Taken from Liu et al.[289]

IV. CONCLUSION

In the present tutorial, we took a journey on electroporation from the single cell level through increasingly complex cell assemblies up to tissues and nanostructures. The first obvious conclusion that we can obtain, is that whatever the complexity of the environment in which the cells are, electroporation will be initiated provided that local electric field is sufficiently enhanced. This points to the universality of the phenomenon but also stresses the importance of our knowledge on how well we can predict the electric field distribution. Applications of electroporation are diverse ranging from gene transfection in single cells to ablating tissues. In applications where preserving cell survival is not critically important, it is also of lesser significance how we tailor the experimental protocol. However, in applications where cell survival is of crucial importance (e.g. gene transfection[36,270], cell fusion[293,294], cryopreservation[295,296], tissue electroporation in the proximity of vital structures such as nerves and major blood vessels[297]), the positioning of the electrodes and parameters of the applied electric pulses need to be carefully adjusted as to prevent cell damage. In tissues, which are highly heterogeneous, it is particularly necessary that we combine the treatment with theoretical modeling. Electric field distribution namely depends on tissue electrical properties, underlying cell structure, and local conductive pathways, which cannot be seen by naked eye. As pointed out in Section III, the electric field distribution also depends on transient conductivity changes during the pulse application. Although we can make a phenomenological description on how the increase in tissue conductivity depends on the electric field strength, in general, such description needs to be obtained for every specific type of tissue. As we already know from experiments on single cells, electroporation depends on the cell type, size, shape, and inter-cellular organization, meaning that every type of tissue can quantitatively express different characteristics. The increase in tissue conductivity during the pulse, though, primarily arises from the increase in conductivity of the cell membranes. Thereby, a much more general approach would be to develop theoretical models that track down to cells, i.e., to model the resolved tissue structure. Yet, in order to progress towards this direction, we need to have a good knowledge on electroporation of single cells as well as how proximity of other cells and structures influences the overall electroporation process. This is in fact one of the main motivations for studying electroporation of cells in so many different, relatively simple environments.

There has indeed been considerable progress achieved in developing tissue models by scaling up from the single cell level[257,259,274–276]. Let us give one final example. Dymek et al.[296] developed a model of the heterogeneous structure of the spinach leaf by representing individual cells as well as other leaf components in the tissue model. They probed the model's electrical properties with alternating electric fields as well as with electroporative pulses and found good agreement with corresponding measurements on spinach leafs. The model is intended to help optimize cryopreservation of spinach leaves, where it is highly important that all cells in the tissue are electroporated but also that all cells survive the pulses. Namely in cryoprotection, leaves are electroporated in order to allow the cryoprotectant to enter the cells and protect the cell membrane from both sides, as required to increase the freezing tolerance of the leaves[298]. The main experimental difficulty is though that only the tissue layers close to the surface can be examined microscopically. Consequently a model can give valuable insights on the ongoing in the central part of the leaf and help optimize parameters of electric pulses leading to homogeneous leaf electroporation.

Nevertheless, in order to fully understand and model electroporation of single cells properly and with confidence, we have to scale down even further, right to the structural changes in the cell membranes. Thereby, we need to investigate electroporation also on pure lipid systems, as to clarify to what extent we can attribute the structural changes to the lipid domains of the membrane. And we need to have insights from molecular dynamics simulations, since it is necessary that we understand what could be happening on the molecular level and build accordingly our theoretical description based on this knowledge. By bringing the pieces of information arriving from different systems and methods, there is little doubt that we will progress to understand and efficiently model electroporation in tissues or any other complex material.

ACKNOWLEDGMENTS

Research was supported by the Slovenian Research Agency (ARRS) with program P2-0249 and funding for Junior Researchers. The study was conducted in the scope of the European Associated Laboratory for Pulsed Electric Field Applications in Biology and Medicine (LEA EBAM).

REFERENCES

[1] R. Stampfli, Acad Bras Cienc. **30**, (1958).
[2] H.G. Coster, Biophys. J. **5**, 669 (1965).
[3] E. Neumann and K. Rosenheck, J. Membr. Biol. **10**, 279 (1972).
[4] K. Kinosita Jr. and T.Y. Tsong, Proc. Natl. Acad. Sci. **74**, 1923 (1977).
[5] K. Kinosita Jr. and T.Y. Tsong, Biochim. Biophys. Acta **471**, 227 (1977).
[6] I.G. Abidor, V.B. Arakelyan, L.V. Chernomordik, Y.A. Chizmadzhev, V.F. Pastushenko, and M.R. Tarasevich, Bioelectrochem. Bioenerg. **6**, 37 (1979).
[7] E. Neumann, M. Schaefer-Ridder, Y. Wang, and P.H. Hofschneider, EMBO J. **1**, 841 (1982).
[8] L.M. Mir, H. Banoun, and C. Paoletti, Exp. Cell Res. **175**, 15 (1988).
[9] J.M. Escoffre, B. Nikolova, L. Mallet, J. Henri, C. Favard, M. Golzio, J. Teissie, I. Tsoneva, and M.P. Rols, Curr. Gene Ther. **12**, 417 (2012).
[10] D. Miklavčič, B. Mali, B. Kos, R. Heller, and G. Serša, Biomed. Eng. OnLine **13**, 29 (2014).
[11] D. Knorr, M. Geulen, T. Grahl, and W. Sitzmann, Trends Food Sci. Technol. **5**, 71 (1994).
[12] S. Mahnič-Kalamiza, E. Vorobiev, and D. Miklavčič, J. Membr. Biol. **247**, 1279 (2014).
[13] K. El Ouagari, B. Gabriel, H. Benoist, and J. Teissié, Biochim. Biophys. Acta **1151**, 105 (1993).
[14] S. Raffy, C. Lazdunski, and J. Teissié, Mol. Membr. Biol. **21**, 237 (2004).
[15] U. Zimmermann, Biochim. Biophys. Acta **694**, 227 (1982).
[16] M. Kandušer and M. Ušaj, Expert Opin. Drug Deliv. **11**, 1885 (2014).
[17] A.C. Saito, T. Ogura, K. Fujiwara, S. Murata, and S.M. Nomura, PLoS ONE **9**, e106853 (2014).
[18] R. Heller and R.J. Grasso, Biochim. Biophys. Acta **1024**, 185 (1990).
[19] A. Castro, G. Barbosacanovas, and B. Swanson, J. Food Process. Preserv. **17**, 47 (1993).
[20] L. Miller, J. Leor, and B. Rubinsky, Technol. Cancer Res. Treat. **4**, 699 (2005).
[21] O.N. Pakhomova, B.W. Gregory, I. Semenov, and A.G. Pakhomov, PLoS ONE **8**, e70278 (2013).
[22] S.J. Beebe, N.M. Sain, and W. Ren, Cells **2**, 136 (2013).
[23] R. Nuccitelli, R. Wood, M. Kreis, B. Athos, J. Huynh, K. Lui, P. Nuccitelli, and E.H. Epstein Jr, Exp. Dermatol. **23**, 135 (2014).
[24] P.T. Vernier, Y. Sun, L. Marcu, S. Salemi, C.M. Craft, and M.A. Gundersen, Biochem. Biophys. Res. Commun. **310**, 286 (2003).
[25] J. Zhang, P.F. Blackmore, B.Y. Hargrave, S. Xiao, S.J. Beebe, and K.H. Schoenbach, Arch. Biochem. Biophys. **471**, 240 (2008).
[26] A.S. Torres, A. Caiafa, A.L. Garner, S. Klopman, N. LaPlante, C. Morton, K. Conway, A.D. Michelson, A.L. Frelinger, and V.B. Neculaes, J. Trauma Acute Care Surg. **77**, S94 (2014).
[27] N. Grimi, N. Lebovka, E. Vorobiev, and J. Vaxelaire, J. Texture Stud. **40**, 208 (2009).
[28] A. Polak, M. Tarek, M. Tomšič, J. Valant, N.P. Ulrih, A. Jamnik, P. Kramar, and D. Miklavčič, Bioelectrochemistry **100**, 18 (2014).
[29] T. Kotnik, W. Frey, M. Sack, S. Haberl Meglič, M. Peterka, and D. Miklavčič, Trends Biotechnol. **33**, 480 (2015).

[30] R. Benz, F. Beckers, and U. Zimmermann, J. Membr. Biol. **48**, 181 (1979).
[31] J. Teissie and T.Y. Tsong, Biochemistry **20**, 1548 (1981).
[32] H. Aranda-Espinoza, H. Bermudez, F.S. Bates, and D.E. Discher, Phys. Rev. Lett. **87**, 208301 (2001).
[33] D. Miklavčič, J. Membr. Biol. **245**, 591 (2012).
[34] M.L. Yarmush, A. Golberg, G. Serša, T. Kotnik, and D. Miklavčič, Annu. Rev. Biomed. Eng. **16**, 295 (2014).
[35] D.E. Spratt, E.A.G. Spratt, S. Wu, A. DeRosa, N.Y. Lee, M.E. Lacouture, and C.A. Barker, J. Clin. Oncol. **32**, 3144 (2014).
[36] L.M. Mir, Mol. Biotechnol. **43**, 167 (2009).
[37] K.E. Broderick and L.M. Humeau, Expert Rev. Vaccines **14**, 195 (2015).
[38] H.J. Scheffer, K. Nielsen, M.C. de Jong, A.A.J.M. van Tilborg, J.M. Vieveen, A.R.A. Bouwman, S. Meijer, C. van Kuijk, P.M.P. van den Tol, and M.R. Meijerink, J. Vasc. Interv. Radiol. JVIR **25**, 997 (2014).
[39] J. Lavee, G. Onik, P. Mikus, and B. Rubinsky, Heart Surg. Forum **10**, E162 (2007).
[40] K. Neven, V. van Driel, H. van Wessel, R. van Es, B. du Pré, P.A. Doevendans, and F. Wittkampf, Circ. Arrhythm. Electrophysiol. **7**, 913 (2014).
[41] V.J.H.M. van Driel, K. Neven, H. van Wessel, A. Vink, P.A.F.M. Doevendans, and F.H.M. Wittkampf, Heart Rhythm Off. J. Heart Rhythm Soc. **12**, 1838 (2015).
[42] H. Bouzrara and E. Vorobiev, Int. Sugar J. **102**, 194 (2000).
[43] H. Bluhm and M. Sack, in *Electrotechnol. Extr. Food Plants Biomater.* (Springer New York, 2009), pp. 237–269.
[44] H. Mhemdi, O. Bals, N. Grimi, and E. Vorobiev, Food Bioprocess Technol. **7**, 795 (2013).
[45] M. Sack, J. Sigler, S. Frenzel, C. Eing, J. Arnold, T. Michelberger, W. Frey, F. Attmann, L. Stukenbrock, and G. Müller, Food Eng. Rev. **2**, 147 (2010).
[46] X. Yu, O. Bals, N. Grimi, and E. Vorobiev, Ind. Crops Prod. **74**, 309 (2015).
[47] S. Brianceau, M. Turk, X. Vitrac, and E. Vorobiev, Innov. Food Sci. Emerg. Technol. **29**, 2 (2015).
[48] M. Pavlin, M. Kandušer, M. Reberšek, G. Pucihar, F.X. Hart, R. Magjarević, and D. Miklavčič, Biophys. J. **88**, 4378 (2005).
[49] E.M. Dunki-Jacobs, P. Philips, and R.C.G. Martin 2nd, J. Am. Coll. Surg. **218**, 179 (2014).
[50] K.A. Riske and R. Dimova, Biophys. J. **88**, 1143 (2005).
[51] J. Voldman, Annu. Rev. Biomed. Eng. **8**, 425 (2006).
[52] J. Teissie and T.Y. Tsong, J. Membr. Biol. **55**, 133 (1980).
[53] S.W.I. Siu and R.A. Böckmann, J. Struct. Biol. **157**, 545 (2007).
[54] F. Maglietti, S. Michinski, N. Olaiz, M. Castro, C. Suárez, and G. Marshall, PLoS ONE **8**, e80167 (2013).
[55] R. Rodaite-Riseviciene, R. Saule, V. Snitka, and G. Saulis, IEEE Trans. Plasma Sci. **42**, 249 (2014).
[56] D.E. Chafai, A. Mehle, A. Tilmatine, B. Maouche, and D. Miklavčič, Bioelectrochemistry **106, Part B**, 249 (2015).
[57] U. Zimmermann, in *Rev. Physiol. Biochem. Pharmacol. Vol. 105* (Springer Berlin Heidelberg, 1986), pp. 175–256.
[58] J. Teissie, M. Golzio, and M.P. Rols, Biochim. Biophys. Acta **1724**, 270 (2005).
[59] K. Kinosita Jr. and T.Y. Tsong, Biochim. Biophys. Acta **554**, 479 (1979).
[60] M. Hibino, M. Shigemori, H. Itoh, K. Nagayama, and K. Kinosita, Biophys. J. **59**, 209 (1991).
[61] M. Hibino, H. Itoh, and K. Kinosita, Biophys. J. **64**, 1789 (1993).
[62] W. Frey, J.A. White, R.O. Price, P.F. Blackmore, R.P. Joshi, R. Nuccitelli, S.J. Beebe, K.H. Schoenbach, and J.F. Kolb, Biophys. J. **90**, 3608 (2006).
[63] J.A. White, U. Pliquett, P.F. Blackmore, R.P. Joshi, K.H. Schoenbach, and J.F. Kolb, Eur. Biophys. J. **40**, 947 (2011).
[64] M. Pavlin, V. Leben, and D. Miklavčič, Biochim. Biophys. Acta **1770**, 12 (2007).
[65] G. Pucihar, T. Kotnik, D. Miklavčič, and J. Teissié, Biophys. J. **95**, 2837 (2008).
[66] M.R. Prausnitz, J.D. Corbett, J.A. Gimm, D.E. Golan, R. Langer, and J.C. Weaver, Biophys. J. **68**, 1864 (1995).
[67] B. Gabriel and J. Teissie, Biophys. J. **76**, 2158 (1999).
[68] K. Kinosita Jr. and T.Y. Tsong, Nature **268**, 438 (1977).
[69] M.L. Escande-Geraud, M.P. Rols, M.A. Dupont, N. Gas, and J. Teissie, Biochim. Biophys. Acta **939**, 247 (1988).
[70] A. Lopez, M.P. Rols, and J. Teissie, Biochemistry **27**, 1222 (1988).
[71] M.P. Rols and J. Teissie, Biophys. J. **58**, 1089 (1990).
[72] G. Saulis, M.S. Venslauskas, and J. Naktinis, J. Electroanal. Chem. Interfacial Electrochem. **321**, 1 (1991).
[73] M.P. Rols and J. Teissie, Biophys. J. **75**, 1415 (1998).
[74] E. Neumann, K. Toensing, S. Kakorin, P. Budde, and J. Frey, Biophys. J. **74**, 98 (1998).
[75] A.G. Pakhomov, J.F. Kolb, J.A. White, R.P. Joshi, S. Xiao, and K.H. Schoenbach, Bioelectromagnetics **28**, 655 (2007).
[76] C.S. Djuzenova, U. Zimmermann, H. Frank, V.L. Sukhorukov, E. Richter, and G. Fuhr, Biochim. Biophys. Acta **1284**, 143 (1996).
[77] R. Shirakashi, V.L. Sukhorukov, I. Tanasawa, and U. Zimmermann, Int. J. Heat Mass Transf. **47**, 4517 (2004).
[78] M. Kandušer, M. Šentjurc, and D. Miklavčič, Eur. Biophys. J. **35**, 196 (2006).
[79] G. Saulis and R. Saulė, Biochim. Biophys. Acta **1818**, 3032 (2012).
[80] M.P. Rols, P. Femenia, and J. Teissie, Biochem. Biophys. Res. Commun. **208**, 26 (1995).
[81] B. Gabriel and J. Teissié, Biochim. Biophys. Acta **1266**, 171 (1995).
[82] R. Lin, D.C. Chang, and Y.K. Lee, Biomed. Microdevices **13**, 1063 (2011).
[83] D. Gross, L.M. Loew, and W.W. Webb, Biophys. J. **50**, 339 (1986).
[84] T. Kotnik and G. Pucihar, in *Adv. Electroporation Tech. Biol. Med.*, edited by A.G. Pakhomov, D. Miklavcic, and M.S. Markov (CRC Press, Boca Raton, 2010), pp. 51–70.

[85] B. Gabriel and J. Teissié, Biophys. J. **73**, 2630 (1997).
[86] T. Kotnik, G. Pucihar, and D. Miklavcic, J. Membr. Biol. **236**, 3 (2010).
[87] Z. Lojewska, D.L. Farkas, B. Ehrenberg, and L.M. Loew, Biophys. J. **56**, 121 (1989).
[88] T. Kotnik, F. Bobanovic, and D. Miklavcic, Bioelectrochem. Bioenerg. **43**, 285 (1997).
[89] T. Kotnik and D. Miklavcic, IEEE Trans. Biomed. Eng. **47**, 1074 (2000).
[90] T. Kotnik and D. Miklavcic, Biophys. J. **79**, 670 (2000).
[91] G. Pucihar, T. Kotnik, B. Valič, and D. Miklavcic, Ann. Biomed. Eng. **34**, 642 (2006).
[92] W. Mehrle, U. Zimmermann, and R. Hampp, FEBS Lett. **185**, 89 (1985).
[93] E. Tekle, R.D. Astumian, and P.B. Chock, Biochem. Biophys. Res. Commun. **172**, 282 (1990).
[94] B.E. Henslee, A. Morss, X. Hu, G.P. Lafyatis, and L.J. Lee, Anal. Chem. **83**, 3998 (2011).
[95] S. Sixou and J. Teissie, Biochim. Biophys. Acta **1028**, 154 (1990).
[96] B. Valic, M. Golzio, M. Pavlin, A. Schatz, C. Faurie, B. Gabriel, J. Teissie, M.P. Rols, and D. Miklavcic, Eur. Biophys. J. **32**, 519 (2003).
[97] R. Susil, D. Semrov, and D. Miklavcic, Electro-Magnetobiology **17**, 391 (1998).
[98] R. Benz and U. Zimmermann, Bioelectrochem. Bioenerg. **7**, 723 (1980).
[99] J. Teissié and M.P. Rols, Biophys. J. **65**, 409 (1993).
[100] A.G. Pakhomov, E. Gianulis, P.T. Vernier, I. Semenov, S. Xiao, and O.N. Pakhomova, Biochim. Biophys. Acta **1848**, 958 (2015).
[101] A.M. Bowman, O.M. Nesin, O.N. Pakhomova, and A.G. Pakhomov, J. Membr. Biol. **236**, 15 (2010).
[102] O.M. Nesin, O.N. Pakhomova, S. Xiao, and A.G. Pakhomov, Biochim. Biophys. Acta **1808**, 792 (2011).
[103] A. Macek-Lebar and D. Miklavcic, Radiol. Oncol. **35**, (2001).
[104] Z. Vasilkoski, A.T. Esser, T.R. Gowrishankar, and J.C. Weaver, Phys. Rev. E **74**, 021904 (2006).
[105] M. Cemazar, T. Jarm, D. Miklavcic, A. Macek-Lebar, A. Ihan, N.A. Kopitar, and G. Sersa, Electro-Magnetobiology **17**, 263 (1998).
[106] U. Zimmermann, G. Pilwat, C. Holzapfel, and K. Rosenheck, J. Membr. Biol. **30**, 135 (1976).
[107] U. Zimmermann, M. Groves, H. Schnabl, and G. Pilwat, J. Membr. Biol. **52**, 37 (1980).
[108] L. Towhidi, T. Kotnik, G. Pucihar, S.M.P. Firoozabadi, H. Mozdarani, and D. Miklavčič, Electromagn. Biol. Med. **27**, 372 (2008).
[109] M. Puc, T. Kotnik, L.M. Mir, and D. Miklavcic, Bioelectrochemistry **60**, 1 (2003).
[110] M. Usaj and M. Kanduser, J. Membr. Biol. **245**, 583 (2012).
[111] C.S. Djuzenova, V.L. Sukhorukov, G. Klöck, W.M. Arnold, and U. Zimmermann, Cytometry **15**, 35 (1994).
[112] U. Zimmermann, G. Pilwat, and F. Riemann, Biophys. J. **14**, 881 (1974).
[113] S. Hojo, K. Shimizu, H. Yositake, M. Muraji, H. Tsujimoto, and W. Tatebe, IEEE Trans. Nanobioscience **2**, 35 (2003).
[114] V.L. Sukhorukov, C.S. Djuzenova, H. Frank, W.M. Arnold, and U. Zimmermann, Cytometry **21**, 230 (1995).
[115] T. Kotnik and D. Miklavcic, Biophys. J. **90**, 480 (2006).
[116] K.H. Schoenbach, S.J. Beebe, and E.S. Buescher, Bioelectromagnetics **22**, 440 (2001).
[117] T.B. Napotnik, M. Reberšek, T. Kotnik, E. Lebrasseur, G. Cabodevila, and D. Miklavčič, Med. Biol. Eng. Comput. **48**, 407 (2010).
[118] K.H. Schoenbach and R.P. Joshi, Crit. Rev. Biomed. Eng. **38**, 255 (2010).
[119] L.V. Chernomordik, S.I. Sukharev, S.V. Popov, V.F. Pastushenko, A.V. Sokirko, I.G. Abidor, and Y.A. Chizmadzhev, Biochim. Biophys. Acta **902**, 360 (1987).
[120] A.T. Esser, K.C. Smith, T.R. Gowrishankar, Z. Vasilkoski, and J.C. Weaver, Biophys. J. **98**, 2506 (2010).
[121] K.A. DeBruin and W. Krassowska, Biophys. J. **77**, 1213 (1999).
[122] T. Kotnik, D. Miklavcic, and L.M. Mir, Bioelectrochemistry **54**, 91 (2001).
[123] C. Chen, J.A. Evans, M.P. Robinson, S.W. Smye, and P. O'Toole, Phys. Med. Biol. **55**, 1219 (2010).
[124] L. Towhidi, S. Firoozabadi, H. Mozdarani, and D. Miklavcic, Radiol. Oncol. **46**, 119 (2012).
[125] Z. Shankayi, S.M.P. Firoozabadi, and M.G. Mansurian, Cell Biochem. Biophys. **65**, 211 (2012).
[126] V. Novickij, A. Grainys, J. Švedienė, S. Markovskaja, A. Paškevičius, and J. Novickij, Bioelectromagnetics **35**, 347 (2014).
[127] S. Xiao, S. Guo, V. Nesin, R. Heller, and K.H. Schoenbach, IEEE Trans. Biomed. Eng. **58**, 1239 (2011).
[128] F. Guo, C. Yao, C. Bajracharya, S. Polisetty, K.H. Schoenbach, and S. Xiao, Bioelectromagnetics **35**, 145 (2014).
[129] P.T. Vernier, Z.A. Levine, M.-C. Ho, S. Xiao, I. Semenov, and A.G. Pakhomov, J. Membr. Biol. **248**, 837 (2015).
[130] K.H. Schoenbach, S. Xiao, R.P. Joshi, J.T. Camp, T. Heeren, J.F. Kolb, and S.J. Beebe, IEEE Trans. Plasma Sci. **36**, 414 (2008).
[131] J.T. Camp, Y. Jing, J. Zhuang, J.F. Kolb, S.J. Beebe, J. Song, R.P. Joshi, S. Xiao, and K.H. Schoenbach, IEEE Trans. Plasma Sci. **40**, 2334 (2012).
[132] T. Kotnik and D. Miklavcic, Bioelectromagnetics **21**, 385 (2000).
[133] V.F. Pastushenko, Y.A. Chizmadzhev, and V.B. Arakelyan, Bioelectrochem. Bioenerg. **6**, 53 (1979).
[134] L.V. Chernomordik and I.G. Abidor, Bioelectrochem. Bioenerg. **7**, 617 (1980).
[135] R. Benz and U. Zimmermann, Biochim. Biophys. Acta **640**, 169 (1981).
[136] R.W. Glaser, S.L. Leikin, L.V. Chernomordik, V.F. Pastushenko, and A.I. Sokirko, Biochim. Biophys. Acta **940**, 275 (1988).
[137] K.C. Melikov, V.A. Frolov, A. Shcherbakov, A.V. Samsonov, Y.A. Chizmadzhev, and L.V. Chernomordik, Biophys. J. **80**, 1829 (2001).

[138] M. Szabo and M.I. Wallace, Biochim. Biophys. Acta. In Press. DOI: 10.1016/j.bbamem.2015.07.009
[139] S. Kakorin, S.P. Stoylov, and E. Neumann, Biophys. Chem. **58**, 109 (1996).
[140] T. Portet and R. Dimova, Biophys. J. **99**, 3264 (2010).
[141] J.C. Weaver and Y.A. Chizmadzhev, Bioelectrochem. Bioenerg. **41**, 135 (1996).
[142] M. Pavlin, T. Kotnik, D. Miklavčič, P. Kramar, and A. Maček Lebar, in *Adv. Planar Lipid Bilayers Liposomes*, edited by A. Leitmannova Liu (Academic Press, 2008), pp. 165–226.
[143] D.C. Chang and T.S. Reese, Biophys. J. **58**, 1 (1990).
[144] D.P. Tieleman, BMC Biochem. **5**, 10 (2004).
[145] M. Tarek, Biophys. J. **88**, 4045 (2005).
[146] P.T. Vernier, Z.. Levine, and M.. Gundersen, Proc. IEEE **101**, 494 (2013).
[147] M. Tarek and L. Delemotte, in *Adv. Electroporation Tech. Biol. Med.*, edited by A.G. Pakhomov, D. Miklavcic, and M.S. Markov (CRC Press, Boca Raton, 2010).
[148] A.A. Gurtovenko, J. Anwar, and I. Vattulainen, Chem. Rev. **110**, 6077 (2010).
[149] M.J. Ziegler and P.T. Vernier, J. Phys. Chem. B **112**, 13588 (2008).
[150] R.A. Bockmann, B.L. de Groot, S. Kakorin, E. Neumann, and H. Grubmuller, Biophys. J. **95**, 1837 (2008).
[151] L. Delemotte and M. Tarek, J. Membr. Biol. **245**, 531 (2012).
[152] Z.A. Levine and P.T. Vernier, J. Membr. Biol. **236**, 27 (2010).
[153] F. Dehez, L. Delemotte, P. Kramar, D. Miklavcic, and M. Tarek, J. Phys. Chem. C **118**, 6752 (2014).
[154] A.A. Gurtovenko and I. Vattulainen, Biophys. J. **92**, 1878 (2007).
[155] M.C. Ho, M. Casciola, Z.A. Levine, and P.T. Vernier, J. Phys. Chem. B **117**, 11633 (2013).
[156] A.A. Gurtovenko and I. Vattulainen, J. Am. Chem. Soc. **127**, 17570 (2005).
[157] A.A. Gurtovenko and I. Vattulainen, in *Biomembr. Front.*, edited by R. Faller, M.L. Longo, S.H. Risbud, and T. Jue (Humana Press, 2009), pp. 121–139.
[158] M. Tokman, J.H. Lee, Z.A. Levine, M.C. Ho, M.E. Colvin, and P.T. Vernier, PLoS ONE **8**, e61111 (2013).
[159] Q. Hu, Z. Zhang, H. Qiu, M.G. Kong, and R.P. Joshi, Phys. Rev. E **87**, 032704 (2013).
[160] S.K. Kandasamy and R.G. Larson, J. Chem. Phys. **125**, 074901 (2006).
[161] A. Polak, D. Bonhenry, F. Dehez, P. Kramar, D. Miklavcic, and M. Tarek, J. Membr. Biol. **246**, 843 (2013).
[162] A.A. Gurtovenko and A.S. Lyulina, J. Phys. Chem. B **118**, 9909 (2014).
[163] M. Breton, L. Delemotte, A. Silve, L.M. Mir, and M. Tarek, J. Am. Chem. Soc. **134**, 13938 (2012).
[164] M.L. Fernández, G. Marshall, F. Sagués, and R. Reigada, J. Phys. Chem. B **114**, 6855 (2010).
[165] M. Casciola, D. Bonhenry, M. Liberti, F. Apollonio, and M. Tarek, Bioelectrochemistry **100**, 11 (2014).
[166] T.J. Piggot, D.A. Holdbrook, and S. Khalid, J. Phys. Chem. B **115**, 13381 (2011).
[167] Z.A. Levine and P.T. Vernier, J. Membr. Biol. **245**, 599 (2012).
[168] R. Reigada, Biochim. Biophys. Acta **1838**, 814 (2014).
[169] J. Teissié and C. Ramos, Biophys. J. **74**, 1889 (1998).
[170] T. Kotnik, G. Pucihar, M. Reberšek, D. Miklavčič, and L.M. Mir, Biochim. Biophys. Acta **1614**, 193 (2003).
[171] M.R. Prausnitz, B.S. Lau, C.D. Milano, S. Conner, R. Langer, and J.C. Weaver, Biophys. J. **65**, 414 (1993).
[172] M.R. Prausnitz, C.D. Milano, J.A. Gimm, R. Langer, and J.C. Weaver, Biophys. J. **66**, 1522 (1994).
[173] P.J. Canatella, J.F. Karr, J.A. Petros, and M.R. Prausnitz, Biophys. J. **80**, 755 (2001).
[174] P.J. Canatella and M.R. Prausnitz, Gene Ther. **8**, 1464 (2001).
[175] B. Gabriel and J. Teissié, Bioelectrochem. Bioenerg. **47**, 113 (1998).
[176] D.S. Dimitrov and A.E. Sowers, Biochim. Biophys. Acta **1022**, 381 (1990).
[177] J. Li and H. Lin, Bioelectrochemistry **82**, 10 (2011).
[178] K.C. Smith and J.C. Weaver, Biochem. Biophys. Res. Commun. **412**, 8 (2011).
[179] E. Tekle, R.D. Astumian, W.A. Friauf, and P.B. Chock, Biophys. J. **81**, 960 (2001).
[180] K. Kinosita, H. Itoh, S. Ishiwata, K. Hirano, T. Nishizaka, and T. Hayakawa, J. Cell Biol. **115**, 67 (1991).
[181] I. Semenov, C. Zemlin, O.N. Pakhomova, S. Xiao, and A.G. Pakhomov, Biochim. Biophys. Acta **1848**, 2118 (2015).
[182] T.R. Gowrishankar, A.T. Esser, Z. Vasilkoski, K.C. Smith, and J.C. Weaver, Biochem. Biophys. Res. Commun. **341**, 1266 (2006).
[183] P.T. Vernier, Y. Sun, and M.A. Gundersen, BMC Cell Biol. **7**, 1 (2006).
[184] M.P. Rols and J. Teissie, Eur. J. Biochem. **179**, 109 (1989).
[185] K.J. Müller, V.L. Sukhorukov, and U. Zimmermann, J. Membr. Biol. **184**, 161 (2001).
[186] J. Li, W. Tan, M. Yu, and H. Lin, Biochim. Biophys. Acta **1828**, 461 (2013).
[187] A. Paganin-Gioanni, E. Bellard, J.M. Escoffre, M.P. Rols, J. Teissié, and M. Golzio, Proc. Natl. Acad. Sci. **108**, 10443 (2011).
[188] M. Golzio, J. Teissié, and M.P. Rols, Proc. Natl. Acad. Sci. **99**, 1292 (2002).
[189] M. Pavlin and M. Kandušer, Sci. Rep. **5**, 9132 (2015).
[190] M. Kandušer, D. Miklavčič, and M. Pavlin, Bioelectrochemistry **74**, 265 (2009).
[191] S. Haberl, M. Kandušer, K. Flisar, D. Hodžić, V.B. Bregar, D. Miklavčič, J.M. Escoffre, M.P. Rols, and M. Pavlin, J. Gene Med. **15**, 169 (2013).
[192] C. Rosazza, J.M. Escoffre, A. Zumbusch, and M.P. Rols, Mol. Ther. **19**, 913 (2011).
[193] M. Wu and F. Yuan, PLoS ONE **6**, e20923 (2011).
[194] C. Rosazza, E. Phez, J.M. Escoffre, L. Cézanne, A. Zumbusch, and M.P. Rols, Int. J. Pharm. **423**, 134 (2012).

[195] B. Markelc, E. Skvarca, T. Dolinsek, V.P. Kloboves, A. Coer, G. Sersa, and M. Cemazar, Bioelectrochemistry **103**, 111 (2015).
[196] C. Sun, Z. Cao, M. Wu, and C. Lu, Anal. Chem. **86**, 11403 (2014).
[197] C.G. Pack, M.R. Song, E. Lee Tae, M. Hiroshima, K.H. Byun, J.S. Kim, and Y. Sako, J. Controlled Release **163**, 315 (2012).
[198] M. Glogauer, W. Lee, and C.A.G. McCulloch, Exp. Cell Res. **208**, 232 (1993).
[199] Y. Rosemberg and R. Korenstein, Bioelectrochem. Bioenerg. **42**, 275 (1997).
[200] Y. Antov, A. Barbul, and R. Korenstein, Exp. Cell Res. **297**, 348 (2004).
[201] N. Mahrour, R. Pologea-Moraru, M.G. Moisescu, S. Orlowski, P. Levêque, and L.M. Mir, Biochim. Biophys. Acta **1668**, 126 (2005).
[202] N. Ben-Dov, I. Rozman Grinberg, and R. Korenstein, PLoS ONE **7**, e50299 (2012).
[203] W. Krassowska and P.D. Filev, Biophys. J. **92**, 404 (2007).
[204] A.M. Lebar, G.C. Troiano, L. Tung, and D. Miklavcic, IEEE Trans. NanoBioscience **1**, 116 (2002).
[205] M. Kotulska, J. Basalyga, M.B. Derylo, and P. Sadowski, J. Membr. Biol. **236**, 37 (2010).
[206] M. Pavlin and D. Miklavčič, Bioelectrochemistry **74**, 38 (2008).
[207] M. Schmeer, T. Seipp, U. Pliquett, S. Kakorin, and E. Neumann, Phys. Chem. Chem. Phys. **6**, 5564 (2004).
[208] I.P. Sugar and E. Neumann, Biophys. Chem. **19**, 211 (1984).
[209] I.P. Sugar, W. Förster, and E. Neumann, Biophys. Chem. **26**, 321 (1987).
[210] J.C. Shillcock and U. Seifert, Biophys. J. **74**, 1754 (1998).
[211] M. Fosnaric, V. Kralj-Iglic, K. Bohinc, A. Iglic, and S. May, J. Phys. Chem. B **107**, 12519 (2003).
[212] K.C. Smith, J.C. Neu, and W. Krassowska, Biophys. J. **86**, 2813 (2004).
[213] R.P. Joshi and Q. Hu, IEEE Trans. Plasma Sci. **40**, 2355 (2012).
[214] J. Teissie and M.-P. Rols, Ann. N. Y. Acad. Sci. **720**, 98 (1994).
[215] M. Leguèbe, A. Silve, L.M. Mir, and C. Poignard, J. Theor. Biol. **360**, 83 (2014).
[216] M.P. Rols and J. Teissié, Biochim. Biophys. Acta **1111**, 45 (1992).
[217] E. Niki, Y. Yoshida, Y. Saito, and N. Noguchi, Biochem. Biophys. Res. Commun. **338**, 668 (2005).
[218] A. Reis and C.M. Spickett, Biochim. Biophys. Acta **1818**, 2374 (2012).
[219] P. Jurkiewicz, A. Olżyńska, L. Cwiklik, E. Conte, P. Jungwirth, F.M. Megli, and M. Hof, Biochim. Biophys. Acta **1818**, 2388 (2012).
[220] J. Wong-ekkabut, Z. Xu, W. Triampo, I.-M. Tang, D.P. Tieleman, and L. Monticelli, Biophys. J. **93**, 4225 (2007).
[221] V. Jarerattanachat, M. Karttunen, and J. Wong-ekkabut, J. Phys. Chem. B **117**, 8490 (2013).
[222] K.A. Runas and N. Malmstadt, Soft Matter **11**, 499 (2015).
[223] P. Boonnoy, V. Jarerattanachat, M. Karttunen, and J. Wong-ekkabut, J. Phys. Chem. Lett. 4884 (2015).
[224] B. Gabriel and J. Teissié, Eur. J. Biochem. **223**, 25 (1994).
[225] B. Gabriel and J. Teissié, Eur. J. Biochem. **228**, 710 (1995).
[226] L.C. Benov, P.A. Antonov, and S.R. Ribarov, Gen. Physiol. Biophys. **13**, 85 (1994).
[227] M. Maccarrone, N. Rosato, and A.F. Agro, Biochem. Biophys. Res. Commun. **206**, 238 (1995).
[228] M. Maccarrone, M.R. Bladergroen, N. Rosato, and A.F. Agro, Biochem. Biophys. Res. Commun. **209**, 417 (1995).
[229] O.N. Pakhomova, V.A. Khorokhorina, A.M. Bowman, R. Rodaitė-Riševičienė, G. Saulis, S. Xiao, and A.G. Pakhomov, Arch. Biochem. Biophys. **527**, 55 (2012).
[230] K. Walker, O.N. Pakhomova, J. Kolb, K.S. Schoenbach, B.E. Stuck, M.R. Murphy, and A.G. Pakhomov, Bioelectromagnetics **27**, 221 (2006).
[231] P.T. Vernier, Z.A. Levine, Y.-H. Wu, V. Joubert, M.J. Ziegler, L.M. Mir, and D.P. Tieleman, PLoS ONE **4**, e7966 (2009).
[232] M.P. Rols, C. Delteil, M. Golzio, and J. Teissié, Eur. J. Biochem. **254**, 382 (1998).
[233] M.P. Rols and J. Teissie, Biochemistry **29**, 4561 (1990).
[234] M.P. Rols, F. Dahhou, K.P. Mishra, and J. Teissie, Biochemistry **29**, 2960 (1990).
[235] G.V. Gass and L.V. Chernomordik, Biochim. Biophys. Acta **1023**, 1 (1990).
[236] O.N. Pakhomova, B.W. Gregory, V.A. Khorokhorina, A.M. Bowman, S. Xiao, and A.G. Pakhomov, PLoS ONE **6**, e17100 (2011).
[237] O.N. Pakhomova, B.W. Gregory, and A.G. Pakhomov, J. Cell. Mol. Med. **17**, 154 (2013).
[238] A. Silve, A. Guimerà Brunet, B. Al-Sakere, A. Ivorra, and L.M. Mir, Biochim. Biophys. Acta **1840**, 2139 (2014).
[239] C. Jiang, Z. Qin, and J. Bischof, Ann. Biomed. Eng. **42**, 193 (2014).
[240] C. Jiang, Q. Shao, and J. Bischof, Ann. Biomed. Eng. **43**, 887 (2015).
[241] Y. Demiryurek, M. Nickaeen, M. Zheng, M. Yu, J.D. Zahn, D.I. Shreiber, H. Lin, and J.W. Shan, Biochim. Biophys. Acta **1848**, 1706 (2015).
[242] P.L. McNeil and R.A. Steinhardt, Annu. Rev. Cell Dev. Biol. **19**, 697 (2003).
[243] P.L. McNeil and T. Kirchhausen, Nat. Rev. Mol. Cell Biol. **6**, 499 (2005).
[244] C. Huynh, D. Roth, D.M. Ward, J. Kaplan, and N.W. Andrews, Proc. Natl. Acad. Sci. **101**, 16795 (2004).
[245] A.J. Jimenez, P. Maiuri, J. Lafaurie-Janvore, S. Divoux, M. Piel, and F. Perez, Science **343**, 1247136 (2014).
[246] A. Sharei, R. Poceviciute, E.L. Jackson, N. Cho, S. Mao, G.C. Hartoularos, D.Y. Jang, S. Jhunjhunwala, A. Eyerman, T. Schoettle, R. Langer, and K.F. Jensen, Integr. Biol. **6**, 470 (2014).
[247] C. Blangero and J. Teissié, J. Membr. Biol. **86**, 247 (1985).
[248] B.E. Henslee, A. Morss, X. Hu, G.P. Lafyatis, and L.J. Lee, Biomicrofluidics **8**, 052002 (2014).

[249] E. Barrera-Escorcia, A. Muñóz-Torres, A. Vilches-Flores, M. Fregoso-Padilla, J. Martínez-Aguilar, I. Castillo-Padilla, A. Vargas-Vera, J.D. Méndez, M. Betancourt-Rule, and R. Román-Ramos, Biomed. Pharmacother. **59**, 275 (2005).
[250] E.W.M. Kemna, F. Wolbers, I. Vermes, and A. van den Berg, Electrophoresis **32**, 3138 (2011).
[251] N. Hu, J. Yang, S.W. Joo, A.N. Banerjee, and S. Qian, Sens. Actuators B Chem. **178**, 63 (2013).
[252] W. Mehrle, R. Hampp, and U. Zimmermann, Biochim. Biophys. Acta **978**, 267 (1989).
[253] W. Mehrle, R. Hampp, U. Zimmermann, and H.P. Schwan, Biochim. Biophys. Acta **939**, 561 (1988).
[254] L. Rems, M. Ušaj, M. Kandušer, M. Reberšek, D. Miklavčič, and G. Pucihar, Sci. Rep. **3**, 3382 (2013).
[255] K. Trontelj, M. Rebersek, M. Kanduser, V.C. Serbec, M. Sprohar, and D. Miklavcic, Bioelectrochemistry Amst. Neth. **74**, 124 (2008).
[256] M. Pavlin, N. Pavselj, and D. Miklavcic, IEEE Trans. Biomed. Eng. **49**, 605 (2002).
[257] M.E. Mezeme, G. Pucihar, M. Pavlin, C. Brosseau, and D. Miklavčič, Appl. Phys. Lett. **100**, 143701 (2012).
[258] G. Pucihar, T. Kotnik, J. Teissié, and D. Miklavčič, Eur. Biophys. J. **36**, 173 (2007).
[259] M.E. Mezeme, M. Kranjc, F. Bajd, I. Serša, C. Brosseau, and D. Miklavčič, Appl. Phys. Lett. **101**, 213702 (2012).
[260] I.G. Abidor, A.I. Barbul, D.V. Zhelev, P. Doinov, I.N. Bandrina, E.M. Osipova, and S.I. Sukharev, Biochim. Biophys. Acta **1152**, 207 (1993).
[261] I.G. Abidor, L.H. Li, and S.W. Hui, Biophys. J. **67**, 418 (1994).
[262] M. Usaj, K. Flisar, D. Miklavcic, and M. Kanduser, Bioelectrochemistry **89**, 34 (2013).
[263] H. Mekid and L.M. Mir, Biochim. Biophys. Acta **1524**, 118 (2000).
[264] T. Kotnik, G. Pucihar, and D. Miklavčič, in *Clin. Asp. Electroporation*, edited by S.T. Kee, J. Gehl, and E.W. Lee (Springer New York, 2011), pp. 19–29.
[265] R.M. Sutherland, Science **240**, 177 (1988).
[266] M.T. Santini, G. Rainaldi, and P.L. Indovina, Crit. Rev. Oncol. Hematol. **36**, 75 (2000).
[267] P.J. Canatella, M.M. Black, D.M. Bonnichsen, C. McKenna, and M.R. Prausnitz, Biophys. J. **86**, 3260 (2004).
[268] L. Gibot, L. Wasungu, J. Teissié, and M.-P. Rols, J. Controlled Release **167**, 138 (2013).
[269] L. Gibot and M.P. Rols, J. Membr. Biol. **246**, 745 (2013).
[270] L. Chopinet, L. Wasungu, and M.P. Rols, Int. J. Pharm. **423**, 7 (2012).
[271] L. Wasungu, J.M. Escoffre, A. Valette, J. Teissie, and M.P. Rols, Int. J. Pharm. **379**, 278 (2009).
[272] B. Marrero and R. Heller, Biomaterials **33**, 3036 (2012).
[273] G. Sersa, T. Jarm, T. Kotnik, A. Coer, M. Podkrajsek, M. Sentjurc, D. Miklavcic, M. Kadivec, S. Kranjc, A. Secerov, and M. Cemazar, Br. J. Cancer **98**, 388 (2008).
[274] S. Huclova, D. Erni, and J. Fröhlich, J. Phys. Appl. Phys. **43**, 365405 (2010).
[275] S. Huclova, D. Baumann, M.S. Talary, and J. Fröhlich, Phys. Med. Biol. **56**, 7777 (2011).
[276] S. Huclova, D. Erni, and J. Fröhlich, J. Phys. Appl. Phys. **45**, 025301 (2012).
[277] S. Gabriel, R.W. Lau, and C. Gabriel, Phys. Med. Biol. **41**, 2251 (1996).
[278] D. Miklavcic, D. Semrov, H. Mekid, and L.M. Mir, Biochim. Biophys. Acta **1523**, 73 (2000).
[279] D. Sel, D. Cukjati, D. Batiuskaite, T. Slivnik, L.M. Mir, and D. Miklavcic, IEEE Trans. Biomed. Eng. **52**, 816 (2005).
[280] S. Corovic, I. Lackovic, P. Sustaric, T. Sustar, T. Rodic, and D. Miklavcic, Biomed. Eng. OnLine **12**, 16 (2013).
[281] M. Kranjc, B. Markelc, F. Bajd, M. Čemažar, I. Serša, T. Blagus, and D. Miklavčič, Radiology **274**, 115 (2014).
[282] S. Huang, Y. Zu, and S. Wang, in *Electroporation Protoc.*, edited by S. Li, J. Cutrera, R. Heller, and J. Teissie (Springer New York, 2014), pp. 69–77.
[283] S. Huang, H. Deshmukh, K.K. Rajagopalan, and S. Wang, Electrophoresis **35**, 1837 (2014).
[284] P.E. Boukany, A. Morss, W. Liao, B. Henslee, H. Jung, X. Zhang, B. Yu, X. Wang, Y. Wu, L. Li, K. Gao, X. Hu, X. Zhao, O. Hemminger, W. Lu, G.P. Lafyatis, and L.J. Lee, Nat. Nanotechnol. **6**, 747 (2011).
[285] P.E. Boukany, Y. Wu, X. Zhao, K.J. Kwak, P.J. Glazer, K. Leong, and L.J. Lee, Adv. Healthc. Mater. **3**, 682 (2014).
[286] K. Gao, L. Li, L. He, K. Hinkle, Y. Wu, J. Ma, L. Chang, X. Zhao, D.G. Perez, S. Eckardt, J. Mclaughlin, B. Liu, D.F. Farson, and L.J. Lee, Small **10**, 1015 (2014).
[287] X. Xie, A.M. Xu, S. Leal-Ortiz, Y. Cao, C.C. Garner, and N.A. Melosh, ACS Nano **7**, 4351 (2013).
[288] C. Xie, Z. Lin, L. Hanson, Y. Cui, and B. Cui, Nat. Nanotechnol. **7**, 185 (2012).
[289] C. Liu, X. Xie, W. Zhao, N. Liu, P.A. Maraccini, L.M. Sassoubre, A.B. Boehm, and Y. Cui, Nano Lett. **13**, 4288 (2013).
[290] R. Guduru, P. Liang, C. Runowicz, M. Nair, V. Atluri, and S. Khizroev, Sci. Rep. **3**, (2013).
[291] D.T. Schoen, A.P. Schoen, L. Hu, H.S. Kim, S.C. Heilshorn, and Y. Cui, Nano Lett. **10**, 3628 (2010).
[292] C. Liu, X. Xie, W. Zhao, J. Yao, D. Kong, A.B. Boehm, and Y. Cui, Nano Lett. **14**, 5603 (2014).
[293] G. Yanai, T. Hayashi, Q. Zhi, K.C. Yang, Y. Shirouzu, T. Shimabukuro, A. Hiura, K. Inoue, and S. Sumi, PLoS ONE **8**, e64499 (2013).
[294] F. Gouaillier-Vulcain, E. Marchand, R. Martinez, J. Picquet, and B. Enon, Ann. Vasc. Surg. **29**, 801 (2015).
[295] S. Shayanfar, O.P. Chauhan, S. Toepfl, and V. Heinz, Int. J. Food Sci. Technol. **49**, 1224 (2014).
[296] K. Dymek, L. Rems, B. Zorec, P. Dejmek, F.G. Galindo, and D. Miklavčič, Innov. Food Sci. Emerg. Technol. **29**, 55 (2015).
[297] B. Kos, P. Voigt, D. Miklavcic, and M. Moche, Radiol. Oncol. **49**, 234 (2015).
[298] P.Y. Phoon, F. Gómez Galindo, A.A. Vicente, and P. Dejmek, (2008).

Paper 2

Title: **Electroporation of intracellular liposomes using nanosecond electric pulses – A theoretical study**

Authors: Lea Retelj (Rems), Gorazd Pucihar, and Damijan Miklavčič

Publication: IEEE Trans. Biomed. Eng. 60: 2624-2635, 2013
DOI: 10.1109/TBME.2013.2262177

Journal information

IEEE TRANSACTIONS ON BIOMEDICAL ENGINEERING		
Publisher	IEEE-INST ELECTRICAL ELECTRONICS ENGINEERS INC, 445 HOES LANE, PISCATAWAY, NJ 08855-4141 USA	
ISSN eISSN	0018-9294	
Research domain	Engineering	
Impact factor	2.347 (2014) 2.567 (5 year)	
JCR® category	Rank in category	Quartile in category
ENGINEERING, BIOMEDICAL	28 of 76	Q2

Source: Web of Science™ (December 2015)

Author contributions of L. Rems

L. Rems contributed to the design of the study, constructed the numerical models, performed numerical calculations and analyzed the results, contributed to the interpretation of the results and wrote most of the manuscript.

2624 IEEE TRANSACTIONS ON BIOMEDICAL ENGINEERING, VOL. 60, NO. 9, SEPTEMBER 2013

Electroporation of Intracellular Liposomes Using Nanosecond Electric Pulses—A Theoretical Study

Lea Retelj, Gorazd Pucihar, and Damijan Miklavčič*

***Abstract*—Nanosecond (ns) electric pulses of sufficient amplitude can provoke electroporation of intracellular organelles. This paper investigates whether such pulses could provide a method for controlled intracellular release of a content of small internalized artificial lipid vesicles (liposomes). To estimate the pulse parameters needed to selectively electroporate liposomes while keeping the plasma and nuclear membranes intact, we constructed a numerical model of a biological cell containing a nucleus and liposomes of different sizes (with radii from 50 to 500 nm), which were placed in various sites in the cytoplasm. Our results show that under physiological conditions selective electroporation is only possible for the largest liposomes and when using very short pulses (few ns). By increasing the liposome interior conductivity and/or decreasing the cytoplasmic conductivity, selective electroporation of even smaller liposomes could be achieved. The location of the liposomes inside the cell does not play a significant role, meaning that liposomes of similar size could all be electroporated simultaneously. Our results indicate the possibility of using ns pulse treatment for liposomal drug release.**

***Index Terms*—Electroporation, finite-element model, liposomes, nanosecond (ns) electric pulses.**

I. Introduction

EXPOSING the cell to an external electric field causes accumulation of charges on both sides of the plasma membrane and consequently the formation of an induced transmembrane voltage (ITV) [1], [2]. If ITV reaches a certain value (∼0.2–1 V), membrane permeability increases, allowing molecules for which the plasma membrane is under physiological conditions poorly permeable to enter or exit the cell [2]–[4]. Theories supported by molecular dynamics simulations suggest that the observed increase in membrane permeability results from the formation of hydrophilic pores in the lipid bilayer, which gives the phenomenon its name—electroporation [5]–[8]. When the electric field is not too strong and the exposure is not too long, the pores reseal in seconds to minutes after exposure and the cells restore their normal activity. Today, electroporation is commonly used in many fields of biology, biotechnology, and medicine, for applications such as cell fusion [9], [10], electrochemotherapy [11]–[14], gene electrotransfer [15]–[17], food processing [18], [19], and others.

In "classical" electroporation, rectangular pulses of micro- or milli-second duration with rise times in the order of μs and amplitudes in the range of kilovolt per centimeter are used. As the charging time of a cell is typically much shorter than the pulse duration (for a cell with radius of ∼10 μm the charging time in physiological medium is in the order of 100 ns), classical electroporation pulses primarily affect the plasma membrane while the cell interior practically remains shielded from the external electric field. However, if the cells are exposed to pulses with duration in the nanosecond range and amplitudes of several tens of kilovolts per centimeter, a high electric field is also present in the cell interior and affects the membranes of cell organelles [20]. Nanosecond (ns) pulses were reported to permeabilize intracellular granules [21], large endocytosed vacuoles [22], endocytotic vesicles [23], the nuclear envelope [24], the inner mitochondrial membrane [25], and also stimulate the release of calcium from endoplasmic reticulum [26]–[28].

The effects of ns pulses are primarily nonthermal. When pulses are applied in the moderate number, the overall increase in the temperature of the pulsed sample is practically negligible due to short pulse duration [29]. Yet, recent modeling results suggest that considerable temperature increases could indeed occur at local membrane sites and contribute to the observed biophysical responses of cells [30].

The feasibility of intracellular organelle electroporation motivated us to study the possibility of using ns pulses for selective electroporation of intracellular artificial lipid vesicles (liposomes). Liposomes present a convenient way to deliver various solutions containing drugs, proteins, or nucleic acids into cells, as they protect their content from the hostile environment (e.g., nucleic acids from endogenous nucleases in the blood plasma), reduce the toxicity of the containing drug for the nontargeted cells, increase the uptake of the drug into the targeted cells and consequently increase the drug efficacy [31], [32]. We hypothesize that when the liposomes reach the cell interior, ns pulses could provide a method for a controlled release of their content into the cytosol.

Recently, attention has been devoted to liposomes made of archaeal lipids (archaeosomes). These liposomes have several advantages over conventional liposomes, made of phospholipids,

Manuscript received January 12, 2013; revised March 25, 2013 and April 22, 2013; accepted May 1, 2013. Date of publication May 7, 2013; date of current version August 16, 2013. This work was supported by the Slovenian Research Agency. Research was conducted within the scope of the European Associated Laboratory for Pulsed Electric Field Applications in Biology and Medicine (LEA EBAM). *Asterisk indicates corresponding author.*

L. Retelj is with the Faculty of Electrical Engineering, University of Ljubljana, Ljubljana SI-1000, Slovenia (e-mail: lea.retelj@fe.uni-lj.si)

G. Pucihar, deceased, was with the Faculty of Electrical Engineering, University of Ljubljana, Ljubljana SI-1000, Slovenia (e-mail: gorazd.pucihar@fe.uni-lj.si).

*D. Miklavčič is with the Faculty of Electrical Engineering, University of Ljubljana, Ljubljana SI-1000, Slovenia (e-mail: damijan.miklavcic@fe.uni-lj.si).

Color versions of one or more of the figures in this paper are available online at http://ieeexplore.ieee.org.

Digital Object Identifier 10.1109/TBME.2013.2262177

regarding their preparation, storage conditions, and stability under wide temperature and pH ranges. Archaeosomes can cross the intact plasma membrane, and when administrated in moderate dosages *in vitro* or *in vivo*, they generally do not affect the cell viability or animal physiology. Extensive research has focused on archaeosomes as vaccine delivery systems due to their adjuvant properties, though the delivery of other drugs is also considered [33]–[35]. When drug-carrying archaeosomes enter the targeted cells, electroporation with ns pulses could be used to release the drug.

On the contrary, ns pulses can also exhibit lethal effects on cells and tissues, which could result from DNA and nuclear damage, change in the mitochondrial membrane potential, and/or plasma membrane permeabilization [36]. Namely, ns pulses were reported to induce apoptosis or necrosis in cells *in vitro* and tumors *in vivo* [28], [29], [36]–[44]. Whereas treatment with ns pulses appears to be a promising drug-free nonthermal therapy for treating cancer [40], [41], the detrimental effects of ns pulses should be avoided, if we want to use the pulses for drug release from liposomes. For this reason appropriate pulse parameters need to be determined.

In our study, we employed numerical modeling to investigate whether liposome electroporation could be achieved without causing severe damage to the cell and its organelles. Such modeling can also provide us with useful information on how to design the experiments. There are several parameters on which we can influence in experimental settings, such as electric pulse parameters, size of the liposomes, liposome interior conductivity, extracellular medium conductivity, etc. We explored the influence of all these and some other parameters on the ITV and electroporation of the plasma membrane, the nuclear envelope, and membranes of liposomes. By placing the liposomes in various locations inside the cell, we also investigated whether liposomes electroporate differently with respect to their position. Potential risks of ns pulses are discussed and guidelines that might help reduce damaging effects of ns pulses to the cell and its organelles when electroporating liposomes are proposed.

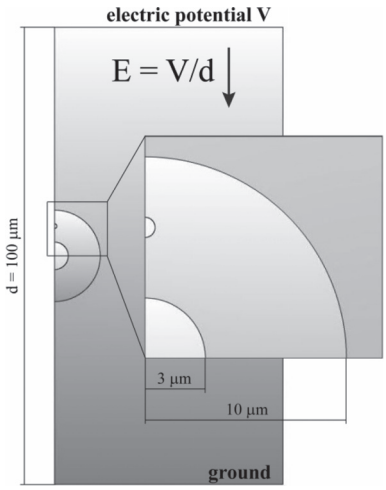

Fig. 1. 2-D axisymmetric model of a cell containing a nucleus and a liposome. The radii of the cell and the nucleus were 10 and 3 μm, respectively. The radius of the liposome was varied from 50 to 500 nm, with the center of the liposome always positioned in the middle between the nuclear envelope and the plasma membrane. The inset shows enlarged view of the cell, nucleus, and liposome.

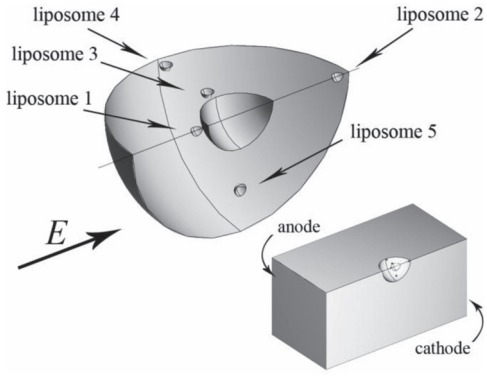

Fig. 2. 3-D model of a cell containing a nucleus and five liposomes. The dimensions of the cell and the nucleus were identical as in Fig. 1. *Bottom*: The cell was placed in the center of a block representing the extracellular medium. Two opposite sides of the block were modeled as electrodes. *Top:* Enlarged view of the intracellular position of the liposomes. The distance from the center of the cell to the center of the liposomes is 4 μm for liposomes 1 and 3, 9 μm for liposomes 2 and 4, and 6.5 μm for liposome 5.

II. Methods

A. Construction of the Model

The finite-element model of a cell containing the nucleus and intracellular liposomes was constructed in COMSOL Multiphysics 4.2a (COMSOL, Burlington, MA, USA). Most calculations were performed with a 2-D axisymmetric model, which is presented in Fig. 1. The axial symmetry of the geometry allowed us to perform calculations in two dimensions, which considerably reduced the calculation time. However, since the liposome position in this model was confined to the left vertical axis of the model, we also constructed a 3-D model with five differently positioned liposomes, shown in Fig. 2, which allowed us to study the influence of liposome position on their electroporation.

The 2-D model was constructed from a rectangle with dimensions 50 μm $\times$ 100 μm representing the extracellular medium, in which a semicircle with radius of 10 μm (the cell) was placed. The cell contained a smaller concentric semicircle with radius of 3 μm representing the nucleus. Another semicircle representing a liposome was positioned in the middle between the plasma membrane and the nuclear envelope with its radius varying between 50 and 500 nm. The boundary condition for the left side of the rectangle was set to *Axial Symmetry*, the right side was modeled as electrically insulated, whereas the upper and the lower sides of the rectangle were modeled as electrodes by assigning them an electric potential. One electrode was set to ground and the other was excited by a single ns pulse. The pulse was obtained by subtracting two Heaviside functions, one being delayed from the other for 4, 10, 20 or 50 ns, using the COMSOL function *flc1hs*. The pulse rise and fall times were set to 1 ns, which is close to the characteristic rise time of some

nanosecond pulse generators [45], [46]. The pulse duration, to which we refer in this paper, is defined as the pulse width at half maximum amplitude. The pulse amplitude was set to a value resulting in a desired electric field between the electrodes, calculated as the potential difference between the electrodes divided by the electrode distance.

For construction of the 3-D model, spheres, and boxes were used instead of circles and rectangles. Also, the cell contained five differently positioned liposomes with radii of 250 nm. Due to the symmetry of the geometry only a quarter of the complete model was used in calculations (see Fig. 2).

Electric potential V in both the 2-D and 3-D model was calculated in the *Electric Currents* application mode of the *AC/DC module* (*Time Dependent Study*) by

$$-\nabla\left(\sigma_i \nabla V\right) - \nabla \frac{\partial\left(\varepsilon_i \nabla V\right)}{\partial t} = 0 \tag{1}$$

where σ_i and ε_i denote the conductivity and dielectric permittivity of a given subdomain, respectively. For each subdomain (extracellular medium, cell, nucleus, and liposomes), a separate application mode of the same type was used, and in each application mode only the corresponding subdomain was activated to calculate V [47], [48].

Plasma membrane, nuclear envelope, and liposome membranes were modeled as the boundary conditions of each of the corresponding application modes by assigning a current density $\boldsymbol{J}$ through the thin shell representing the membrane using *Distributed Impedance* boundary condition [47], [48]

$$\boldsymbol{n} \cdot \boldsymbol{J} = \frac{\sigma_m}{d_m}\left(V - V_{\mathrm{ref}}\right) + \frac{\varepsilon_m}{d_m}\left(\frac{\partial V}{\partial t} - \frac{\partial V_{\mathrm{ref}}}{\partial t}\right). \tag{2}$$

Here, $\boldsymbol{n}$ is the unit vector normal to the surface, V is the electric potential on the interior side of the boundary, V_{ref} is the potential on the exterior side of the boundary, and σ_m, ε_m, and d_m, are the membrane conductivity, membrane dielectric permittivity, and membrane thickness, respectively. The ITV is then calculated as the difference between the electric potentials on each side of the boundary.

Cells also have an intrinsic (resting) membrane voltage of few 10 mV, with the cell interior being negative relative to its exterior. The ITV superimposes onto this voltage, so that the transmembrane voltage at the anodic pole of the cell is slightly higher compared to the voltage at the opposite pole in its absolute value. A slight asymmetry in membrane electroporation across the two poles can, therefore, appear. However, in our calculations, we neglected the influence of the resting potential, as significant electroporation is expected to occur at considerably higher values ($\sim$1 V) compared to the resting voltage and thus the expected asymmetry in electroporation is small [49].

To model membrane electroporation, we included the asymptotic model of electroporation proposed by DeBruin and Krassowska [49]. Although the model in its basic form does not account for pore expansion, it was found to be particularly appropriate for studies of ns pulses, since it is not expected for the pores to expand significantly on such a short time scale [6]. The dynamics of pore formation is described by differential equation

$$\frac{\mathrm{d}N}{\mathrm{d}t} = \alpha \mathrm{e}^{\left(\frac{\mathrm{ITV}}{V_{\mathrm{ep}}}\right)^2}\left(1 - \frac{N}{N_0}\mathrm{e}^{-q\left(\frac{\mathrm{ITV}}{V_{\mathrm{ep}}}\right)^2}\right) \tag{3}$$

where N is the membrane pore density, N_0 the pore density in the nonelectroporated membrane, and α, q, and V_{ep} are electroporation parameters. This equation was incorporated in the model with the *Weak Form Boundary PDE* application mode on all surfaces corresponding to the membranes [48].

The increase in the membrane conductivity due to electroporation was determined as follows:

$$\sigma_{\mathrm{ep}} = \pi r_p^2 \sigma_p N \frac{\mathrm{e}^{\nu_m} - 1}{\frac{w\mathrm{e}^{w-n\nu_m} - n\nu_m}{w - n\nu_m}\mathrm{e}^{\nu_m} - \frac{w\mathrm{e}^{w+n\nu_m} + n\nu_m}{w + n\nu_m}}. \tag{4}$$

Parameters r_p and σ_p are the radius and internal conductivity of a single pore, respectively, and ν_m is the nondimensional transmembrane voltage, given by expression $\nu_m = \mathrm{ITV}{\cdot}F/(R{\cdot}T)$, where F is the Faraday constant, R is the universal gas constant, and T is the temperature. The expression at the end of (4) accounts for the pore shape and the interactions between the pore wall and ions that are passing through the pore [49], [50]. Assuming a toroidal pore, n is the length of pore entrance area, relative to the membrane thickness. Parameter w is the energy cost for moving an ion from a region of high dielectric constant (water) to a small pore in the lipid bilayer with low dielectric constant. The foundation of the electroporation model is described in detail in [49] and references therein.

The total membrane conductivity σ_m was calculated at each time step as the sum of the passive membrane conductivity and the conductivity due to electroporation σ_{ep}. Equations (1)–(4) were solved simultaneously with a linear system solver *MUMPS*.

B. Parameters of the Model

In experiments concerning liposome electroporation, some parameters can be varied. Liposomes can be made of different sizes [51], [52] and can be loaded with a medium of arbitrary conductivity. When performing experiments *in vitro*, the extracellular medium conductivity can also be adjusted. Furthermore, by electroporating the cells with microsecond pulses the conductivity of the plasma membrane can be increased by several orders of magnitude [1], [49] without affecting the membranes of the organelles. If electroporation is performed in a low conductivity medium, the efflux of cytosolic ions reduces the cytoplasmic conductivity [53], [54]. In order to explore, how a change in these parameters could influence the results, we performed calculations for a range of parameter values, given in Table I.

In our calculations, however, we neglected the changes in the extracellular, cytoplasmic, and nucleoplasmic conductivity, which could arise due to electroporation during the pulse application. This is justified since it is not expected for significant transport of ions to occur *during* an ns pulse because of its extremely short duration [55]. Our results are namely based only on exposure during a single pulse.

TABLE I
PARAMETERS OF THE MODEL

Parameter	Symbol	Default value	Range of values
Cell radius	R_c (μm)	10 [a]	
Nuclear radius	R_n (μm)	3 [a]	
Liposome radius	R_{lip} (nm)		50–500 [i]
Plasma membrane thickness	d_{pm} (nm)	5 [a]	
Nuclear envelope thickness	d_{ne} (nm)	10 [b]	
Liposome membrane thickness	d_{lm} (nm)	5 [c]	
Extracellular medium conductivity	σ_e (S·m^{-1})	1.2 [a]	0.01–1.6 [j]
Extracellular medium permittivity	ε_e	72.3 [a]	
Cytoplasmic conductivity	σ_{cp} (S·m^{-1})	0.5 [d]	0.1–1.3 [e]
Cytoplasmic permittivity	ε_{cp}	72.3 [a]	
Plasma membrane conductivity	σ_{pm} (S·m^{-1})	$3\cdot10^{-7}$ [a]	10^{-10}–10^{-4} [d]
Plasma membrane permittivity	ε_{pm}	5 [a]	
Nucleoplasmic conductivity	σ_{np} (S·m^{-1})	1 [e]	$2\cdot\sigma_{cp}$ [e]
Nucleoplasmic permittivity	ε_{np}	72.3 [c]	
Nuclear envelope conductivity	σ_{ne} (S·m^{-1})	$1\cdot10^{-4}$ [f]	
Nuclear envelope permittivity	ε_{ne}	10 [g]	
Liposome interior conductivity	σ_{lip} (S·m^{-1})	0.5 [c]	0.01–2 [k]
Liposome interior permittivity	ε_{lip}	72.3 [c]	
Liposome membrane conductivity	σ_{lm} (S·m^{-1})	$3\cdot10^{-7}$ [c]	
Liposome membrane permittivity	ε_{lm}	2.1 [h]	2–5 [k]
Conductivity of aqueous solution in pores	σ_p (S·m^{-1})	1.3 [d]	
Pore radius	r_p (nm)	0.76 [d]	
Relative entrance length of pores	n	0.15 [d]	
Electroporation constant	q	2.46 [d]	
Electroporation parameter	α (m^{-2}·s^{-1})	10^9 [d]	
Characteristic voltage of electroporation	V_{ep} (V)	0.258 [d]	
Equilibrium pore density	N_0 (m^{-2})	$1.5\cdot10^9$ [d]	
Energy barrier within pore	w	2.65 [d]	
Temperature	T (K)	295 [d]	

[a]From [58].
[b]Set to $2\cdot d_{pm}$.
[c]Set equal to the cytoplasm or the plasma membrane.
[d]From [49].
[e]From [54] and [56].
[f]From [57].
[g]Set between values reported in [56] and [59].
[h]From [6] and [52].
[i]From [51] and [52].
[j]From [60] and [61].
[k]Arbitrary.

According to dielectric spectroscopy measurements of cell electric properties by Polevaya *et al.* [56] and Garner *et al.* [54], the ratio between the nucleoplasmic conductivity $\sigma_{\rm np}$ and the cytoplasmic conductivity $\sigma_{\rm cp}$ is $\sim$2, even if the cytoplasmic conductivity reduces due to electroporation in a low conductivity medium [54]. The same ratio was thus kept when $\sigma_{\rm cp}$ was varied. Although the nuclear envelope is covered with large nuclear pore complexes, experiments have confirmed that the nuclear envelope can actively transport ions [57].

We modeled the nuclear envelope as a boundary condition similarly as the plasma membrane and the liposome membrane. However, the nuclear envelope consists of two membranes separated by a thin perinuclear space filled with electrolyte [57]. For simplicity, we assumed that both membranes have equal electric properties, and that the voltage drop across the perinuclear space is negligible. In this case the voltage equally distributes between both membranes. This allowed us to calculate the ITV across one of the nuclear membranes as half of the ITV across the whole nuclear envelope and apply this value to (3). In short, twice the value of ITV was required for electroporation of the nuclear envelope compared to the plasma membrane or the liposome membrane. Still, in Figs. 3(a) and 5(a), we show only the ITV across one nuclear membrane. The above principle is similar to the one used in [20], where calculations were performed based on a transport lattice approach. The authors modeled the nuclear envelope with three impedances in series; two representing each nuclear membrane and one representing the space between nuclear membranes (we neglected the contribution of the latter).

C. Comparison of Plasma Membrane, Nuclear Envelope, and Liposome Membrane Electroporation

The objective of the parametric study was to find such parameters for electroporation of liposomes that would not result in significant electroporation of the plasma membrane or the nuclear envelope. We varied the pulse amplitude at constant pulse duration and calculated the pore density induced over the membranes at the end of the pulse. If a pore density of $N = 10^{14}$ m^{-2} was reached at the pole of a membrane (the point where it was the highest), the membrane was considered to be electroporated (threshold of significant, i.e., observable electroporation). This value was taken from the model of DeBruin and Krassowska [49], which compared simulations with the experiments of Hibino *et al.* [1]. The pore density of 10^{14} m^{-2} and higher was also used for presenting the areas of significant membrane electroporation in a similar modeling study [62].

D. Model Validation

The time course and spatial distribution of the ITV on the cell membrane and the organelle membrane, if the organelle is positioned in the center of the cell, can be analytically derived using the Laplace equation [58]. The model was validated by comparing the analytical solution for the ITV with numerical calculations obtained in COMSOL Multiphysics. The maximum error for the ITV on the plasma membrane and the organelle membrane (in our case the nuclear envelope or the liposome membranes) was less than 1% for the 2-D and 3-D model. Therefore, we considered our numerical model to be sufficiently accurate for the calculations performed in our study.

III. RESULTS

The model was used to calculate the ITV and the pore density N on the plasma membrane, the nuclear envelope, and the liposome membrane, when the cell is exposed to a single electric pulse of different durations and different amplitudes. A typical example of the time course of ITVs during and shortly after exposure to a 10 ns, 50 kV/cm pulse, as observed at the pole of each membrane, is presented in Fig. 3(a). The first 11 ns in the figure refer to the time during the pulse (including the pulse rise and fall times) and the next 9 ns to the time after the pulse.

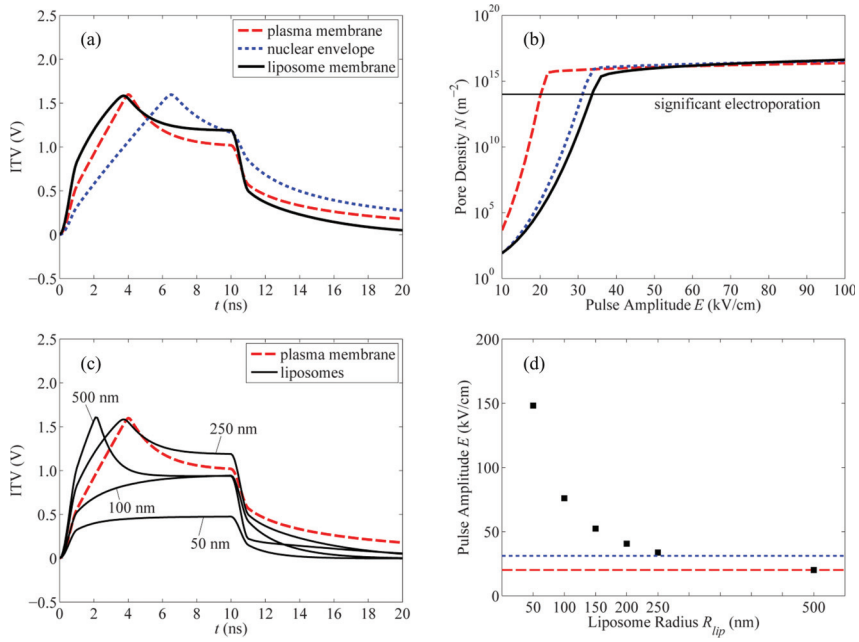

Fig. 3. (a) Time courses of the ITV on the plasma membrane (red dashed line), nuclear envelope (blue dotted line), and liposome membrane (radius 250 nm) (black solid line) for a cell exposed to a 10 ns, 50 kV/cm pulse. The first 11 ns in the figure refer to the time during the pulse (including the pulse rise and fall times) and the next 9 ns to the time after the pulse. (b) Pore density N, calculated at the membrane poles (the points where the normal to the membrane surface is parallel to the direction of the electric field) at the end of a 10 ns pulse for a range of amplitudes from 10 to 100 kV/cm. The color code is the same as in (a). The black horizontal line indicates a pore density of 10^{14} m^{-2}, referred to as significant electroporation. (c) Time courses of the ITV for liposomes with radii of 50, 100, 250, and 500 nm. (d) Amplitudes for which the pore density at the liposome pole, depending on the liposome size, reaches significant electroporation at the end of a 10 ns pulse. The red dashed and blue dotted horizontal lines indicate the pulse amplitudes for significant electroporation of the plasma membrane and the nuclear envelope, respectively.

At the beginning of the pulse, the ITV on the plasma membrane [red dashed line in Fig. 3(a)] and the liposome membrane (black solid line) rise to approximately 1.6 V in few ns and afterward decrease to a lower value. The decrease in the ITV is due to increase in the pore density in the membranes (electroporation), which considerably increases the membrane conductivity and consequently reduces the voltage drop across the membranes. Similar behavior is observed on the nuclear envelope (blue dotted line).

Fig. 3(b) shows the pore density N at the membrane poles at the end of a 10 ns pulse for pulse amplitudes in the range from 10 to 100 kV/cm. To obtain this figure, a series of time courses of ITV for pulse amplitudes in steps of 2 kV/cm were calculated and the values of the pore density at the end of the pulse were extracted. The figure shows that the plasma membrane becomes significantly electroporated (pore density N higher than 10^{14} m^{-2}, see *Methods*) at 20 kV/cm, whereas higher amplitudes, 31 and 34 kV/cm, are needed to electroporate the nucleus and the liposome, respectively.

While Fig. 3(a) and (b) show calculations for a liposome with 250 nm radius, Fig. 3(c) presents the time courses of the ITV for liposomes with radii of 50, 100, 250, and 500 nm, again for a 10 ns, 50 kV/cm pulse. The ITV on the liposome is strongly affected by its size, namely, the ITV on smaller liposomes is significantly lower than on larger liposomes. As a consequence, higher amplitudes are required for electroporation of smaller liposomes, as demonstrated in Fig. 3(d). The red dashed and blue dotted horizontal lines in Fig. 3(d) indicate the amplitudes for significant plasma membrane and nuclear envelope electroporation, respectively.

We then performed a parametric analysis, where we investigated the influence of the pulse duration and electric properties of the cell and the liposomes on the pulse amplitudes required to obtain electroporation. These amplitudes are presented in Fig. 4 as dots. The range of the parameters was taken from the literature and is also presented in Table I.

A brief look at Fig. 4 shows that the pulse duration mostly affects the amplitudes for the plasma membrane and nuclear envelope electroporation, which are shifted toward lower values with longer pulses, whereas the amplitudes for liposome electroporation are less affected regardless of the liposome size. However, liposomes of different size electroporate at different amplitudes. While the amplitude needed to electroporate a 50 nm liposome is usually close to or higher than 150 kV/cm, the amplitude for electroporation of a 500 nm liposome is generally lower than 30 kV/cm.

The amplitudes for plasma membrane, nuclear envelope, and liposome electroporation can, nevertheless, significantly change when varying the values of specific electric parameters. Fig. 4(a)–(d) present the results of calculations for different values of extracellular medium conductivity ($\sigma_e = 0.01$–1.6 S/m). In low conductivity medium, higher amplitudes are required to

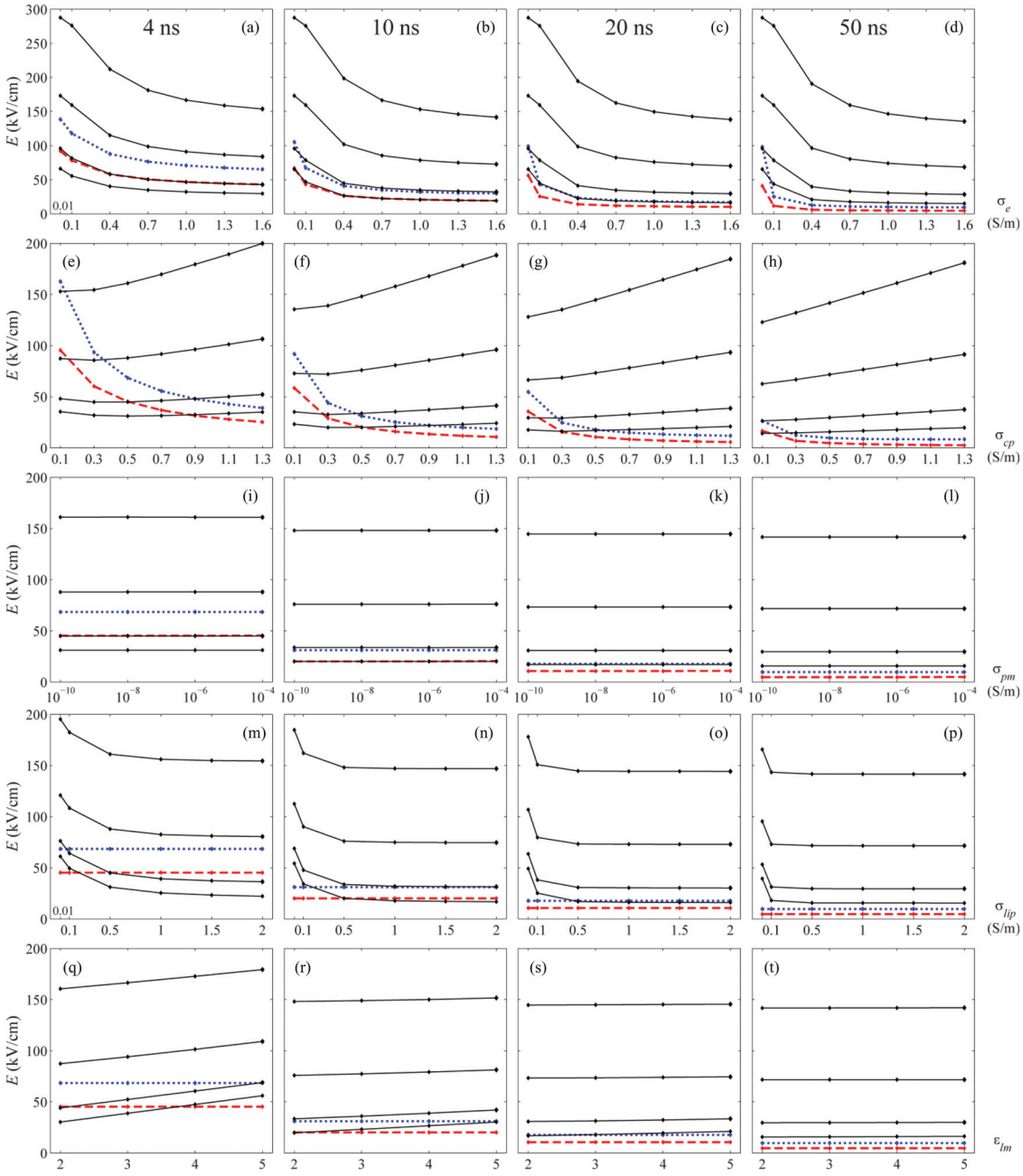

Fig. 4. Amplitudes required for electroporation of the plasma membrane (red dashed line), nuclear envelope (blue dotted line), and liposome membranes (black solid lines). The results are presented for liposomes with radii of 50, 100, 250, and 500 nm. Smaller liposomes are always electroporated at higher amplitudes; thus, the top black solid line refers to the 50 nm liposome and the bottom line to the 500 nm liposome. The pulse duration, for which the results were calculated, is indicated on the top of each column (e.g. Fig. (a), (e), (i), (m), and (q) present results for a 4 ns pulse). In each row an individual parameter was varied, while other parameters were kept at their default values (see Table I).

achieve significant electroporation of all membranes, and this is more pronounced for conductivities below 0.7 S/m.

Fig. 4(e)–(h) show the influence of the cytoplasmic conductivity ($\sigma_{\mathrm{cp}} = 0.1$–$1.3$ S/m) on the amplitude for electroporation. We should note that the nucleoplasmic conductivity (σ_{np}) was also proportionally reduced to obtain a $\sigma_{\mathrm{np}}/\sigma_{\mathrm{cp}}$ ratio of 2, as explained in *Methods*. An increase in σ_{cp} considerably decreases the amplitude needed for electroporation of the plasma membrane and the nuclear envelope, and this is more pronounced with shorter pulses. The amplitudes for liposome electroporation

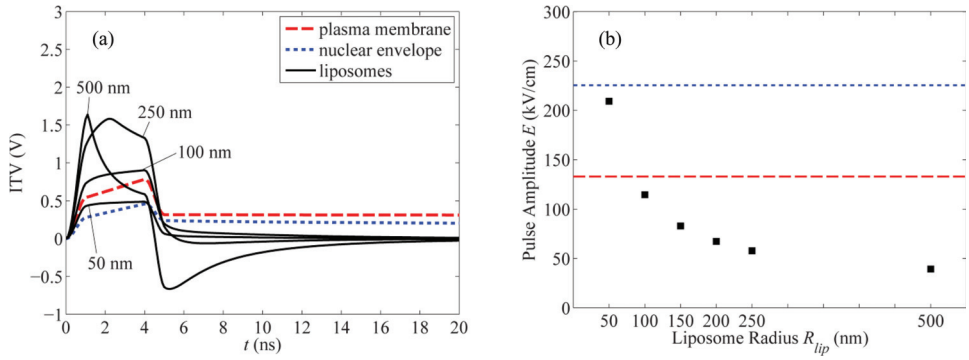

Fig. 5. Calculations for a combination of parameter values that are in favor for liposome electroporation (see text). (a) Time courses of the ITV at the poles of the plasma membrane (red dashed line), nuclear envelope (blue dotted line), and membranes of liposomes with radii of 50, 100, 250, and 500 nm (black solid lines), when the cell is exposed to a 4 ns, 70 kV/cm pulse. (b) Amplitudes for which the pore density at the liposome pole, depending on the liposome size, reaches significant electroporation at the end of a 4 ns pulse. The red dashed and blue dotted horizontal lines indicate the pulse amplitudes for significant electroporation of the plasma membrane and the nuclear envelope, respectively.

take the opposite direction and increase, though to a smaller extent, with the increase of σ_{cp}. This leads to an important observation, namely, that at certain σ_{cp} it is possible to selectively electroporate only liposomes, while the plasma and nuclear membranes remain intact. For example, with 4 ns pulse and with $\sigma_{\mathrm{cp}} = 0.1$ S/m, 50 kV/cm pulse would be enough to electroporate 250 and 500 nm liposomes, while 50 and 100 nm liposomes, as well as the plasma and nuclear membranes, would remain nonelectroporated.

Fig. 4(i)–(l) present the influence of the plasma membrane conductivity ($\sigma_{\mathrm{pm}} = 10^{-10}$–$10^{-4}$ S/m). The calculated amplitudes for electroporation are not affected by σ_{pm}. Similar can be observed also when changing the liposome membrane conductivity (data not shown). However, the sole effect of the pulse duration on the electroporation amplitudes can be clearly seen. With longer pulses, lower pulse amplitudes are needed to obtain electroporation, but this effect is much more pronounced for the plasma and nuclear membranes.

Fig. 4(m)–(p) show the calculations for different values of the liposome interior conductivity ($\sigma_{\mathrm{lip}} = 0.01$–2 S/m). This parameter does not impact the amplitude for electroporation of the plasma membrane or the nuclear envelope. In contrast, if liposomes are filled with a more conductive medium, they electroporate at lower amplitudes. The effect of σ_{lip} is greater for shorter pulses (4 and 10 ns).

Fig. 4(q)–(t) show the influence of the liposome membrane permittivity ($\varepsilon_{\mathrm{lm}} = 2$–5). Similar to liposome interior conductivity, this parameter also influences only the amplitudes for electroporation of the liposomes. Liposomes with lower membrane permittivity electroporate at lower amplitudes. Again, the effect of $\varepsilon_{\mathrm{lm}}$ is greater for shorter pulses (4 and 10 ns), whereas for longer pulses (20 and 50 ns) it becomes diminished.

The aforementioned parametric analysis demonstrated that some parameters have a considerable impact on plasma membrane, nuclear envelope, and liposome electroporation. Therefore, we performed calculations combining parameter values that are in favor for selective liposome electroporation. These are pulse duration 4 ns, $\sigma_{\mathrm{cp}} = 0.1$ S/m, $\sigma_{\mathrm{lip}} = 2$ S/m, $\sigma_{\mathrm{pm}} = 3{\cdot}10^{-7}$ S/m (parameter was left unchanged as it was shown not to affect the results), and $\varepsilon_{\mathrm{lm}} = 2.1$ (parameter was left unchanged as it was already optimal). We also decreased the extracellular medium conductivity to 0.1 S/m as incubation of cells in a medium of low ionic strength could result in a decrease of the cytoplasmic conductivity. Results are shown in Fig. 5. Fig. 5(a) presents the time courses of the ITV on the plasma membrane, the nuclear envelope, and liposomes of different sizes for a 4 ns, 70 kV/cm pulse, and Fig. 5(b) presents the amplitudes required for their electroporation. The dots present the amplitudes for electroporation of liposomes, depending on their radius, while the horizontal lines present the amplitudes for electroporation of the plasma membrane (red dashed line) and the nuclear envelope (blue dotted line). Under such conditions, 100 nm liposomes and larger electroporate at lower amplitudes than the plasma membrane and the nuclear envelope, in contrast to results in Fig. 3(d) where none of the liposomes electroporated below the amplitude for plasma membrane electroporation.

Finally, Fig. 6 presents the influence of the liposome intracellular position on the time courses of the ITV, and pore densities on the plasma membrane and membranes of differently positioned liposomes, when the cell is exposed to a 10 ns, 50 kV/cm pulse. The liposome positioned close to the nuclear pole (liposome 1, see Fig. 2) electroporates at somewhat lower amplitude (31 kV/cm), while other liposomes electroporate between 34 and 37 kV/cm. Although this indicates that the charging of other larger organelles could affect electroporation of nearby liposomes, most of the liposomes would be electroporated at similar amplitudes.

IV. Discussion

A. Appropriate Choice of Pulse Parameters for Electroporation of Liposomes (Avoiding the Cytotoxic Effects of Nanosecond Pulses)

The effects of ns pulses on mammalian cells have been extensively studied in the past decade, since the first experiments performed on human eosinophils showed that ns pulses could electroporate intracellular granules [21]. Subsequent studies further confirmed the initial hypothesis that ns pulses breach

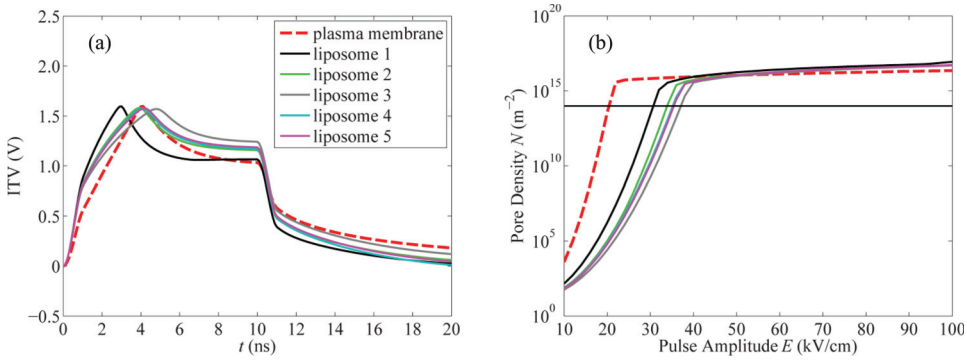

Fig. 6. Influence of the liposome position on liposome electroporation. The arrangement of the liposomes is given in Fig. 2. (a) Time courses of the ITV at the cell and liposome poles for exposure to a 10 ns, 50 kV/cm pulse. (b) Pore density, reached at the cell and liposome poles at the end of a 10 ns pulse for a range of amplitudes from 10 to 100 kV/cm. The color code is the same as in (a). Horizontal line indicates the pore density for significant electroporation (10^{14} m^{-2}).

the plasma membrane, providing a tool for intracellular manipulation [39]. Beside organelle membrane permeabilization [21]–[28], ns pulses were also shown to cause DNA damage, caspase activation, and induction of apoptosis [28], [36]–[41], [63], [64], or profound plasma membrane damage, following long pulse trains, that eventually lead to cell death by necrosis [29], [42]–[44].

The purpose of our study was to explore the possibility of using ns pulses for electroporation of liposomes preloaded with a specific drug for intracellular drug delivery. Liposomes as a drug delivery system provide protection to its content from degradation and increase the uptake of the drug into the targeted cells. However, when the liposomes enter the cells, their cargo must be released for the drug to become effective. Electroporation of liposomes could present a way to control this release. The main objective of such application is to use pulses that effectively electroporate liposomes but cause as little damage as possible to the cell and other cell organelles. For example, is the liposomes are loaded with specific genes, the cell must remain alive after transfection in order to express these genes. Appropriate choice of pulse parameters is thus of high importance.

Using numerical modeling, we found that it takes about 10 to 20 ns to fully charge the liposomes considered in our study, which is the reason why the amplitudes for liposome electroporation do not significantly change when the pulses are longer than 10 ns. On the contrary, the cell and the nucleus need more time to charge (since they are larger than liposomes), so they electroporate at considerably lower amplitudes when exposed to a 50 ns pulse compared to a 10 ns pulse.

Experimental data indicate that the cytotoxic effects of ns pulses increase with increasing pulse duration and pulse amplitude [28], [29], [36]–[44]. As liposomes would electroporate at similar amplitudes for pulse durations, longer than the charging time of liposomes, pulses with duration equal to or shorter than this charging time (∼10 ns) should be used for their electroporation. It is also important to note that the amplitude needed for liposome electroporation strongly depends on their size. According to our calculations, liposomes with radius of 500 nm could be electroporated at ∼20 kV/cm, while 50 nm liposomes require rather high amplitudes, exceeding 150 kV/cm [see Fig. 3(d) and 4]. When using 10 ns pulses, electroporation of liposomes, larger than 100 nm, does not seem challenging with respect to retaining the cell viability. This is in agreement with the results of Ibey and coworkers [44], who demonstrated that exposure of cells to a moderate number of 10 ns pulses with amplitudes of up to 105 kV/cm does not significantly affect the cell survival. Our results indicate that such liposomes would electroporate below 80 kV/cm. Electroporation of 50 nm liposomes, however, appears to be more difficult, as these liposomes would electroporate at ∼150 kV/cm, which could impact the cell survival more profoundly. Ten pulses with such parameters were already shown to decrease the cell survival to ∼50% in Jurkat cells [43], [44]. Nevertheless, the cytotoxic effects of ns pulses vary between different cell lines [29], [42]–[44], [63], [64] with some indications that adherent cell lines are more resistant compared to cells grown in suspension [63], possibly due to a more complex cytoskeleton network [64]. While 10 ns, 150 kV/cm pulses were damaging to Jurkat cells, they only negligibly affected the survival of HeLa cells [44]. Therefore, applying 150 kV/cm pulses may not be detrimental to all cell types [29], [44].

Nevertheless, electroporation with pulses of such high amplitudes would probably also electroporate other larger organelles in the cell interior. We only included the nucleus in our model; however, the endoplasmic reticulum (ER) was also demonstrated as a target of ns pulses. Numerical modeling suggested that observed increases in intracellular calcium levels after ns pulse exposure is due to ER electroporation [20], [65]. Cell death, caused by ns pulse exposure, is dependent on the presence of intracellular calcium, but an increase in the intracellular calcium level itself is not sufficient enough to cause cell death [37]. Namely, intracellular calcium release was detected at pulse amplitudes below observable effect on the cell viability [26]–[28], [37]. The processes, which lead to cell apoptosis, are complex, and it is difficult to predict whether a cell would survive the exposure only based on plasma and organelle membrane electroporation. For this reason, we decided to compare our predicted pulse parameters for liposome electroporation

with experimental data on cell survival after exposure to pulses of similar parameters, in order to evaluate the possibility of the damaging effects on cells, which could arise from liposome electroporation.

B. Selective Electroporation of Liposomes

Some early experimental reports on ns pulses implied that cells organelles could be electroporated without disrupting the plasma membrane. Schoenbach *et al.* [21] reported permeabilization of intracellular granules in human eosinophils after exposure to 3–5 pulses of 60 ns, 36 and 53 kV/cm, while the plasma membrane remained impermeable to fluorescent dye calcein. Chen *et al.* [24] showed nuclear membrane permeabilization in HL-60 cells after a single 10 ns, 65 kV/cm pulse, without detectable uptake of propidium iodide (PI) into the cells. Tekle *et al.* [22] electroporated endocytosed vacuoles in COS-7 cells with one hundred 50 ns, 6.7 kV/cm pulses, while leaving the plasma membrane impermeable to ethidium homodimer.

Although in these experiments plasma membrane electroporation was not detected, modeling studies suggested that pores indeed can form in the plasma membrane, however, they are smaller and appear in larger numbers compared to pores induced by conventional microsecond pulses [6], [20], [58], [62]. This was also confirmed experimentally by showing an increase in plasma membrane conductance using patch-clamp measurements [42], [66], by introducing smaller molecules into the cell (e.g. YO-PRO-1 and Tl^+) while plasma membrane remained impermeable to larger molecules (e.g. PI) [67], [68], and by measuring cell volume changes after exposure to ns pulses in the presence of polyethylene glycol and sugar molecules of different sizes [69]. Indeed, two recent studies by Batista Napotnik *et al.* [23], [25] showed that electroporation of endocytotic vesicles in B16-F1 cells with ten 60 ns, 50 kV/cm pulses, and mitochondrial membrane permeabilization in Jurkat cells with five 4 ns, 100 kV/cm pulses was accompanied by plasma membrane electroporation, detected with PI and YO-PRO-1, respectively.

Nevertheless, a theoretical study by Kotnik and Miklavčič [58] demonstrated that the ITV on the organelle membrane can exceed the ITV on the plasma membrane for some time after the onset of a ns pulse, when the organelle interior conductivity is higher than the cytoplasmic and when the organelle membrane has a lower permittivity or is thicker than the plasma membrane, suggesting that selective electroporation of organelles is possible. If we consider that liposomes are made of pure lipids (membrane permittivity $\sim$2) and that they can be filled with a medium with conductivity substantially higher than the cytoplasmic, liposomes can have the properties required for selective electroporation.

Our results are consistent with these predictions. The model showed that under physiological conditions, selective electroporation is possible for the largest, 500 nm liposomes, but only when using the shortest, 4 ns pulses. Despite the fact that liposomes are an order of magnitude smaller than the cell, they charge considerably faster than the plasma membrane due to smaller liposome size and lower liposome membrane permittivity. The size of the 500 nm liposomes is just enough for their ITV to notably exceed the ITV on the plasma membrane [see Fig. 3(c)]. Therefore, when applying a sufficiently short pulse, they can be electroporated selectively with respect to the plasma membrane. We must note, though, that the pulse rise time plays and important role. For considerably longer pulse rise times than used in our study (1 ns), exceeding of the liposome ITV above the ITV on the plasma membrane would not be observed.

Our calculations further demonstrated that the selectivity for liposome electroporation could be increased by modifying some of the parameters in the model. When liposomes would be filled with a conductive medium (above 1 S/m), 4 ns pulses could also selectively electroporate 250 nm liposomes. Adjusting the liposome interior conductivity is not a difficult task, as liposomes can be filled with a medium of arbitrary conductivity in the process of the liposome preparation. Furthermore, a higher liposome interior conductivity might favor electroporation of liposomes before other vesicles, naturally present in the cell (lysosomes, peroxisomes and endosomes), that are comparable in size. We can assume that most of these vesicles have an internal conductivity similar to the cytoplasmic as they are formed in this space. Still, since the size of the liposome/vesicle is an important factor determining the pulse amplitude for electroporation, vesicles considerably larger than liposomes would probably be always electroporated as well.

Furthermore, a reduction in the cytoplasmic conductivity would lower the threshold for electroporation of the liposomes and increase the threshold for electroporation of the plasma membrane and the nuclear envelope, extending the possibility to selectively electroporate even smaller liposomes with even longer pulses (10 ns). In contrast to liposome interior conductivity, the cytoplasmic conductivity is more difficult to manipulate. One option would be incubating the cells in the presence of a low conductivity medium or even moderately electroporate them using classical electroporation protocols, as this causes efflux of ions from the cytoplasm [53]. Similarly, efflux of cytosolic ions could also occur between application of several ns pulses. In this study, we only considered exposure to a single pulse, whereas in practice usually more than one pulse is applied. Although the transport of ions through electroporated membrane during a ns pulse is not expected to be significant due to extremely short pulse duration [55], notable changes in the conductivity could occur between pulses, when ions would have enough time to diffuse through pores. However, since prolonged incubation of cells in a low conductivity medium is not well tolerated by cells [60], the exposure time of the cells outside their growth medium should be minimized.

Liposomes can also be made from different lipids and some can even have protein molecules incorporated into the liposome membrane. This could affect the effective liposome membrane permittivity, which is the reason why we also investigated this parameter. A lower membrane permittivity decreases the charging time, therefore, a liposome composed of pure lipids might be electroporated at lower amplitudes than a similar sized intracellular organelle, which has proteins incorporated in its membrane, but only when 4 or 10 ns pulses are employed.

Nonetheless, the significant variation in results for different values of the cytoplasmic conductivity, liposome interior

conductivity and liposome membrane permittivity indicate that these parameters should be carefully selected also in numerical modeling.

In addition, we explored the influence of the intracellular liposome position on liposome electroporation. The electric field inside the cell can be locally deformed due to charging of other intracellular organelles. We included the nucleus in our model, which is the largest organelle and could influence the local electric field most profoundly. Indeed, liposome 1, which is positioned close to the nuclear pore, is exposed to somewhat higher electric field compared to other liposomes, and is thus electroporated at lower amplitude. Nevertheless, all liposomes are electroporated in a range of amplitudes from 31 to 37 kV/cm, meaning that their position does not play a major role in electroporation. Consequently, most liposomes of similar size are expected to be electroporated simultaneously and to a similar extent regardless of their position inside the cell.

C. Validity of the Predicted Thresholds for Electroporation

The model, which we used in our study, does account for electroporation, but is still very simplistic compared to the complexity of biological cells. It predicts that detectable electroporation occurs when the ITV reaches $\sim$1 V; however, it was found that the electroporation threshold can vary between different cell lines when either microsecond or nanosecond pulses are applied [42], [70]. Still, it was experimentally confirmed that electroporation of the plasma membrane depends on the membrane charging characteristics also with ns pulses [67]. Therefore, the model gives at least important qualitative information on the plasma membrane and organelle membrane electroporation.

We predicted that significant electroporation occurs when a pore density of 10^{14} m^{-2} is reached in the membrane. One should note, though, that even if we used an order of magnitude lower or higher threshold pore density, in most cases this would not significantly alter the calculated pulse amplitude for electroporation E due to the steep slope of the curve $E(N)$ around 10^{14} m^{-2} [see Fig. 3(b)].

We assumed that the threshold voltage for liposome electroporation is the same as for the plasma membrane. We calculated the amplitude for electroporation of 50 nm liposomes to be $\sim$150 kV/cm when the liposomes are filled with a conductive medium, and $\sim$190 kV/cm, when they are filled with a medium with conductivity of 0.01 S/m [exposure to a 10 ns pulse, Fig. 4(n)]. Tekle *et al.* [22] exposed salt-filled and sucrose-filled liposomes of similar size (median diameter 103 nm) to a single 10 ns pulse of either 80, 160 or 240 kV/cm. They observed that none of the liposomes electroporated at 80 kV/cm, only salt-filled liposomes electroporated at 160 kV/cm, and both salt- and sucrose-filled liposomes electroporated at 240 kV/cm. The liposomes were exposed outside the cell in a low-conductivity sucrose medium, therefore, we cannot directly compare the amplitudes from the experiment with the predicted ones from the model. However, these data qualitatively agree with our calculations and suggest that the predicted amplitudes are not exaggerated.

The parameters, which govern the electroporation process (α, q, N_0, V_{ep}) were assumed to be equal for all membranes, although in practice they can differ for membranes of different composition. Considering that the plasma and the organelle membranes are mostly constituted of phospholipids, it can be expected that these parameters are similar for the plasma membrane and the nuclear envelope. On the contrary, liposomes can also be made of archaeal lipids, which have a different structure compared to phospholipids [33], [34], [51]. This difference in structure might affect pore formation. The threshold voltage for electroporation of such archaeosomes has, to our knowledge, not yet been determined, but some preliminary results from planar lipid bilayer experiments and molecular dynamics simulations indicate, that they require a higher ITV for electroporation (unpublished data). In this case, the amplitudes predicted for electroporation by the model would be an underestimate. Furthermore, the liposomes usually enter the cells by endocytosis [31], [32]. This also appears to be true for archaeosomes [35]. If the plasma membrane was still present around the liposome membrane when exposing the cells to ns pulses, the voltage drop across the liposome membrane would be lower, and again, the calculated amplitudes would be an underestimate. Similarly, higher amplitude would also be required to electroporate multilamellar liposomes. All the above indicate that it is important to carefully optimize the experimental protocol in order to avoid the damaging effects of ns pulses, especially when the drug delivery with very small liposomes (up to 200 nm in diameter) would be unavoidable, e.g., in the case of intravenous administration of liposomes, when liposomes need to be sufficiently small to be able to cross the vascular endothelium wall [32].

V. Conclusion

Overall, our model suggests two important factors for successful optimization of liposome drug delivery with ns pulses. The first is the pulse duration and the second is the liposome size. Using both shorter pulses and larger liposomes would increase the possibility of selective electroporation of liposomes with respect to other intracellular organelles and the cell itself, and consequently present a smaller risk for compromising the cell viability after the treatment. Liposomes that have a higher internal conductivity and lower membrane permittivity compared to other similar-sized organelles could be favorably electroporated, but only when the pulses are few nanoseconds long.

There is, however, one drawback of using very short pulses for drug delivery. The small size of pores induced by ns pulses ($\sim$1 nm [69]), which allows the permeation of only small ions and molecules, could prevent the release of larger molecules or macromolecules (e.g., siRNA) from the liposomes. Nevertheless, a recent experimental study on Chinese hamster lung cells showed that a small population of larger pores may also form in the plasma membrane during exposure to a single 10 ns, 40 kV/cm pulse, which allowed the passage of at least 500 molecules of bleomycin [71]. Furthermore, a single 10 ns pulse was efficient enough to translocate siRNA into giant unilamellar vesicles [72]. The accompanying molecular dynamics

simulations demonstrated how a complete translocation of the siRNA molecule can occur on such short time scales.

Based on our calculations and other experimental data, we can conclude that with appropriately adjusted pulse parameters, nanosecond pulses have the potential to be used as a tool for controlled drug release from intracellular liposomes. This study should serve as a guideline for further experiments in this area.

REFERENCES

[1] M. Hibino, M. Shigemori, H. Itoh, K. Nagayama, and K. Kinosita Jr, "Membrane conductance of an electroporated cell analyzed by submicrosecond imaging of transmembrane potential," *Biophys. J.*, vol. 59, no. 1, pp. 209–220, Jan. 1991.

[2] T. Kotnik, G. Pucihar, and D. Miklavčič, "Induced transmembrane voltage and its correlation with electroporation-mediated molecular transport," *J. Membr. Biol.*, vol. 236, no. 1, pp. 3–13, Jul. 2010.

[3] T. Y. Tsong, "Electroporation of cell membranes," *Biophys. J.*, vol. 60, no. 2, pp. 297–306, Aug. 1991.

[4] J. Teissié and M. P. Rols, "An experimental evaluation of the critical potential difference inducing cell membrane electropermeabilization," *Biophys. J.*, vol. 65, no. 1, pp. 409–413, Jul. 1993.

[5] E. Neumann, M. Schaefer-Ridder, Y. Wang, and P. H. Hofschneider, "Gene transfer into mouse lyoma cells by electroporation in high electric fields," *EMBO J.*, vol. 1, no. 7, pp. 841–845, 1982.

[6] Z. Vasilkoski, A. T. Esser, T. R. Gowrishankar, and J. C. Weaver, "Membrane electroporation: The absolute rate equation and nanosecond time scale pore creation," *Phys. Rev. E*, vol. 74, no. 2, pp. 021904-1–021904-12, Aug. 2006.

[7] A. A. Gurtovenko, J. Anwar, and I. Vattulainen, "Defect-mediated trafficking across cell membranes: Insights from in silico modeling," *Chem. Rev.*, vol. 110, no. 10, pp. 6077–6103, Oct. 2010.

[8] L. Delemotte and M. Tarek, "Molecular dynamics simulations of lipid membrane electroporation," *J. Membr. Biol.*, vol. 245, no. 9, pp. 531–543, Sep. 2012.

[9] U. Zimmermann, P. Gessner, R. Schnettler, S. Perkins, and S. K. Foung, "Efficient hybridization of mouse-human cell lines by means of hypoosmolar electrofusion," *J. Immunol. Methods*, vol. 134, no. 1, pp. 43–50, Nov. 1990.

[10] M. Ušaj and M. Kandušer, "The systematic study of the electroporation and electrofusion of B16-F1 and CHO cells in isotonic and hypotonic buffer," *J. Membr. Biol.*, vol. 245, no. 9, pp. 583–590, Sep. 2012.

[11] R. Heller, M. J. Jaroszeski, D. S. Reintgen, C. A. Puleo, R. C. DeConti, R. A. Gilbert, and L. F. Glass, "Treatment of cutaneous and subcutaneous tumors with electrochemotherapy using intralesional bleomycin," *Cancer*, vol. 83, no. 1, pp. 148–157, Jul. 1998.

[12] L. M. Mir, J. Gehl, G. Serša, C. G. Collins, J.-R. Garbay, V. Billard, P. F. Geertsen, Z. Rudolf, G. C. O'Sullivan, and M. Marty, "Standard operating procedures of the electrochemotherapy: Instructions for the use of bleomycin or cisplatin administered either systemically or locally and electric pulses delivered by the Cliniporator^{TM} by means of invasive or non-invasive electrodes," *Eur. J. Cancer Suppl.*, vol. 4, no. 11, pp. 14–25, Nov. 2006.

[13] G. Serša, T. Čufer, S. M. Paulin, M. Čemažar, and M. Snoj, "Electrochemotherapy of chest wall breast cancer recurrence," *Cancer Treat. Rev.*, vol. 38, no. 5, pp. 379–386, Aug. 2012.

[14] J. Teissié, J. M. Escoffre, A. Paganin, S. Chabot, E. Bellard, L. Wasungu,, M. P. Rols, and M. Golzio, "Drug delivery by electropulsation: Recent developments in oncology," *Int. J. Pharm.*, vol. 423, no. 1, pp. 3–6, Feb. 2012.

[15] M. Bettan, M. A. Ivanov, L. M. Mir, F. Boissière, P. Delaere, and D. Scherman, "Efficient DNA electrotransfer into tumors," *Bioelectrochemistry*, vol. 52, no. 1, pp. 83–90, Sep. 2000.

[16] M. Kandušer, D. Miklavčič, and M. Pavlin, "Mechanisms involved in gene electrotransfer using high- and low-voltage pulses-an in vitro study," *Bioelectrochemistry*, vol. 74, no. 2, pp. 265–271, Feb. 2009.

[17] J. M. Escoffre, T. Portet, C. Favard, J. Teissié, D. S. Dean, and M. P. Rols, "Electromediated formation of DNA complexes with cell membranes and its consequences for gene delivery," *Biochim. Biophys. Acta*, vol. 1808, no. 6, pp. 1538–1543, Jun. 2011.

[18] N. J. Rowan, S. J. MacGregor, J. G. Anderson, R. A. Fouracre, and O. Farish, "Pulsed electric field inactivation of diarrhoeagenic Bacillus cereus through irreversible electroporation," *Lett. Appl. Microbiol.*, vol. 31, no. 2, pp. 110–114, Aug. 2000.

[19] S. Toepfl, V. Heinz, and D. Knorr, "High intensity pulsed electric fields applied for food preservation," *Chem. Eng. Process.: Process Intensif.*, vol. 46, no. 6, pp. 537–546, Jun. 2007.

[20] T. R. Gowrishankar, A. T. Esser, Z. Vasilkoski, K. C. Smith, and J. C. Weaver, "Microdosimetry for conventional and supra-electroporation in cells with organelles," *Biochem. Biophys. Res. Commun.*, vol. 341, no. 4, pp. 1266–1276, Mar. 2006.

[21] K. H. Schoenbach, S. J. Beebe, and E. S. Buescher, "Intracellular effect of ultrashort electrical pulses," *Bioelectromagnetics*, vol. 22, no. 6, pp. 440–448, Sep. 2001.

[22] E. Tekle, H. Oubrahim, S. M. Dzekunov, J. F. Kolb, K. H. Schoenbach, and P. B. Chock, "Selective field effects on intracellular vacuoles and vesicle membranes with nanosecond electric pulses," *Biophys. J.*, vol. 89, no. 1, pp. 274–284, Jul. 2005.

[23] T. Batista Napotnik, M. Reberšek, T. Kotnik, E. Lebrasseur, G. Cabodevila, and D. Miklavčič, "Electropermeabilization of endocytotic vesicles in B16 F1 mouse melanoma cells," *Med. Biol. Eng. Comput.*, vol. 48, no. 5, pp. 407–413, May 2010.

[24] N. Chen, K. H. Schoenbach, J. F. Kolb, R. J. Swanson, A. L. Garner, J. Yang, R. P. Joshi, and S. J. Beebe, "Leukemic cell intracellular responses to nanosecond electric fields," *Biochem. Biophys. Res. Commun.*, vol. 317, no. 2, pp. 421–427, Apr. 2004.

[25] T. Batista Napotnik, Y. H. Wu, M. A. Gundersen, D. Miklavčič, and P. T. Vernier, "Nanosecond electric pulses cause mitochondrial membrane permeabilization in Jurkat cells," *Bioelectromagnetics*, vol. 33, no. 3, pp. 257–264, Apr. 2012.

[26] P. T. Vernier, Y. Sun, L. Marcu, S. Salemi, C. M. Craft, and M. A. Gundersen, "Calcium bursts induced by nanosecond electric pulses," *Biochem. Biophys. Res. Commun.*, vol. 310, no. 2, pp. 286–295, Oct. 2003.

[27] S. S. Scarlett, J. A. White, P. F. Blackmore, K. H. Schoenbach, and J. F. Kolb, "Regulation of intracellular calcium concentration by nanosecond pulsed electric fields," *Biochim. Biophys. Acta*, vol. 1788, no. 5, pp. 1168–1175, May 2009.

[28] S. J. Beebe, J. White, P. F. Blackmore, Y. Deng, K. Somers, and K. H. Schoenbach, "Diverse effects of nanosecond pulsed electric fields on cells and tissues," *DNA Cell Biol.*, vol. 22, no. 12, pp. 785–796, Dec. 2003.

[29] A. G. Pakhomov, A. Phinney, J. Ashmore, K. Walker, J. F. Kolb, S. Kono, K. H. Schoenbach, and M. R. Murphy, "Characterization of the cytotoxic effect of high-intensity, 10-ns duration electrical pulses," *IEEE Trans. Plasma Sci.*, vol. 32, no. 4, pp. 1579–1586, Aug. 2004.

[30] J. Song, R. P. Joshi, and K. H. Schoenbach, "Synergistic effects of local temperature enhancements on cellular responses in the context of high-intensity, ultrashort electric pulses," *Med. Biol. Eng. Comput.*, vol. 49, no. 6, pp. 713–718, Jun. 2011.

[31] H. Hillaireau and P. Couvreur, "Nanocarriers' entry into the cell: relevance to drug delivery," *Cell. Mol. Life Sci.*, vol. 66, no. 17, pp. 2873–2896, Sep. 2009.

[32] L. Huang and Y. Liu, "*In vivo* delivery of RNAi with lipid-based nanoparticles," *Annu. Rev. Biomed. Eng.*, vol. 13, pp. 507–530, Aug. 2011.

[33] T. Benvegnu, L. Lemiègre, and S. Cammas-Marion, "New generation of liposomes called archaeosomes based on natural or synthetic archaeal lipids as innovative formulations for drug delivery," *Recent. Pat. Drug Del. Formul.*, vol. 3, no. 3, pp. 206–220, Nov. 2009.

[34] G. B. Patel and W. Chen, "Archaeosomes as drug and vaccine nanodelivery systems," in *Nanocarrier Technologies*, M. R. Mozafari, Ed. Dordrecht, the Netherlands: Springer-Verlag, 2006, pp. 17–40.

[35] G. D. Sprott, S. Sad, L. P. Fleming, C. J. Dicaire, G. B. Patel, and L. Krishnan, "Archaeosomes varying in lipid composition differ in receptor-mediated endocytosis and differentially adjuvant immune responses to entrapped antigen," *Archaea*, vol. 1, no. 3, pp. 151–164, Oct. 2003.

[36] S. J. Beebe, P. M. Fox, L. J. Rec, K. Somers, R. H. Stark, and K. H. Schoenbach, "Nanosecond pulsed electric field (nsPEF) effects on cells and tissues: Apoptosis induction and tumor growth inhibition," *IEEE Trans. Plasma Sci.*, vol. 30, no. 1, pp. 286–292, Feb. 2002.

[37] S. Beebe, N. Sain, and W. Ren, "Induction of cell death mechanisms and apoptosis by nanosecond pulsed electric fields (nsPEFs)," *Cells*, vol. 2, no. 1, pp. 136–162, Mar. 2013.

[38] E. H. Hall, K. H. Schoenbach, and S. J. Beebe, "Nanosecond pulsed electric fields induce apoptosis in p53-wildtype and p53-null HCT116 colon carcinoma cells," *Apoptosis*, vol. 12, no. 9, pp. 1721–1731, Sep. 2007.

[39] K. Schoenbach, B. Hargrave, R. Joshi, J. Kolb, R. Nuccitelli, C. Osgood, A. Pakhomov, M. Stacey, R. Swanson, J. White, S. Xiao, J. Zhang, S. Beebe, P. Blackmore, and E. Buescher, "Bioelectric effects of intense nanosecond pulses," *IEEE Trans. Dielectr. Electr. Insul.*, vol. 14, no. 5, pp. 1088–1109, Oct. 2007.

[40] R. Nuccitelli, X. Chen, A. G. Pakhomov, W. H. Baldwin, S. Sheikh, J. L. Pomicter, W. Ren, C. Osgood, R. J. Swanson, J. F. Kolb, S. J. Beebe, and K. H. Schoenbach, "A new pulsed electric field therapy for melanoma disrupts the tumor's blood supply and causes complete remission without recurrence," *Int. J. Cancer*, vol. 125, no. 2, pp. 438–445, Jul. 2009.

[41] R. Nuccitelli, K. Tran, S. Sheikh, B. Athos, M. Kreis, and P. Nuccitelli, "Optimized nanosecond pulsed electric field therapy can cause murine malignant melanomas to self-destruct with a single treatment," *Int. J. Cancer*, vol. 127, no. 7, pp. 1727–1736, Oct. 2010.

[42] A. G. Pakhomov, R. Shevin, J. A. White, J. F. Kolb, O. N. Pakhomova, R. P. Joshi, and K. H. Schoenbach, "Membrane permeabilization and cell damage by ultrashort electric field shocks," *Arch. Biochem. Biophys.*, vol. 465, no. 1, pp. 109–118, Sep. 2007.

[43] B. L. Ibey, A. G. Pakhomov, B. W. Gregory, V. A. Khorokhorina, C. C. Roth, M. A. Rassokhin, J. A. Bernhard, G. J. Wilmink, and O. N. Pakhomova, "Selective cytotoxicity of intense nanosecond-duration electric pulses in mammalian cells," *Biochim. Biophys. Acta*, vol. 1800, no. 11, pp. 1210–1219, Nov. 2010.

[44] B. L. Ibey, C. C. Roth, A. G. Pakhomov, J. A. Bernhard, G. J. Wilmink, and O. N. Pakhomova, "Dose-dependent thresholds of 10-ns electric pulse induced plasma membrane disruption and cytotoxicity in multiple cell lines," *PLoS ONE*, vol. 6, no. 1, pp. e15642-1–e15642-11, 2011.

[45] J. F. Kolb, S. Kono, and K. H. Schoenbach, "Nanosecond pulsed electric field generators for the study of subcellular effects," *Bioelectromagnetics*, vol. 27, no. 3, pp. 172–187, Apr. 2006.

[46] J. Sanders, A. Kuthi, Y. H. Wu, P. Vernier, and M. Gundersen, "A linear, single-stage, nanosecond pulse generator for delivering intense electric fields to biological loads," *IEEE Trans. Dielectr. Electr. Insul.*, vol. 16, no. 4, pp. 1048–1054, Aug. 2009.

[47] G. Pucihar, T. Kotnik, B. Valič, and D. Miklavčič, "Numerical determination of transmembrane voltage induced on irregularly shaped cells," *Ann. Biomed. Eng.*, vol. 34, no. 4, pp. 642–652, Apr. 2006.

[48] G. Pucihar, D. Miklavčič, and T. Kotnik, "A time-dependent numerical model of transmembrane voltage inducement and electroporation of irregularly shaped cells," *IEEE Trans. Biomed. Eng.*, vol. 56, no. 5, pp. 1491–1501, May 2009.

[49] K. A. DeBruin and W. Krassowska, "Modeling electroporation in a single cell. I. Effects Of field strength and rest potential," *Biophys. J.*, vol. 77, no. 3, pp. 1213–1224, Sep. 1999.

[50] R. W. Glaser, S. L. Leikin, L. V. Chernomordik, V. F. Pastushenko, and A. I. Sokirko, "Reversible electrical breakdown of lipid bilayers: Formation and evolution of pores," *Biochim. Biophys. Acta*, vol. 940, no. 2, pp. 275–287, May 1988.

[51] D. Gmajner, P. Ahlin Grabnar, M. Žnidarič Tušek, J. Štrus, M. Šentjurc, and N. Poklar Ulrih, "Structural characterization of liposomes made of di-ether archaeal lipids and dipalmitoyl-L-α-phosphatidylcholine," *Biophys. Chem.*, vol. 158, no. 2–3, pp. 150–156, Oct. 2011.

[52] A. Di Biasio and C. Cametti, "Dielectric properties of aqueous zwitterionic liposome suspensions," *Bioelectrochemistry*, vol. 70, no. 2, pp. 328–334, May 2007.

[53] M. Pavlin, M. Kandušer, M. Reberšek, G. Pucihar, F. X. Hart, R. Magjarević, and D. Miklavčič, "Effect of cell electroporation on the conductivity of a cell suspension," *Biophys. J.*, vol. 88, no. 6, pp. 4378–4390, Jun. 2005.

[54] A. L. Garner, G. Chen, N. Chen, V. Sridhara, J. F. Kolb, R. J. Swanson, S. J. Beebe, R. P. Joshi, and K. H. Schoenbach, "Ultrashort electric pulse induced changes in cellular dielectric properties," *Biochem. Biophys. Res. Commun.*, vol. 362, no. 1, pp. 139–144, Oct. 2007.

[55] K. C. Smith and J. C. Weaver, "Transmembrane molecular transport during versus after extremely large, nanosecond electric pulses," *Biochem. Biophys. Res. Commun.*, vol. 412, no. 1, pp. 8–12, Aug. 2011.

[56] Y. Polevaya, I. Ermolina, M. Schlesinger, B. Z. Ginzburg, and Y. Feldman, "Time domain dielectric spectroscopy study of human cells—Part II: Normal and malignant white blood cells," *Biochim. Biophys. Acta*, vol. 1419, no. 2, pp. 257–271, Jul. 1999.

[57] M. Mazzanti, J. O. Bustamante, and H. Oberleithner, "Electrical dimension of the nuclear envelope," *Physiol. Rev.*, vol. 81, no. 1, pp. 1–19, Jan. 2001.

[58] T. Kotnik and D. Miklavčič, "Theoretical evaluation of voltage inducement on internal membranes of biological cells exposed to electric fields," *Biophys. J.*, vol. 90, no. 2, pp. 480–491, Jan. 2006.

[59] A. Irimajiri, K. Asami, T. Ichinowatari, and Y. Kinoshita, "Passive electrical properties of the membrane and cytoplasm of cultured rat basophil leukemia cells—Part II: Effects of osmotic perturbation," *Biochim. Biophys. Acta*, vol. 896, no. 2, pp. 214–223, Jan. 1987.

[60] V. L. Sukhorukov, R. Reuss, D. Zimmermann, C. Held, K. J. Müller, M. Kiesel, P. Gessner, A. Steinbach, W. A. Schenk, E. Bamberg, and U. Zimmermann, "Surviving high-intensity field pulses: Strategies for improving robustness and performance of electrotransfection and electrofusion," *J. Membr. Biol.*, vol. 206, no. 3, pp. 187–201, Aug. 2005.

[61] G. Pucihar, T. Kotnik, M. Kandušer, and D. Miklavčič, "The influence of medium conductivity on electropermeabilization and survival of cells in vitro," *Bioelectrochemistry*, vol. 54, no. 2, pp. 107–115, Nov. 2001.

[62] K. C. Smith and J. C. Weaver, "Active mechanisms are needed to describe cell responses to submicrosecond, megavolt-per-meter pulses: cell models for ultrashort pulses," *Biophys. J.*, vol. 95, no. 4, pp. 1547–1563, Aug. 2008.

[63] M. Stacey, J. Stickley, P. Fox, V. Statler, K. Schoenbach, S. J. Beebe, and S. Buescher, "Differential effects in cells exposed to ultra-short, high intensity electric fields: Cell survival, DNA damage, and cell cycle analysis," *Mutat. Res.*, vol. 542, no. 1–2, pp. 65–75, Dec. 2003.

[64] M. Stacey, P. Fox, S. Buescher, and J. Kolb, "Nanosecond pulsed electric field induced cytoskeleton, nuclear membrane and telomere damage adversely impact cell survival," *Bioelectrochemistry*, vol. 82, no. 2, pp. 131–134, Oct. 2011.

[65] R. P. Joshi, A. Nguyen, V. Sridhara, Q. Hu, R. Nuccitelli, S. J. Beebe, J. Kolb, and K. H. Schoenbach, "Simulations of intracellular calcium release dynamics in response to a high-intensity, ultrashort electric pulse," *Phys. Rev. E*, vol. 75, no. 4, pp. 041920-1–041920-10, Apr. 2007.

[66] B. L. Ibey, D. G. Mixon, J. A. Payne, A. Bowman, K. Sickendick, G. J. Wilmink, W. P. Roach, and A. G. Pakhomov, "Plasma membrane permeabilization by trains of ultrashort electric pulses," *Bioelectrochemistry*, vol. 79, no. 1, pp. 114–121, Aug. 2010.

[67] P. T. Vernier, Y. Sun, and M. A. Gundersen, "Nanoelectropulse-driven membrane perturbation and small molecule permeabilization," *BMC Cell Biol.*, vol. 7, pp. 37-1–37-16, 2006.

[68] A. M. Bowman, O. M. Nesin, O. N. Pakhomova, and A. G. Pakhomov, "Analysis of plasma membrane integrity by fluorescent detection of Tl^+ uptake," *J. Membr. Biol.*, vol. 236, no. 1, pp. 15–26, Jul. 2010.

[69] O. M. Nesin, O. N. Pakhomova, S. Xiao, and A. G. Pakhomov, "Manipulation of cell volume and membrane pore comparison following single cell permeabilization with 60- and 600-ns electric pulses," *Biochim. Biophys. Acta*, vol. 1808, no. 3, pp. 792–801, Mar. 2011.

[70] M. Čemažar, T. Jarm, D. Miklavčič, A. Maček Lebar, A. Ihan, N. A. Kopitar, and G. Serša, "Effect of electric-field intensity on electropermeabilization and electrosensitivity of various tumor-cell lines in vitro," *Electro. Magnetobiol.*, vol. 17, no. 2, pp. 263–272, Jan. 1998.

[71] A. Silve, I. Leray, and L. M. Mir, "Demonstration of cell membrane permeabilization to medium-sized molecules caused by a single 10 ns electric pulse," *Bioelectrochemistry*, vol. 87, pp. 260–264, Oct. 2012.

[72] M. Breton, L. Delemotte, A. Silve, L. M. Mir, and M. Tarek, "Transport of siRNA through lipid membranes driven by nanosecond electric pulses: an experimental and computational study," *J. Amer. Chem. Soc.*, vol. 134, no. 34, pp. 13938–13941, Aug. 2012.

Authors, photographs and biographies not available at the time of publication.

Paper 3

Title: **Cell electrofusion using nanosecond electric pulses**

Authors: Lea Rems, Marko Ušaj, Maša Kandušer, Matej Reberšek, Damijan Miklavčič, and Gorazd Pucihar

Publication: Sci. Rep. 3: 3382, 2013
DOI: 10.1038/srep03382

Journal information

SCIENTIFIC REPORTS		
Publisher	NATURE PUBLISHING GROUP, MACMILLAN BUILDING, 4 CRINAN ST, LONDON N1 9XW, ENGLAND	
ISSN eISSN	2045-2322	
Research domain	Science & Technology - Other Topics	
Impact factor	5.578 (2014) 5.597 (5 year)	
JCR® category	Rank in category	Quartile in category
MULTIDISCIPLINARY SCIENCES	5 of 57	Q1

Source: Web of Science™ (December 2015)

Author contributions of L. Rems

L. Rems contributed to the design of the study, constructed the numerical models, performed numerical calculations and analyzed the results, contributed to the design of experiments, performed the experiments and analyzed the experimental data, contributed to the interpretation of the results and wrote most of the manuscript.

SCIENTIFIC REPORTS

OPEN

SUBJECT AREAS:
ANTIBODY GENERATION
COMPUTATIONAL MODELS
BIOPHYSICAL METHODS
BIOMEDICAL ENGINEERING

Received
12 June 2013

Accepted
13 November 2013

Published
29 November 2013

Correspondence and requests for materials should be addressed to D.M. (damijan.miklavcic@fe.uni-lj.si)

* These authors contributed equally to this work.

Cell electrofusion using nanosecond electric pulses

Lea Rems*, Marko Ušaj*, Maša Kandušer, Matej Reberšek, Damijan Miklavčič & Gorazd Pucihar

University of Ljubljana, Faculty of Electrical Engineering, Tržaška cesta 25, SI-1000 Ljubljana, Slovenia.

Electrofusion is an efficient method for fusing cells using short-duration high-voltage electric pulses. However, electrofusion yields are very low when fusion partner cells differ considerably in their size, since the extent of electroporation (consequently membrane fusogenic state) with conventionally used microsecond pulses depends proportionally on the cell radius. We here propose a new and innovative approach to fuse cells with shorter, nanosecond (ns) pulses. Using numerical calculations we demonstrate that ns pulses can induce selective electroporation of the contact areas between cells (i.e. the target areas), regardless of the cell size. We then confirm experimentally on B16-F1 and CHO cell lines that electrofusion of cells with either equal or different size by using ns pulses is indeed feasible. Based on our results we expect that ns pulses can improve fusion yields in electrofusion of cells with different size, such as myeloma cells and B lymphocytes in hybridoma technology.

Cell fusion is of interest not only as an essential process in cell biology, but also as a useful method in biotechnology and medicine. Artificially induced fusion can be used to investigate and treat different diseases, like diabetes[1–3], regenerate axons of the central nerve system[4], and produce cells with desired properties, such as in cell vaccines for cancer immunotherapy[5–7]. However, the first and most known application of cell fusion is production of monoclonal antibodies in hybridoma technology, where hybrid cell lines (hybridomas) are formed by fusing specific antibody-producing B lymphocytes with a myeloma (B lymphocyte cancer) cell line[8,9]. Myeloma cells were selected for their ability to grow in culture, since B lymphocytes do not survive outside their natural environment.

Initially, in hybridoma technology polyethylene glycol (PEG) was used for cell fusion, and in some laboratories it is still the most preferable fusogen[10]. Nevertheless, cell fusion based on cell membrane electroporation – electrofusion – was suggested as a more efficient technique[11–13]. Electrofusion in comparison to PEG fusion improved not only the number of fused cells obtained (i.e. fusion yield), but also the hybridoma growing rate; electrofused cells grew more vigorously than the ones fused with PEG[11]. Electrofusion also holds great promise for the use of hybridomas in clinical environment, since the method does not require viral or chemical additives.

By definition, electrofusion is a two-condition process: (i) close physical contact between cells has to be established, and (ii) cell membranes have to be brought into fusogenic state[14]. A physical contact between cells can be achieved in various ways, though the most widely used is dielectrophoresis, where cells are aligned in pearl chains using alternating electric field[15]. Dielectrophoresis is most frequently used especially in the field of hybridoma technology and production of cell vaccines, since it enables establishing contacts between cells in suspension.

The second condition for electrofusion, the membrane fusogenic state, is achieved by electric pulse application resulting in structural rearrangement of the lipid bilayer. It is generally accepted that the transmembrane voltage, which is induced on the cell membrane during exposure to high electric fields, reduces the energy barrier for formation of hydrophilic pores in the lipid bilayer[16], although other explanations are also plausible[17]. The phenomenon is termed electroporation and is related to experimentally observed dramatic increase in membrane permeability[16,17]. At the same time, membrane fusogenicity correlates with electroporation[18]. Both, the extent of electroporation and the fusion yield, can be controlled by the amplitude, duration, and number of the applied pulses; namely, increasing any of the pulse parameters mentioned leads to a higher level of membrane electroporation and consequently higher number of fused cells[18]. However, parameters of the electric pulses must be carefully chosen as to ensure that electroporation is reversible, i.e., cells survive. Failing to respect this leads to irreversible cell electroporation, thereby reducing cell survival and consequently reducing the yield of viable fused cells.

At a given electric field strength the extent of membrane electroporation further depends on the cell size[16,19]. One of the major advantages of electrofusion is the possibility of optimizing electroporation conditions for each

cell line individually. Unfortunately, there is a substantial challenge in fusing cell lines that differ considerably in their size. Electric pulses that are usually used for electrofusion range from 10 to 100 μs, which ensures that cell membranes become fully charged during their exposure to electric pulse. Under such conditions, the induced transmembrane voltage is proportional to the cell radius, which means that small cells are electroporated (i.e. brought into fusogenic state) at higher electric field strengths[19]. Applying pulses that effectively electroporate small cells, thus inevitably leads to excessive electroporation and consequently death of large fusion partner cells. An example where a difference in cell size hinders the optimization of pulse parameters is also hybridoma technology, since B lymphocytes (approximate radius of human B lymphocytes corresponds to 3.85 ± 0.35 μm) are considerably smaller than myeloma cells (approximate radii of human and mouse NS1 cells correspond to 5.25 ± 0.25 μm and 7.75 ± 0.25 μm, respectively)[20].

In the past, the problem of obtaining viable hybridomas by means of electrofusion was addressed using different approaches. A very promising one, the pulse-first electrofusion protocol, was proposed by Teissié and co-workers[14,21]. In their protocol cells are first electroporated and then the contact between cells is established. The advantage of the pulse-first protocol is the possibility to separately electroporate fusion partners that require different electric pulse parameters[14]. However, the pulse first protocol did not gain much attention in hybridoma technology, since it seems to be limited to very specific conditions, as demonstrated recently[22]. Another approach for increasing the number of viable hybridomas was to increase the concentration of myeloma cells in the samples. Experiments conducted by Yu and co-workers suggested that a myeloma cell to B lymphocyte cell ratio of 2 : 1 is the most efficient[13]. Zimmermann and co-workers yet used a different approach, where they performed as gentle electroporation as possible, in order to minimize the stress exerted on large cells, but at the same time achieve sufficient electroporation of small cells[23]. They calculated the relaxation time of the exponential membrane charging process for fusion partners with different size in low conductive electrofusion solutions and used only five-times longer pulses (10–20 μs) to ensure full charging of the cell membranes. They found that 1–3 pulses of such duration and with appropriate pulse amplitude (2–3 kV/cm) are enough for efficient electroporation of both fusion partners[23]. With some variations this protocol has, indeed, proved to be optimal in many cases[15,24–27] and also found its way into manuals of some commercial electrofusion systems (e.g. Eppendorf).

The efficiency of electrofusion, nevertheless, not only depends on the pulse parameters, but also on the composition of the fusion medium, osmolarity of the fusion medium, temperature, post pulse incubation of cells and other factors[13–15,22–29]. However, despite many efforts for improving electrofusion of cells with different size, higher susceptibility of large cells to electric pulses remained one of the obstacles, and the number of viable hybridomas obtained with respect to the number of input B lymphocytes reached only ~1% or less[13,26,30].

We here propose a new approach for fusing cells by reducing the pulse duration to nanoseconds. In contrast to "classical" microsecond pulses, nanosecond (ns) pulses are short enough for cell membranes to remain in their charging phase during pulse exposure (assuming that the membrane conductivity has not yet changed considerably due to electroporation[31]). More importantly, during the membrane charging phase the induced transmembrane voltage rapidly increases, and its value depends less on the cell size and more on the electrical properties of the external medium and of the cells themselves. The effects of high voltage ns electric pulses have been a subject of extensive research in the past decade due to their ability to "penetrate" into the cell, affect membranes of cell organelles, modulate cell functions, and induce cell apoptosis[32–35]. However, if the pulses are not too intense, cell viability can be preserved[34–36]. Experiments also indicate that cell size and shape are not important factors in electroporation with ns pulses[37]. For this reason, ns pulses seem to have the potential to overcome the problem of low survival of large cells due to their excessive electroporation when electrofusing cells with different size[38].

In this paper we thus address the possibility of fusing cells using ns pulses in terms of numerical modelling and experiments *in vitro*. Based on finite element models of cells in contact we demonstrate that exposure of cells with different size to ns pulses in low conductive medium can result in selective electroporation of the cell contact areas. We then confirm experimentally on B16-F1 cells that electrofusion with ns pulses is indeed feasible. Moreover, we present results of a numerical model, which was constructed according to experiments on B16-F1 cells. We compare our experimental results with numerical ones and verify that experiments agree with model predictions of cell contact area electroporation. Finally, we present electrofusion experiments on two cell lines, B16-F1 and CHO, and demonstrate that nanosecond pulses are able to fuse cells of different type and with different size (radii of B16-F1 and CHO cells are 8.1 ± 1.1 μm and 6.1 ± 0.6 μm, respectively[28]).

Results

Numerical calculations. We constructed a 2-D finite element model of two cells with radii of 7.75 μm and 3.85 μm, positioned next to each other, with part of their membranes forming a contact area (Fig. 1). The chosen radii correspond to radii of myeloma cells and B lymphocytes in isoosmolar medium, respectively[20]. Both cells contained a nucleus that occupies 60% of the cytoplasmic volume, which is considered typical for lymphocyte cells[39]. The axial symmetry of the model geometry allowed us to preform calculations in two dimensions only.

Fig. 1a shows an example of the spatial distribution of the induced transmembrane voltage (ITV) along cell membranes, starting from the pole of the left cell and ending at the pole of the right cell, at times 100 ns, 1 μs and 10 μs. From Fig. 1a we can see that the ITV, which establishes at 10 μs is considerably higher on the large cell compared to the small cell.

Fig. 1b presents the time course of the absolute value of ITV at different points on the membranes: on poles of both cells, the point in the middle of the contact area, and on poles of both nuclei. Fig. 1c shows the same ITVs; however, the values are normalized to the ITV on the pole of the small cell. Note that the time is presented on a logarithmic scale as this allows one to study the ITV during its transient state (membrane charging phase) as well as its steady state (when membranes are fully charged) on the same graph. The ITV on the contact area exceeds the ITV on all other membranes during the first 1.9 μs of the time considered. The ITVs on both cell poles are quite similar for times below 1 μs; however, the ITV on the large cell afterwards increases substantially above the ITV on the small cell and also above the ITV on the contact area. The ITVs on both nuclei remain below the ITV on the contact area for all times.

When the ITV reaches sufficiently high value (~1 V), a large number of conductive pores form in the membrane (membrane is electroporated) and membrane conductivity increases by several orders of magnitude[40]. The following calculations were thus performed by upgrading our existing model with a model of electroporation[40].

Fig. 2 compares pore density, induced along cell membranes and nuclear membranes for exposure to pulses with two different durations, 10 μs (Fig. 2a) and 100 ns (Fig. 2b). For each pulse duration the amplitude was chosen such that a pore density 10^{13} m^{-2} (10 pores per μm^2)[40,41] was exceeded over the entire contact area. This value of pore density was taken from literature[40], and it was also used by other authors to present electroporated membrane areas[41]. Moreover, when performing calculations for myeloma cells and B lymphocytes exposed to 10 μs pulse, this pore density was achieved by amplitude 2.2 kV/cm (Fig. 2a), which is in good agreement with the optimal

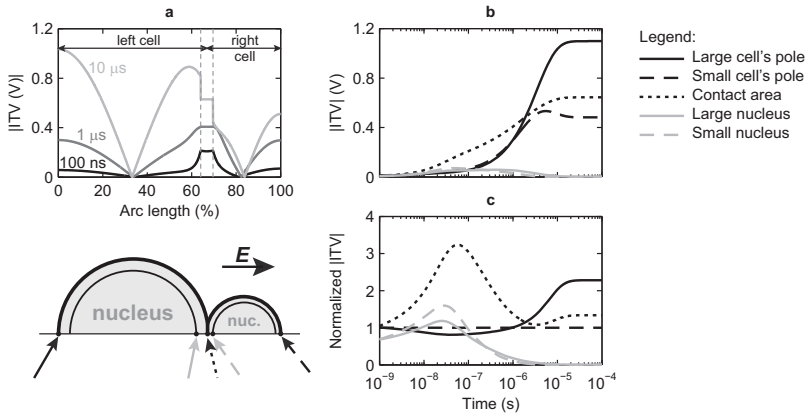

Figure 1 | Calculations of the induced transmembrane voltage (ITV). ITV on the membranes of two cells with different size in contact, after the onset of exposure to an electric field of 1 kV/cm. (a) ITV along the cell membranes at times 100 ns, 1 μs, and 10 μs. The contact areas are marked with vertical lines. (b) Calculated time course of the absolute value of ITV at the pole of the large cell (black solid line), the pole of the small cell (black dashed line), the point in the middle of the contact area (black dotted line), the pole of the large nucleus (grey solid line), and the pole of the small nucleus (grey dashed line). These points are indicated with arrows under the image of the cell model. (c) ITVs, calculated in (b), normalized to the ITV on the pole of the small cell.

amplitudes for hybridoma production (2.0–2.25 kV/cm), as reported by Neil and Zimmermann[23].

Membrane areas with pore density $\geq 10^{13}$ m^{-2} are marked with thick red lines in the images of the cell model in Fig. 2. Besides electroporation of the contact area, exposure to 10 μs, 2.2 kV/cm pulse results also in electroporation of a considerable part of the large cell's membrane (34.4% of membrane area reaches pore density $\geq 10^{13}$ m^{-2}), whereas the small cell is less electroporated compared to the large one (9.1% of membrane area reaches pore density $\geq 10^{13}$ m^{-2}). On the contrary, exposure to 100 ns, 6.6 kV/cm pulse causes electroporation of the contact area only. The nuclear membranes in both cases remain virtually unaffected.

Electrofusion of B16-F1 cells: fusion yield. Cells were first incubated in hypoosmolar medium, since hypoosmolar pretreatment in electrofusion protocols is known to enhance fusion yield[25–28]. Cells were then aligned by means of dielectrophoresis and exposed to twenty pulses of different durations (50, 100, or 150 ns) and different amplitudes (6, 9, or 12 kV/cm). Prior to experiments the cells were stained with cell-permeable blue nuclear acid stain Hoechst in order to simplify detection of polynucleated (fused) cells obtained with electrofusion. Fusion yield was determined eight minutes after ns pulse application as the percentage of polynucleated cells with respect to all exposed cells (Fig. 3a). Fusion yield increased with pulse amplitude and pulse duration, though only to a certain level. When longer pulses (100 and 150 ns) with the highest amplitude (12 kV/cm) were applied, the fusion yield decreased. The highest fusion yield (8.7 ± 1.5%) was achieved with 100 ns, 9 kV/cm pulses, but relatively high fusion yields were also obtained with 150 ns, 6 kV/cm and 9 kV/cm pulses (6.9 ± 2.1% and 6.4 ± 2.0%, respectively). Sham-exposed cells showed a small baseline percentage of cells containing two nuclei (0.3 ± 0.2%), i.e., cells in the process of cell division. There was no significant difference between sham-exposed cells and cells exposed to dielectrophoresis only.

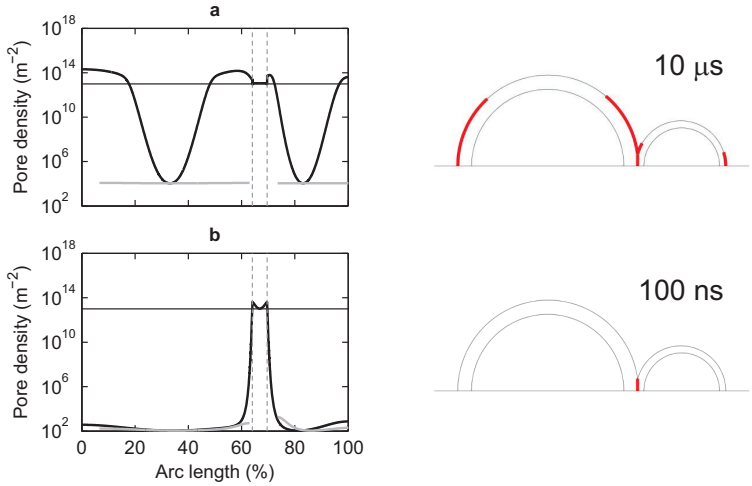

Figure 2 | Calculations of the pore density. Pore density induced along the cell membranes and nuclear membranes of two cells with different size in contact. (a) Calculations for 10 μs, 2.2 kV/cm pulse. (b) Calculations for 100 ns, 6.6 kV/cm pulse. Black solid line corresponds to the cell membrane and grey solid line to the nuclear membrane. Thin horizontal lines indicate a pore density of 10^{13} m^{-2}. Vertical lines mark the contact area. Areas of the membranes, where the pore density exceeds 10^{13} m^{-2}, are indicated with thick red lines on the images of the cell model.

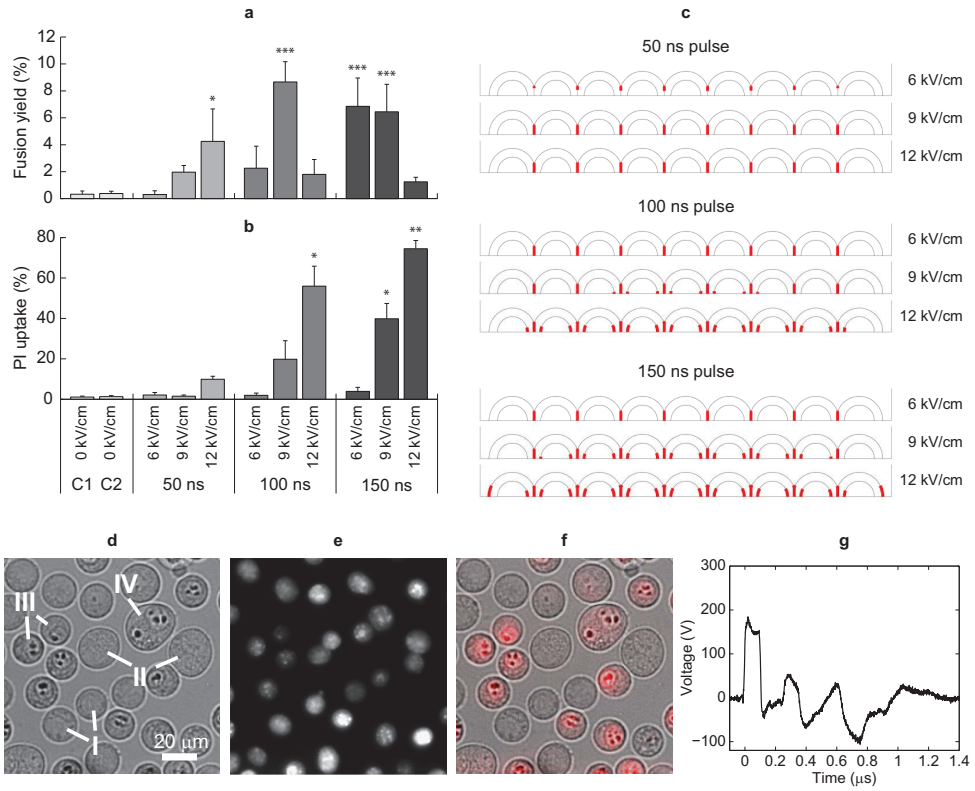

Figure 3 | Results of experiments on B16-F1 cells. (a) Fusion yield and (b) percentage of cells, stained with PI, obtained with different parameters of ns pulses. These parameters are indicated at the bottom of the graphs. C1–sham, C2–cells exposed only to dielectrophoresis. Data in (a) and (b) are means from at least three individual experiments; error bars show s.d. Asterisks *** ($P < 0.001$), ** ($P < 0.01$) and * ($P < 0.05$) mark significant difference versus C1. (c) Results of calculations on the model of cells arranged in pearl chain. Similar cell arrangement was observed during experiments. The areas of the membranes, where the pore density exceeds 10^{13} m^{-2}, are indicated with thick red lines. (d) Bright field image indicating changes in cell morphology after exposure to ns pulses: I–cells with normal morphology, II–fused cells with normal morphology, III–cells with changed morphology, IV–fused cell with changed morphology. (e) Fluorescence image of cells in (d), showing Hoechst-stained nuclei. Cells were stained with Hoechst prior to experiments. (f) Two channel fluorescence image showing red PI-stained nuclei. PI was added to the cell suspension 10 minutes after application of ns pulses. Images (d–f) were captured 15 minutes after exposure to twenty 150 ns, 9 kV/cm pulses. (g) An example of a single 100 ns, 180 V pulse (results in 9 kV/cm), delivered to B16-F1 cells with nanosecond pulse generator. The complete presented pulse shape was used in numerical calculations on the model of experiments on B16-F1 cells.

Electrofusion of B16-F1 cells: propidium iodide uptake. Ten minutes after exposure to ns pulses, the cells were stained with cell-impermeable red nuclear acid fluorescent stain propidium iodide (PI), in order to detect cells which were unable to reseal their membranes within this time. The percentage of PI-stained cells was $< 1.3\%$ in control groups, however, it increased with pulse amplitude and pulse duration (Fig. 3b). In the group exposed to the most intense pulses (150 ns, 12 kV/cm), PI uptake was 75 $\pm$ 4%. We must stress, though, that PI fluorescence in most of the stained cells was very weak and only few cells, which were probably already dead before pulse exposure, fluoresced brightly. To clearly see the stained cells, we needed to process the images of PI fluorescence by multiplication and subtraction of image background (see also Methods).

Generally, the PI-stained cells also showed marked change in their morphology (cf. Fig. 3d and 3f). These cells shrank and in their nuclei we observed condensed dark areas in the bright field images; the dark areas coincided with areas where small bright dots in Hoechst fluorescence images appeared, indicating chromatin condensation (Fig. 3e).

Electrofusion of B16-F1 cells: numerical model of experiments. We also performed calculations on a numerical model of experiments on B16-F1 cells. We constructed a model of nine cells arranged in pearl chain (such pearl chains formed during experiments, when cells were aligned by means of dielectrophoresis). We also took the following parameters from the experiments: we measured the radius of B16-F1 cells and the radius of their nuclei to be 11.4 $\pm$ 1.0 μm and 7.3 $\pm$ 0.6 μm, respectively; we measured the conductivity of the fusion medium, which was 0.012 S/m; we captured the shape of the pulses, delivered to cells by the nanosecond pulse generator (Fig. 3g); and we exposed cells in the model to these captured pulses. Results of numerical calculations considering exposure to a single pulse with given pulse parameters are presented in Fig. 3c. Thick red lines mark the membrane areas, where calculations showed pore density $\geq 10^{13}$ m^{-2} (full calculations of the pore density along cell and nuclear membranes are given in Supplementary Fig. S1 online). For all pulse parameters, calculations showed contact area electroporation. However, 50 ns, 6 kV/cm pulse induced a considerably lower pore density, which exceeded 10^{13} m^{-2} only over a small part of the contact area. At the same time, for these pulse parameters we observed practically no fused cells in experiments. On the contrary, for all other pulse parameters the model showed a pore density higher than 10^{13} m^{-2} over the entire contact area. For all these other pulse parameters we observed low to relatively high number of fused cells in experiments (Figs. 3a and 3b).

For pulses longer than 50 ns, with amplitudes higher than 6 kV/cm, calculations also showed nuclear membrane electroporation. Note that for pulse parameters, where the model showed extensive nuclear electroporation, we also observed a significant number of PI-stained cells. These were also the pulses for which lower fusion yields were obtained (Figs. 3a and 3b).

Electrofusion of B16-F1 and CHO cells. Experiments on B16-F1 cells demonstrated that electrofusion with nanosecond pulses is feasible for cells of the same type. In the next set of experiments we used both B16-F1 cells and CHO cells. The aim of these experiments was to demonstrate fusion between cells of different type and with different size as well (CHO cells are considerably smaller than B16-F1[28]). The feasibility of such fusion is demonstrated by the sequence of images presented in Fig. 4. The images were captured after exposure of cells to twenty 150 ns, 6 kV/cm pulses (these were the pulse parameters for which high fusion yield and low percentage of PI-stained cells was obtained in experiments on B16-F1 cells). The last image is a two channel fluorescence image of cells, prestained with Hoechst. In the fused cell, two blue nuclei can be detected.

Discussion

Electrofusion of cells with different size results in low fusion yields, since the extent of electroporation with conventionally used tens to hundreds microsecond-duration pulses depends on the cell size. The aim of our study was to numerically determine the potential advantage of fusing cells with different size using shorter nanosecond (ns) electric pulses, and to experimentally investigate the feasibility of such fusion.

Firstly, we performed numerical calculations on a model of two cells with different size. The time course of the induced transmembrane voltage (ITV) implied that if pulses were sufficiently short (in the nanosecond range), contact areas between cells (i.e. the target areas) could be selectively electroporated. This was further confirmed by calculations of the pore density across the cell membranes, induced by electroporation. In exposure of cells to 10 μs pulse, electroporation of cell contact area was also accompanied by extensive electroporation of the large cell's membrane. On the contrary, exposure to ns pulse of appropriate amplitude caused electroporation of the contact area only. Since excessive cell electroporation can lead to cell death, our numerical results agree with experimentally observed low survival rate of myeloma cells and consequently low fusion yields of hybridomas when using microseconds pulses[9,23]. Even though 10–20 μs pulses were shown to be optimal for hybridoma technology, our numerical results suggest that the fusion yield could be even further improved by using ns pulses.

The possibility of selective contact area electroporation can be explained by membrane charging process in low conductive medium. The contact area is surrounded by relatively highly conductive cytoplasm (0.25 S/m) from both sides, whereas the rest of the membrane is from one side surrounded by low conductive fusion medium (calculations were performed for medium with conductivity 0.01 S/m, which is often used in electrofusion protocols, where cell contacts are established by means of dielectrophoresis[13,22,27]), which was also used in our experiments. Higher conductivity of the cytoplasm, therefore, causes faster charging of the contact area compared to other membrane areas. Consequently, the contact area can be electroporated at lower pulse amplitude compared to other membrane areas. Note, however, that this can only be observed in the nanosecond range, when cell membranes are still in the charging phase (Fig. 1).

Furthermore, even if cells are not in direct contact, but are separated by a small distance, the electric field around the contact area reaches the highest value, and selective contact electroporation can still be observed (see Supplementary Figs. S2 and S3 online). This confirms that the predictions of our model are quite robust and are not a result of numerical artefacts. Still, one should note that in order to achieve electroporation of the contact area, this area must be oriented in the direction perpendicular to the electric field (as in our calculations), since the highest ITV is achieved on the areas where the membrane normal is perpendicular to the electric field[15,16,40].

Secondly, we performed experiments on B16-F1 cells to verify the feasibility of cell fusion with ns pulses. We demonstrated that the fusion yield in B16-F1 cell experiments increased with the pulse amplitude and pulse duration, which is qualitatively similar as in electrofusion with microsecond pulses. However, the fusion yield increased only to a certain level. If the pulses were too intense, the number of fused cells decreased. The fusion yields, which we obtained using our protocol (up to ~8%, if we subtract the baseline percentage of polynucleated cells in control groups), are comparable to our previous study (up to ~4%)[22], where B16-F1 cells were also aligned with dielectrophoresis but exposed to 100 μs pulses. In that study the fusion yield was determined as the percentage of dually labelled cells, which considers only approximately half of all fused cells.

Pulse parameters, for which we observed a decrease in the fusion yield, also caused a substantial increase in the number of cells that

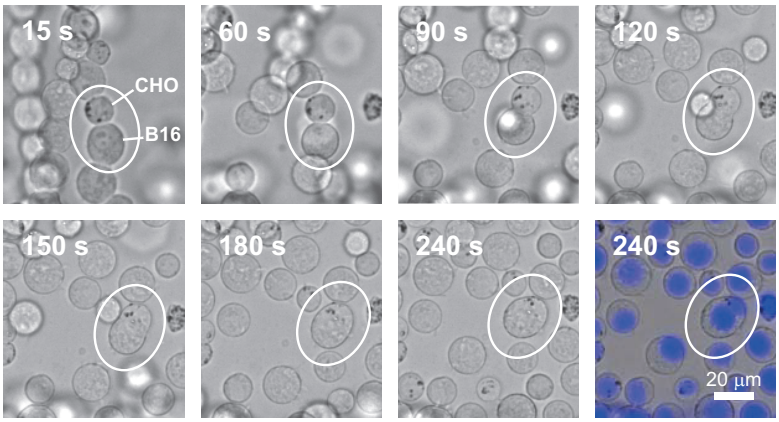

Figure 4 | Results of experiments on B16-F1 and CHO cells. Example of an image sequence showing the fusion process between a B16-F1 and a CHO cell. Cells were exposed to twenty 150 ns, 6 kV/cm pulses. CHO cells can be recognized as cells, which contain small dark dots. The time after application of ns pulses, when each image was captured, is indicated at the top left corner of the image. The last image is a two channel fluorescence image of cells, prestained with Hoechst (blue).

were permeable to PI (which was added 10 minutes after application of ns pulses). Furthermore, we observed morphological changes in PI-stained cells. These cells shrank, which could be the reason why fusion was prevented.

There are two possible explanations for the observed PI uptake: (i) electroporated membranes were unable to reseal 10 minutes after exposure to ns pulses or (ii) membranes lost their ability to act as a barrier due to cell damage caused by ns pulses.

In a number of experimental reports, in which cells were exposed to ns pulses in the presence of PI, investigators observed no or minor PI uptake, whereas uptake of smaller ions and molecules was readily detected[37,42,43]. Inability of PI to pass the electroporated membranes in those reports was attributed to the large size of the propidium molecule, too large to pass nanometre-sized pores formed during ns pulse exposure. Theoretical predictions namely show that the pores, induced by ns pulses, are greater in number but smaller in size compared to those, induced by microsecond pulses, as pores cannot significantly expand in the nanosecond time range[44]. However, when using appropriate pulse parameters, pores that develop during ns pulse exposure can indeed become permeable to PI. For example, Batista Napotnik et al.[33] showed that five 60 ns, 50 kV/cm pulses were enough to detect PI in B16-F1 cells using fluorescence microscopy.

In our experiments PI was added to the cell suspension 10 minutes after electroporation and could pass the membranes only if the pores have not resealed within this time. The resealing time for B16-F1 cells after electroporation with microsecond pulses at room temperature and in isoosmolar medium was found to be 5 and 10 minutes for ~50% and ~80% of all cells, respectively[45]. In experiments with ns pulses, pore resealing in various cell lines was found to be on the order of 10 minutes[37]. There is also experimental evidence that in hypoosmolar medium (in which cells were pulsed in our experiments) membrane resealing time is considerably faster than in isoosmolar medium[46]. Furthermore, exposure to 150 ns, 6 kV/cm pulses, which induced significant electrofusion (which is also indicative for electroporation), resulted in practically no PI-stained cells. This means that cells were able to reseal their membranes within 10 minutes after ns pulse application, which prevented PI uptake. However, it is still possible, that PI-stained cells were electroporated to a much greater extent and required longer time for their resealing (or were even irreversibly electroporated) compared to unstained cells.

On the other hand, researchers demonstrated that ns pulses of sufficiently high amplitudes and/or sufficiently long durations induce cell apoptosis, which *in vitro* is followed by a secondary necrosis[32,34,35]. The mechanisms of apoptosis induction by ns pulses are, however, not fully understood. During ns pulse exposure, high electric field is also present in the cell interior. Therefore, it is possible that apoptosis arises from organelle damage and modifications of intracellular signalling pathways, whereas cell membrane electroporation might also play at least a supporting role in observed apoptosis[34,35]. In B16-F1 cells, ns pulses seem to mimic the extrinsic apoptotic pathway without release of pro-apoptotic factors from mitochondria, but include activation of initiator and executioner caspases[34]. In experiments conducted by Ford and co-workers[34], exposure to ten 300 ns, 60 kV/cm pulses resulted in almost 100% decrease in B16-F1 cell survival 24 hours post treatment. When PI in these experiments was added to the cell suspension at various times after pulsing, its uptake began 15 min post-pulse, reaching a maximum at 25–30 min when ~30% cells (only about a third of the dead cells) were stained with PI as determined by flow cytometry. The latter results imply that PI uptake was not a direct consequence of electroporation, but rather a secondary effect of pulse treatment and an indicator of cell death[32,34,47].

Although the pulses used in our study were much shorter (up to 150 ns) and had lower amplitudes (up to 12 kV/cm), experimental data also suggest that cell damage caused by ns pulses can be enhanced, if the cytoskeleton network is disrupted prior to pulse exposure[48]. Since cells in our experiments were incubated in hypoosmolar medium, reorganization of their cytoskeleton occurred due to cell swelling, which could made cells more vulnerable to ns pulse effects. The observed morphological changes with chromatin condensation (which is also characteristic for apoptosis[49]) in PI-stained cells further support the possibility that PI uptake was an indicator of cell death also in our study.

Long term cell viability after electrofusion with ns pulses thus requires further investigation and is a subject of our future work. Nonetheless, with appropriate choice of pulse parameters we were able to obtain fused cells, while keeping the number of morphologically changed, PI-stained cells low (e.g., 100 ns, 9 kV/cm and 150 ns, 6 kV/cm).

In order to evaluate the validity of our numerical calculations we also built a numerical model of experiments on B16-F1 cells. Numerical results confirmed that for pulse parameters, which induced cell fusion, cell contact area electroporation was indeed predicted. For pulse parameters, where fusion yield was negligible (50 ns, 6 kV/cm), the model showed substantially lower pore density over the contact area. In experiments, where large numbers of morphologically changed, PI-stained cells appeared, the model predicted also extensive electroporation of the nuclear membrane. Although nuclear membrane electroporation itself might not lead to cell death, the model predictions of nuclear membrane electroporation imply that the electric field inside the cells was sufficiently high and present long enough to potentially affect other intracellular structures[41]. For instance, the pulses could cause electroporation of the endoplasmic reticulum with subsequent release of intracellular calcium, which could adversely impact cell survival[32,35]. These observations also agree with observed damage of B16-F1 cells.

We must note, though, that we performed calculations only for a single ns pulse, whereas we delivered twenty pulses to the cells in experiments. Multiple pulses were delivered since we observed practically no fused cells after a single pulse. The reason for this is not completely clear; consecutive pulses could stabilize the pores, induce formation of additional pores, or induce pore expansion, which may contribute to successful fusion. However, we did not perform optimization of the pulse number yet. We chose to only vary the pulse duration and pulse amplitude, since both can be easily taken into account in our numerical model. On the contrary, modelling exposure to several pulses would require modelling of pore expansion, pore resealing and possible "memory effects" present on the membrane[17]. Since the asymptotic electroporation model used in our study does not account for pore expansion or "memory effects", it is questionable whether modelling multiple pulses would give meaningful results.

Finally, we performed experiments on two cell lines of different size, B16-F1 and CHO. We were able to obtain fused B16-F1 and CHO cells with same pulse parameters as in experiments on B16-F1 cells only. Since numerical calculations predict selective electroporation of contact areas with ns pulses when cells have either equal or different size (Fig. 2b, Fig. 3c), these experimental results give further confidence to the validity of our numerical results.

To conclude, electrofusion of cells with different size with conventionally used microseconds pulses results in low fusion yields; pulses which efficiently electroporate small cells namely cause death of large ones. We hypothesize that this problem could be overcome by reducing the pulse duration to nanoseconds. Our numerical calculations reveal a crucial advantage of fusing cells with ns pulses – the contact areas between cells can be selectively electroporated, regardless of the cell size. By performing experiments on B16-F1 cells we demonstrated that with ns pulses it is indeed possible to obtain fusion yields comparable as with microsecond pulses. We are confident that with additional optimization of the electrofusion protocol, the fusion yield

can be further improved[22]. For example, high fusion yield can be achieved by establishing high quality cell-to-cell contact, and electrofusing cells on microchip or by sucking them as a monolayer on filter with calibrated pores[30,50]. Furthermore, by demonstrating successful fusion between B16-F1 and CHO cells, we confirmed that ns pulses are able to fuse cells of different type and with different size. Results of numerical calculations were verified based on experiments on B16-F1 cells; for pulse parameters, which induced cell fusion, numerical calculations indeed predicted electroporation of the contact areas. On the basis of our numerical results and cell fusion experiments we believe that ns pulses can increase the fusion yield, in particular in cases where fusion partner cells differ considerably in size, such as in hybridoma technology. However, since ns pulses seem to enable targeted electroporation of cell contact areas, they may increase the fusion yield also in other applications of cell fusion, such as preparation of cell vaccines for cancer treatment[5–7], and production of insulin-releasing cells for treatment of diabetes[1–3].

Methods

Numerical modelling. Finite element models of cells in contact, exposed to electric pulses, were constructed in Comsol Multiphysics 4.3 b (Comsol). First, calculations were performed for two spherical cells of different size (with radii of 7.75 μm and 3.85 μm), which contained a nucleus that occupied 60% of the cytoplasmic volume. The cells were positioned one next to the other with part of their membranes forming a contact area. The radius of the contact area was set to 1 μm[51] (Fig. 5). Second, a model of nine cells arranged in a pearl chain was constructed. The radii of the cells (11.4 μm) and their nuclei (7.3 μm) were set equal to the measured average radius of B16-F1 cells and the radius of their nuclei. The radius of the contact area was estimated from images of cells during dielectrophoresis and was set to 4.3 μm.

Both models were axisymmetric, which allowed us to perform calculations in two dimensions. Fig. 5 presents an example of two spherical cells with nuclei, which are placed in an extracellular medium represented by a rectangle with dimensions 200 μm × 100 μm. The left and right side of the rectangle were modelled as electrodes by assigning them an electric potential. The boundary conditions of the rectangle are indicated in Fig. 5.

In calculations for two cells in contact, electric pulses were obtained by subtracting two Heaviside functions using Comsol function *flc1hs*. The rise and fall times were 10 ns for 100 ns pulse and 1 μs for 10 μs pulse. In calculations for cells arranged in a pearl chain, a different approach was used. Using a digital oscilloscope (WaveSurfer 422, LeCroy) and a high voltage probe (PPE 2 kV, LeCroy) realistic shapes of single pulses delivered to B16-F1 cells were captured. The pulse signals (Fig. 3g) were then smoothed with Butterworth filter in Matlab 2012a (MathWorks), to remove the noise, and imported into Comsol.

The electric potential V in each subdomain of the model (extracellular medium, cytoplasm, nucleoplasm) was calculated in application mode *Electric Currents* of the *AC/DC* module (*Time Dependent Study*) by equation

$$-\nabla(\sigma_i \nabla V) - \nabla \frac{\partial(\varepsilon_i \nabla V)}{\partial t} = 0, \quad (1)$$

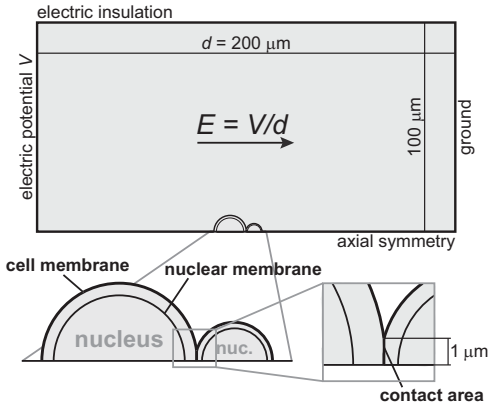

Figure 5 | Model of two cells in contact, exposed to electric field. The cell radii are 7.75 μm and 3.85 μm. The magnitude of the electric field was determined as the voltage difference between the left and the right side of the rectangle (the electrodes) divided by the electrode distance. The direction of the electric field is indicated with an arrow.

where σ_i and ε_i denote the conductivity and dielectric permittivity of a given subdomain, respectively. The membranes were not physically included in the model, however, they were modelled with a boundary condition *Distributed Impedance*[52,53]:

$$n \cdot J = \frac{\sigma_m}{d_m}(V - V_{ref}) + \frac{\varepsilon_m}{d_m}\left(\frac{\partial V}{\partial t} - \frac{\partial V_{ref}}{\partial t}\right). \quad (2)$$

Here, $\boldsymbol{n}$ is the unit vector normal to the boundary surface, $\boldsymbol{J}$ is the electric current density, V is the electric potential on the interior side of the boundary, V_{ref} is the electric potential on the exterior side of the boundary, and σ_m, ε_m, and d_m, are the membrane conductivity, membrane dielectric permittivity, and membrane thickness, respectively. The ITV was then determined as the difference between electric potentials on each side of the boundary.

In calculations presented in Figs. 2 and 3, we also included a model of electroporation[40], which predicts that the pore formation dynamics are governed by differential equation

$$\frac{dN}{dt} = \alpha e^{\left(\frac{ITV}{V_{ep}}\right)^2}\left(1 - \frac{N}{N_0} e^{-q\left(\frac{ITV}{V_{ep}}\right)^2}\right), \quad (3)$$

where N denotes the induced pore density in the membrane, N_0 the pore density in the nonelectroporated membrane, whereas parameters α, q, and V_{ep} describe the characteristics of the electroporation process. Equation (3) was incorporated into Comsol with the *Weak Form Boundary PDE* application mode[53].

The inducement of pores considerably alters the membrane conductivity. The increase in the membrane conductivity due to electroporation σ_{ep} can be described by expression[40,54]:

$$\sigma_{ep} = N\frac{2\pi r_p^2 \sigma_p d_m}{\pi r_p + 2d_m}, \quad (4)$$

where r_p and σ_p are the radius and internal conductivity of a single pore. Note that σ_{ep} is proportional to the pore density N. We did not take into account the interactions between the pore wall and ions that are passing through the pore[40], since we found this parameter to have negligible influence on our results. The total membrane conductivity σ_m in equation (2) was calculated at each time step as the sum of the passive membrane conductivity (which is given in Table 1) and the conductivity due to electroporation σ_{ep}.

Equations (1)–(4) were solved simultaneously with system solver *PARDISO*. The values of model parameters are given in Table 1.

In calculations for the pore density on the nuclear envelope we took into account that the nuclear envelope consists of two lipid membranes. We assumed that both membranes have equal electrical properties and that the ITV equally distributes between them. Therefore, the ITV across one membrane was calculated as half of the voltage across the entire nuclear envelope. ITV across one nuclear membrane was then applied to equation (3) and this ITV is also presented in Fig. 1 in *Results*. Segments of cell membranes that formed the contact areas between adjacent cells were considered in the same way.

Cell culture. Mouse melanoma B16-F1 and Chinese hamster ovary cells CHO-K1 (European Collection of Cell Cultures) were grown in DMEM and F-12 HAM (PAA Laboratories), respectively. Both culture media were supplemented with 10% foetal bovine serum (PAA Laboratories), L-glutamine (Sigma-Aldrich), and antibiotics gentamicin and penicillin/streptomycin (PAA Laboratories). Cells were grown plated on the bottom of 25 mm^2 flasks (TPP) at 37°C in a humidified 5% CO_2 atmosphere until reaching 70–90% confluence.

Fusion media. Fusion media consisted of Mg^{2+} acetate (0.5 mM), Ca^{2+} acetate (0.1 mM), bovine serum albumin (1 mg/ml), and glucose (all from Sigma-Aldrich). The isoosmolar fusion medium contained 280 mM glucose (osmolarity ~280 mOsm) and the hypoosmolar fusion medium contained 90 mM glucose (osmolarity ~90 mOsm). The composition of the fusion media closely resembled those from Eppendorf (order no. 4308 070.536 and 4308 070.528). Conductivity of both fusion media, measured with conductometer (MA 5950, Metrel), was 0.012 S/m.

Measurements of B16-F1 cell and nuclear radii. Cells were prepared as described below in *Cell Preparation*. For measurements of cell diameters, bright field images (×20 objective magnification) were captured from three randomly chosen fields on the fusion chamber three minutes after incubation of cells in hypoosmolar fusion medium. For measuring the nuclear diameters, we used differential interference contrast (DIC) microscopy (×40 objective magnification). Images from three different fields of the fusion chamber were taken from 2 min 30 s to 3 min 30 s after incubation in hypoosmolar fusion medium.

Cell and nuclear diameters were measured in MetaMorph 7.7 (Visitron) from images taken on three different days and using cells of three different passages. In each experiment we measured cell diameters of 55–60 cells (altogether 173 cells) and 40–50 nuclei (altogether 136 nuclei). The radii were determined as half of the measured diameters. Data are presented as mean ± standard deviation.

Cell preparation. Before experiments, cells were stained with cell-permeable blue nuclear acid fluorescent stain Hoechst 33342 (10 mg/ml solution in water, Invitrogen, Molecular Probes). We added 1 μl (3.2 μM) of the dye into 5 ml of

Table 1 | Model parameters

Parameter	Symbol	Value	Reference
Cell radius	R_c (μm)	3.85, 7.75 11.4	20 Measured radius of B16-F1 cells.
Nuclear radius	R_n (μm)	3.25, 6.54 7.3	Set to $\sqrt[3]{0.6R_c^3}$[39]. Measured nuclear radius of B16-F1 cells.
Extracellular medium conductivity	σ_e (S · m^{-1})	0.010 0.012	Arbitrary. Measured hypoosmolar medium conductivity.
Extracellular medium permittivity	ε_e	80	41
Cytoplasmic conductivity	σ_{cp} (S · m^{-1})	0.25	27,56,57
Cytoplasmic permittivity	ε_{cp}	70	56
Cell membrane conductivity	σ_{cm} (S · m^{-1})	$5 \cdot 10^{-7}$	57
Cell membrane permittivity	ε_{cm}	4.5	27,56,57
Cell membrane thickness	d_{cm} (nm)	5	40
Nucleoplasmic conductivity	σ_{np} (S · m^{-1})	0.5	Set to $2 \cdot \sigma_{cp}$[39,58].
Nucleoplasmic permittivity	ε_{np}	70	Set equal to ε_{cp}.
Nuclear envelope conductivity	σ_{nm} (S · m^{-1})	$1 \cdot 10^{-4}$	59
Nuclear envelope permittivity	ε_{nm}	7	60
Nuclear envelope thickness	d_{nm} (nm)	10	Set to $2 \cdot d_{cm}$.
Pore conductivity (cell membrane)	σ_p (S · m^{-1})	$(\sigma_e \cdot \sigma_{cp})/\ln(\sigma_e/\sigma_{cp})$	54
Pore conductivity (nuclear membrane)	σ_p (S · m^{-1})	$(\sigma_{cp} \cdot \sigma_{np})/\ln(\sigma_{cp}/\sigma_{np})$	54
Pore radius	r_p (nm)	0.76	40
Electroporation constant	q	2.46	40
Electroporation parameter	α (m^{-2} s^{-1})	10^9	40
Characteristic voltage of electroporation	V_{ep} (V)	0.258	40
Equilibrium pore density	N_0 (m^{-2})	$1.5 \cdot 10^9$	40

culture medium and incubated the cells at 37°C for 5 min. Cells were then washed twice with 5 ml 0.9% NaCl solution (B Braun) to remove the excess dye. To harvest the cells we added 2.5 ml of trypsin/EDTA (Sigma-Aldrich) for 60 s, then we removed trypsin/EDTA and incubated the cells at 37°C for additional 30–60 s. After that we added 3 ml of culture medium, gently washed the cells from the bottom of the flask with a pipette, and counted the cells using haemocytometer.

For experiments on B16-F1 cells, an amount of suspension containing ~$4.4 \cdot 10^5$ cells was pipetted into 1.5 ml plastic tubes and centrifuged (5 min, 270 g, 4°C). The culture medium was removed and the cells were washed with 1 ml isoosmolar fusion medium. After second centrifugation (30 s, room temperature, Labnet C1301, Labnet International), the cells were incubated in 200 μl of the hypoosmolar fusion medium. A droplet (20 μl) of the cell suspension was transferred onto the Micro fusion chamber (electrode gap width 200 μm, Eppendorf), that was placed on the microscope stage. The fusion chamber was then covered with a cover glass to prevent evaporation of the medium.

For experiments on both B16-F1 and CHO cells the preparation protocol slightly differed. Since CHO are smaller than B16-F1, higher number of cells was used. Suspension with ~$5.2 \cdot 10^5$ cells was pipetted into centrifuge tubes, separately for B16-F1 and CHO. Cells were centrifuged (5 min, 270 g, 4°C), the culture medium was removed, and 1 ml of isoosmolar medium was added to tubes containing either B16-F1 or CHO cells. Afterwards, 500 μl of B16-F1 cells and 500 μl of CHO cells were transferred into an empty 1.5 ml tube, and the cells were centrifuged again (30 s, room temperature, Labnet C1301). The following protocol was equal as described in the preceding paragraph.

Experiments on B16-F1 cells. Cells were prepared as described in *Cell Preparation*. Two to three minutes after incubation in the hypoosmolar fusion medium, when most of the cells became roundly shaped, we established contacts between cells by means of dielectrophoresis (sine wave, 2 MHz, 5 V_{pp}, function generator Agilent 33220A, Agilent Technologies). After 30 s of dielectrophoresis, twenty ns pulses of a given duration (50, 100, 150 ns) and amplitude (120, 180, 240 V), with a repetition frequency of 1 kHz were delivered by a custom made nanosecond pulse generator[55]. Taking into account the electrode gap width of 200 μm, the peak electric field magnitudes were estimated to be 6, 9 and 12 kV/cm. After ns pulses were delivered, the electrodes were reconnected to a sine wave signal (2 MHz, 5 V_{pp}) for another 30 s, to maintain the cells in contact. The cells were then left to fuse at room temperature.

Eight minutes after delivering ns pulses, we captured bright field images and blue fluorescence images of the cells prestained with Hoechst dye (excitation/emission 350 nm/461 nm). Once the images were captured (i.e. approximately 10 minutes after ns pulse application), we added 2 μl (0.15 mM) of red cell-impermeable nuclear acid stain propidium iodide (PI) (1 mg/ml solution in water, Invitrogen, Molecular Probes) to the cell suspension. Five minutes later (15 to 16 minutes after ns pulse application) we captured bright field images and fluorescence images of PI (excitation/emission 535 nm/617 nm). In both cases we captured images from four randomly chosen fields between the electrodes.

Experiments on B16-F1 and CHO cells. Cells were prepared as described in *Cell Preparation*. Exposure to dielectrophoresis and ns pulses was equal as in experiments on B16-F1 cells; however, only one set of ns pulse parameters was used (twenty 150 ns, 6 kV/cm pulses with 1 kHz repetition frequency). Immediately after application of ns pulses we started capturing bright field images and followed the fusion process between a B16-F1 and a CHO cell. After the cells were completely fused, we also captured a fluorescence image of Hoechst.

The experiments were repeated nine times on three different days with cells of two different passages in order to verify that experiments are repeatable. Characteristic sequence of images demonstrating fusion between a B16-F1 and a CHO cell is presented in *Results*.

Image capture. Cells were monitored under an inverted fluorescence microscope Axiovert 200 (Zeiss) with × 20 objective magnification (except for measurement of B16-F1 nuclear radii, where × 40 objective magnification was used). Images were captured with a digital camera VisiCam 1280 using software package MetaMorph 7.7.

Switching between dielectrophoretic signal and nanosecond pulses. Switching between dielectrophoretic signal from the function generator and ns pulses delivered by the nanosecond pulse generator was carried out with a relay (T7NS5D4-24, Siemens), which was controlled by S7-1200 controller (CPU 1214C, Siemens). By manually triggering the electrofusion protocol, the relay connected the dielectrophoretic signal to the electrodes of the fusion chamber. After 30 s, the electrodes were automatically switched to the nanosecond pulse generator, which was then manually triggered. When the pulses were delivered, we reconnected the dielectrophoretic signal to the electrodes for another 30 s, by pressing a portable button. The delay between the dielectrophoretic signal and ns pulse application was approximately 1 s.

An example of a delivered ns pulse is presented in Fig. 3g. Since the impedance of the pulse delivery coaxial cable (100 Ω) did not match the impedance of the fusion chamber (50 Ω), the initial generated pulse was followed by six of its reflections.

Determination of the fusion yield and the percentage of cells stained with PI. Image processing and cell counting was performed in ImageJ (http://rsbweb.nih.gov/ij/). Two channel images of the bright field and Hoechst fluorescence were created, and the fusion yield was determined as the ratio between the number of polynucleated cells and the number of all cells between the electrodes.

To determine the percentage of PI-cells stained, we created two-channel images of the bright field and PI fluorescence, counted the number of stained cells and divided this number by the number of all cells between the electrodes. Since PI fluorescence in most cells was very weak, we needed to multiply fluorescence images by ~10–15 and carefully subtract the image background prior to creating two-channel images. When counting the cells on two-channel images, we also verified on fluorescence images whether a cell is indeed stained with PI or not.

In all images cells at the bottom of the chamber were counted and only 80% area between the electrodes was considered, as cells were often not clearly seen in the close proximity of the electrodes.

Statistical analyses. Results of B16-F1 cell experiments are presented as mean ± standard deviation. Each experiment on B16-F1 cells was repeated four times (experimental groups: cells exposed to ns pulses) or three times (control groups: sham-exposed cells and cells exposed only to dielectrophoresis) on different days and with cells of four different passages. SigmaPlot 11.0 (Systat Software) was used to analyse statistically significant difference between sham control and other experimental groups. Data were tested for normality (Shapiro-Wilk test with P value to reject 0.05) and equal variance (with P value to reject 0.05). Since the data for fusion yield passed the normality and equal variance test, they were analysed with One Way ANOVA and Bonferroni's t-test (with alpha value 0.05). The data for PI-staining failed the normality test; therefore, they were analysed with Kruskal-Wallis One Way ANOVA on Ranks and Dunn's test.

1. McClenaghan, N. H. Physiological regulation of the pancreatic *β*-cell: functional insights for understanding and therapy of diabetes. *Exp. Physiol.* **92**, 481–496 (2007).
2. Yanai, G. *et al.* Electrofusion of mesenchymal stem cells and islet cells for diabetes therapy: A rat model. *PLoS ONE* **8**, e64499 (2013).
3. McCluskey, J. T. *et al.* Development and functional characterization of insulin-releasing human pancreatic beta cell lines produced by electrofusion. *J. Biol. Chem.* **286**, 21982–21992 (2011).
4. Sretavan, D. W., Chang, W., Hawkes, E., Keller, C. & Kliot, M. Microscale surgery on single axons. *Neurosurgery* **57**, 635–646 (2005).
5. Guo, W., Guo, Y., Tang, S., Qu, H. & Zhao, H. Dendritic cell-Ewing's sarcoma cell hybrids enhance antitumor immunity. *Clin. Orthop.* **466**, 2176–2183 (2008).
6. Koido, S. *et al.* Regulation of tumor immunity by tumor/dendritic cell fusions. *Clin. Dev. Immunol.* **2010**, 516768 (2010).
7. Avigan, D., Rosenblatt, J. & Kufe, D. Dendritic/tumor fusion cells as cancer vaccines. *Semin. Oncol.* **39**, 287–295 (2012).
8. Vor dem Esche, U. *et al.* Passive vaccination with a human monoclonal antibody: generation of antibodies and studies for efficacy in *Bacillus anthracis* infections. *Immunobiology* **216**, 847–853 (2011).
9. Trontelj, K. *et al.* Optimization of bulk cell electrofusion in vitro for production of human-mouse heterohybridoma cells. *Bioelectrochemistry* **74**, 124–129 (2008).
10. Golestani, R., Pourfathollah, A. A. & Moazzeni, S. M. Cephalin as an efficient fusogen in hybridoma technology: can it replace poly ethylene glycol? *Hybridoma (Larchmt)* **26**, 296–301 (2007).
11. Karsten, U. *et al.* Direct comparison of electric field-mediated and PEG-mediated cell fusion for the generation of antibody producing hybridomas. *Hybridoma* **7**, 627–633 (1988).
12. Hui, S. W. & Stenger, D. A. Electrofusion of cells: hybridoma production by electrofusion and polyethylene glycol. *Methods Enzymol.* **220**, 212–227 (1993).
13. Yu, X., McGraw, P. A., House, F. S. & Crowe, Jr, J. E. An optimized electrofusion-based protocol for generating virus-specific human monoclonal antibodies. *J. Immunol. Methods* **336**, 142–151 (2008).
14. Teissié, J. & Rols, M. P. Fusion of mammalian cells in culture is obtained by creating the contact between cells after their electropermeabilization. *Biochem. Biophys. Res. Commun.* **140**, 258–266 (1986).
15. Zimmermann, U. Electric field-mediated fusion and related electrical phenomena. *Biochim. Biophys. Acta* **694**, 227–277 (1982).
16. Kotnik, T., Kramar, P., Pucihar, G., Miklavcic, D. & Tarek, M. Cell membrane electroporation—Part 1: The phenomenon. *IEEE Electr. Insul. Mag.* **28**, 14–23 (2012).
17. Teissié, J., Golzio, M. & Rols, M. P. Mechanisms of cell membrane electropermeabilization: a minireview of our present (lack of?) knowledge. *Biochim. Biophys. Acta* **1724**, 270–280 (2005).
18. Teissié, J. & Ramos, C. Correlation between electric field pulse induced long-lived permeabilization and fusogenicity in cell membranes. *Biophys. J.* **74**, 1889–1898 (1998).
19. Sixou, S. & Teissié, J. Specific electropermeabilization of leucocytes in a blood sample and application to large volumes of cells. *Biochim. Biophys. Acta* **1028**, 154–160 (1990).
20. Trontelj, Katja. Cell fusion *in vitro* by means of electropermeabilization, PhD thesis. University of Ljubljana (2010).
21. Sowers, A. E. A long-lived fusogenic state is induced in erythrocyte ghosts by electric pulses. *J. Cell Biol.* **102**, 1358–1362 (1986).
22. Usaj, M., Flisar, K., Miklavcic, D. & Kanduser, M. Electrofusion of B16-F1 and CHO cells: the comparison of the pulse first and contact first protocols. *Bioelectrochemistry* **89**, 34–41 (2013).
23. Neil, G. A. & Zimmermann, U. Electrofusion. *Methods Enzymol.* **220**, 174–196 (1993).
24. Stenger, D. A., Kubiniec, R. T., Purucker, W. J., Liang, H. & Hui, S. W. Optimization of electrofusion parameters for efficient production of murine hybridomas. *Hybridoma* **7**, 505–518 (1988).
25. Schmitt, J. J. & Zimmermann, U. Enhanced hybridoma production by electrofusion in strongly hypo-osmolar solutions. *Biochim. Biophys. Acta* **983**, 42–50 (1989).
26. Perkins, S., Zimmermann, U. & Foung, S. K. Parameters to enhance human hybridoma formation with hypoosmolar electrofusion. *Hum. Antibodies Hybridomas* **2**, 155–159 (1991).
27. Sukhorukov, V. L. *et al.* Surviving high-intensity field pulses: strategies for improving robustness and performance of electrotransfection and electrofusion. *J. Membr. Biol.* **206**, 187–201 (2005).
28. Usaj, M. & Kanduser, M. The systematic study of the electroporation and electrofusion of B16-F1 and CHO cells in isotonic and hypotonic buffer. *J. Membr. Biol.* **245**, 583–590 (2012).
29. Blangero, C. & Teissié, J. Ionic modulation of electrically induced fusion of mammalian cells. *J. Membr. Biol.* **86**, 247–253 (1985).
30. Kemna, E. W. M., Wolbers, F., Vermes, I. & van den Berg, A. On chip electrofusion of single human B cells and mouse myeloma cells for efficient hybridoma generation. *Electrophoresis* **32**, 3138–3146 (2011).
31. White, J. A. *et al.* Plasma membrane charging of Jurkat cells by nanosecond pulsed electric fields. *Eur. Biophys. J.* **40**, 947–957 (2011).
32. Joshi, R. P. & Schoenbach, K. H. Bioelectric effects of intense ultrashort pulses. *Crit. Rev. Biomed. Eng.* **38**, 255–304 (2010).
33. Batista Napotnik, T. *et al.* Electropermeabilization of endocytotic vesicles in B16 F1 mouse melanoma cells. *Med. Biol. Eng. Comput.* **48**, 407–413 (2010).
34. Ford, W. E., Ren, W., Blackmore, P. F., Schoenbach, K. H. & Beebe, S. J. Nanosecond pulsed electric fields stimulate apoptosis without release of pro-apoptotic factors from mitochondria in B16f10 melanoma. *Arch. Biochem. Biophys.* **497**, 82–89 (2010).
35. Beebe, S., Sain, N. & Ren, W. Induction of cell death mechanisms and apoptosis by nanosecond pulsed electric fields (nsPEFs). *Cells* **2**, 136–162 (2013).
36. Ibey, B. L. *et al.* Selective cytotoxicity of intense nanosecond-duration electric pulses in mammalian cells. *Biochim. Biophys. Acta* **1800**, 1210–1219 (2010).
37. Bowman, A. M., Nesin, O. M., Pakhomova, O. N. & Pakhomov, A. G. Analysis of plasma membrane integrity by fluorescent detection of Tl^+ uptake. *J. Membr. Biol.* **236**, 15–26 (2010).
38. Pucihar, G. & Miklavcic, D. in *5th Eur. Conf. Int. Fed. Med. Biol. Eng.* (Jobbágy, Á.) **37**, 1326–1329 (Springer Berlin Heidelberg, 2011).
39. Polevaya, Y., Ermolina, I., Schlesinger, M., Ginzburg, B. Z. & Feldman, Y. Time domain dielectric spectroscopy study of human cells. II. Normal and malignant white blood cells. *Biochim. Biophys. Acta* **1419**, 257–271 (1999).
40. DeBruin, K. A. & Krassowska, W. Modeling electroporation in a single cell. I. Effects of field strength and rest potential. *Biophys. J.* **77**, 1213–1224 (1999).
41. Gowrishankar, T. R., Esser, A. T., Vasilkoski, Z., Smith, K. C. & Weaver, J. C. Microdosimetry for conventional and supra-electroporation in cells with organelles. *Biochem. Biophys. Res. Commun.* **341**, 1266–1276 (2006).
42. Nesin, O. M., Pakhomova, O. N., Xiao, S. & Pakhomov, A. G. Manipulation of cell volume and membrane pore comparison following single cell permeabilization with 60- and 600-ns electric pulses. *Biochim. Biophys. Acta* **1808**, 792–801 (2011).
43. Vernier, P. T., Sun, Y. & Gundersen, M. A. Nanoelectropulse-driven membrane perturbation and small molecule permeabilization. *BMC Cell Biol.* **7**, 37 (2006).
44. Vasilkoski, Z., Esser, A. T., Gowrishankar, T. R. & Weaver, J. C. Membrane electroporation: The absolute rate equation and nanosecond time scale pore creation. *Phys. Rev. E* **74**, 021904 (2006).
45. Kanduser, M., Sentjurc, M. & Miklavcic, D. Cell membrane fluidity related to electroporation and resealing. *Eur. Biophys. J.* **35**, 196–204 (2006).
46. Sukhorukov, V. L., Djuzenova, C. S., Frank, H., Arnold, W. M. & Zimmermann, U. Electropermeabilization and fluorescent tracer exchange: the role of whole-cell capacitance. *Cytometry* **21**, 230–240 (1995).
47. Pakhomova, O. N. *et al.* Electroporation-induced electrosensitization. *PLoS ONE* **6**, e17100 (2011).
48. Stacey, M., Fox, P., Buescher, S. & Kolb, J. Nanosecond pulsed electric field induced cytoskeleton, nuclear membrane and telomere damage adversely impact cell survival. *Bioelectrochemistry* **82**, 131–134 (2011).
49. Kluza, J. *et al.* Induction of apoptosis in HL-60 leukemia and B16 melanoma cells by the acronycine derivative S23906-1. *Biochem. Pharmacol.* **63**, 1443–1452 (2002).
50. Ramos, C., Bonenfant, D. & Teissie, J. Cell hybridization by electrofusion on filters. *Anal. Biochem.* **302**, 213–219 (2002).
51. Stenger, D. A., Kaler, K. V. & Hui, S. W. Dipole interactions in electrofusion. Contributions of membrane potential and effective dipole interaction pressures. *Biophys. J.* **59**, 1074–1084 (1991).
52. Pucihar, G., Kotnik, T., Valic, B. & Miklavcic, D. Numerical determination of transmembrane voltage induced on irregularly shaped cells. *Ann. Biomed. Eng.* **34**, 642–652 (2006).
53. Pucihar, G., Miklavcic, D. & Kotnik, T. A time-dependent numerical model of transmembrane voltage inducement and electroporation of irregularly shaped cells. *IEEE Trans. Biomed. Eng.* **56**, 1491–1501 (2009).
54. Li, J. & Lin, H. The current-voltage relation for electropores with conductivity gradients. *Biomicrofluidics* **4**, 013206 (2010).
55. Rebersek, M. *et al.* Blumlein configuration for high-repetition-rate pulse generation of variable duration and polarity using synchronized switch control. *IEEE Trans. Biomed. Eng.* **56**, 2642–2648 (2009).
56. Sukhorukov, V. L. *et al.* A biophysical approach to the optimisation of dendritic-tumour cell electrofusion. *Biochem. Biophys. Res. Commun.* **346**, 829–839 (2006).
57. Kiesel, M. *et al.* Swelling-activated pathways in human T-lymphocytes studied by cell volumetry and electrorotation. *Biophys. J.* **90**, 4720–4729 (2006).

58. Garner, A. L. *et al.* Ultrashort electric pulse induced changes in cellular dielectric properties. *Biochem. Biophys. Res. Commun.* **362**, 139–144 (2007).
59. Mazzanti, M., Bustamante, J. O. & Oberleithner, H. Electrical dimension of the nuclear envelope. *Physiol. Rev.* **81**, 1–19 (2001).
60. Asami, K., Takahashi, Y. & Takashima, S. Dielectric properties of mouse lymphocytes and erythrocytes. *Biochim. Biophys. Acta* **1010**, 49–55 (1989).

Acknowledgments

This work was supported by the Slovenian Research Agency (ARRS) with program P2-0249. Research was conducted within the scope of the European Associated Laboratory for Pulsed Electric Field Applications in Biology and Medicine (LEA EBAM). Authors would like to thank D. Hodžić for her kind help with cell culture, A. Retelj for lending the control unit and for his valuable suggestions on automatization of the pulse delivery system, T. Jarm for his help with statistical analyses, and T. Batista Napotnik for discussions on experimental results.

Author contributions

G.P. performed the initial numerical calculations and designed and directed the study. M.U. designed and directed the *in vitro* experimental part of the study and contributed to data interpretation. G.P. and M.U. performed the initial experiments based on experimental laboratory protocols established by M.U. and M.K. L.R. performed numerical calculations and experiments presented in the paper and contributed to the design of the study. M.R. designed the custom made nanosecond pulse generator, the pulse delivery and measurement system. M.K. and D.M. contributed to the design of the study and interpretation of results. L.R. and M.U. co-wrote the paper. Other authors all contributed to the writing of the paper.

Additional information

Supplementary information accompanies this paper at http://www.nature.com/scientificreports

Competing financial interests: The authors declare no competing financial interests.

How to cite this article: Rems, L. *et al.* Cell electrofusion using nanosecond electric pulses. *Sci. Rep.* **3**, 3382; DOI:10.1038/srep03382 (2013).

Supplementary Information for:

Cell electrofusion using nanosecond electric pulses

Lea Rems[1,2], Marko Ušaj[1,2], Maša Kandušer[1], Matej Reberšek[1], Damijan Miklavčič[1] & Gorazd Pucihar[1]

[1]University of Ljubljana, Faculty of Electrical Engineering, Tržaška cesta 25, SI-1000 Ljubljana, Slovenia.
[2]These authors contributed equally to this work.

Correspondence and requests for materials should be addressed to D.M. (damijan.miklavcic@fe.uni-lj.si).

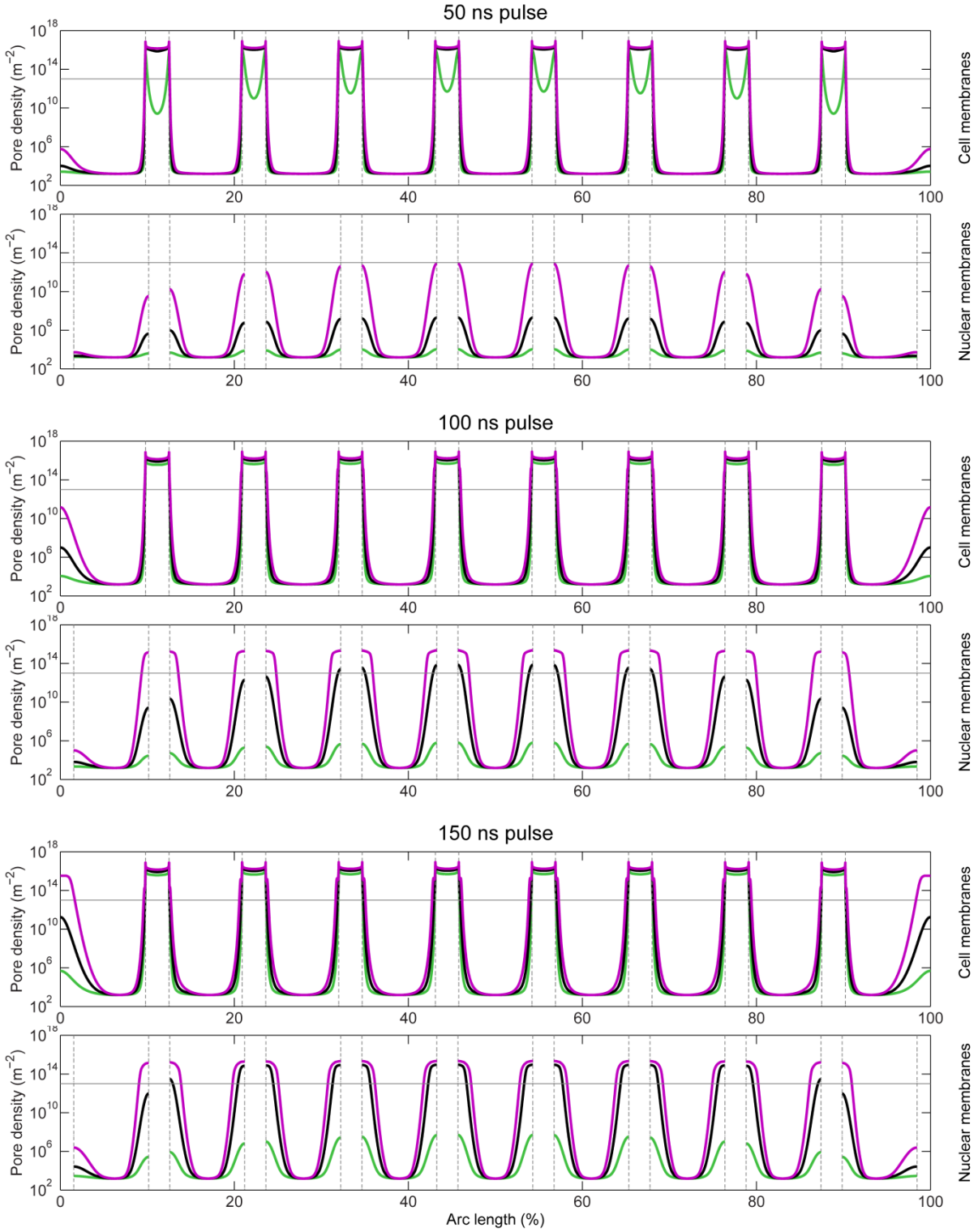

Supplementary Figure S1. Pore density along cell and nuclear membranes calculated with the model of experiments on B16-F1 cells. Calculations for each pulse duration are indicated above graphs. The amplitudes are colour-coded as follows: green (6 kV/cm), black (9 kV/cm), magenta (12 kV/cm). In calculations for the cell membranes, vertical lines mark the contact areas. In calculations for the nuclear membranes, vertical lines mark both nuclear poles. Horizontal lines in all graphs mark pore density 10^{13} m^{-2}.

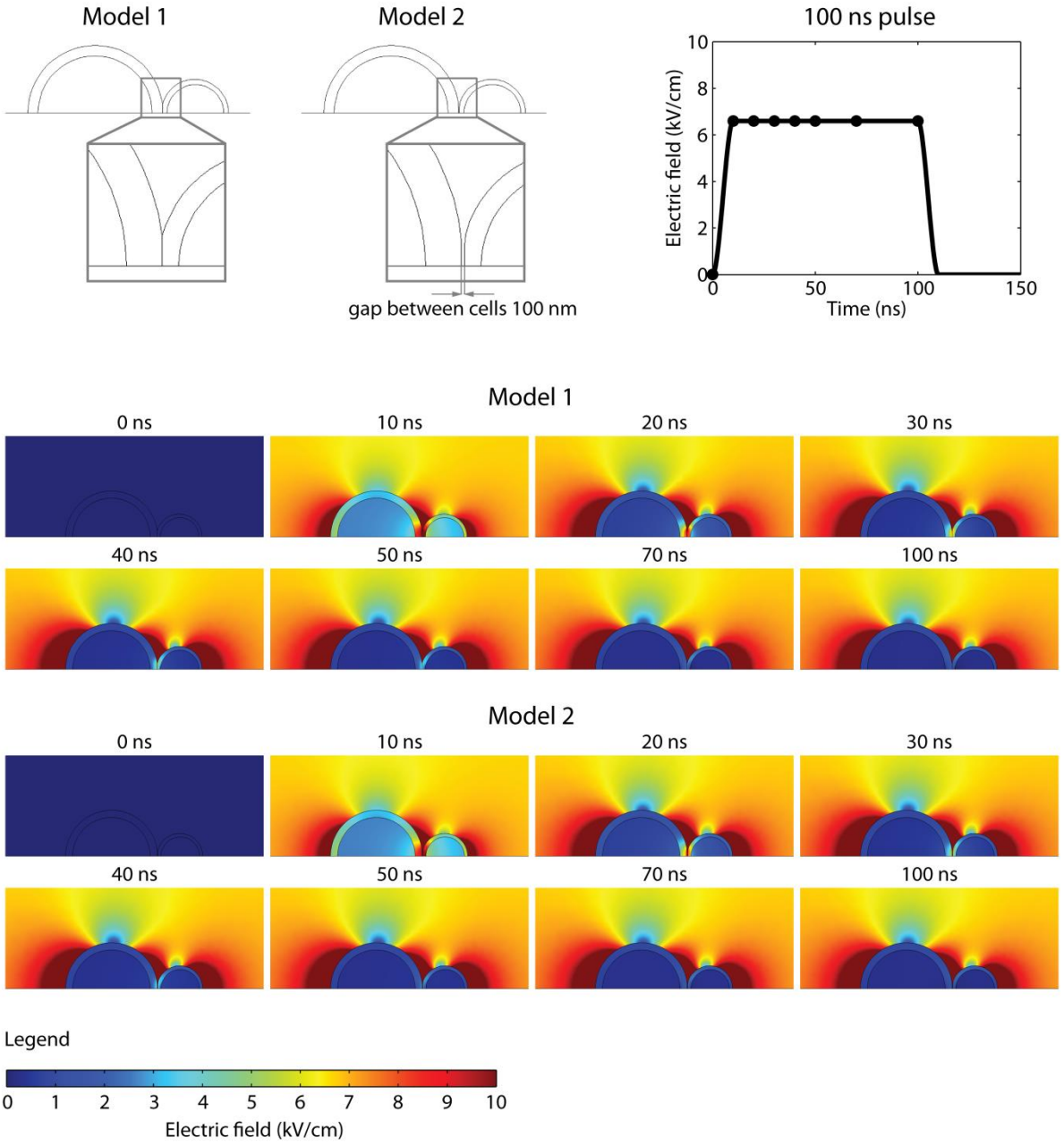

Supplementary Figure S2. Spatial distribution of the absolute value of the electric field after exposure to 100 ns, 6.6 kV/cm pulse. These pulse parameters were also used in calculations in Fig. 2b of the manuscript. Calculations were performed with two different models. Model 1 is equal to the one used to obtain other results presented in the manuscript. Model 2 considers two cells which are not in direct contact but are separated by a gap of 100 nm. The time after pulse application, for which the electric field is calculated, is indicated above each image. These times are also indicated with black dots on the image of the pulse in the top right corner. For electric field values higher than 10 kV/cm, the same colour is used as for 10 kV/cm. Note that the electric field reaches high values around the contact area regardless of the gap between cells.

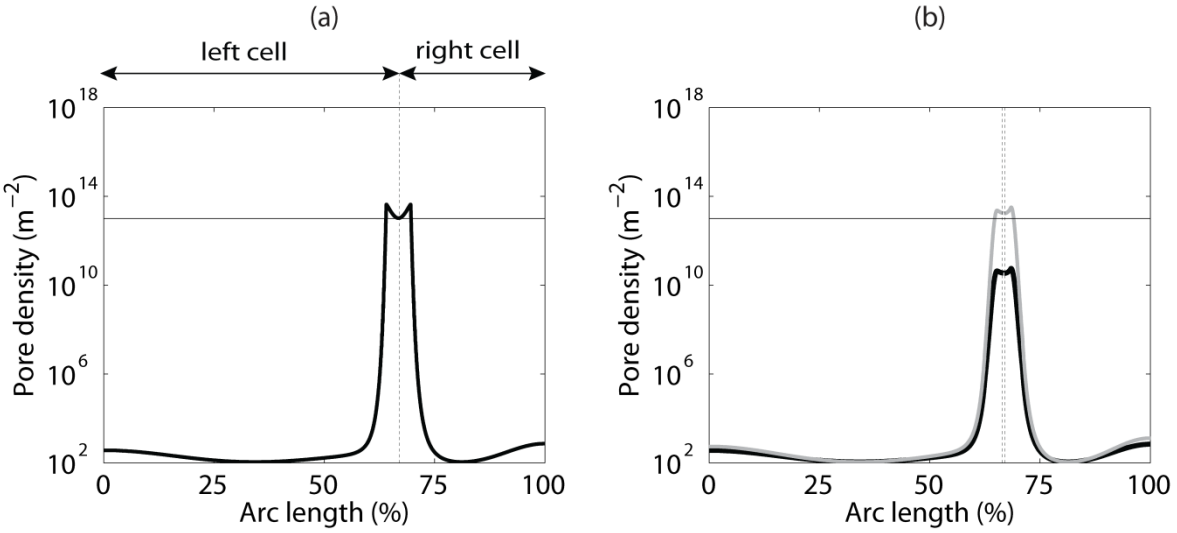

Supplementary Figure S3. Comparison of the pore density along cell membranes, calculated with (a) Model 1 and (b) Model 2 (see Supplementary Figure S2). Black line corresponds to pulse amplitude 6.6 kV/cm and grey line to 7.5 kV/cm. Vertical lines mark the middle of the contact area and horizontal lines mark pore density 10^{13} m^{-2}. Although Model 2 predicts a lower pore density, only moderate increase of the pulse amplitude is required to obtain similar results as with Model 1. Both models predict selective electroporation of the contact area. This means that a gap between cells, which could result from a relaxation of the forced contact area, would not greatly influence these results.

Paper 4

Title: **Modeling electroporation of the non-treated and vacuum impregnated heterogeneous tissue of spinach leaves**

Authors: Katarzyna Dymek, Lea Rems, Barbara Zorec, Petr Dejmek, Federico Gómez Galindo, and Damijan Miklavčič

Publication: Innov. Food Sci. Emerg. Technol. 29: 55–64, 2015
DOI: 10.1016/j.ifset.2014.08.006

Journal information

INNOVATIVE FOOD SCIENCE & EMERGING TECHNOLOGIES		
Publisher	ELSEVIER SCI LTD, THE BOULEVARD, LANGFORD LANE, KIDLINGTON, OXFORD OX5 1GB, OXON, ENGLAND	
ISSN eISSN	1466-8564 1878-5522	
Research domain	Food Science & Technology	
Impact factor	3.273 (2014) 3.699 (5 year)	
JCR® category	Rank in category	Quartile in category
FOOD SCIENCE & TECHNOLOGY	10 of 123	Q1

Source: Web of Science™ (December 2015)

Author contributions of L. Rems

L. Rems contributed to the construction and design of numerical models and numerical calculations, contributed to interpretation of the numerical results and writing of the manuscript.

Innovative Food Science and Emerging Technologies 29 (2015) 55–64

Contents lists available at ScienceDirect

Innovative Food Science and Emerging Technologies

journal homepage: www.elsevier.com/locate/ifset

Modeling electroporation of the non-treated and vacuum impregnated heterogeneous tissue of spinach leaves

Katarzyna Dymek [a,*], Lea Rems [b], Barbara Zorec [b], Petr Dejmek [a], Federico Gómez Galindo [a], Damijan Miklavčič [b]

[a] Food Technology, Engineering and Nutrition, Lund University, PO Box 124, SE-221 00 Lund, Sweden
[b] Faculty of Electrical Engineering, University of Ljubljana, Trzaska 25, SI-1000 Ljubljana, Slovenia

ARTICLE INFO

Article history:
Received 24 May 2014
Accepted 25 August 2014
Available online 30 August 2014

Keywords:
Spinach leaf
Electroporation
Numerical modeling
Vacuum impregnation

ABSTRACT

Uniform electroporation of the heterogeneous structure of spinach leaf cross section is a technological challenge that is addressed in this investigation. Three dimensional models were created with cells arranged in specific tissue types, considering a leaf with its air fraction and a leaf where the air fraction was replaced by a solution of known properties using vacuum impregnation. The models were validated before electroporation, in the frequency domain, where alternating voltage and current signal at frequencies from 20 Hz to 1 MHz were used to measure conductivity of the tissue. They were also validated through measurements of current during electroporation when a single 250 μs rectangular pulse with amplitudes ranging from 50 to 500 V was applied. Model validations show that both the frequency dependent conductivity and electroporation are well predicted. The importance of the wax layer and stomata in the model is thoroughly discussed.

Industrial relevance: Our aim was to investigate electroporation of the spinach leaf by developing a model which would enable us to meet the technological challenge of achieving uniform electroporation in a highly heterogeneous structure in the context of a process aimed at improving freezing stability of plant foods. Pulsed electric field treatment may be used to introduce the cryoprotectant molecules into the cells, and hence improve the structure and properties of frozen food plants.

1. Introduction

Electroporation of a cell membrane is defined as an increase in its permeability due to exposure of the cell to a sufficiently strong, external electric field (Kotnik, Kramar, Pucihar, Miklavcic, & Tarek, 2012; Neumann & Rosenheck, 1972; Neumann, Schaefer-Ridder, Wang, & Hofschneider, 1982; Zimmermann, Pilwat, & Riemann, 1974; Zimmermann & Vienken, 1982). Depending on the amplitude and duration of the applied electric field, electroporation may occur in two forms: irreversible (Phillips, Maor, & Rubinsky, 2011; Rowan, MacGregor, Anderson, Fouracre, & Farish, 2000) or reversible (Glaser, Leikin, Chernomordik, Pastushenko, & Sokirko, 1988; Miklavčič, Serša, Brecelj, Gehl, Soden, Bianchi, et al., 2012). For either purpose, theoretical studies coupled with experimental investigation contribute to the understanding of events taking place in cells and tissues during electroporation.

Theoretical studies of single cell electroporation have been conducted from different perspectives. Aspects such as the dynamics of pore formation and the transmembrane voltage distribution (DeBruin & Krassowska, 1999), the electroporation caused by bipolar pulses and dynamic pore radii (Talele, Gaynor, Cree, & van Ekeran, 2010), the conductance of electroporated cell membrane (Suzuki, Ramos, Ribeiro, Cazarolli, Silva, Leite, et al., 2011), the number of pores and pore radii in the cell membrane (Talele & Gaynor, 2010), the process of pore disappearance in the cell membrane (Saulis, 1997) and the electroporation of intracellular membranes (Gowrishankar, Esser, Vasilkoski, Smith, & Weaver, 2006; Retelj, Pucihar, & Miklavcic, 2013) have been widely studied in the literature using single cell models. Electroporation was also studied by using a model of dense cell suspension (Mezeme, Pucihar, Pavlin, Brosseau, & Miklavčič, 2012).

Electroporation of tissues has attracted great attention. Electroporation is an important technology used for medical purposes such as cancer treatment (electrochemotherapy) (Yarmush, Golberg, Serša, Kotnik, & Miklavčič, 2014), where the modeling of the electroporation process in the tissue becomes essential for treatment planning (Pavliha, Kos, Zupanič, Marčan, Serša & Miklavčič, 2012; Pavšelj & Miklavčič, 2008). In these models describing tissue electroporation, the representation of the heterogeneity and anisotropy of the tissues becomes a challenge. There are number of models describing electroporation in different types of tissues such as tumors, muscle, liver and skin, where the heterogeneous tissue layers are considered and the thermal effects of electroporation and transdermal drug delivery are studied (Pavšelj & Miklavčič, 2011; Zorec, Becker, Reberšek, Miklavčič, & Pavšelj, 2013). Electroporation of skin was also studied in terms of the effect of bipolar pulses (Arena, Sano, Rylander, & Davalos, 2011). Three dimensional models were used to evaluate the local electric field created

* Corresponding author. Tel.: +46 462229806; fax: +46 4622 24622.
E-mail address: katarzyna.dymek@food.lth.se (K. Dymek).

http://dx.doi.org/10.1016/j.ifset.2014.08.006
1466-8564/

in the anisotropic skeletal muscle during the application of electric pulses (Corovic, Zupanic, Kranjc, Al Sakere, Leroy-Willig, Mir, et al., 2010) and two dimensional models of nerves, blood vessels and ducts have been used to theoretically analyze irreversible electroporation (Daniels & Rubinsky, 2009).

The models describing electroporation are however mostly focused on a simplified geometry which shows the tissues as stacks of layers with specific bulk properties. In this paper we use a three dimensional model, containing a well-defined structure built from individual cells arranged in specific tissue types. Cells belonging to a certain tissue possess shape, dimensions and location mimicking the tissues in the real spinach leaf. The entire cross section of the leaf was considered including elements such as the cuticular wax and stomata.

Our aim was to investigate electroporation of the spinach leaf cross section by developing a model which would enable us to meet the technological challenge of achieving uniform electroporation in a highly heterogeneous structure in the context of a process aimed at improving freezing stability of plant foods (Phoon, Gómez Galindo, Vicente, & Dejmek, 2008; Shayanfar, Chauhan, Toepfl, & Heinz, 2013). The influence of specific elements such as cell size, cell arrangement, cuticular wax layer and stomata on the creation of pores (i.e. electroporation of the cell membranes under different applied pulse parameters), was investigated. The effects of the connections between cells and the air fraction in the tissue are also discussed. The model was first analyzed in the frequency domain, where alternating voltage and current signal at frequencies from 20 Hz to 1 MHz were used to measure conductivity in the tissue and validate the model.

2. Theoretical considerations

2.1. Spinach leaf structure

Spinach leaf has a typical thickness of 0.4 ± 0.1 mm. The cross section of the leaf consists of different tissues arranged in four layers. The spinach cross section is shown in Fig. 1A, where leaves were incubated with fluorescein diacetate as described by Dymek, Dejmek, and Gómez Galindo (2014) and examined under a microscope (Eclipse Ti-U, Nikon, Japan). At the top of the leaf cross section there is an upper epidermal tissue, which consists of a single layer of star-shaped cells. Epidermal cells are covered by a cuticular wax layer. Underneath the upper epidermis the palisade mesophyll is built from elongated cells which are formed by two cell layers. Below the palisade mesophyll, the spongy mesophyll is located. It has a multi-cell layer structure characterized by round cells distributed in a loose and apparently random structure. The majority of the intercellular air fraction is located in the spongy mesophyll (Warmbrodt & Woude, 1990). The air fraction accounts for approximately 30% of the leaf volume (Winter, Robinson, & Heldt, 1994). At the bottom, the lower epidermis is located.

2.2. Simplifications used to model the leaf

The model represents the internal tissues of a spinach leaf, restricting the elements included in the model to the essential ones. The leaf tissue possesses an extremely complex structure; therefore, the following simplifications were introduced into the model.

Veins were not included in the model. Since obtaining a time-dependent, finite-element solution for a 3D model with a complex structure consisting of multiple cells is relatively demanding with respect to computational time and random-access memory requirement, only a small part of the leaf with an area 107 μm × 107 μm was modeled. In the spinach leaf the minor veins are located within the distance from 49 to 231 μm (Warmbrodt & Woude, 1990) and were neglected in the model.

In the leaf the majority of the air fraction is located in the spongy mesophyll. Therefore, in the model, air fraction was neglected in the epidermal tissue and palisade mesophyll. In these tissues the cells were completely surrounded by extracellular liquid. However, in the spongy mesophyll the cells were surrounded by a thin layer of

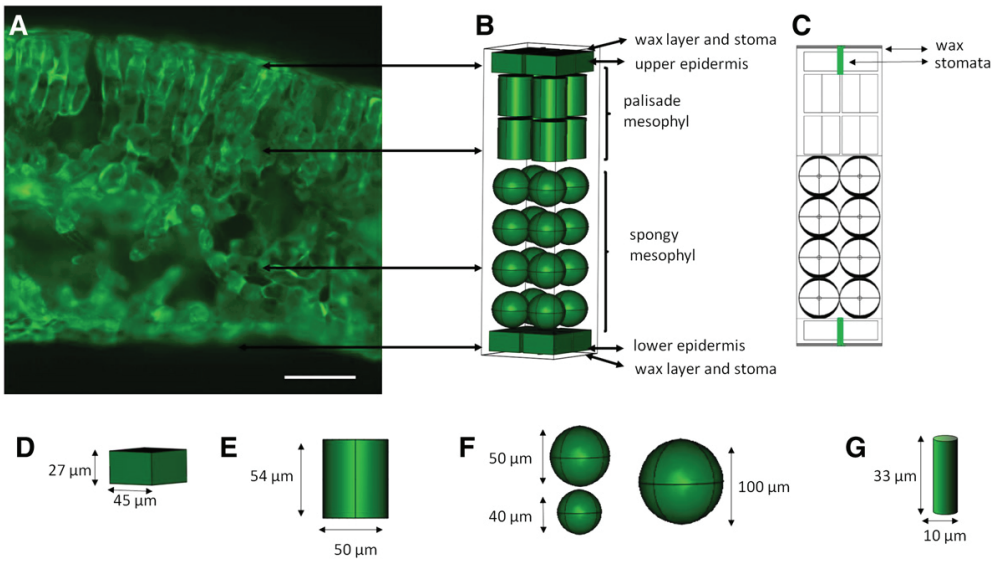

Fig. 1. The geometry of the model. A, B. The geometry of the model representing the whole spinach cross section is shown in relation with the microscopic picture. The scale bar represents 100 μm. C. Side view of the model with connections between cells marked with black. Stomata are marked in green and the cuticular wax layer in black. The dimensions of the different elements included in the model are shown in: D. epidermal cell, E. palisade mesophyll cell, F. spongy mesophyll cells, G. stoma.

extracellular liquid, which mimics the apoplastic pathway (space between the cell membrane and the cell wall) and connects all the cells in the spongy mesophyll. This thin layer was then directly surrounded by air, avoiding the need to specifically include the cell walls.

The shape of the epidermal cells was also simplified to avoid a too complex structure leading to excessive number of finite elements in the model and meshing problems. In the spinach leaf, epidermal cells are star-shaped, whereas in the model they are represented as blocks.

3. Numerical model

COMSOL Multiphysics 3.5a (COMSOL AB, Stockholm, Sweden), a commercial finite element software package, was used to perform calculations of the leaf conductivity at different frequencies when AC voltage was applied, and to simulate pore formation in the cell membranes when DC voltage (electroporative electric pulse) was applied.

3.1. Geometry of the model

The model of the spinach leaf cross section was created based on microscopic pictures from previously published papers (Warmbrodt & Woude, 1990; Winter, Robinson & Heldt, 1994) as well as our observations and measurements.

The model represents a part of the spinach leaf with an area of 107 μm × 107 μm and thickness of 420 μm. Fig. 1B shows how the cells were arranged in the four tissue layers: lower and upper epidermis and mesophyll differentiated into palisade and spongy cells. The proportions of the tissues were based on the micrographs (Warmbrodt & Woude, 1990; Winter, Robinson & Heldt, 1994). Epidermal cells were presented as blocks with dimensions of 45 μm × 45 μm × 27 μm (Fig. 1D). There was a single layer with four epidermal cells located at the bottom and top of the leaf. Palisade mesophyll cells were presented as 54 μm long cylinders having a diameter of 50 μm (Fig. 1E). They were arranged in two layers, each consisting of four cells. Spongy mesophyll is the most irregularly structured tissue due to its high air fraction. Therefore, to examine the influence of the cell distribution and size on the electrical properties of the spinach leaf, three models with different arrangements of spongy mesophyll cells were built, as shown in Fig. 2. Model A contained two large spongy mesophyll cells with a diameter of 100 μm; model B contained 4 rows of cells having a diameter of 50 μm, with 4 cells placed in each of the rows; and model C contained randomly located spongy mesophyll cells with two different diameters: 50 and 40 μm.

Additionally, model D was built, which had the same cell arrangement as model B. However, at the top and bottom of the leaf there were also 0.3 μm thick cuticular wax layers (Hardin, Jones, Weckler, Maness, Dillwith, & Madden, 2013; Riederer & Schreiber, 2001) (Fig. 1C). Both wax layers contained ellipsoidal holes filled with air (10 μm long and 4.5 μm wide), which were extended further into the epidermal tissue in the shape of elliptic cylinders, representing the stomata (Fig. 1C and G, marked with green).

3.2. Connections between cells

The proper function of the whole plant organism is enabled by connections between cells. Since the cells are surrounded by non-conductive air fraction, their connections influence significantly the current flow through the tissues. In the model, the air fraction was included only in the spongy mesophyll. To model the connections between cells (the apoplastic pathway), in each of the different models (A, B, C and D) the spongy mesophyll cells were surrounded by a thin layer of extracellular fluid (shown in black in Fig. 1C and also in white in side views of the models in Fig. 2). This layer was built by slightly increased and elongated elements overlapping each other at the poles; the minimum thickness of the layer was 0.5 μm, whereas at the poles of the spongy cells, its thickness was increased to 4 μm, to allow connecting the cells. The rest of the volume in spongy mesophyll was filled with air. The interface between the layer representing the apoplastic pathway and the air then mimicked the cell walls.

Another model was built representing a vacuum impregnated leaf, where the air fraction was removed and all cells were surrounded by an external solution of known properties, resulting in a continuously conductive pathway trough the leaf. In this case, the connections between cells were neglected. The cell walls could be omitted as well, because they influence neither the electroporation process nor the transport of small molecules (Kandušer, & Miklavčič, 2008).

3.3. Model parameters

To model the electrodes, an electric potential was assigned to the upper and lower boundaries of the leaf model. One side was grounded and the other was excited by a single, rectangular 250 μs pulse with amplitudes ranging from 50 to 500 V. The pulse was modeled as described by Retelj, Pucihar and Miklavcic (2013) using the COMSOL function flc1hs. The pulse rise and fall times were set to 1 μs. The vertical sides of the model were modeled as electrically insulated. Mathematical

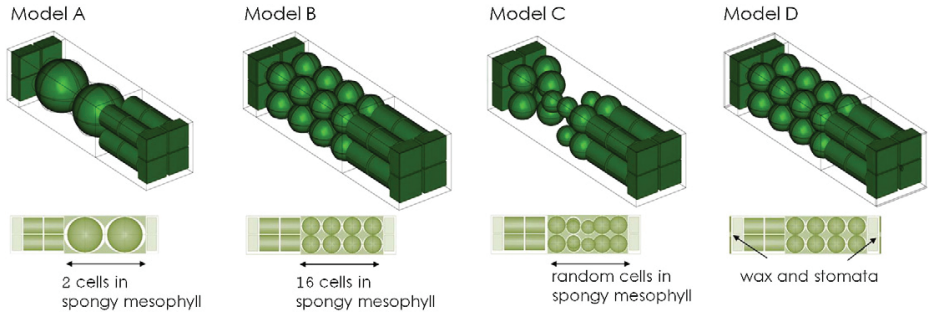

Fig. 2. The geometry of investigated models of untreated spinach leaf cross section with highlighted main differences between models. The three dimensional view as well as the schematic side view of the models is shown. Model A. The model represents the spinach leaf cross section with two large cells in the spongy mesophyll tissue. Model B. The model represents the spinach leaf cross section with 16 cells in the spongy mesophyll tissue arranged in the 4 rows with 4 cells per row. Model C. The model represents the spinach leaf cross section with randomly located cells in the spongy mesophyll tissue. Model D. The model represents the spinach leaf cross section with 16 cells in the spongy mesophyll tissue arranged in the 4 rows with 4 cells per row, the same as model B, but in model D also the cuticular wax layers and stomata are included.

equations describing electroporation of the cell membrane were taken from DeBruin and Krassowska (1999) and the method for calculating the induced transmembrane voltage was adopted from Pucihar, Miklavcic, and Kotnik (2009). Electric potential V was calculated by

$$-\nabla(\sigma_i\nabla V)-\nabla\frac{\partial(\varepsilon_i\nabla V)}{\partial t}=0 \tag{1}$$

where σ_i and ε_i are the conductivity and dielectric permittivity, respectively. The cell membrane was modeled using *Distributed Impedance* boundary condition by

$$\boldsymbol{n}\cdot\boldsymbol{J}=\frac{\sigma_m}{d_m}\left(V-V_{ref}\right)+\frac{\varepsilon_m}{d_m}\left(\frac{\partial V}{\partial t}-\frac{\partial V_{ref}}{\partial t}\right) \tag{2}$$

where $\boldsymbol{J}$ is the current density through the cell membrane, $\boldsymbol{n}$ is the unit vector normal to the membrane surface, V and V_{ref} are the potentials on each side of the membrane, d_m is the membrane thickness, σ_m is the membrane conductivity and ε_m is the membrane dielectric permittivity. A difference between the electric potential on each side of the boundary gives the induced transmembrane voltage (ITV).

The differential equation describing the dynamics of pore formation is

$$\frac{dN}{dt}=\alpha e^{\left(\frac{ITV}{V_{ep}}\right)^2}\left(1-\frac{N}{N_0}e^{-q\left(\frac{ITV}{V_{ep}}\right)^2}\right) \tag{3}$$

where N is the pore density, N_0 is the pore density in non-electroporated cell membrane and α, q and V_{ep} are electroporation parameters. Formation of pores considerably increases the conductivity of the cell membrane. This increase in conductivity due to electroporation can be calculated as (DeBruin & Krassowska, 1999)

$$\sigma_{ep}=\pi r_p^2\sigma_p N\frac{e^V m-1}{\frac{we^{w-nV}m-nV_m}{w-nV_m}e^{V_m}-\frac{we^{w-nV}m+nV_m}{w+nV_m}} \tag{4}$$

where r_p is the radius and σ_p is the internal conductivity of a pore. $V_m = ITV\cdot F/(R\cdot T)$ is the nondimensional transmembrane voltage, where F is the Faraday constant, R is the universal gas constant, and T is the temperature. Parameter n represents the length of pore entrance area, and w accounts for the energy cost for moving an ion from a region of high dielectric constant (water) to a small pore in the lipid bilayer with low dielectric constant. The total membrane conductivity, as used in Eq. (2), is then calculated in each time step as the sum of the passive membrane conductivity (given in Table 1) and σ_{ep}.

The conductivity and relative permittivity of the particular elements, such as cytoplasm and cell membranes, were set according to the published data and are listed in Table 1.

4. Measurements

4.1. Raw material

Spinach leaves were collected from the local supermarket. Leaves were stored at 1–2 °C in closed plastic bags and used for experiments until the expiration date established by the producer (9 days from the packaging date). Leaves of similar size (6 ± 0.5 cm long and 2.5 ± 0.3 cm wide) were selected for the experiments.

4.2. Measurements of leaf electric conductivity

Samples (1 cm × 1 cm) were cut from the leaf. Each sample was cut in the same spot at the center of the leaf, from the central vein towards the edge. Samples were immersed in a 0.25 S/m PBS buffer (Phosphate Buffered Saline) and placed between two flat stainless steel electrodes, which were smaller than the sample, hence a leaf area of 64 mm^2 was enclosed between the electrodes. Conductivity of the PBS was measured with a conductivity meter (Orion 150, Orion Research Inc., Jacksonville, FL, USA). Electrodes were squeezed with a plastic clamp and connected to an impedance analyzer (4192A LF, Hewlett Packard, California, USA). A sinusoidal signal of 1 V amplitude was applied to the leaf samples and the resistance (in Ohms) was recorded at frequencies from 20 Hz to 1 MHz. The measurement was done for untreated samples (with air fraction) and for samples after vacuum impregnation (without air fraction).

4.2.1. Evaluation of the effect of the air fraction on leaf electric conductivity

To determine the influence of the air fraction on the electrical properties of the spinach leaf and to analyze the importance of its presence in the model, the air fraction of the leaf was removed and replaced by an external solution using vacuum impregnation.

Three leaves were immersed in 100 ml PBS buffer with conductivity of 0.25 S/m. Immersed leaves were placed in a vessel connected to a vacuum pump and vacuum controller (S.I.A., Bologna, Italy) as described by Panarese, Dejmek, Rocculi and Gómez Galindo (2013). The pressure was decreased to 150 mbar in 3.5 min. It was kept constant at 150 mbar for 1 min and increased for 4.5 min until atmospheric pressure was recorded. Samples were kept under atmospheric pressure for 10 min. The entire cycle was repeated twice (Demir, 2012). The relative increase in the leaf mass after vacuum impregnation was 39 ± 5%.

4.3. Measurements of current changes during electroporation

Leaves were placed between two flat stainless steel electrodes. The gap between electrodes was 4 mm and it was filled with PBS buffer of conductivity 0.25 S/m. The area of the leaf samples enclosed between the electrodes was 64 mm^2. A single electric pulse of 250 μs with amplitude of 50, 100, 200, 300, 400 or 500 V was applied. The pulse was delivered by a CEPT® electroporator (ARC AROMA PURE, Lund, Sweden). The current was recorded by a scopemeter (Fluke 123, Industrial Scopemeter, Washington, USA) equipped with a current probe.

5. Results and discussion

5.1. Influence of the cell size, cell arrangement, cuticular wax layer and stomata on the frequency-dependent conductivity of the spinach leaf model

Results obtained using models A–C (Fig. 2) were compared with measurements of the frequency-dependent conductivity of the spinach leaves (Fig. 3). When comparing models A–C with experimental measurements, it can be clearly seen that the models resulted in higher conductivity values for frequencies lower than 10 kHz and failed to predict the increase in conductivity measured from 100 kHz to 1 MHz. Furthermore, results obtained from models A, B and C show that the influence of the spongy mesophyll cell size and cell arrangement on the calculated conductivity is not significant. Two large cells located in the spongy mesophyll (Fig. 2, model A) showed a very similar conductivity (differed by 0.15 mS/m) as 16 cells located in the spongy mesophyll (Fig. 2, model B) at 10 Hz. Randomly located cells (Fig. 2, model C) resulted in slightly lower conductivities.

Model D (Fig. 2) contains additional elements to model B: cuticular wax layer and stomata, which has a significant influence on the overall electrical properties of the spinach leaf. Model D resulted in conductivity values increasing from 0.56 mS/m at 10 Hz to 4 mS/m at 1 MHz and was thus the only one able to predict (at least qualitatively) the measured increase in conductivity with increasing frequency. This clearly demonstrates that the electrical properties of the cuticular wax layer predominantly determine the properties of the leaf in the observed frequency range (stomata were filled with air and hence could not

Table 1
Parameters used in the model.

Parameter	Value
Extracellular liquid conductivity (σ_{ex})	0.0084 S/m (Stout, Hall, & McLaughlin, 1987)
Extracellular liquid permittivity (ε_{ex})	80 (Gavish & Promislow, 2012)
Cell membrane conductivity (σ_m)	0.00003 S/m (Wanichapichart, Bunthawin, Kaewpaiboon, & Kanchanapoom, 2002)
Cell membrane permittivity (ε_m)	10 (Wanichapichart, Bunthawin, Kaewpaiboon & Kanchanapoom, 2002)
Cytoplasm conductivity (σ_{cyt})	0.2 S/m (Harris & Kell, 1983)
Cytoplasm permittivity (ε_{cyt})	80 (Asami, Hanai, & Koizumi, 1980)
Cuticular wax layer conductivity (σ_{cut})	5×10^{-8} S/m (Ramos-Barrado, Benavente & Heredia, 1993), 5×10^{-7} S/m
Cuticular wax layer permittivity (ε_{cut})	10, 45, 80 (Gavish & Promislow, 2012)
Air conductivity (σ_{air})	8×10^{-15} S/m (Pawar, Murugavel, & Lal, 2009)
Air permittivity (ε_{air})	1.006 (Hector & Schultz, 1936)
Impregnating solution conductivity (σ_{im})	0.25 S/m
Impregnating solution permittivity (ε_{im})	80 (Gavish & Promislow, 2012)
Electroporation parameter (α)	10^9 m^{-2} s^{-1} (DeBruin & Krassowska, 1999)
Characteristic voltage of electroporation (V_{ep})	0.258 V (DeBruin & Krassowska, 1999)
Electroporation constant (q)	2.46 (DeBruin & Krassowska, 1999)
Equilibrium pore density (N_0)	1.5×10^9 m^{-2} (DeBruin & Krassowska, 1999)
Energy barrier within pore (w)	2.65 (DeBruin & Krassowska, 1999)
Pore radius (r_p)	0.76 nm (DeBruin & Krassowska, 1999)
Relative entrance length of pores (n)	0.15 (DeBruin & Krassowska, 1999)

contribute to the calculated increase in conductivity). This also explains why models A–C, although possessing different cell sizes and arrangements, responded similarly; the polarization of cell membranes (known as the Maxwell–Wagner effect) does not considerably affect the calculated overall conductivity of the leaf at this frequency range.

One can also note that at high frequencies (>10 kHz) model D with cuticular wax layer gives similar results as models A, B and C without cuticular wax. This means that at these frequencies, the cuticular wax becomes electrically 'transparent' and the rest of the leaf tissues determine the leaf conductivity. Since the values predicted by the model are lower compared to the measured conductivity for frequencies above 10 kHz, apparently the model underestimates the overall conductivity of internal leaf tissues. This may be due to different factors such as the number of cell membranes, cell volumes, as well as extra- and intracellular conductivities. An important factor influencing the disagreement between the data obtained theoretically and experimentally may also be the connections between the cells. In the plant tissue all cells are connected by the plasmodesmata for the proper functioning of the whole organism. The symplast, which is the continuum created by the connected cytoplasms, is not included in the model, since the cells are modeled as membrane-separated elements. The symplast may influence the electrical properties of the tissue by creating additional conductive pathways to the apoplast.

The air fraction is clearly another factor influencing the disparity of the theoretical and experimental results. The average amount of air in the tissue is known, however the location and the size of the air spaces are not uniform in the highly unorganized structure, while in the model the structure is simplified and symmetrical.

Moreover, there are assumptions made considering the conductivities of the cytoplasm and extracellular liquid. The values are taken from previously published data (Table 1), which may also introduce certain differences between the theoretical and experimental data.

5.2. Influence of the air fraction on the conductivity of the spinach leaf

To avoid the randomness introduced by the air fraction in plant tissues, a model without the air fraction was created and investigated. The model of vacuum impregnated leaf is simpler, and hence, less random than the model of non-treated leaf as the connections between cells and the air fraction is removed. The air fraction was exchanged

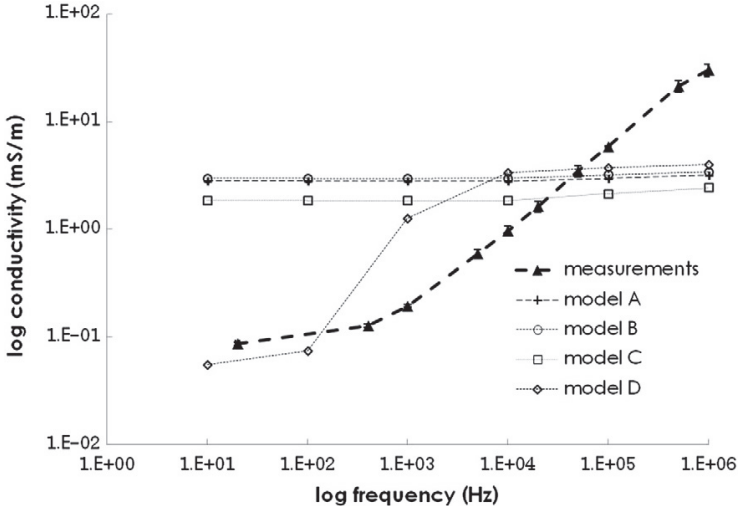

Fig. 3. Comparison of the conductivity changes over the frequency range for experimental measurements and 4 different models with different arrangements of cells in the spongy mesophyll represented in Fig. 2. Error bar represents standard deviation of three replicates.

with a solution of 0.25 S/m conductivity. The model was compared to the experimental data obtained by investigating the conductivity of the leaf samples after vacuum impregnation. For investigating the vacuum impregnated leaf, model D was chosen (4 rows, 4 cells per row). Opened stomata after vacuum impregnation (which were observed under the microscope — results not shown) suggest that they were not fully flooded with buffer after the vacuum impregnation process (Sibbernsen & Mott, 2010). Therefore, in the model representing the vacuum impregnated leaf (without air fraction) stomata were filled with air.

In Section 5.1. we stressed the important influence of the cuticular wax layer on the overall conductivity of the leaf. However, to the best of our knowledge, there are no studies describing the conductivity and permittivity of the spinach cuticular wax layer. For this reason we tested different values of cuticular wax conductivity and permittivity and compared the calculated results with experimental measurements. The conductivity of tomato cuticular wax, 5×10^{-8} S/m, was taken as a reference from the existing literature (Ramos-Barrado, Benavente, & Heredia, 1993), and in addition, a higher conductivity of 5×10^{-7} S/m was also tested. The relative permittivity of the cuticular wax was investigated in the range from 10 to 80, since it is composed from a cuticle matrix with a relative permittivity of approximately 10, containing aqueous pores filled with ionic solutes with relative permittivity of approximately 80 (Schönherr, 2006).

Fig. 4 shows the comparison of the theoretical and experimental data of the vacuum impregnated leaf. The measured conductivity increases with frequency (bold dashed line, Fig. 4). All of the tested values of cuticular wax conductivity and relative permittivity reasonably agreed with the measurements. However, the model using 5×10^{-7} S/m (dashed line B, Fig. 4) had the best prediction of the conductivity values at low frequencies (10–1000 Hz). The final conductivity (at 1 MHz) is similar (90.2–99.8 mS/m) for all tested conductivities and permittivities of the wax layer, consistent with the previously noted observation that the cuticular wax becomes electrically 'transparent' at this frequency, and its influence on the overall leaf conductivity is negligible. The wider transition of the frequency-dependent increase in the measured data compared to model predictions is also indicative of multiple relaxation processes, which could be described by a constant phase element, such as for tomato cuticle (Ramos-Barrado, Benavente & Heredia, 1993).

Indeed, the model of vacuum impregnated leaf even slightly overestimates the measured conductivity at 1 MHz. In the model an ideal process of vacuum impregnation (100% of the air is replaced by the solution) is considered, which may have contributed to the observed discrepancy between the models and experimental data. It was observed that when spinach leaves were impregnated with a sugar solution and examined with micro-X-ray tomography (Panarese, unpublished data), random air pockets remained in the structure accounting for approximately 2–3% of the total volume. These air pockets would decrease the general conductivity of the leaf.

5.3. Electroporation of the spinach leaf cross section

Electroporation of the vacuum impregnated spinach tissue was investigated and compared with the theoretical results by measuring the electric current during the pulse at applied voltages from 50 to 500 V (Fig. 6). Since the leaf is covered with a cuticular wax layer of high resistance, the stomata seem to play a critical role in the electric field distribution within the leaf and the current flow through the leaf cross section.

Stomata were investigated in two hypothetical situations (i) with air in the stomata. This scenario is supported by microscopic observations (Fig. 5A), done as described by Dymek, Dejmek and Gómez Galindo (2014), showing opened stomata (marked with arrows) after vacuum impregnation. According to Sibbernsen and Mott (2010) stomata would close if totally flooded with solution. (ii) It is assumed that electroporation provokes leakage from electroporated cells with a consequent temporal wetting of the solution of the guard cells of stomata. This scenario is supported by microscopic observations (Fig. 5B) showing electroporated guard cells when propidium iodide was used as an electroporation indicator (Dymek, Dejmek & Gómez Galindo, 2014). With pulse amplitudes of 200 V–500 V all the guard cells were uniformly electroporated within the leaf samples (Fig. 5B). With pulse amplitude of 100 V, some of the guard cells in the leaf sample were not electroporated and with pulse amplitude of 50 V, none of the observed guard cells were electroporated. Electric current values obtained by the models at 50 and 100 V are enclosed within the error bars of the measurements. Cells wetting by electroporation may be regarded as temporal as it is well known that a cell membrane that is partially damaged has the ability to recover even if the damage has caused enhanced ion leakage. ATPase activity will help the cell to take up leaked ions against the concentration gradient (Arora & Palta, 1991). We have here considered the application of a single pulse. It is worth to underline that if a train of pulses would be applied to cause reversible permeabilization, the first pulse or pulses affecting stomata will change the modeling situation from a tissue with air-filled stomata to a tissue with stomata filled with cell sap.

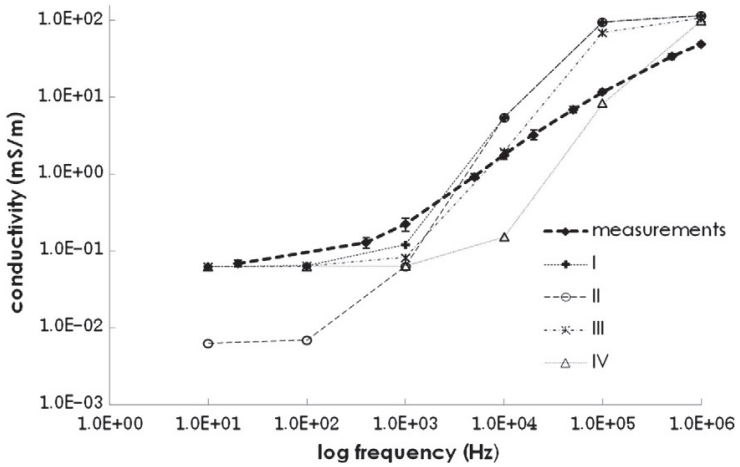

Fig. 4. The measured conductivity of vacuum impregnated spinach leaves compared with the model solved for different values of the conductivity (σ) and permittivity (ε) of the cuticular wax layer: I. $\varepsilon = 80, \sigma = 5 \times 10^{-7}$ S/m II. $\varepsilon = 80, \sigma = 5 \times 10^{-8}$ S/m III. $\varepsilon = 45, \sigma = 5 \times 10^{-7}$ S/m IV. $\varepsilon = 10, \sigma = 5 \times 10^{-7}$ S/m. Error bar represents standard deviation of three replicates.

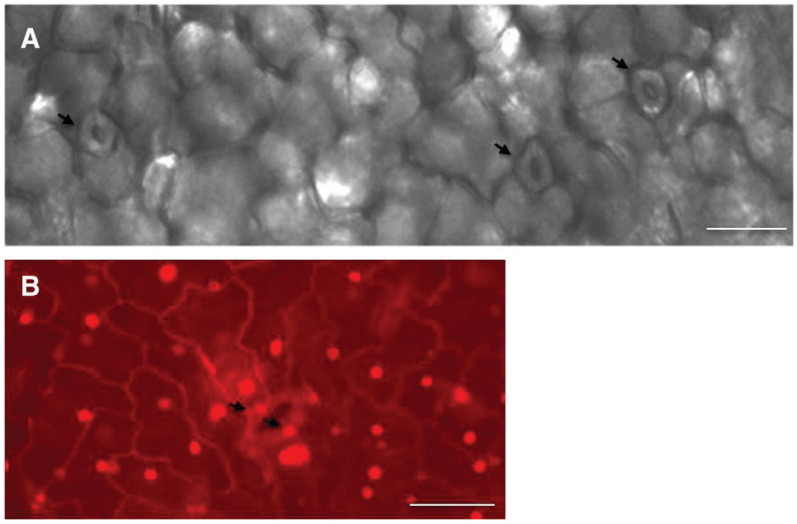

Fig. 5. Representative microscopic pictures showing: A. open stomata after vacuum impregnation process (marked with arrows). B. electroporated guard cells of stomata previously stained with propidium iodide as described in Dymek et al. (2014). One 250 μm rectangular, monopolar pulse with amplitude of 200 V was applied to previously vacuum impregnated leaf. The scale bars represent 20 μm.

In Fig. 6, the current predicted for the two models based on the hypothetical situations described above was compared with measured values of the current during the application of the electric pulse. The model with cell sap in stomata shows good agreement between theoretical and experimental values during the application of electric pulses, whereas the model with air in stomata shows significantly lower values than the measurements. The experimentally measured current increased from 0.1 A at 50 V to 4.5 A at 500 V. The model with air in stomata resulted in currents from 0.00055 A at 50 V to 0.0054 at 500 V. The current obtained by solving the model with solution in stomata was 0.33 A at 50 V and it increased up to 3.9 A at 500 V.

Fig. 7 shows the calculated values of the resistance (i.e. inversed value of conductance) of the spinach leaf cross section for voltages from 50 to 500 V. The resistance was calculated from measured current by R = V/I, where R — resistance (Ω), V — voltage (V), and I — current (A). The resistance decreased significantly as the voltages applied were increased from 50 to 300 V and did not further decrease with increasing amplitude of pulses from 300 V to 500 V. Electroporation of the cell membranes causing the decrease of resistance is accompanied by the increasing number of the average pore density calculated by the model (Fig. 7). Fig. 7 also shows that pore density increases markedly in the range from 50 V to 300 V for both models. At applied voltages in the range from 300 V to 500 V pore density however is not further increased. We can conclude that the evolution of pore density corresponds well to the observed decrease in resistance as the function of the applied pulse amplitude.

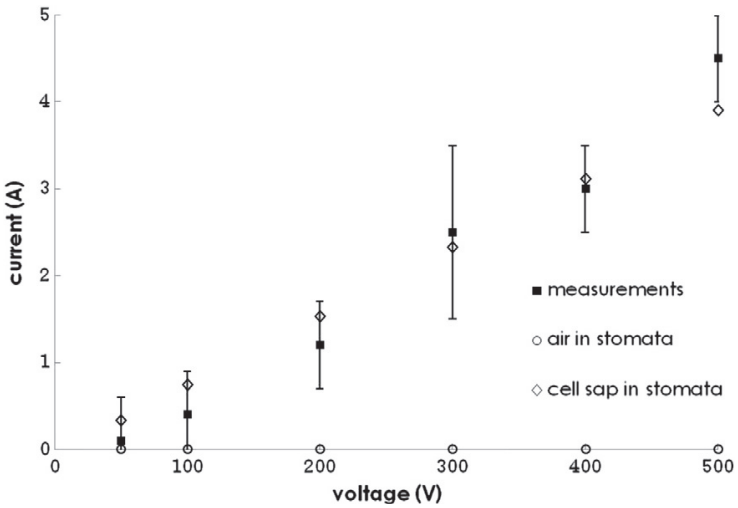

Fig. 6. The measured electric current through vacuum impregnated spinach leaf at different applied voltages, compared with the model solved for two different situations in which stomata are either filled with air or with leaked cell sap from electroporated guard cells. Error bar represents standard deviation of three replicates.

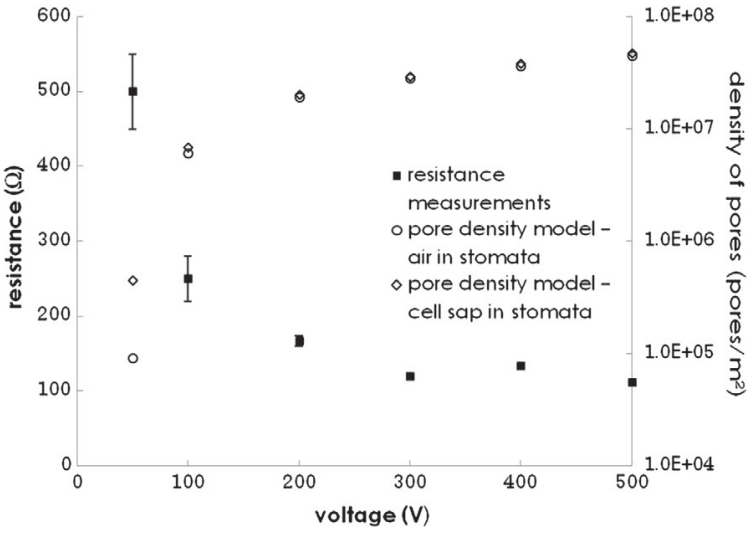

Fig. 7. Calculated average pore density from two models and change in resistance with increasing voltage. The resistance at different applied voltages is plotted together with calculated average pore density for the entire leaf section for two models: air in stomata and call sap in stomata. Resistance was calculated from measured current by R = V/I, where R — resistance (Ω), V — voltage (V), and I — current (A).

A detailed representation of pore density at various applied voltages, indicating electroporation of the different types of cells in the entire cross section of the leaf, was calculated as described by DeBruin and Krassowska (1999) and is shown in Fig. 8. The density of pores is compared between the model with air and the model with cell sap in the stomata. The main difference in pore density can be seen at 50 V, where the model with cell sap in the stomata results in higher pore density than the model with stomata filled with air.

Even if the two tested models show very different results on the changes of current with increasing voltage (Fig. 6), the pore density in the range from 100 to 500 V is similar for the model with air in stomata and for the model with cell sap in stomata (Fig. 8). Since the resistance of the outer layers (upper and lower cuticular wax) is significantly higher than the interior of the leaf cross section (epidermal, mesophyll cells and solution surrounding the cells) the current is determined by the stomata filled either with air or cell sap. However, the pore density is not influenced by the change of settings in the models (air in stomata or cell sap in stomata) due to the still significantly higher resistance of the cuticular wax layer from the internal tissues, regardless of how stomata is filled.

At 50 V the model with air filled stomata is electroporated only at the external surface of the epidermal cells, while the spongy and palisade mesophyll is slightly electroporated. The model with solution in the stomata shows that at 50 V the epidermal cells are electroporated mostly at the surface but also the internal tissues (palisade and spongy mesophyll) are electroporated showing higher pore density than that for the model with air in the stomata. Worth highlighting is the different pattern of pore formation at 50 V. For the model with stomata filled with air electroporation starts at the central part of the epidermal cells surface, while in the model with stomata filled with solution the pores are created around the stomata and at the central part of the epidermal cells surface. With higher voltages (100–500 V) the density of pore increases uniformly in all tissue types. Interesting, the progression of pores density with higher applied voltage (from 100 V to 500 V) is similar for both models. At 100 V the cells of all the tissue types are electroporated at the poles facing the electric field direction. At 200 V it can be seen that the spongy mesophyll cells are uniformly electroporated, while for the palisade mesophyll cells higher pore density is still visible at the poles than at the sides. With higher voltages (300–500 V) the pore density becomes uniform for all the cells.

6. Conclusions

This study has focused on modeling electroporation of the complex heterogeneous structure of spinach leaves. The following remarks underline important findings:

1. In the model of vacuum impregnated leaf, the impregnating solution considerably contributes to the conductive pathways through the leaf cross section. The frequency-dependent conductivity obtained with the model of vacuum impregnated leaf agrees well with the measurements. In the model of nontreated leaf, however, the extent of conductive pathways was probably underestimated.
2. The general conductivity of the leaf is significantly determined by the low conductive wax layer. Since stomata are 'holes' in the wax layer, they play a crucial role in the current flow throughout the leaf cross section. The current is, therefore, markedly affected if stomata are filled with air/gas or cell sap.
3. This theoretical investigation of electroporation shows that, under the investigated PEF conditions, pores start to be created in the membranes of epidermal cells at low voltages (50 V) and with higher voltages the pore density becomes uniform in the entire leaf cross section.

Acknowledgments

This work was in part supported by the Slovenian Research Agency (ARRS) with program numbers P2-0249 and IP-0510. Research was conducted within the scope of the European Associated Laboratory for Pulsed Electric Field Applications in Biology and Medicine (LEA EBAM).

The article is a result of the networking efforts of COST Action TD1104 (www.electroporation.net). Part of the calculations and experimental work was performed during the Short-Term Scientific Mission (Grant ECOST-STSM-TD1104-030912-021795, to Katarzyna Dymek).

The research which led us to these results received funding from the European Community's Seventh Framework Program (FP7/2007-2013) under grant agreement no. 245280, also known under the acronym PRESERF.

Authors would also like to express their deep appreciation to Dr. Matej Reberšek and Dr. Nataša Pavšelj for their initial help with measurements and modeling, respectively.

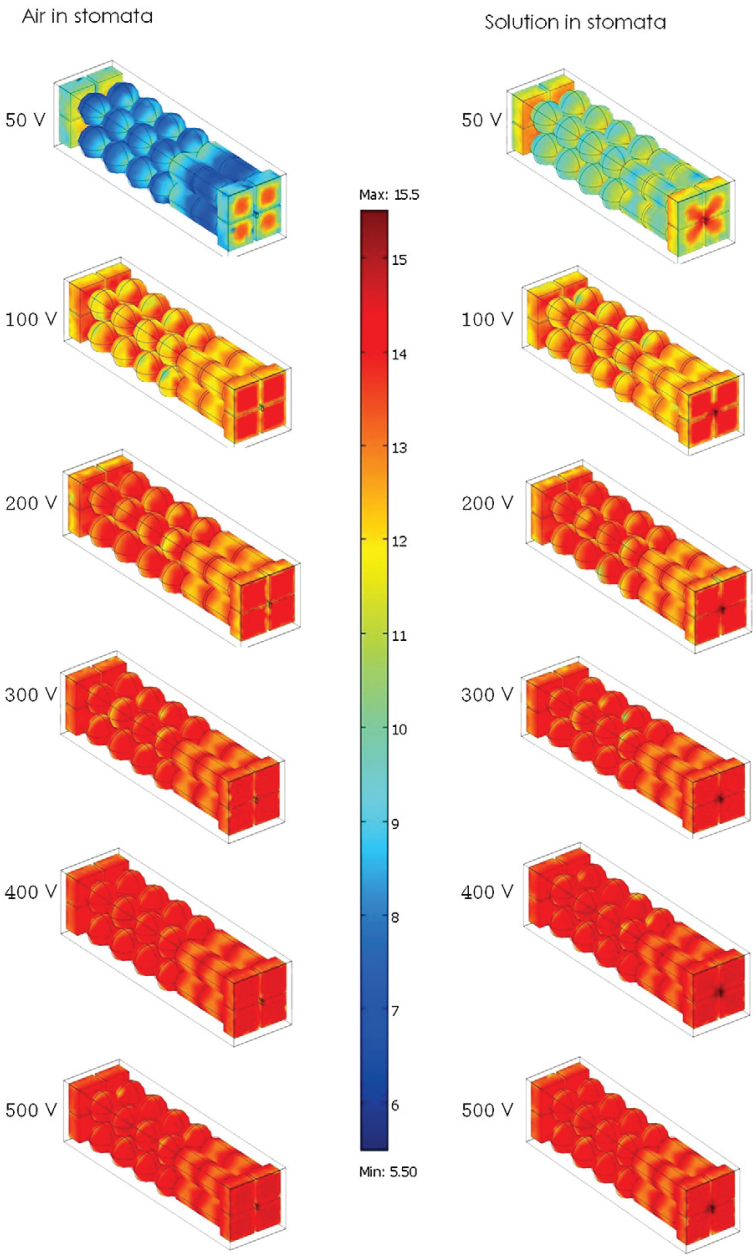

Fig. 8. Distribution of pore density in the electroporated cells investigated with the model of vacuum impregnated spinach leaf after applying electric pulses with different amplitudes. Models, where the stomata are either filled with solution or with air, were investigated. The color scale is logarithmic, from dark blue representing low pore density, to dark red representing high pore density. Pore density is shown in pores/m^2.

References

Arena, C. B., Sano, M. B., Rylander, M. N., & Davalos, R. V. (2011). Theoretical considerations of tissue electroporation with high-frequency bipolar pulses. *IEEE Transactions on Biomedical Engineering, 58*, 1474–1482.

Arora, R., & Palta, J. P. (1991). A loss in the plasma membrane ATPase activity and its recovery coincides with incipient freeze–thaw injury and postthaw recovery in onion bulb scale tissue. *Plant Physiology, 95*, 846–852.

Asami, K., Hanai, T., & Koizumi, N. (1980). Dielectric approach to suspensions of ellipsoidal particles covered with a shell in particular reference to biological cells. *Japanese Journal of Applied Physics, 19*, 359–365.

Corovic, S., Zupanic, A., Kranjc, S., Al Sakere, B., Leroy-Willig, A., Mir, L. M., et al. (2010). The influence of skeletal muscle anisotropy on electroporation: In vivo study and numerical modeling. *Medical & Biological Engineering & Computing, 48*, 637–648.

Daniels, C., & Rubinsky, B. (2009). Electrical field and temperature model of nonthermal irreversible electroporation in heterogeneous tissues. *Journal of Biomechanical Engineering, 131*.

DeBruin, K. A., & Krassowska, W. (1999). Modeling electroporation in a single cell. I. Effects of field strength and rest potential. *Biophysical Journal, 77*, 1213–1224.

Demir, E. (2012). *Optimization of vacuum impregnation and pulsed electric field parameters for improving the cryoprotection of spinach leaves.* (Master Thesis). Lund University.

Dymek, K., Dejmek, P., & Gómez Galindo, F. (2014). Influence of pulsed electric field protocols on the reversible permeabilization of rucola leaves. *Food and Bioprocess Technology*, *7*, 761–773.

Gavish, N., & Promislow, K. (2012). Dependence of the dielectric constant of electrolyte solutions on ionic concentration. arXiv:1208.5169 ([physics.chem-ph]. Retrieved from http://arxiv.org/abs/1208.5169).

Glaser, R., Leikin, S., Chernomordik, L., Pastushenko, V., & Sokirko, A. (1988). Reversible electrical breakdown of lipid bilayers — Formation and evolution of pores. *Biochimica et Biophysica Acta*, *940*, 275–287.

Gowrishankar, T. R., Esser, A. T., Vasilkoski, Z., Smith, K. C., & Weaver, J. C. (2006). Microdosimetry for conventional and supra-electroporation in cells with organelles. *Biochemical and Biophysical Research Communications*, *341*, 1266–1276.

Hardin, J. A., Jones, C. L., Weckler, P. R., Maness, N. O., Dillwith, J. W., & Madden, R. D. (2013). Rapid quantification of spinach leaf cuticular wax using Fourier transform infrared attenuated total reflectance spectroscopy. *Transactions of the ASABE*, *56*, 331–339.

Harris, C. M., & Kell, D. B. (1983). The radio-frequency dielectric properties of yeast cells measured with a rapid, automated, frequency-domain dielectric spectrometer. *Bioelectrochemistry and Bioenergetics*, *11*, 15–28.

Hector, L. G., & Schultz, H. L. (1936). The dielectric constant of air at radiofrequencies. *Physics*, *7*, 133–136.

Kandušer, M., & Miklavčič, D. (2008). Electroporation in biological cell and tissue: An overview. In E. Vorobiev, & N. Lebovka (Eds.), *Electrotechnologies for extraction from food plants and biomaterials food engineering series* (pp. 1–37). New York: Springer.

Kotnik, T., Kramar, P., Pucihar, G., Miklavcic, D., & Tarek, M. (2012). Cell membrane electroporation — Part 1: The phenomenon. *IEEE Electrical Insulation Magazine*, *28*, 14–23.

Mezeme, M. E., Pucihar, G., Pavlin, M., Brosseau, C., & Miklavčič, D. (2012). A numerical analysis of multicellular environment for modeling tissue electroporation. *Applied Physics Letters*, *100*, 143701.

Miklavčič, D., Serša, G., Brecelj, E., Gehl, J., Soden, D., Bianchi, G., et al. (2012). Electrochemotherapy: Technological advancements for efficient electroporation-based treatment of internal tumors. *Medical & Biological Engineering & Computing*, *50*, 1213–1225.

Neumann, E., & Rosenheck (1972). Permeability changes induced by electric impulses in vesicular membranes. *Journal of Membrane Biology*, *10*, 279–290.

Neumann, E., Schaefer-Ridder, M., Wang, Y., & Hofschneider, P. (1982). Gene transfer into mouse lyoma cells by electroporation in high electric fields. *EMBO Journal*, *1*, 841–845.

Panarese, V., Dejmek, P., Rocculi, P., & Gómez Galindo, F. (2013). Microscopic studies providing insight into the mechanisms of mass transfer in vacuum impregnation. *Innovative Food Science & Emerging Technologies*, *18*, 169–176.

Pavliha, D., Kos, B., Zupanič, A., Marčan, M., Serša, G., & Miklavčič, D. (2012). Patient-specific treatment planning of electrochemotherapy: Procedure design and possible pitfalls. *Bioelectrochemistry*, *87*, 265–273.

Pavšelj, N., & Miklavčič, D. (2008). Numerical modeling in electroporation-based biomedical applications. *Radiology and Oncology*, *42*, 159–168.

Pavšelj, N., & Miklavčič, D. (2011). Resistive heating and electropermeabilization of skin tissue during in vivo electroporation: A coupled nonlinear finite element model. *International Journal of Heat and Mass Transfer*, *54*, 2294–2302.

Pawar, S. D., Murugavel, P., & Lal, D.M. (2009). Effect of relative humidity and sea level pressure on electrical conductivity of air over Indian Ocean. *Journal of Geophysical Research*, *114* (D02205).

Phillips, M., Maor, E., & Rubinsky, B. (2011). Principles of tissue engineering with nonthermal irreversible electroporation. *Journal of Heat Transfer—Transactions of the ASME*, *133*, 011004.

Phoon, P. Y., Gómez Galindo, F., Vicente, A., & Dejmek, P. (2008). Pulsed electric field in combination with vacuum impregnation with trehalose improves the freezing tolerance of spinach leaves. *Journal of Food Engineering*, *88*, 144–148.

Pucihar, G., Miklavcic, D., & Kotnik, T. (2009). A time-dependent numerical model of transmembrane voltage inducement and electroporation of irregularly shaped cells. *IEEE Transactions on Biomedical Engineering*, *56*, 1491–1501.

Ramos-Barrado, J., Benavente, J., & Heredia, A. (1993). Electrical conductivity of differently treated isolated cuticular membranes by impedance spectroscopy. *Archives of Biochemistry and Biophysics*, *306*, 337–341.

Retelj, L., Pucihar, G., & Miklavcic, D. (2013). Electroporation of intracellular liposomes using nanosecond electric pulses — A theoretical study. *IEEE Transactions on Biomedical Engineering*, *60*, 2624–2635.

Riederer, M., & Schreiber, L. (2001). Protecting against water loss: Analysis of the barrier properties of plant cuticles. *Journal of Experimental Botany*, *52*, 2023–2032.

Rowan, N. J., MacGregor, S. J., Anderson, J. G., Fouracre, R. A., & Farish, O. (2000). Pulsed electric field inactivation of diarrhoeagenic *Bacillus cereus* through irreversible electroporation. *Letters in Applied Microbiology*, *31*, 110–114.

Saulis, G. (1997). Pore disappearance in a cell after electroporation: Theoretical simulation and comparison with experiments. *Biophysical Journal*, *73*, 1299–1309.

Schönherr, J. (2006). Characterization of aqueous pores in plant cuticles and permeation of ionic solutes. *Journal of Experimental Botany*, *57*, 2471–2491.

Shayanfar, S., Chauhan, O., Toepfl, S., & Heinz, V. (2013). The interaction of pulsed electric fields and texturizing–antifreezing agents in quality retention of defrosted potato strips. *International Journal of Food Science & Technology*, *48*, 1289–1295.

Sibbernsen, E., & Mott, K. A. (2010). Stomatal responses to flooding of the intercellular air spaces suggest a vapor-phase signal between the mesophyll and the guard cells. *Plant Physiology*, *153*, 1435–1442.

Stout, D.G., Hall, J. W., & McLaughlin, N.B. (1987). In vivo plant impedance measurements and characterization of membrane electrical properties: The influence of cold acclimation. *Cryobiology*, *24*, 148–162.

Suzuki, D. O. H., Ramos, A., Ribeiro, M. C. M., Cazarolli, L. H., Silva, F. R. M. B., Leite, L. D., et al. (2011). Theoretical and experimental analysis of electroporated membrane conductance in cell suspension. *IEEE Transactions on Biomedical Engineering*, *58*, 3310–3318.

Talele, S., & Gaynor, P. (2010). Modelling control of pore number and radii distribution in single-cell electroporation. In K. Elleithy, T. Sobh, M. Iskander, V. Kapila, M.A. Karim, & A. Mahmood (Eds.), *Technological developments in networking, education and automation* (pp. 231–236). Netherlands: Springer.

Talele, S., Gaynor, P., Cree, M. J., & van Ekeran, J. (2010). Modelling single cell electroporation with bipolar pulse parameters and dynamic pore radii. *Journal of Electrostatics*, *68*, 261–274.

Wanichapichart, P., Bunthawin, S., Kaewpaiboon, A., & Kanchanapoom, K. (2002). Determination of cell dielectric properties using dielectrophoretic technique. *Science Asia*, *28*, 113–119.

Warmbrodt, R. D., & Woude, W. J. V. (1990). Leaf of *Spinacia oleracea* (Spinach): Ultrastructure, and plasmodesmatal distribution and frequency, in relation to sieve-tube loading. *American Journal of Botany*, *77*, 1361–1377.

Winter, H., Robinson, D.G., & Heldt, H. W. (1994). Subcellular volumes and metabolite concentrations in spinach leaves. *Planta*, *193*, 530–535.

Yarmush, M. L., Golberg, A., Serša, G., Kotnik, T., & Miklavčič, D. (2014). Electroporation-based technologies for medicine: Principles, applications, and challenges. *Annual Review of Biomedical Engineering*, *16*, 295–320.

Zimmermann, U., Pilwat, G., & Riemann, F. (1974). Dielectric breakdown of cell membranes. *Biophysical Journal*, *14*, 881–899.

Zimmermann, U., & Vienken, J. (1982). Electric field-induced cell-to-cell fusion. *Journal of Membrane Biology*, *67*, 165–182.

Zorec, B., Becker, S., Reberšek, M., Miklavčič, D., & Pavšelj, N. (2013). Skin electroporation for transdermal drug delivery: The influence of the order of different square wave electric pulses. *International Journal of Pharmaceutics*, *457*, 214–223.

Paper 5

Title: **Properties of lipid electropores I: Molecular dynamics simulations of stabilized pores by constant charge imbalance**

Authors: Maura Casciola, Marina A. Kasimova, Lea Rems, Sara Zullino, Francesca Apollonio, and Mounir Tarek

Publication: Bioelectrochemistry. Submitted for review.

Journal information

BIOELECTROCHEMISTRY		
Publisher	ELSEVIER SCIENCE SA, PO BOX 564, 1001 LAUSANNE, SWITZERLAND	
ISSN eISSN	1567-5394 1521-186X	
Research domain	Biochemistry & Molecular Biology; Life Sciences & Biomedicine - Other Topics; Biophysics; Electrochemistry	
Impact factor	4.172 (2014) 3.854 (5 year)	
JCR® category	Rank in category	Quartile in category
BIOCHEMISTRY & MOLECULAR BIOLOGY	75 of 290	Q2
BIOLOGY	13 of 85	Q1
BIOPHYSICS	15 of 73	Q1
ELECTROCHEMISTRY	5 of 28	Q1

Source: Web of Science™ (December 2015)

Author contributions of L. Rems

L. Rems contributed to the analysis of the results from molecular dynamics simulations, interpretation of the results and writing of the manuscript.

Properties of lipid electropores I: Molecular dynamics simulations of stabilized pores by constant charge imbalance

Maura Casciola[a,b,c], Marina A. Kasimova[a], Lea Rems[d], Sara Zullino[a,b], Francesca Apollonio[b], and Mounir Tarek [a,e]

[a]Université de Lorraine, UMR 7565, F-54506 Vandoeuvre les Nancy, France;
[b]Department of Information Engineering, Electronics and Telecommunications (D.I.E.T), Sapienza University of Rome, 00184, Rome, Italy;
[c]Center for Life Nano Science@Sapienza, Istituto Italiano di Tecnologia, 00161, Rome, Italy;
[d]University of Ljubljana, Faculty of Electrical Engineering, Tržaška 25, SI-1000 Ljubljana, Slovenia;
[e]CNRS, UMR 7565, F-54506 Vandoeuvre les Nancy, France.

*Corresponding author: mounir.tarek@univ-lorraine.fr

Abstract

Molecular dynamics (MD) simulations have become a powerful tool to study electroporation (EP) in atomic detail. In the last decade, numerous MD studies have been conducted to model the effect of pulsed electric fields on membranes, providing molecular models of the EP process of lipid bilayers. Here we extend these investigations by modeling for the first time conditions comparable to experiments using long (μs–ms) low intensity (~kV/cm) pulses, by studying the characteristics of pores formed in lipid bilayers maintained at a constant surface tension and subject to constant charge imbalance. This enables the evaluation of structural (size) and electrical (conductance) properties of the pores formed, providing information hardly accessible directly by experiments. Extensive simulations of EP of simple phosphatidylcholine bilayers in 1 M NaCl show that hydrophilic pores with stable radii (1–2.5 nm) form under transmembrane voltages between 420 and 630 mV, allowing for ionic conductance in the range of 6.4–29.5 nS. We discuss in particular these findings and characterize both convergence and size effects in the MD simulations. We further extend these studies in a follow-up paper (Rems et al., Bioelectrochemistry, Submitted), by proposing an improved continuum model of pore conductance consistent with the results from the MD simulations.

Keywords: electroporation, millisecond pulses, membrane model, pore, conductance.

1 Introduction

Experimental evidence indicates that application of an external electric field to biological cells affects transiently or permanently the integrity of their plasma membrane [1–8]. The changes in membrane integrity are manifested by a substantial increase in the membrane ionic conductance, an increase in molecular uptake into the cell and a release of the cytosolic content from the cell [9–13]. This effect has been rationalized by evidence demonstrating that an electrical pulse induces a large change in the transmembrane voltage resulting in rearrangements of the membrane components, in particular the lipid bilayer, leading to the formation of aqueous transmembrane pores [4–8,14–16]. This process of 'aqueous pores' formation under the application of an external electric field is known as electroporation (EP) [1,12,17]. Today, EP is widely used in biomedicine and biotechnology for delivery of drugs or genetic material into cells [13,18–24].

The size of pores formed as a result of EP together with their morphology and conductive properties are crucial in determining the permeability and selectivity of the plasma membrane to different ionic and molecular species and consequently the potential efficacy of a given EP application. While extensive experimental work on cells and model lipid membranes (*e.g.* planar lipid bilayers and lipid vesicles) has been devoted to the structural characterization of these pores [25–35], the data emerging so far is very scarce. The nanometer-range size of the pores unfortunately limits the possibility of their direct observation by conventional techniques. Only very recently, time resolved visualization of pores in droplet interface bilayers was made possible using total internal reflection fluorescence microscopy [16]. Nevertheless, such fluorescence imaging currently does not allow the spatial resolution required to measure the pore size, nor the temporal resolution corresponding to conventional microsecond and millisecond pulses generally used in EP. Experimentally, therefore, one is able to estimate the nanopore dimension only indirectly by measuring either membrane permeability to molecules of different sizes, or membrane conductance recovered from the current/voltage relationship. Both approaches, however, have their specific limitations.

Estimates of pore size based on monitoring the transmembrane transport of small molecules (e.g. sugars, polyethylene glycols [33], bleomycin [34]) and fluorescent dyes (*e.g.* thallium ions [32], YO-PRO, propidium iodide [35]) were mostly obtained from *in vitro* experiments on cells after exposing them to nanosecond long (≤600 ns) electric pulses. Results of these studies suggested that nanosecond pulses induce a high number of long-lived yet small pores, most of them with radii of about 0.5–0.7 nm, which allow the transport of larger molecules such as propidium iodide, but prevent the massive flux reported for longer (millisecond) less intense (kV/cm) pulses [35–38]. The direct correlation between the size of a molecule and that of a pore is though debatable for molecules that might interact strongly with the pore walls. Indeed an interacting molecule requires certain time to dissociate from the bilayer and diffuse into the cytosolic milieu where it can be detected. In addition, a charged molecule can significantly perturb the local electrostatic environment in the pore proximity, leading to changes in pore dimensions and pore morphology [39]. Even neutral sugar molecules can strongly interact with lipid headgroups through hydrogen bonding, consequently modifying the bilayer properties [40]. Such measurements may therefore not reflect properly the properties of pores as directly induced by electric pulses.

Estimates of pore size based on measurements of membrane conductance were on the other hand mostly obtained from planar lipid bilayers when applying a constant current (chronopotentiometry) to the membrane [25,26,29]. The benefit of controlling the current instead of the voltage is that once a pore is formed, the voltage across the membrane can reduce due to ionic transport through the pore, hence stabilizing the pore and preventing membrane rupture. For phosphatidylcholine based planar lipid bilayers, pore radii from 1.9 to 6.0 nm were reported, with larger pores observed when imposing a higher current. Conductance measurements have also been performed on dense cell suspensions during exposures to trains of 100 μs pulses [28] and on single cells using patch clamp techniques [30]. These studies suggested that pore radii can vary from ~1 to 55 nm, depending on the experimental conditions. However, the major limitation of estimating the pore size from conductance measurements is that the experimental data needs to be fitted to a certain model, which relates the pore conductance with the pore size. For such purpose, analytical models deriving from the continuum Nernst-Planck theory are normally used, which inherently impose simplified assumptions about the pore geometry and the effective conductivity of the electrolyte inside the pore [41–43]. The choice of such parameters and characteristics are in general arbitrary or too approximate, which may casts doubts on the accuracy of the predictions arising from the models. Moreover, continuum theories can fail to properly describe the physics in a molecular-scale system, which was indeed observed for ion channels [44,45]. One way of testing, validating, and if needed improving the continuum models is to compare them with molecular dynamics (MD) simulations, which provide full atomistic details of the entire process of ionic conduction through a pore.

This is precisely the approach we are undertaking hereafter. In a series of papers, we pursue a line of research where we use MD simulations to determine the structural (shape, size) and electrical (conductance, selectivity) properties of electropores formed in a model lipid bilayer in its liquid crystal L_α phase, when subject to increased transmembrane (TM) voltage. In the first (present) paper, we introduce a new MD simulation protocol that allows one to observe stable pores and extract their equilibrium properties under EP conditions. The results from the simulations are then further analyzed in our subsequent paper [46], where they are compared to the predictions of a continuum model constructed based on the model system in MD simulations. As we will demonstrate, improvement of the standard models is required in order to obtain results which are consistent with the molecular modeling.

In MD simulations, there are two common methods that allow the modeling of a TM voltage (trigger of EP): applying an external electric field and imposing a charge imbalance across a lipid bilayer. An external electric field is introduced into the system as an additional force acting on all the atoms charged [14,47–50]. In such a scheme, the reorientation of water molecules located at the solution/bilayer interface induces a TM voltage that, when overcoming a certain threshold, triggers EP. It was demonstrated, however, that in simulations with an external electric field, the pores keep expanding in their size while the field is maintained above the EP threshold, indicating their instability [51]. Stabilization can be reached by lowering the intensity of the external electric field [52,53], but an arbitrary control of the field intensity hardly corresponds to a clear experiment.

In the charge imbalance method, a TM potential is generated by submitting lipid bilayers to ionic salt concentration gradients either considering two solution baths separated by two bilayers [54–56] (the double

bilayer scheme) or by a bilayer and a vacuum slab [57] (the single bilayer scheme). Unlike the external electric field method, which rather mimics an experiment using high intensity nanosecond pulses [57,58], the charge imbalance method corresponds to the traditional EP setup where low microsecond/millisecond pulses are applied. Such a pulse applied to the membrane results indeed in the accumulation of charged species at both solution/membrane interfaces; if one considers the membrane as a capacitor embedded into conductive medium, a TM potential created by the accumulation of charges on this capacitor can be accordingly described.

The charge imbalance protocols used so far in simulations to model EP, suffer from two important shortcomings. First, the charge imbalance is not re-set during the simulation. Thus, in studies with the double [55,56] and single bilayer [57,58] schemes, after the EP occurs, the imposed charge imbalance at the beginning decreases significantly within several tens/hundreds ps (depending on the system size) due to an exchange of ions through the pores in the bilayer. The decrease of the charge imbalance results in a TM voltage drop, which may ultimately lead to the pore collapse or resealing. A procedure to maintain the charge imbalance at a constant level was recently proposed by Kutzner *et al.* [59] to study the transport in ion channels. In this procedure, named "swapping", the number of ions in the two solution baths is frequently estimated and if the latter differs from the initial setup, a "swapping" event takes place: an ion of one solution is exchanged by a water molecule of the other solution bath.

The second shortcoming of the charge imbalance method as used so far in MD simulations concerns the membrane lateral expansion: the latter can hardly be controlled in the double bilayer scheme due to the fact that only one bilayer undergoes EP, and is prohibited in the single bilayer scheme because in this case the simulations are carried out at a constant volume. As a result, the pores are not allowed to relax to their equilibrium conformation and the quantitative estimation of their properties (*e.g.* size, current, selectivity to different ionic species, *etc.*) becomes unreliable.

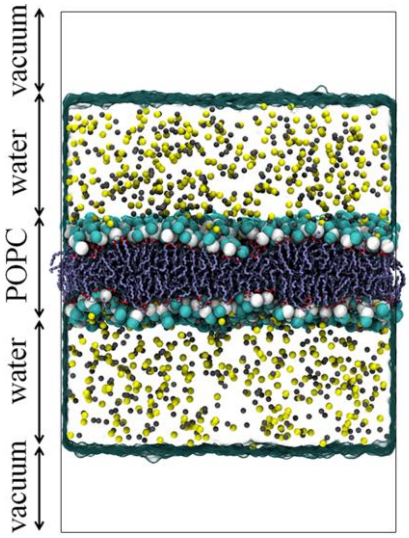

Fig. 1. The single bilayer scheme used in this work: two solution baths are separated by a lipid bilayer (POPC) and a vacuum slab, which prevent an exchange of ions and, hence, collapse of the charge imbalance. The POPC headgroups are shown as cyan and white beads, the tails are shown as purple sticks; sodium and chloride ions are colored in yellow and gray; water is transparent.

In this work, we present a protocol that deals with both shortcomings of the charge imbalance method discussed so far. In particular, we used the "swapping" procedure [59] to maintain the charge imbalance at a constant level. Here, instead of considering the system with two bilayers, as used by Kutzner *et al*., we adapted the procedure for the single bilayer scheme (see Fig. 1). In order to overcome the second shortcoming, which concerns the membrane lateral expansion, we used an assumption that in 'experimental' macroscopic systems (cells, liposomes or planar lipid bilayers) the formation of pores does not lead to any dramatic change in the membrane surface tension due to its dissipation. Hence we performed our simulations at a constant null surface tension. Using this protocol, we were able to model for the first time the EP process in conditions comparable with experiments. We show that in contrast to previous simulations [60–62], the pores relax to a stable conformation, which allow the estimation of their average size, ionic current and selectivity.

2 Methods

2.1 Systems preparation

Two systems with a hydrated Palmitoyl-Oleoyl-PhosphatidylCholine (POPC) bilayer were considered: a small one, composed by 256 POPC molecules (POPC_256), with a total size of 8.9 x 8.9 x 19 nm^3, and a big one, composed by 1024 POPC molecules (POPC_1024), with a total size of 17.8 x 17.8 x 19 nm^3. In both systems, the bilayers were surrounded by 1 M NaCl solution. The CHARMM36 force field [63] was used for POPC, and the TIP3P model was considered for water [64].

2.2 Parameters of MD

The MD simulations were performed using Gromacs 4.6. [65]. The equations of motion were integrated using the leap-frog algorithm, with a time step of 2.0 fs. The long-range electrostatic was calculated using Particle Mesh Ewald (PME). The cut-off distance of the short-range electrostatic was taken to be 1.2 nm. A switching function was used between 0.8 and 1.2 nm to smoothly bring the van der Waals forces and energies to 0 at 1.2 nm. During the simulations, chemical bonds between hydrogen and heavy atoms were constrained to their equilibrium values using LINCS. Periodic boundary conditions were applied in all directions.

2.3 Equilibration

The POPC_256 system was equilibrated during 100 ns in the NPT ensemble: pressure and temperature of the system were kept constant at 1 atm (using the Parrinello-Rahman barostat) and 300 K (using the Nose-Hoover thermostat), respectively. Note that at the temperature set for the study, the POPC bilayer is in its biologically relevant liquid crystal L_α phase. To verify the convergence of the equilibration we estimated the area per lipid along the run. The latter rapidly reached the plateau of ~61.8 $Å^2$, which is in agreement with the previously reported data for bare POPC bilayers [66].

The big system (POPC_1024) was further constructed by replicating the equilibrated POPC_256 in the bilayer plane. The POPC_1024 was additionally equilibrated during 20 ns.

2.4 Estimation of the total surface tension

During the equilibration, the total surface tension (γ/mN/m) in the system was zero since the lateral and the normal pressure to the solution/bilayer interface are set equal as in the NPT ensemble. However, in our further simulations we considered the scheme with a vacuum slab [57,58], which introduces an additional solution/vacuum interface with a non-zero surface tension. In the system with a vacuum slab, the total surface tension (γ_{tot}/mN/m) is the sum of the surface tension at the solution/bilayer ($\gamma_{sol/bilayer}$/mN/m) and solution/vacuum interfaces ($\gamma_{vacuum/sol}$/mN/m): $\gamma_{tot} = 2\gamma_{vacuum/sol} + \gamma_{bilayer/sol}$. Since the area per lipid was kept constant when switching to the NVT ensemble, the lateral pressure on the lipid bilayer stays at zero. Thus, considering that $\gamma_{bilayer/sol}$ ~0 mN/m, the total surface tension is double the surface tension at the vacuum/solution interface: $\gamma_{tot} = 2\gamma_{vacuum/sol}$.

In order to estimate the total surface tension, arising from the solution/vacuum interfaces we fixed its volume and performed short MD simulations (10 ns). Based on the obtained trajectories, a surface tension of ~100 mN/m was obtained from the lateral (P_l/bar) and the normal pressure to the solution/bilayer interface (P_t/bar) as: $\gamma = \int [P_l - P_t]\, dz$, i.e. the surface tension at each of the two vacuum/solution interfaces was ~50 mN/m, in agreement with the experimental measurements and modeling [67,68].

2.5 Transmembrane (TM) potential

The electrostatic potential U_z/V along the normal to the bilayer can be calculated by solving Poisson's equation (1), *i.e.* derived as double integral of ρ_z/(C/m^3), the volume charge density distribution, being ε_0/(F/m) the vacuum permittivity:

$$U_z = U(z) - U_0 = -\frac{1}{\varepsilon_0}\int_0^z\int \rho_z\left(z''\right)\, dz''dz' \qquad (1)$$

As reference, U_0 was set to zero in the lower bulk solution. Practically, we calculated the electrostatic potential by dividing the system into 0.1 nm slices along Z-axis, summing the charges in each slice and integrating the resulting charge distribution for 10,000 configurations spread out over 20 ns time-windows. The TM voltage U_m/V was calculated as the difference between the electrostatic potential measured at the lower and the upper baths.

2.6 Swapping protocol

In order to maintain the applied charge imbalance ΔQ/C at a constant value, we used the "swapping" protocol [59] implemented in Gromacs. Briefly, the protocol works the following way: the program estimates the number of ions in the two solution baths and if this number differs from the initial setup, an ion of one solution bath is exchanged by a water molecule of the other solution bath. Here, we adapted the "swapping" protocol for the single bilayer scheme considering the Z-planes separating the two solution baths as the Z-coordinates of the water molecule center of mass placed in vacuum, and of the center of mass of the bilayer. The centers of mass of both groups were restrained during the simulations.

2.7 Production runs

The production runs of 100 ns each were performed in the NPγT ensemble (constant surface tension) using the single-bilayer scheme [57,58] and the "swapping" protocol [59]. In order to keep the total surface tension of the membrane/water at zero, we considered 100 mN/m as a reference value for the total surface tension γ_{tot} (see subsection 2.4). To avoid the collapse of the vacuum slab we changed the compressibility of the system in the Z-direction (perpendicular to the bilayer) to zero, using the Berendsen barostat.

For the POPC_256 and POPC_1024 the following ΔQ/C were applied: $0q_e$, $12q_e$ and $14q_e$, and $0q_e$, $20q_e$, $32q_e$, $40q_e$, $48q_e$ and $56q_e$ respectively (q_e/C is the elementary charge). Notice that the $48q_e$ ΔQ was considered only in our subsequent paper [46] to increase the statistic needed for a more detailed analysis of the pore conductance, carried out over time windows of 20 ns each. In fact, when the ΔQ is too high the bilayer shows a less stable behavior in time in terms of membrane area (see Supplementary Material). This is probably due to the osmotic pressure imposed by the water flow (see subsection 3.1) that results in non-equal volumes of water in the two baths of the bilayer as well as in a corresponding increase in the ionic concentration where the water volume is reduced. Therefore, like in the case of $48q_e$, if such not predictable behavior was observed before 80 ns, the simulation was rejected. The $56q_e$ run exhibits this behavior after 80 ns, which allowed us to carry out the analysis until that.

2.8 Analysis of the pore

Based on the obtained trajectories, the minimum pore radius (R/nm), ionic current (I/nA), conductance (G/nS) and selectivity (S) were analyzed. The pore radius was estimated using HOLE [69] at each 250 ps; the ionic current was evaluated as the slope of the ionic flux at each 0.2 ps; and the conductance was estimated as the ratio between the average ionic current and the TM potential applied. In order to verify the convergence, the cumulative values of the pore radius and ionic current were calculated along the MD runs. The simulations were assumed to converge when the cumulative values reached their plateau values. Accordingly, the average values and their standard deviations were estimated for the plateau regions. The bilayer density (d/a.u.), thickness (t_m/nm) and an average molecular order parameters (P_{CH}) were extracted using the protocol suggested by Castillo *et al.* [70].

3 Results and discussion

Experimentally, when macroscopic systems are exposed to an electric pulse causing EP, the formation of the pores does not lead to dramatic changes in the membrane surface tension, as it is re-distributed along the entire membrane surface. Hence, if one wishes to model the EP process in conditions comparable with the experimental ones, the membrane surface tension should be kept constant (and null). In the single bilayer charge imbalance scheme that we considered in this work, the total surface tension is the sum of the surface tension at the bilayer/solution and the surface tension at the solution/vacuum interfaces (see subsection 2.4). While the total surface tension is constant when the bilayer is intact, it rises abruptly after the pore formation occurs [14,71]. To avoid such unrealistic increase, we estimated the total surface tension during the equilibration step (no charge

imbalance) and used this value to maintain the surface tension constant when the system was exposed to the charge imbalance (see subsection 2.4). In order to prevent the collapse of the vacuum slab, we maintained the compressibility of the system in the Z-direction (perpendicular to the bilayer) to zero (see subsection 2.7). Finally, the simulations were performed using the "swapping" procedure proposed by Kutzner *et al*. [59] which allows to maintain the charge imbalance constant (see subsection 2.6).

The protocol that combines the constant surface tension and constant charge imbalance was applied to the big system with 1024 POPC molecules (POPC_1024, see subsection 2.1). Four different ΔQ were considered ($20q_e$, $32q_e$, $40q_e$, $56q_e$), corresponding to the TM voltages U_m of ~ 420, 510, 520 and 630 mV, respectively (note that the TM voltages were estimated after the bilayer electroporation, Fig. 2).

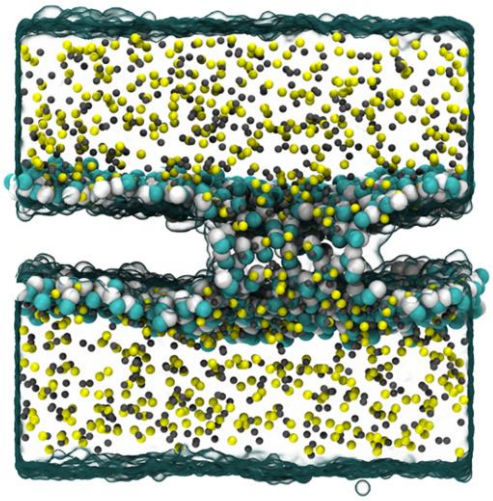

Fig. 2. Cross section of an electroporated POPC_1024 bilayer. The POPC headgroups are shown as cyan and white beads, the tails are transparent; sodium and chloride ions are colored in yellow and gray; water is transparent.

3.1 Pore characteristics

Fig. 3 reports the cumulative average of the pore radius along the MD run and the average pore profile estimated for the four charge imbalances. The cumulative pore radii (Fig. 3A) reach a plateau after 20 ns indicating that the pores are stable and that the corresponding simulations have converged. For each MD run, the average pore radius and the standard deviation were further estimated for the remaining part of the trajectory: from 20 to 80 ns. The average pore radius (Fig. 3B), ranging from 1 to 2.5 nm, was shown to be dependent on the charge imbalance applied to the system, thereby being dependent also on the TM voltage; the dependence of the average pore radius on the TM voltage is approximately linear in the investigated range.

Our observation of stable pores at moderate TM voltages is in general agreement with theoretical predictions [6,72–74]. The theory of EP namely predicts that once the energetic barrier for pore formation is overcome, the formed hydrophilic pore will stabilize at certain radius which corresponds to the local minimum in the pore free energy landscape. The position of this minimum with respect to the pore radius is also expected to shift with increasing TM voltage, resulting in larger stable pores. If the TM voltage exceeds a certain value, however, the

minimum is expected to disappear leading to irreversible expansion of the pore and ultimate rupture of the bilayer provided that the TM voltage remains constant. We interpret our results as being in the range of TM voltages which allow pores to remain stable, at least in the time window considered.

The ionic current through the pore was estimated as the slope of the ionic flux (see Supplementary Material). In Fig. 4A we report the cumulative average of the ionic current for the four charge imbalances over time. As expected, the currents grow to reach a plateau after less than 10 ns until the end of the runs, which proves the convergence of this observable. The stable currents range from 2.69 to 18.58 nA, when the TM voltages from 420 to 630 mV are maintained.

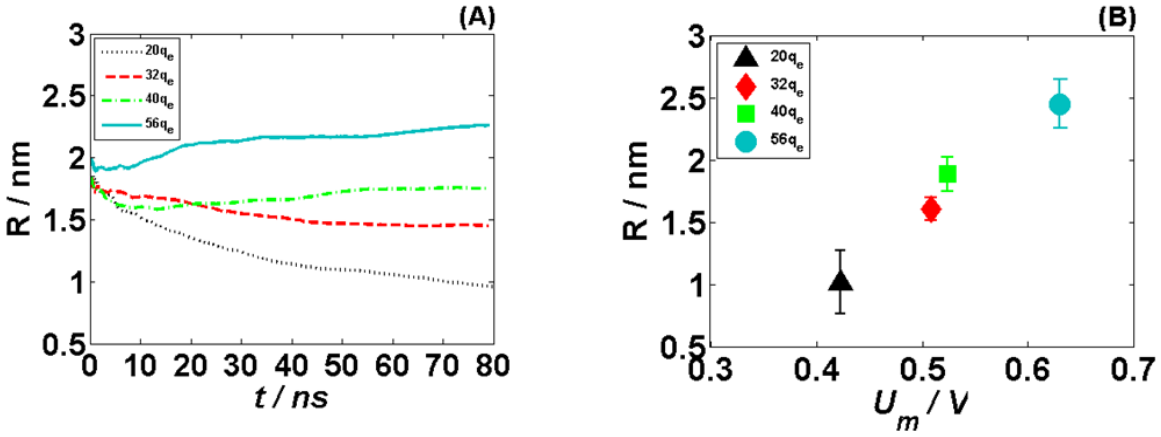

Fig. 3. (A) Cumulative minimum pore radius R/nm along the elapsed time t/ns, corresponding to the charge imbalances ΔQ/C of 20q_e (black dotted line), 32q_e (red dashed line), 40q_e (green dot-dashed line) and 56q_e (cyan solid). (B) Minimum pore radius R/nm versus the TM voltage U_m established at charge imbalances ΔQ/C of 20q_e (black triangle), 32q_e (red diamond), 40q_e (green square) and 56q_e (cyan circle).

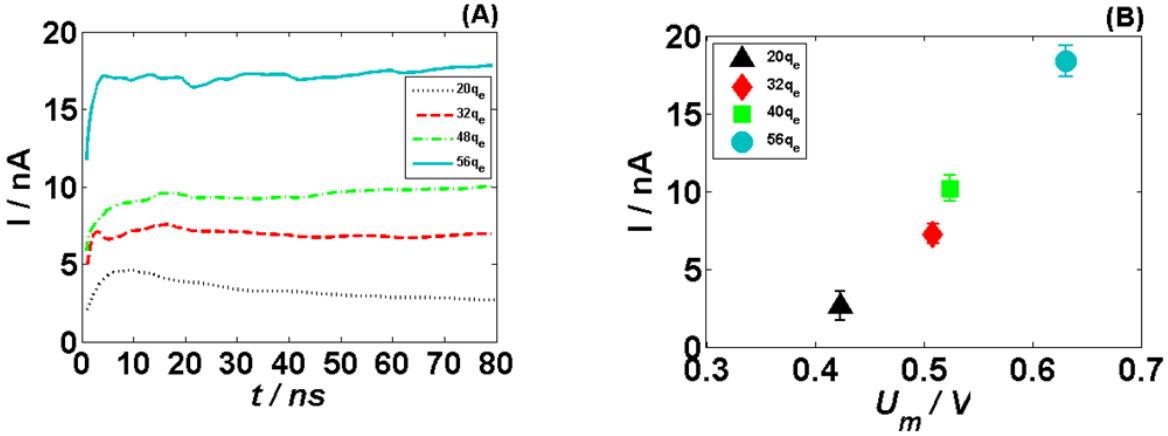

Fig. 4. (A) Cumulative average of the ionic current I/nA along the elapsed time t/ns, corresponding to the charge imbalances ΔQ/C of 20q_e (black dotted line), 32q_e (red dashed line), 40q_e (green dot-dashed line) and 56q_e (cyan solid line). (B) Current/voltage relationship for the charge imbalances ΔQ/C of 20q_e (black triangle), 32q_e (red diamond), 40q_e (green square) and 56q_e (cyan circle).

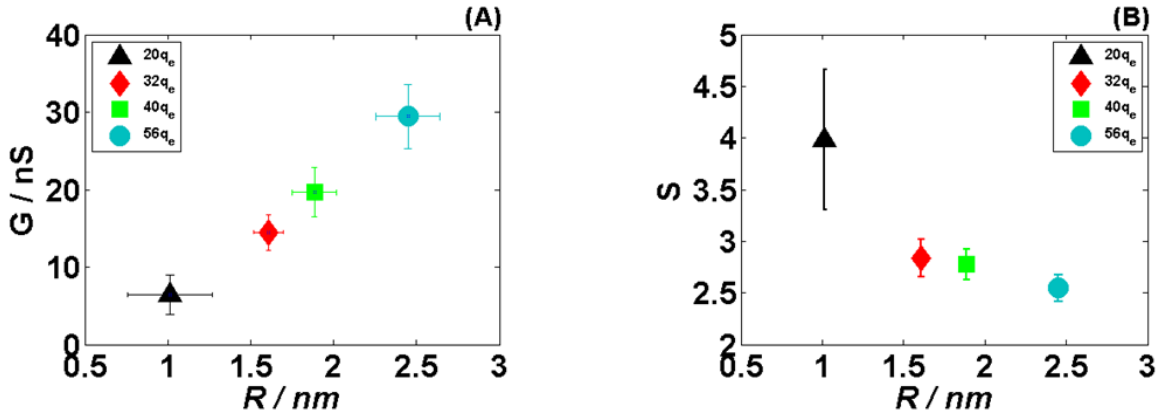

Fig. 5. Ionic conductance G/nS (A) and ionic selectivity S (B) as a function of the minimum pore radius R/nm, corresponding to the charge imbalances ΔQ/C of $20q_e$ (black triangle), $32q_e$ (red diamond), $40q_e$ (green square) and $56q_e$ (cyan circle).

The current/voltage relationship of Fig. 4B shows that as the TM voltage applied is increased, the current flowing through the single electropore rises approximately linearly. Note that with increasing TM voltage the pore radius also increases. Since pores with larger size allow the passage of a higher number of ions, the increase in the current is both due to the increase in the TM voltage by directly increasing the electrophoretic drift of ions, as well as the increase in the pore size.

The conductance (G/nS) of the pore was calculated as the ratio of ionic current (I/nA) and TM voltage (U_m/V); the results are presented in Fig. 5A. We reported G as a function of the pore radius (R/nm) to facilitate the correlation of our results with the experimental ones, where the radius is indirectly deduced from the conductance measured. In the range of TM potentials investigated, the conductance changes almost linearly with the pore radius (for further analyses and discussions on the relationship between the pore conductance, pore shape, and pore radius we refer the reader to our subsequent paper [46]).

Finally, we estimated the pore selectivity (S) as the ratio of anionic (I_{Cl^-}/nA) to cationic (I_{Na^+}/nA) current, Fig. 5B. In agreement with the previous findings [53], the pore was shown to be more selective to chloride ions than to sodium ions. This selectivity arises from the nature of the lipid molecules constituting the pore: the negatively charged phosphate groups that form the walls of the pore attract sodium ions, which hinders their passage across the bilayer, but also makes the pore interior electrostatically unfavorable for other sodium ions. Consequently, as we show in Fig. 5B, the ratio of Cl and Na current decreases as the pore expands. Indeed, the pore expansion results in a higher fraction of those sodium ions that pass the pore without any hindrance as they do not interact with the pore walls. According to the analysis we performed in our subsequent paper [46], the pore selectivity to Cl ions can partially arises also due to electroosmotic flux of water through the pore, which enhances the current of Cl ions and at the same time reduces the current of Na ions.

Indeed, in all performed simulations, we observed a net flux of water in the direction of the flux of Cl ions (i.e., opposite to the direction of the electric potential gradient), which can be attributed to the interactions of water with electrophoretically driven charged ions. The water flux gradually reduces the volume of water on one side

of the bilayer and increases the volume of water on the other side. The changes in water volume limit the time range for which the simulations can be performed (~100 ns) in the absence of excessive osmotic pressure, which can lead to instability of the simulated system.

3.2 Simulation cell and size effects

In MD simulations, the EP of bilayers is commonly studied on relatively small systems composed of 256, 128 and in some cases of 64 lipids. Accordingly, we compared our data discussed so far with a smaller system, containing 256 POPC molecules instead of 1024 (POPC_256, see subsection 2.1); the results of the comparison are presented in Table 1.

We found that at similar TM voltages the pore radius in the POPC_256 bilayer is almost twice lower than that in the POPC_1024 bilayer, which results as well in different values of conductance. We hypothesize that the observed inconsistency of the results stems from the size effect. Indeed, once a pore is formed in the POPC_256, the size of the simulation box prevents its adequate expansion, i.e. the bilayer patch is not large enough to allow for the release of tension induced by the pore spanning which consequently induces a constraint on the pore size.

Table 1: Pore radius R/nm and conductance G/nS estimated at a specific TM voltages U_m/V.

System	U_m/V	R/nm	G/nS
POPC_1024	0.42 ± 0.04	1.0 ± 0.3	6.4 ± 2.5
	0.52 ± 0.05	1.9 ± 0.2	19.6 ± 3.2
POPC_256	0.46 ± 0.06	0.6 ± 0.1	2.3 ± 0.2
	0.54 ± 0.10	0.7 ± 0.2	2.8 ± 1.2

U_m – transmembrane voltage resulting by the charge imbalance.
R – minimum pore radius maintained by a given U_m.
G – conductance of the electropore for the corresponding radius.

In order to test this hypothesis, we analyzed the density, thickness and order parameters of the electroporated POPC_1024 and POPC_256 bilayers (Fig. 6). The lipid order parameter, defined as $P_{CH} = 1/2 < 3\cos^2 \theta - 1 >$, where θ is the angle between the C-H bond vector and the membrane normal, was calculated for all carbons in the lipid acyl chains and then averaged within each voxel over the ensemble of lipids and over the simulation (see subsection 2.8).

The presence of the pore locally changes the bilayer properties; the headgroups surrounding the pore slide along the water column to stabilize it, resulting in a toroidal shape, and causing: a decrease in the order parameter; a local drop in the lipid density, and in the bilayer thickness. Fig. 6A and 6E show clearly that for the small system, the pore is too large with respect to the cell size. The area affected by the pore (where we register a decrease in the value of the properties mentioned above) almost reaches the patch borders, which probably

influences through the periodic boundary condition its own stability and expansion. On the contrary, in the POPC_1024 the values of the density (d/a.u.) and the average molecular order parameter (P_{CH}) (Fig. 6B and 6F respectively) recover when moving away from the water defect.

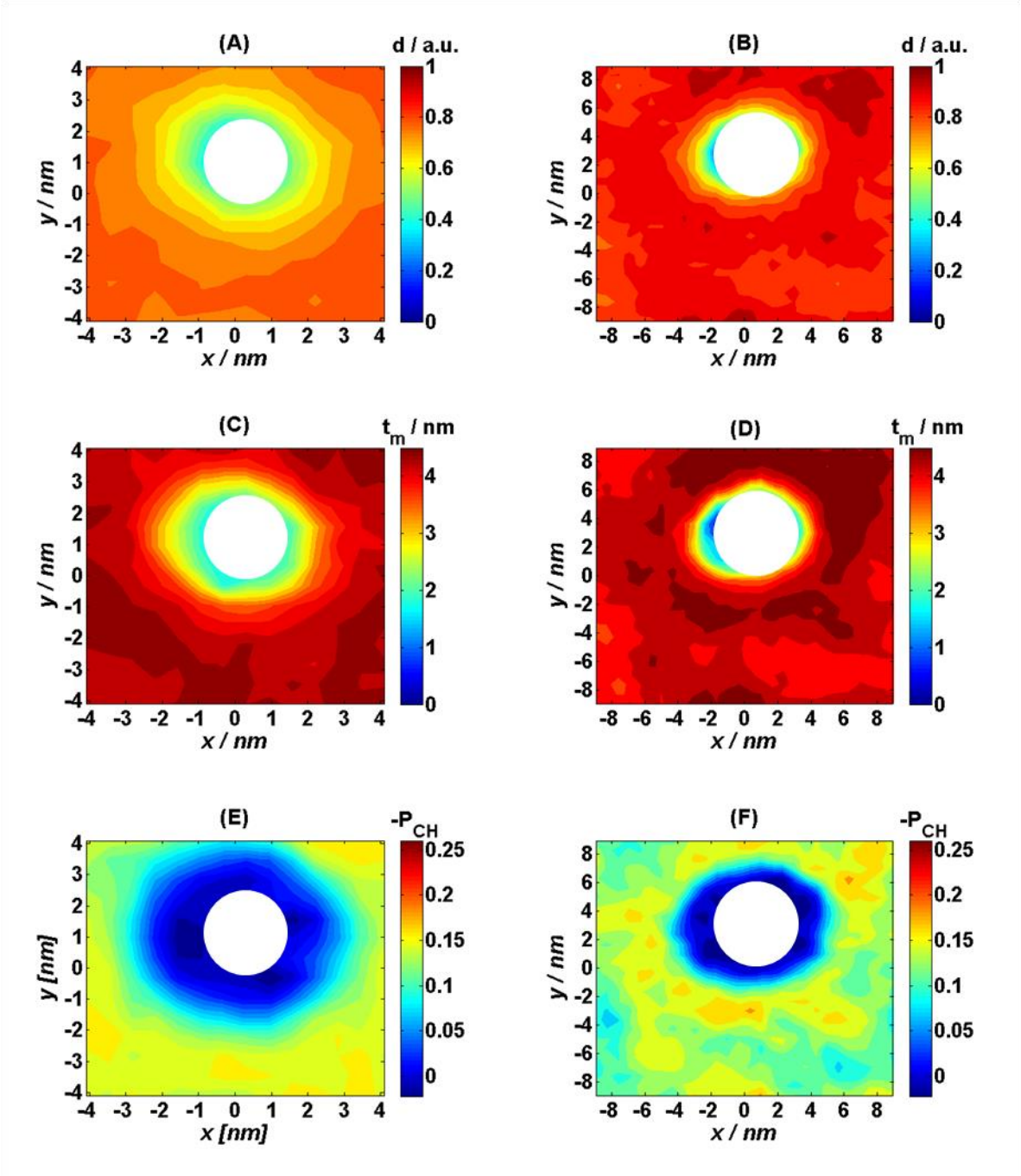

Fig. 6. 2D spatial maps of the density d/a.u (A and B), thickness t_m/nm (C and D) and order parameter P_{CH} (E and F) estimated for the POPC_256 (A, C, E) and POPC_1024 (B, D, F) bilayers subject to 500 mV.

4 Conclusions

Here we introduced a new protocol that enables for the first time to perform MD simulations of electroporated bilayer under conditions similar to those of experiments using low intensity, long (μs-ms) pulses. This is perceived as the most appropriate approach to directly determine the transport of ions and selected molecules across bilayers exposed to electric pulses, which remains a challenge for experimental methods. We proposed the use of an ensemble that allows the membrane surface tension γ_{tot} to be constant, avoiding unrealistic constrains. Then, the establishment of a constant voltage comparable with experimental exposures was guaranteed by the swap procedure. Both these conditions permit the formation of relaxed stable pores that can be characterized geometrically and electrically. The cumulative average of the pore radius and that of the ionic current confirm indeed the convergence of these observables after 20 ns of simulation run.

We found that for TM voltages ranging from 420 mV to 630 mV, the pore radius increases from 1 to 2.5 nm and the conductance from 6.4 to 29.5 nS. Quite interestingly, when the same TM voltage was maintained on the lipid patch of the sizes usually employed in MD simulations (~8.8 x 8.8 nm^2, 256 lipids) the pore radius obtained was twice smaller and the conductance almost three times smaller than what we reported for the large system (~17.8 x 17.8 nm^2, 1024 lipids), likely a consequence of the constrains imposed by the finite size of the simulation box.

Simulations along these lines should contribute to a better understanding of phenomenon of electroporation. Two further applications can be considered. First, investigating the EP of more complex membranes, and second investigating the transport of large molecules, *e.g.* drugs and genetic material to shed light on the uptake mechanisms.

To provide a further insight to the EP process these results need also to be linked with experimental observations. Since the direct comparison is challenging, as stated in the introduction, an intermediate and complementary step could be the use of continuum models. In the following paper, we therefore constructed a numerical model of pore conductance based on the Poisson-Nernst-Planck theory, and found a surprisingly exquisite agreement between the two approaches.

Acknowledgements

We thank Carsten Kutzner for very helpful suggestions on the implementation of the method. Simulations were performed using HPC resources from GENCI-CINES (Grant 2012-2013 075137, and Project number lct2523 with DARI dossier number c2014075136). M.T. acknowledges the support of the French Agence Nationale de la Recherche, under grant (ANR-10_BLAN-916-03-INTCELL). M.C. acknowledges the support of the "Istituto Italiano di Tecnologia" (IIT). L.R. acknowledges the support from the Slovenian Research Agency (ARRS) through funding for Junior Researchers R856. The study was conducted in the scope of the European Associated Laboratory for Pulsed Electric Field Applications in Biology and Medicine (LEA EBAM).

References

[1] E. Neumann, A.E. Sowers, C.A. Jordan, Electroporation and electrofusion in cell biology, Springer Science & Business Media, 1989.
[2] J.A. Nickoloff, Animal cell electroporation and electrofusion protocols, Humana Press,NJ, 1995.
[3] S. Li, Electroporation protocols : Preclinical and clinical gene medicine, Humana press: Totowa, NJ., 2008.
[4] I.G. Abidor, V.B. Arakelyan, L.V. Chernomordik, Y.A. Chizmadzhev, V.F. Pastushenko, M.P. Tarasevich, Electric breakdown of bilayer lipid membranes: I. The main experimental facts and their qualitative discussion, J. Electroanal. Chem. Interfacial Electrochem. 104 (1979) 37–52.
[5] R. Benz, F. Beckers, U. Zimmermann, Reversible electrical breakdown of lipid bilayer membranes: A charge-pulse relaxation study, J. Membr. Biol. 48 (1979) 181–204.
[6] J.C. Weaver, Y.A. Chizmadzhev, Theory of electroporation: A review, Bioelectrochem. Bioenerg. 41 (1996) 135–160.
[7] J.C. Weaver, Electroporation of biological membranes from multicellular to nano scales, IEEE Trans. Dielectr. Electr. Insul. 10 (2003) 754–768.
[8] C. Chen, S.W. Smye, M.P. Robinson, J.A. Evans, Membrane electroporation theories: a review, Med. Biol. Eng. Comput. 44 (2006) 5–14.
[9] G. Pucihar, T. Kotnik, D. Miklavcic, J. Teissié, Kinetics of transmembrane transport of small molecules into electropermeabilized cells, Biophys. J. 95 (2008) 2837–2848.
[10] M. Hibino, M. Shigemori, H. Itoh, K. Nagayama, K. Kinosita, Membrane conductance of an electroporated cell analyzed by submicrosecond imaging of transmembrane potential., Biophys. J. 59 (1991) 209–220.
[11] M. Breton, L. Delemotte, A. Silve, L.M. Mir, M. Tarek, Transport of siRNA through lipid membranes driven by nanosecond electric pulses: An experimental and computational study, J. Am. Chem. Soc. 134 (2012) 13938–13941.
[12] L.M. Mir, H. Banoun, C. Paoletti, Introduction of definite amounts of nonpermeant molecules into living cells after electropermeabilization: direct access to the cytosol, Exp. Cell Res. 175 (1988) 15–25.
[13] J. Teissié, N. Eynard, B. Gabriel, M.P. Rols, Electropermeabilization of cell membranes, Adv. Drug Deliv. Rev. 35 (1999) 3–19.
[14] M. Tarek, Membrane electroporation: A molecular dynamics simulation, Biophys. J. 88 (2005) 4045–4053.
[15] T. Kotnik, G. Pucihar, D. Miklavčič, Induced transmembrane voltage and its correlation with electroporation-mediated molecular transport, J. Membr. Biol. 236 (2010) 3–13.
[16] M. Szabo, M.I. Wallace, Imaging potassium-flux through individual electropores in droplet interface bilayers, Biochim. Biophys. Acta. (2015).
[17] T. Kotnik, P. Kramar, G. Pucihar, D. Miklavcic, M. Tarek, Cell membrane electroporation – Part 1: The phenomenon, IEEE Electr. Insul. Mag. 28 (2012) 14–23.
[18] S. Lakshmanan, G.K. Gupta, P. Avci, R. Chandran, M. Sadasivam, A.E.S. Jorge, et al., Physical energy for drug delivery; poration, concentration and activation, Adv. Drug Deliv. Rev. 71 (2014) 98–114.
[19] J. Villemejane, L.M. Mir, Physical methods of nucleic acid transfer: general concepts and applications, Br. J. Pharmacol. 157 (2009) 207–219.
[20] J. Teissie, Electrically mediated gene delivery: Basic and translational concepts., INTECH Open Access Publisher, 2013.
[21] M. Breton, L.M. Mir, Microsecond and nanosecond electric pulses in cancer treatments, Bioelectromagnetics. 33 (2012) 106–123.
[22] M.L. Yarmush, A. Golberg, G. Serša, T. Kotnik, D. Miklavčič, Electroporation-based technologies for medicine: Principles, applications, and challenges, Annu. Rev. Biomed. Eng. 16 (2014) 295–320.
[23] R. Cadossi, M. Ronchetti, M. Cadossi, Locally enhanced chemotherapy by electroporation: clinical experiences and perspective of use of electrochemotherapy, Future Oncol. 10 (2014) 877–890.
[24] D. Miklavčič, B. Mali, B. Kos, R. Heller, G. Serša, Electrochemotherapy: from the drawing board into medical practice, Biomed. Eng. Online. 13 (2014) 29.
[25] S. Kalinowski, G. Ibron, K. Bryl, Z. Figaszewski, Chronopotentiometric studies of electroporation of bilayer lipid membranes, Biochim. Biophys. Acta 1369 (1998) 204–212.
[26] S. Koronkiewicz, S. Kalinowski, K. Bryl, Programmable chronopotentiometry as a tool for the study of electroporation and resealing of pores in bilayer lipid membranes, Biochim. Biophys. Acta. 1561 (2002) 222–229.
[27] S. Koronkiewicz, S. Kalinowski, Influence of cholesterol on electroporation of bilayer lipid membranes: chronopotentiometric studies, Biochim. Biophys. Acta 1661 (2004) 196–203.
[28] M. Pavlin, M. Kandušer, M. Reberšek, G. Pucihar, F.X. Hart, R. Magjarević, et al., Effect of cell electroporation on the conductivity of a cell suspension, Biophys. J. 88 (2005) 4378–4390.
[29] M. Kotulska, Natural fluctuations of an electropore show fractional Lévy stable motion, Biophys. J. 92 (2007) 2412–2421.
[30] H. Krassen, U. Pliquett, E. Neumann, Nonlinear current–voltage relationship of the plasma membrane of single CHO cells, Bioelectrochemistry. 70 (2007) 71–77.
[31] P. Kramar, L. Delemotte, A.M. Lebar, M. Kotulska, M. Tarek, D. Miklavčič, Molecular-level characterization of lipid membrane electroporation using linearly rising current, J. Membr. Biol. 245 (2012) 651–659.
[32] A.M. Bowman, O.M. Nesin, O.N. Pakhomova, A.G. Pakhomov, Analysis of plasma membrane integrity by fluorescent detection of Tl^+ uptake, J. Membr. Biol. 236 (2010) 15–26.

[33] O.M. Nesin, O.N. Pakhomova, S. Xiao, A.G. Pakhomov, Manipulation of cell volume and membrane pore comparison following single cell permeabilization with 60- and 600-ns electric pulses, Biochim. Biophys. Acta. 1808 (2011) 792–801.
[34] A. Silve, I. Leray, L.M. Mir, Demonstration of cell membrane permeabilization to medium-sized molecules caused by a single 10 ns electric pulse, Bioelectrochemistry. 87 (2012) 260–264.
[35] A.G. Pakhomov, E. Gianulis, P.T. Vernier, I. Semenov, S. Xiao, O.N. Pakhomova, Multiple nanosecond electric pulses increase the number but not the size of long-lived nanopores in the cell membrane, Biochim. Biophys. Acta. 1848 (2015) 958–966.
[36] J. Deng, K.H. Schoenbach, E. Stephen Buescher, P.S. Hair, P.M. Fox, S.J. Beebe, The effects of intense submicrosecond electrical pulses on cells, Biophys. J. 84 (2003) 2709–2714.
[37] P.T. Vernier, Y. Sun, L. Marcu, S. Salemi, C.M. Craft, M.A. Gundersen, Calcium bursts induced by nanosecond electric pulses, Biochem. Biophys. Res. Commun. 310 (2003) 286–295.
[38] P.T. Vernier, Y. Sun, M.A. Gundersen, Nanoelectropulse-driven membrane perturbation and small molecule permeabilization, BMC Cell Biol. 7 (2006) 37.
[39] F. Salomone, M. Breton, I. Leray, F. Cardarelli, C. Boccardi, D. Bonhenry, et al., High-yield nontoxic gene transfer through conjugation of the CM18-Tat11 chimeric peptide with nanosecond electric pulses, Mol. Pharm. 11 (2014) 2466–2474.
[40] J. Kapla, J. Wohlert, B. Stevensson, O. Engström, G. Widmalm, A. Maliniak, Molecular dynamics simulations of membrane-sugar interactions, J. Phys. Chem. B. 117 (2013) 6667–6673.
[41] A. Barnett, The current-voltage relation of an aqueous pore in a lipid bilayer membrane, Biochim. Biophys. Acta 1025 (1990) 10–14.
[42] S. Kakorin, E. Neumann, Ionic conductivity of electroporated lipid bilayer membranes, Bioelectrochemistry 56 (2002) 163–166.
[43] J. Li, H. Lin, The current-voltage relation for electropores with conductivity gradients, Biomicrofluidics. 4 (2010).
[44] G. Moy, B. Corry, S. Kuyucak, S.-H. Chung, Tests of continuum theories as models of ion channels. I. Poisson−Boltzmann theory versus Brownian dynamics, Biophys. J. 78 (2000) 2349–2363.
[45] B. Corry, S. Kuyucak, S.H. Chung, Tests of continuum theories as models of ion channels. II. Poisson–Nernst–Planck theory versus Brownian dynamics, Biophys. J. 78 (2000) 2364–2381.
[46] L. Rems, M. Casciola, M. Tarek, D. Miklavcic, Properties of lipid electropores II: Comparison of continuum-level modeling of pore conductance to molecular dynamics simulations, Bioelectrochemistry. Submitted for Review.
[47] D.P. Tieleman, The molecular basis of electroporation, BMC Biochem. 5 (2004) 10.
[48] Q. Hu, S. Viswanadham, R. Joshi, K. Schoenbach, S. Beebe, P. Blackmore, Simulations of transient membrane behavior in cells subjected to a high-intensity ultrashort electric pulse, Phys. Rev. E. 71 (2005) 031914.
[49] R.A. Böckmann, B.L. de Groot, S. Kakorin, E. Neumann, H. Grubmüller, Kinetics, statistics, and energetics of lipid membrane electroporation studied by molecular dynamics simulations, Biophys. J. 95 (2008) 1837–1850.
[50] M.J. Ziegler, P.T. Vernier, Interface water dynamics and porating electric fields for phospholipid bilayers, J. Phys. Chem. B. 112 (2008) 13588–13596.
[51] Z.A. Levine, P.T. Vernier, Life cycle of an electropore: field-dependent and field-independent steps in pore creation and annihilation, J. Membr. Biol. 236 (2010) 27–36.
[52] M.L. Fernández, G. Marshall, F. Sagués, R. Reigada, Structural and kinetic molecular dynamics study of electroporation in cholesterol-containing bilayers, J. Phys. Chem. B. 114 (2010) 6855–6865.
[53] M.C. Ho, M. Casciola, Z.A. Levine, P.T. Vernier, Molecular dynamics simulations of ion conductance in field-stabilized nanoscale lipid electropores, J. Phys. Chem. B. 117 (2013) 11633–11640.
[54] J.N. Sachs, P.S. Crozier, T.B. Woolf, Atomistic simulations of biologically realistic transmembrane potential gradients, J. Chem. Phys. 121 (2004) 10847–10851.
[55] A.A. Gurtovenko, I. Vattulainen, Pore formation coupled to ion transport through lipid membranes as induced by transmembrane ionic charge imbalance: Atomistic molecular dynamics study, J. Am. Chem. Soc. 127 (2005) 17570–17571.
[56] S.K. Kandasamy, R.G. Larson, Cation and anion transport through hydrophilic pores in lipid bilayers, J. Chem. Phys. 125 (2006) 074901.
[57] L. Delemotte, F. Dehez, W. Treptow, M. Tarek, Modeling membranes under a transmembrane potential, J. Phys. Chem. B. 112 (2008) 5547–5550.
[58] L. Delemotte, M. Tarek, Molecular dynamics simulations of lipid membrane electroporation, J. Membr. Biol. 245 (2012) 531–543.
[59] C. Kutzner, H. Grubmüller, B.L. de Groot, U. Zachariae, Computational electrophysiology: The molecular dynamics of ion channel permeation and selectivity in atomistic detail, Biophys. J. 101 (2011) 809–817.
[60] A. Polak, M. Tarek, M. Tomšič, J. Valant, N.P. Ulrih, A. Jamnik, et al., Electroporation of archaeal lipid membranes using MD simulations, Bioelectrochemistry. 100 (2014) 18–26.
[61] M. Casciola, D. Bonhenry, M. Liberti, F. Apollonio, M. Tarek, A molecular dynamic study of cholesterol rich lipid membranes: comparison of electroporation protocols, Bioelectrochemistry. 100 (2014) 11–17.
[62] F. Dehez, L. Delemotte, P. Kramar, D. Miklavčič, M. Tarek, Evidence of conducting hydrophobic nanopores across membranes in response to an electric field, J. Phys. Chem. C. 118 (2014) 6752–6757.

[63] J.B. Klauda, R.M. Venable, J.A. Freites, J.W. O'Connor, D.J. Tobias, C. Mondragon-Ramirez, et al., Update of the CHARMM all-atom additive force field for lipids: validation on six lipid types, J. Phys. Chem. B. 114 (2010) 7830–7843.
[64] W.L. Jorgensen, J. Chandrasekhar, J.D. Madura, R.W. Impey, M.L. Klein, Comparison of simple potential functions for simulating liquid water, J. Chem. Phys. 79 (1983) 926–935.
[65] B. Hess, C. Kutzner, D. van der Spoel, E. Lindahl, GROMACS 4: Algorithms for highly efficient, load-balanced, and scalable molecular simulation, J. Chem. Theory Comput. 4 (2008) 435–447.
[66] N. Kučerka, S. Tristram-Nagle, J.F. Nagle, Structure of fully hydrated fluid phase lipid bilayers with monounsaturated chains, J. Membr. Biol. 208 (2006) 193–202.
[67] J.N. Israelachvili, Intermolecular and surface forces: Revised Third Edition, Academic Press, 2011.
[68] T.J. Lewis, A model for bilayer membrane electroporation based on resultant electromechanical stress, IEEE Trans. Dielectr. Electr. Insul. 10 (2003) 769–777.
[69] O.S. Smart, J.G. Neduvelil, X. Wang, B.A. Wallace, M.S.P. Sansom, HOLE: A program for the analysis of the pore dimensions of ion channel structural models, J. Mol. Graph. 14 (1996) 354–360.
[70] N. Castillo, L. Monticelli, J. Barnoud, D.P. Tieleman, Free energy of WALP23 dimer association in DMPC, DPPC, and DOPC bilayers, Chem. Phys. Lipids. 169 (2013) 95–105.
[71] T.V. Tolpekina, W.K. den Otter, W.J. Briels, Nucleation free energy of pore formation in an amphiphilic bilayer studied by molecular dynamics simulations, J. Chem. Phys. 121 (2004) 12060–12066.
[72] V.F. Pastushenko, Y.A. Chizmadzhev, Stabilization of conducting pores in BLM by electric current. Gen. Physiol. Biophys. 1 (1982): 43–52.
[73] J.C. Neu, W. Krassowska, Asymptotic model of electroporation, Phys. Rev. E. 59 (1999) 3471–3482.
[74] K.C. Smith, R.S. Son, T.R. Gowrishankar, J.C. Weaver, Emergence of a large pore subpopulation during electroporating pulses, Bioelectrochemistry. 100 (2014) 3–10.

Supplementary material

Properties of lipid electropores I: Molecular dynamics simulations of stabilized pores by constant charge imbalance

Maura Casciola[a,b,c], Marina A. Kasimova[a], Lea Rems[d], Sara Zullino[a,b], Francesca Apollonio[b], and Mounir Tarek [a,e]

[a]Université de Lorraine, UMR 7565, F-54506 Vandoeuvre les Nancy, France;
[b]Department of Information Engineering, Electronics and Telecommunications (D.I.E.T), Sapienza University of Rome, 00184, Rome, Italy;
[c]Center for Life Nano Science@Sapienza, Istituto Italiano di Tecnologia, 00161, Rome, Italy;
[d]University of Ljubljana, Faculty of Electrical Engineering, Tržaška 25, SI-1000 Ljubljana, Slovenia;
[e]CNRS, UMR 7565, F-54506 Vandoeuvre les Nancy, France.

*Corresponding author: mounir.tarek@univ-lorraine.fr

Evaluation of electropore characteristics

In the main paper two systems of a hydrated Palmitoyl-Oleoyl-PhosphatidylCholine (POPC) bilayer were considered: a small one, composed of 256 POPC molecules (POPC_256), with total size of 8.9 x 8.9 x 19 nm^3, and a big one, composed of 1024 POPC molecules (POPC_1024) and a total size of 17.8 x 17.8 x 19 nm^3. In both systems, the bilayers were surrounded by 1 M NaCl solution. Here in the supplementary material we report for both systems the electric potential U_z/V along the direction perpendicular to the bilayer (Z-axes), the ion flux I_f/counts over time, the pore radius R_z/nm along Z, the area A_{XY}/nm^2 in time, as well as the 2D maps of the bilayer density (d/a.u.), the thickness (t_m/nm) and an average molecular order parameters (P_{CH}).

1 POPC_256

1.1 Transmembrane potential and ion flux

For the estimation of electrostatic potential U_z/V see the subsection 2.3 of the main paper. The transmembrane potential was then calculated as the difference in the electrostatic potential in the upper and the lower bath. The ion flux was evaluated by counting the ions swapped by the swapping protocol (see subsection 2.4).

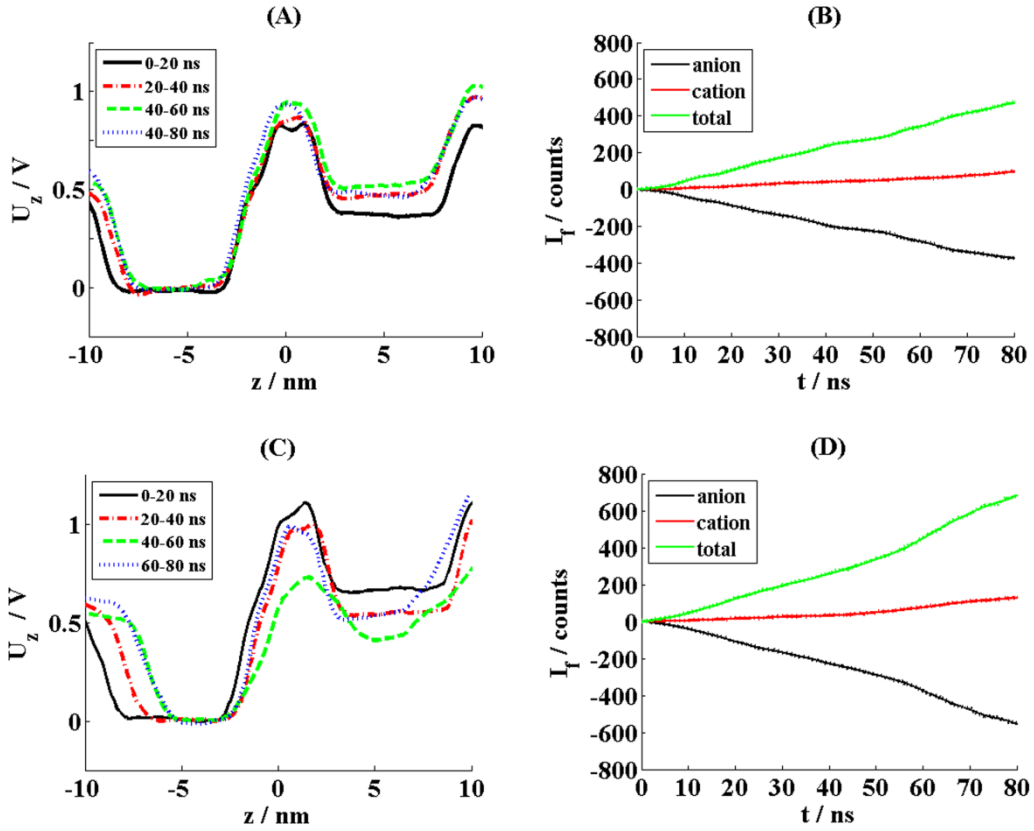

Figure 1. Left panels: Electric potentials profile U_z/V along the axes perpendicular to the bilayer for POPC_256 when $12q_e$ (A) and $14q_e$ (C) of charge imbalances were imposed.. The mean profiles were obtained averaging over 20 ns, the standard deviations calculated in each 20 ns time window. Right panels: corresponding ion fluxes over time ($12q_e$ (B) and $14q_e$ (D)) for the anionic (black), cationic (red) and the total (green) contributions.

1.2 Pore radius along the direction perpendicular to the bilayer

The pore radius was estimated using HOLE [1] at each 250 ps.

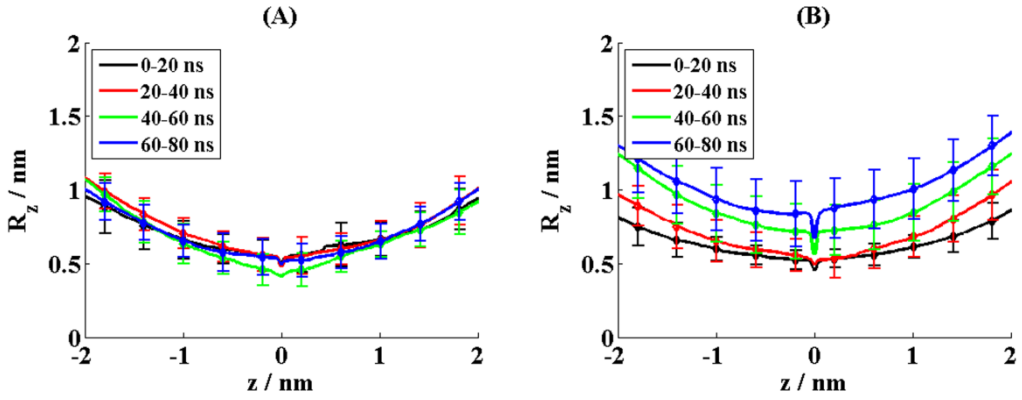

Figure 2. Pore radius R_z/nm along the direction perpendicular to the bilayer subject $12q_e$ (A) and $14q_e$ (B). The mean profiles and the standard deviations were obtained averaging over 20 ns.

2 POPC_1024

2.1 Transmembrane potential and ion flux

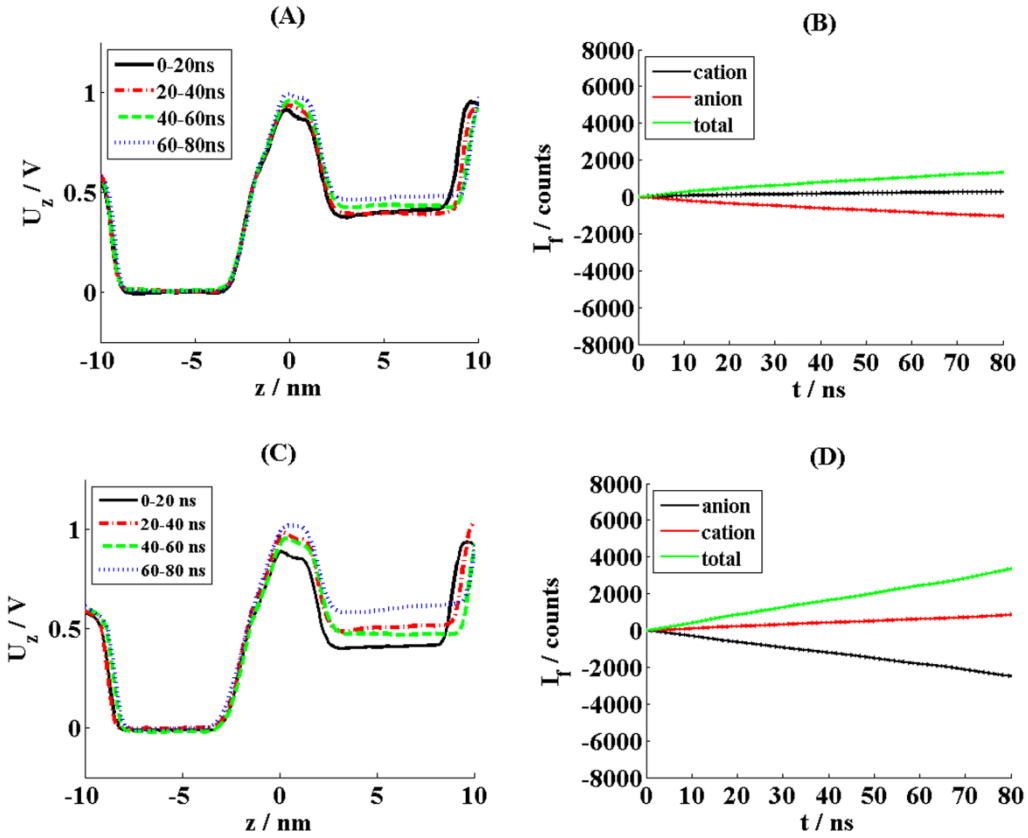

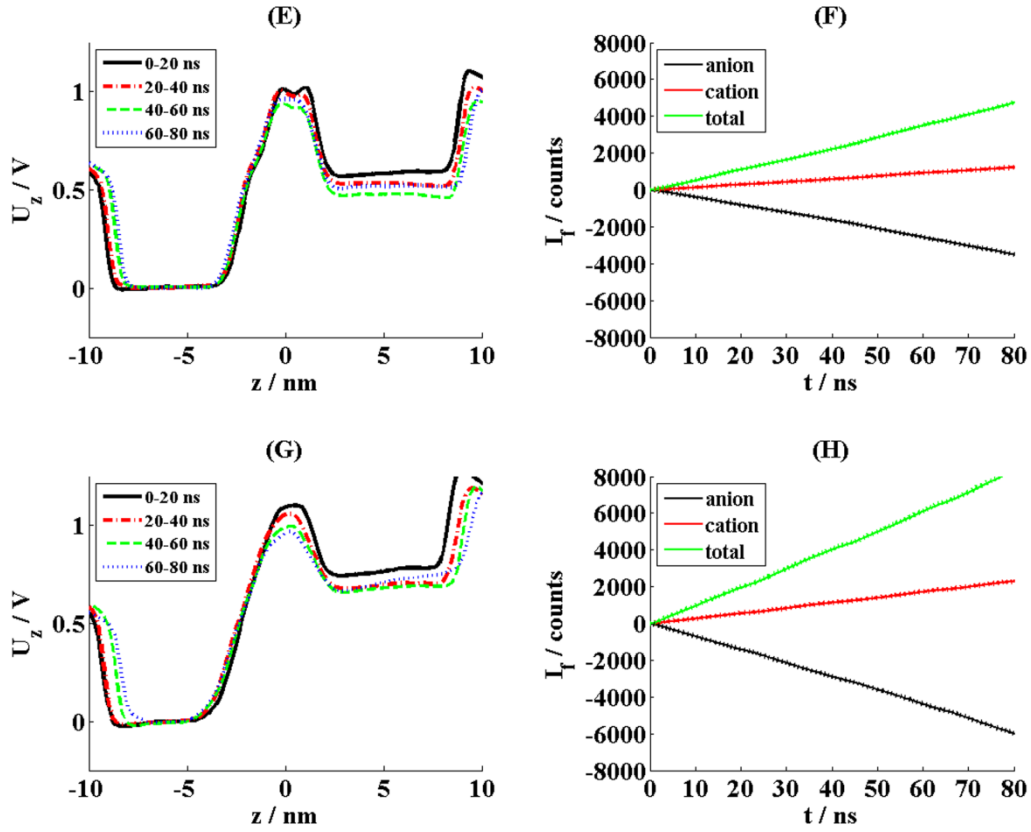

Figure 3. Left panels: Electric potentials profile U_z/V along the axes perpendicular to the bilayer for POPC_1024 when $20q_e$ (A), $32q_e$ (C), $40q_e$ (E) and $56q_e$ (G) of charge imbalances were imposed. The mean profiles and the standard deviations were obtained averaging over 20 ns. Right panels: corresponding ion fluxes over time ($20q_e$ (B), $32q_e$ (D), $40q_e$ (F) and $56q_e$ (H)) for the anionic (black), cationic (red) and the total (green) contributions.

2.2 Pore radius along the direction perpendicular to the bilayer

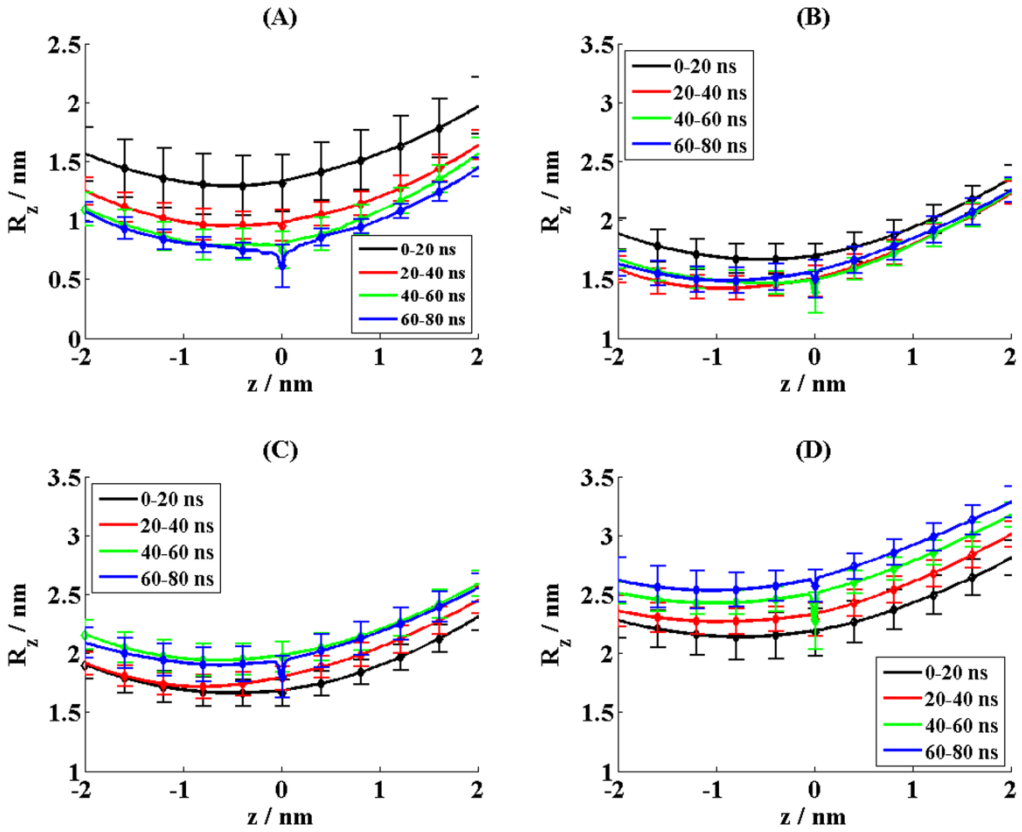

Figure 4. Pore radius R_z/nm along the direction perpendicular to the bilayer subject to $20q_e$ (A), $32q_e$ (B), $40q_e$ (C) and $56q_e$ (D). The mean profiles and the standard deviations were obtained averaging over 20 ns.

3 Bilayer density, thickness, average molecular order parameter, and bilayer area

The bilayer density (d/a.u.), thickness (t_m/nm) and an average molecular order parameter (P_{CH}) were evaluated using the protocol suggested by Castillo *et al* [2].

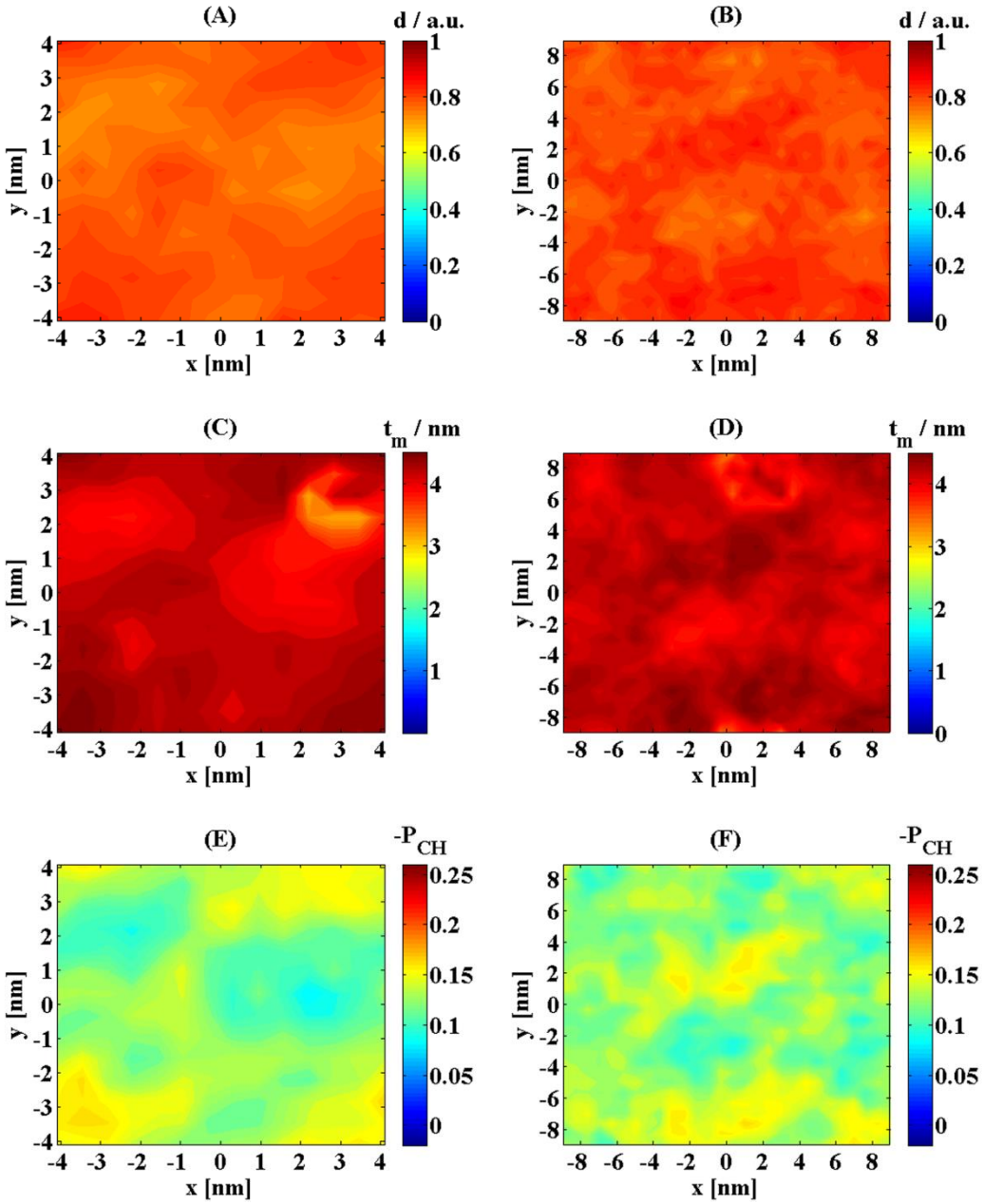

Figure 5. Two dimensional distributions (XY plane parallel to the membrane) of the density (d/a.u.), thickness (t_m/nm) and order parameter (P_{CH}) for the POPC_256 (A, C, E) and for the POPC_1024 (B, D, F) not exposed. The mean values were obtained averaging over 80 ns.

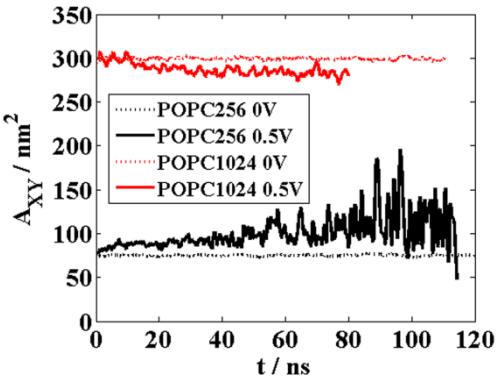

Figure 6. Area of the bilayers A_{XY}/nm^2 in time, in red the POPC_256 and in black the POPC_1024. The same electric potential is applied to the two bilayers (dashed 0 mV, solid ~500 V). The small patch shows after 50 ns of run a marked instability, which results in the rupture of the bilayer.

References

[1] O.S. Smart, J.G. Neduvelil, X. Wang, B.A. Wallace, M.S.P. Sansom, HOLE: A program for the analysis of the pore dimensions of ion channel structural models, J. Mol. Graph. 14 (1996) 354–360.

[2] N. Castillo, L. Monticelli, J. Barnoud, D. P. Tieleman, Free energy of WALP23 dimer association in DMPC, DPPC, and DOPC bilayers., Chem. Phys. Lipids 169 (2013) 95–105.

Paper 6

Title: **Properties of lipid electropores II: Comparison of continuum-level modeling of pore conductance to molecular dynamics simulations**

Authors: Lea Rems, Mounir Tarek, Maura Casciola, and Damijan Miklavčič

Publication: Bioelectrochemistry. Submitted for review.

Journal information

BIOELECTROCHEMISTRY		
Publisher	ELSEVIER SCIENCE SA, PO BOX 564, 1001 LAUSANNE, SWITZERLAND	
ISSN eISSN	1567-5394 1521-186X	
Research domain	Biochemistry & Molecular Biology; Life Sciences & Biomedicine - Other Topics; Biophysics; Electrochemistry	
Impact factor	4.172 (2014) 3.854 (5 year)	
JCR® category	Rank in category	Quartile in category
BIOCHEMISTRY & MOLECULAR BIOLOGY	75 of 290	Q2
BIOLOGY	13 of 85	Q1
BIOPHYSICS	15 of 73	Q1
ELECTROCHEMISTRY	5 of 28	Q1

Source: Web of Science™ (December 2015)

Author contributions of L. Rems

L. Rems contributed to the design of the study, contributed to the analysis of molecular dynamics simulations, designed the numerical models, performed numerical calculations and analyzed the results, contributed to the interpretation of the results and wrote most of the manuscript.

Properties of lipid electropores II: Comparison of continuum-level modeling of pore conductance to molecular dynamics simulations

Lea Rems[a], Mounir Tarek[b,c,*], Maura Casciola[b,d,e], and Damijan Miklavčič[a]

[a]University of Ljubljana, Faculty of Electrical Engineering, Tržaška 25, SI-1000 Ljubljana, Slovenia
[b]Université de Lorraine, SRSMC, UMR 7565, Vandoeuvre-les-Nancy, F-54500, France
[c]CNRS, SRSMC, UMR 7565, Vandoeuvre-les-Nancy, F-54500, France
[d]Department of Information Engineering, Electronics and Telecommunications (D.I.E.T.), Sapienza University of Rome, 00184 Rome, Italy
[e]Center for Life Nano Science@Sapienza, Istituto Italiano di Tecnologia, 00161, Rome, Italy

*Corresponding author: mounir.tarek@univ-lorraine.fr

Abstract

Electrical conductance of an aqueous pore in the lipid bilayer has an important role in the process of membrane electroporation, i.e., formation of pores induced by electric pulses. In our present study we compare the pore conductance as predicted by a theoretical model based on the continuum Poisson-Nernst-Planck theory to the pore conductance obtained with molecular dynamics simulations (Casciola et al., Bioelectrochemistry, Submitted). Our analysis demonstrates that the basic Poisson-Nernst-Planck theory is able to quantitatively predict the dependence of the pore conductance on the pore radius, but fails to reproduce correctly the difference in the pore conductance for Cl and Na ions (the pore selectivity). We show that simplified analytical descriptions of pore conductance can lead to incorrect predictions of the pore size extracted from experimental measurements, and can affect the predictions of electroporation models. We further show that the pore selectivity can be correctly described by the continuum model taking into account the electric double layer next to the lipid-water interface and the electroosmotic flow through the pore. Overall this study demonstrates that continuum modeling can be efficiently used as complementary method to molecular scale models for investigating lipid pores.

Keywords: electroporation, lipid bilayer, pore conductance, molecular dynamics simulations, Poisson-Nernst-Planck theory

1 Introduction

Electroporation, known as a method of breaching the cell membrane barrier by means of electric pulses, has been found valuable in numbers of applications in very different scientific and technological fields: medicine [1–7], food processing and food preservation [8–12], biofuel production [11,13], as well as water decontamination [14,15]. But despite its widespread use, our understanding of electroporation at the molecular level of the membrane itself still lacks a complete picture [16–18]. Consequently, the state of the art of current theoretical models of electroporation may not be at sufficiently high level and further research is necessary in order to develop models that will be able to correctly interpret or predict experimental outcomes.

Theoretical models which are used to describe electroporation on the scale of single cells or cell clusters are based on continuum approaches and are therefore often referred to as continuum electroporation models [19–28]. In continuum description, the molecular structure is neglected and the membrane is simply viewed as a thin homogenous dielectric layer surrounded by an electrolyte solution. Such models constitute an important part of electroporation research as they enable exploration on length scales (more than hundreds of micrometers) and time scales (seconds and more) currently not achievable by molecular dynamics (MD) simulations or molecular models based on the mean field theory [29–31]. Note that the diameters of mammalian cells are of the order of 10 μm and the time scales, over which structural changes in the membrane due to electroporation can be observed, range from nanoseconds to minutes or even hours [16]. Continuum models have indeed considerably contributed to our understanding of electroporation under different experimental conditions [32–36]. They can be probed to give the information on the time course and magnitude of the induced transmembrane voltage, as well as the electric field distribution inside and outside of a model cell or cell cluster [37]. To certain extent, they can even be used to predict the number and size of pores in the membrane and the rate of molecular transmembrane transport [38,36,39]. Hence, they provide a valuable tool for explaining certain experimental observations or for tailoring the experimental protocol in order to give an optimal result [40].

The general physical concept embedded in continuum electroporation models is rather simple: the transmembrane voltage, which is induced across the membrane by an electric pulse, reduces the energetic barrier for nucleation of small water pores in the lipid bilayer [21]. The induced transmembrane voltage (more specifically the corresponding induced electric field in the membrane) also provides a force which tends to expand the formed pores [41,42]. As the expanding pores start to conduct more and more ions, the voltage across the membrane effectively reduces, which in turn limits further pore creation and expansion [33,43]. The pore conductance therefore plays an important role in electroporation models as it implicitly controls the dynamics of the transmembrane voltage and thereby the number and size of membrane pores.

The descriptions of pore conductance used in continuum electroporation models are more or less simplified analytical expressions which in their core derive from coupled Nernst-Planck and Poisson's equations (for derivations see e.g. [44–46], for implementations into electroporation models see e.g. [33,36,38,41,47]). The Nernst-Planck equations describe the electro-diffusion of ions in terms of ionic concentration, where the driving force for the electrophoretic drift – the gradient in the electric potential – is given by the Poisson's equation. The so-called Poisson-Nernst-Planck (PNP) theory is a general and well-established continuum approach to describe

ionic transport in many different fields including research on ion channels and nanochannels [48–52], both closely related to lipid pores investigated in this study.

For descriptions of ionic transport through ion channels the PNP theory has some known limitations, which mainly arise from treating the ions as point charges and neglecting the ion-ion correlations. These limitations are particularly expressed in narrow channels with radii of less than 2–3 Debye lengths [53,54], where the mean field approximation breaks down. For example, the PNP theory allows a certain concentration of ions to be found in a channel, albeit the channel is too narrow to actually fit a finite-size ion. A direct consequence is an overestimate of the electrolytic shielding effects and an underestimate of the repulsive image forces induced in the dielectric channels walls [55], for which the PNP theory usually systematically predicts higher ionic current than the corresponding molecular scale models [54–56].

Indeed, continuum theories are designed to be used in systems containing a large number of ions, so it is not unexpected that the PNP theory will fail to accurately predict ionic current in channels, where only a single or a few ions can be found at a certain moment [54,55]. In such cases, methods that treat the ions explicitly give more reliable results. Atomistic MD simulations provide the most general platform, because they take into account the entire atomistic structure of the investigated system (e.g. the ion channel and its immediate surroundings), but are for the same reason also computationally extremely demanding. Alternative methods such as Brownian dynamics simulations have thus been proposed, where the channel and ions are represented explicitly at the atomic level, whereas the surrounding solvent is treated as featureless dielectric medium incorporated implicitly via stochastic random forces and multi-ion potential of mean force [49,56]. Such methods were shown to provide better agreement with experiment as compared to the PNP theory [48,55,56].

Nevertheless, continuum theories still offer considerably simpler and less time consuming method to study ionic transport [50]. Therefore, a great effort has been made to modify the PNP equations in order to better capture the physics of particles in confined channels [55]. The problem of the finite size of ions has been addressed by including ion repulsion using the hard sphere chemical potential from the density functional theory of inhomogeneous liquids [57–60], or the Lennard-Jones repulsive potential [60–62]. Alternatively, the PNP theory was upgraded by implicitly including the solvent and empty spaces (void volume) between particles as separate species in the electrolyte in addition to ions [63]. The down side of increasingly complex modifications is, though, that they considerably hamper numerical implementations and require specific numerical algorithms to solve the equations [64].

The objective of our study is to test whether the PNP theory in its original form can satisfactorily describe the conductance of a pore in the lipid bilayer and can be further used in continuum electroporation models with confidence. MD simulations performed in our preceding paper [65] provide an excellent opportunity to achieve this objective, as it is experimentally rather difficult to characterize the conductance of single pores. Namely, when a constant voltage is applied to planar lipid bilayers (also called black lipid membranes, BLM), the electroporation theory predicts that multiple pores form simultaneously, which do not have the same size but rather a size distribution [32]. In order to extract the conductance of single pores one therefore needs to know the number of pores in the membrane as well as their size distribution or at least an estimate of the average pore size

[47]. A study by Melikov et al. [66] though showed that constant voltage can be applied to directly characterize single pores when using the patch clamp technique. Measurements at constant or linearly rising electric current provide a better approach, where the fluctuations in transmembrane voltage appearing at moderate enforced currents can be attributed to size fluctuations of single pores [67–72]. Nonetheless, the possibility that the measured conductance in such experiments results from multiple pores cannot be completely excluded.

On the contrary, MD simulations enable straightforward study of single pores [73–75]. The system in MD simulations is also simpler than experimental systems with planar lipid bilayers as it does not contain any traces of solvent used in the preparation of the lipid bilayer or any other impurities, and is not biased by the uncertainties of the measurement systems. In our opinion thus, MD simulations provide the most direct test to verify that the basic PNP theory can adequately describe the pore conductance. In addition, all required model parameters can be extracted directly from the MD trajectories or by performing additional independent simulations, avoiding the need to fit the measurements to simplified models or electroporation theories [47,67,45,76].

The paper is organized as follows. In Methods we first focus on certain observations from MD simulations, which directed the development of our PNP model of ionic conduction through a lipid pore from its basic form to further upgrades. Afterwards we describe the methods how we extracted the required model parameters from MD simulations. In Results and Discussion we compare the pore conductance as well as the electric potential and ionic concentration profiles as obtained from MD simulations and as predicted by the model that we developed. We then continue with discussion on the applicability of the existing analytical derivations of pore conductance used for the determination of pore size from experimental measurements as well as for their use in continuum electroporation models, and end with a concluding remark in Conclusions.

2 Methods

We constructed the PNP model of ionic current flowing through a lipid pore based on the finite element method (FEM) in COMSOL Multiphysics 5.0. Our basic model closely relates to the one proposed by Li and Lin [46], who analytically derived the expression for the conductance of a cylindrical pore in the general case of unequal ionic concentration on either side of the membrane using the PNP theory. However, we avoid certain simplifications which were required in [46] in order to obtain an analytical derivation, and adapt the model to correspond more closely to the MD system studied. Three major differences can be found: (i) Li and Lin considered that the source of the electric potential is infinitely far away from the pore, hence modeling an infinitely large system, whereas we adapt the model domain to the size of the MD system; (ii) we approximate the pore shape as toroidal instead of cylindrical, which is a more reasonable approximation for pores in lipid bilayers (Fig. 1a); (iii) we consider that the anions and cations (in our case Na and Cl ions) have different diffusion coefficients, which moreover depend on the ionic concentration, as found experimentally [77]; whereas Li and Lin assumed that the diffusion coefficient is equal for both species and constant regardless of the ionic concentration.

Before we explain the construction of the FEM model, we will give a brief description of the MD simulations, based on which the model was constructed, and give a note on certain observations, which guided further development of the model. We namely found, that the basic PNP model itself cannot fully capture all of the underlying physics in ionic conduction through the pore.

To avoid confusion, we consistently use the term "MD system" to refer to the atomistic system with which MD simulations were performed, and the term "FEM model" to refer to the PNP model developed based on the results from MD simulations. For brevity we avoid any technical details of the model implementation into the COMSOL environment, as well as the data extraction from MD simulations. For such information we kindly refer the reader to the Supplementary Material.

2.1 Brief description of MD simulations

The system in MD simulations, which are described in detail in our preceding paper [65], consisted of a lipid bilayer made from 1-palmitoyl-2-oleoyl-*sn*-glycero-3-phosphocholine (POPC) molecules, bathed in ~1 M NaCl solution. The bilayer also contained a preformed pore in its center (Fig. 1a). In order to calculate the electric current through the pore, the simulations were run in GROMACS suite using a specific swapping algorithm that maintains a constant charge imbalance across the pore. The algorithm is namely designed such that when an ion crosses the pore from the region A above the bilayer to the region B below the bilayer, a different ion (of the same type) from region B is swapped with a water molecule from region A (or vice versa). Since periodic boundary conditions are applied on all sides of the simulation box, a vacuum layer is present between the region A and B, which ensures that the ions can move between regions solely through the pore. The number of positive and negative ions above and below the bilayer is thus maintained and is not influenced by the ionic current flowing through the pore. If we initially put an excess number of Na ions above the bilayer and a corresponding excess number of Cl ions below the bilayer, the algorithm will maintain this charge imbalance throughout the simulation resulting in relatively steady transmembrane voltage sustaining the pore. In addition, the surface tension of the bilayer is maintained at ~0 mN/m, allowing the pore to freely adapt its size. The size of the pore, however, influences the ionic flux through the pore as well as the electric potential gradient across the simulated system. Hence, the pore radius, the electric current, and the transmembrane voltage are all "free" parameters, which can spontaneously adapt as the system moves towards an energetic minimum.

For the theoretical analysis reported here, we use the results obtained with the system made from 1024 POPC molecules. These simulations were performed for five constant charge imbalances, i.e., $20q_e$, $32q_e$, $40q_e$, $48q_e$, and $56q_e$ (q_e is the elementary charge), as well as for a system without charge imbalance and without a pore ($0q_e$). The analysis of the MD results in this study though deviates from the one used in [65]. We namely took into account that the typical time scale of charge relaxation in an electrolyte with conductivity σ_e = 8.7 S/m, which corresponds to 1 M NaCl in our MD system, is estimated to be $\tau_r = \varepsilon_e\varepsilon_0/\sigma_e$ = 81 ps [46], where $\varepsilon_e \approx 80$ is the relative dielectric permittivity of the electrolyte and ε_0 the permittivity of vacuum. Therefore, we can safely assume that, in terms of electrostatics, a stationary electric current is established very fast with respect to the time scale of the simulations, and any changes in the pore conductance are simply caused by slower changes in the pore size. Since the pore size is slightly changing throughout all simulations, we divided each 80 ns long

trajectory into four 20 ns long parts and analyzed them separately with respect to the transmembrane voltage, the ionic current, and the pore radius. By averaging the analyzed variables over every 20 ns long part, we could obtain 20 data points describing how the pore conductance depends on the pore radius. This enables a more detailed analysis as compared to the one based on averages over 60 ns extracted from each of the simulations performed at different charge imbalances [65]. Indeed we observed that regardless of the charge imbalance imposed, the dependence of the calculated pore conductance on the pore radius falls on the same curve (see e.g. Fig. 7), corroborating our approach of data analysis.

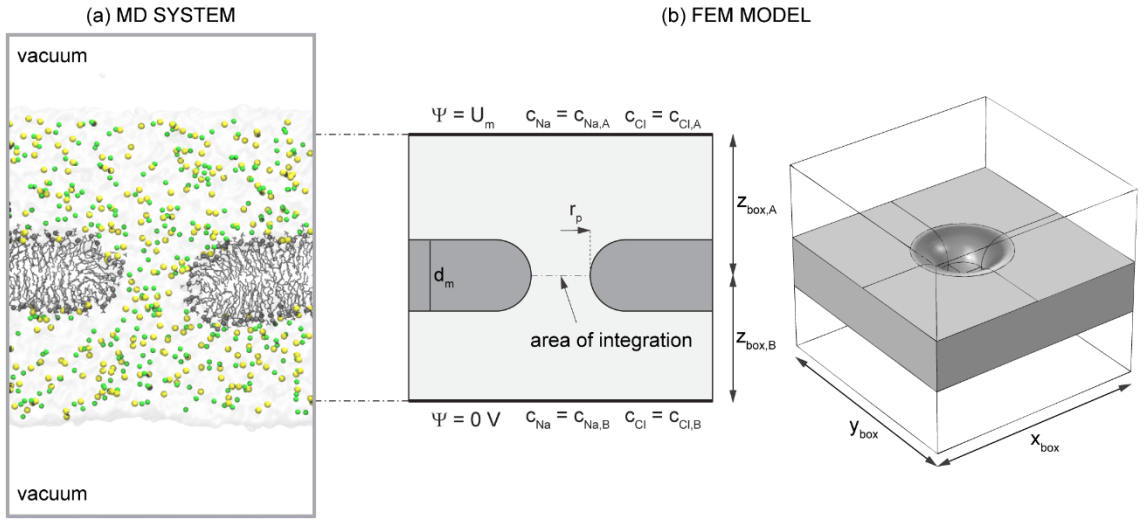

Fig. 1. MD system and corresponding FEM model. (a) Slice across the central region of the MD system. Na ions and Cl ions are presented in yellow and green, respectively, the lipids are in gray with phosphate atoms shown as spheres. Water is shown as light gray surface. The gray rectangle indicates the dimensions of the simulation box in *x* and *z* direction. (b) Slice across the center of the FEM model (left) and 3D view of the model (right). Lipid bilayer is shown in dark gray. The boundaries of the FEM model at the top and bottom side correspond to the *z* planes in the MD system, where bulk properties of the electrolyte are established. The dimensions of the FEM model in *x* and *y* are equal to the dimensions of the MD system.

2.2 Note on net water flux

An important factor that could influence the overall ionic current through the pore is a net water flux we observed in all simulations. The water flux is quite steady, is directed opposite to the electric field, i.e. in the direction of the flow of Cl ions, and increases with increasing charge imbalance imposed in simulations (Fig. 2a).

The water flux can be attributed to electroosmosis, a phenomenon widely exploited in micro- and nano-fluidics to drive fluids through channels by means of an electric field instead of a pressure gradient [78,79]. These channels are designed to have a charged inner surface and hence an interfacial electric double layer which results in charge separation at the interface. The electric field applied parallel to the double layer can thus produce a net force on the mobile counterions. The induced motion of counterions produces a viscous drag force on the surrounding bulk liquid that exceeds the opposing force of the less plentiful coions [80]. The resulting net force on the fluid then induces a bulk fluid motion known as electroosmosis.

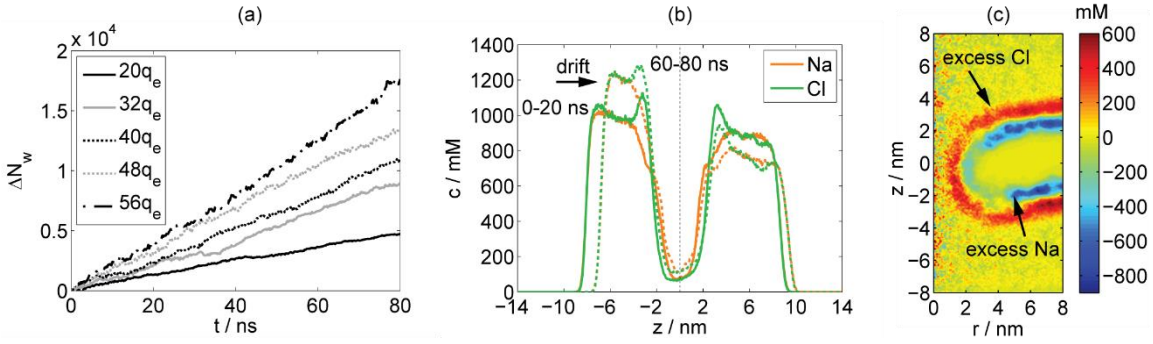

Fig. 2. Net water flux. (a) Increase in the number of water molecules ΔN_w above the center of the bilayer with time, with respect to the beginning of the simulation. (b) Changes in the concentration profiles along the vertical axis of the MD system due to net water flux. The profiles are shown charge imbalance $48q_e$, and were obtained as an average over the first 20 ns (solid lines) and the last 20 ns (dotted lines) of the trajectory. The center of the bilayer is indicated with vertical dotted line. The concentration of ions below the bilayer increases, whereas the concentration above the bilayer decreases with time. (c) Difference in concentration of Cl and Na ions at the lipid-water interface. The profile was obtained by extracting the positions of ions from one of the trajectories and transforming Cartesian coordinates (x, y, z) into axisymmetric cylindrical coordinates (r, z) by placing the center of the cylindrical coordinate system at the center of the pore.

Although POPC lipids are zwitterionic and do not have a net surface charge, the Na ions have a higher affinity to bind to negatively charged oxygen atoms of the lipid headgroups compared to the affinity of Cl ions to bind to positively charged nitrogen atoms, thereby acting similarly as surface charge (we should note the higher binding affinity of Na ions is specifically observed in MD simulations, though a recent study suggests that it may be an artefact of the force fields and that the binding affinities or Na and Cl to lipids are more similar [81]). A double layer is therefore formed at the lipid-water interface, which is also present inside the pore. This can be seen in Fig. 2c, which shows a 2D profile of the difference in concentration of Cl and Na ions. The coordinate system is placed in the center of the pore, where coordinate r corresponds to the horizontal and coordinate z to the vertical distance from the center (we use an axisymmetric coordinate system; see figure caption and Supplementary Material for more details). Note that there is a layer of excess Na ions surrounded by a layer of excess Cl ions along the entire lipid-water interfacial region. Though Na ions are not bound permanently and can contribute to the Na current through the pore, there is a steady number of bound Na ions in the pore wall which influences the electrostatics inside the pore and, as will be shown by results, enhances the conductance of the pore to Cl ions.

On the molecular scale, there are two mechanisms of net water transport in the presence of an electric field, which are captured in MD simulations [82]. The first is the transfer of the momentum from electrophoretically driven ions to neutral water molecules during collisions. The second mechanism is the drag of water molecules, which are associated to moving ions. The Cl ions have higher mass and higher diffusion coefficient, and therefore a higher momentum than Na ions, as well as a higher coordination number and are thereby associated with a higher number of water molecules. As we will describe in section 2.4.5, we calculated the diffusion coefficients of Cl and Na ions in 1 M NaCl to be $1.5 \cdot 10^{-9}$ m^2/s and $1.0 \cdot 10^{-9}$ m^2/s, respectively. The coordination numbers of Cl and Na ions are 7.8 and 5.3, respectively, as obtained from the radial distribution functions. The residence time of water in the first hydration shell in the absence of electric field, which we calculated following [83], is though shorter for Cl; namely 14 ps for Cl and 40 ps for Na. Hence the "transfer of momentum"

mechanism should be dominated by Cl ions, whereas the "dragging" mechanism should actually be dominated by Na ions due to much longer water residence time. Nevertheless, as considerably larger number of Cl ions pass the pore, their number dominance apparently unequivocally determines the direction of the water flow.

The net water flux has two consequences that may influence the electric current through the pore. The first is the change in the overall ionic concentration profile below and above the bilayer, which is a direct consequence of the finite size of the MD system. As the system is canonical, the net water flux results in gradual decrease of the water volume below the bilayer and concomitant increase in the water volume above the bilayer. The swapping algorithm though maintains the number of ions (but not water) below and above the bilayer constant. The changes in water volume hence result in increase/decrease in the bulk NaCl concentration below/above the bilayer (Fig. 1b). The induced concentration gradient could result in diffusive current through the pore. The typical time scale for diffusion can be expressed as $\tau_D = L^2/D$, where L is a typical distance and D is the diffusion coefficient [46]. For Cl ions with diffusion coefficient $D_{Cl} = 1.5 \cdot 10^{-9}$ m/s^2 passing through a ~4 nm thick membrane τ_D = ~11 ns, which is within the timescale of the MD simulations (80 ns), as well as within the 20 ns long piece of trajectory that was analyzed separately. In addition, the concentration gradient across the bilayer could influence the distribution of ions and consequently the electrostatics around the pore [46].

The second consequence of the water flux is a convective ionic current induced by the net fluid motion. The fluid flows in the direction of Cl ions and contributes to the electrophoretic Cl current, whereas it opposes the Na electrophoretic current. The order of magnitude of this contribution can be estimated from the mass flow of water molecules through the pore:

$$\frac{\Delta m_w}{\Delta t} = \frac{\Delta N_w}{\Delta t}\frac{M_w}{N_A} = \rho_w \frac{\Delta V_w}{\Delta t} \tag{1}$$

where $\Delta N_w/\Delta t$ is the number of water molecules passing through the pore per unit time (slope of curves in Fig. 2a), M_w = 18 g/mol is the molar mass of a water molecule, and N_A is the Avogadro constant. The mass flow can then be related to the volumetric flow by scaling it with the water density ρ_w = 972 kg/m^3 (calculated from the density profile of water in the MD system). Since the overall volume of water is much larger than the volume of solvated ions (in present MD system the fraction of ions in the electrolyte is ~3%) we can consider that the volume of fluid (water and ions) is simply equal to the volume of water, hence $\Delta V_w = \Delta V$. The volumetric fluid flow $\Delta V/\Delta t$ can now be related to the convective electric current. The electric current I_i of ions of type i through the pore is the defined as the number of charges $q_e z_i \Delta N_i$ passing through the pore per unit time. If we express the number of ions in terms of ionic concentration $\Delta N_i = c_i N_A \Delta V$, we find that

$$I_i = q_e z_i c_i N_A \frac{\Delta V}{\Delta t} \approx \frac{q_e z_i c_i M_w}{\rho_w}\frac{\Delta N_w}{\Delta t} \tag{2}$$

A simple calculation for a flux of 150 water molecules per ns and 1 M ionic concentration gives a convective electric current of ±0.5 nA. Though this is rather small compared to the total measured electric current (up to ~4 nA for Na and ~12 nA for Cl), the convective current may notably contribute to the higher pore conductance

for Cl ions than for Na ions, which was seen in MD simulations (note that we term the higher pore conductance for Cl than Na ions "the pore selectivity" as is custom in ion channels [59,48,78]).

According to these observations we decided to perform calculations for three increasingly complex variants of the FEM model. In FEM model 1 we neglect the electric double layer and the net fluid flow, which is custom when describing pore conductance in continuum electroporation models. In FEM model 2 we include the electric double layer by modeling the bound Na ions as surface charge at the lipid-water interface. In FEM model 3 we add also the fluid flow by coupling the Poisson-Nernst-Planck equations with Navier-Stokes equation. Comparison between the three models allows us to separately evaluate the contribution of the electric double layer and the fluid flow on the pore conductance and particularly on pore selectivity for Cl ions.

In addition we use two different sets of model parameters. In the first set we consider a simplified system, where we only vary the pore radius, and we keep the size of the system completely symmetric, with equal volume and ionic concentration below and above the bilayer, corresponding to the initial point of the simulations, and use equal transmembrane voltage for all pore radii. In this parameter set we also neglect the dependence of the diffusion coefficient of ions on ionic concentration. In the second set we adapt the size of the electrolyte volume and the ionic concentration below and above the bilayer, the transmembrane voltage, and the pore radius exactly as was extracted from each 20 ns part of the MD trajectories, and moreover take into account that the diffusion coefficients of ions depend on the ionic concentration. We name a model with the first set of parameters as "symmetric", and a model with the second set as "asymmetric". Comparison of calculations from these two sets of parameters allows us to evaluate the influence of geometry and concentration gradient across the bilayer on the overall results, as well as the required complexity of the model to capture the essential features of ion conduction through the pore.

In the following sections we describe the model geometry, the physics of the model, and the methods used to extract the model parameters from MD simulations.

2.3 Finite Element Model

2.3.1 Geometry

The lipid bilayer is represented by a slab with thickness d_m, which contains a toroidal pore in its center (Fig. 1b-c). The radius of the narrowest part of the pore is defined as the pore radius r_p (this directly corresponds to the way how the pore radius was extracted from MD simulations, see section 2.4.1). The bilayer is embedded in a cuboidal box with dimensions x_{box}, y_{box}, z_{box}, which represents the electrolyte. An important consideration that we make is that we neglect the vacuum layer present in the MD system, which is required to maintain a constant charge imbalance across the bilayer. Instead, we "cut" the MD system at horizontal planes below and above the bilayer where the "bulk" properties of the electrolyte are established. As will be explained later, we use Dirichlet boundary conditions at these planes, which are directly extracted from the MD simulations.

2.3.2 Physics

As already noted, we performed calculations for three increasingly complex variants of the FEM model. The description given here is for the most complex variant (FEM model 3) where we take into account the surface

charge on the bilayer and the fluid flow. This model is based on coupled Nernst-Planck, Poisson, and Navier-Stokes equations. The lipid bilayer is only passively included in the model through boundary conditions at the lipid-water interface. Although we performed separate calculations including the bilayer as a nonconductive dielectric with relative permittivity $\varepsilon_l = 2$, we found that this has negligible effect on the results, as had already been observed previously [46].

In the electrolyte, the concentration of Na and Cl ions are described by the steady-state Nernst-Planck equations

$$\mathbf{j_i} = -D_i \nabla c_i - D_i \frac{z_i q_e}{kT} c_i \nabla \Psi + \mathbf{v} c_i \tag{3a}$$

$$\nabla \mathbf{j_i} = 0 \tag{3b}$$

where subscript i corresponds to either Na or Cl, $\mathbf{j_i}$ is the molar flux of ions, D_i denotes the diffusion coefficient, c_i concentration in mol/m^3, $z_i = \pm 1$ the valence of ions, q_e the elementary charge, k the Boltzmann constant, T the absolute temperature, Ψ the electric potential, and $\mathbf{v}$ the fluid velocity. The first term describing the molar flux $\mathbf{j_i}$ accounts for ionic diffusion, the second for electrophoresis, and the third for convection.

The electric potential distribution is given by the Poisson's equation

$$\varepsilon_e \varepsilon_0 \Delta \Psi = -\rho_e \tag{4a}$$

$$\rho_e = F\left(z_{Na} c_{Na} + z_{Cl} c_{Cl}\right) \tag{4b}$$

where ρ_e is the charge density, $\varepsilon_e = 80$ and ε_0 relative permittivity of the electrolyte and permittivity of vacuum, respectively, and F is the Faraday constant. Note that the relative dielectric permittivity of the TIP3P water model, which was used in the MD system, is about ~86 at 300 K [84], but in the presence of ions the permittivity decreases, experimentally to about 70 in 1 M NaCl [85]. Therefore we tested whether the value of the permittivity has a profound effect on the results. In addition to using $\varepsilon_e = 80$ we performed calculations also for $\varepsilon_e = 70$ and 60; however, the difference in results was not significant (up to 2% difference in the calculated total pore conductance for $\varepsilon_e = 70$ and up to 5% for $\varepsilon_e = 60$).

The fluid velocity is given by Navier-Stokes equation for incompressible flow

$$\rho_w \left(\mathbf{v} \cdot \nabla\right) \mathbf{v} = \nabla \left[-p\mathbf{I} + \eta_w \left(\nabla \mathbf{v} + \left(\nabla \mathbf{v}\right)^{\mathrm{T}} \right) \right] \tag{5a}$$

$$\nabla \cdot \mathbf{v} = 0 \tag{5b}$$

where p is the pressure and $\mathbf{I}$ identity matrix. The fluid density and dynamic viscosity are taken as the density of water in the MD system $\rho_w = 972$ kg/m^3, and the viscosity of TIP3P water model $\eta_w = 0.321$ mPa·s [86].

Generally, electroosmotic flux is described by adding a source term $-\rho_e \nabla \Psi$ to the right hand side of (5a) [87]. However, we observed that such description considerably overestmates the velocity of fluid and mass flux compared to the one seen in the MD system, which has been noted before in the case of nanochannels [80]. The overestimate is inherent to the theory and is mainly caused by neglect of the finite size of ions [80]. To be more

close to the MD system with the model, we instead impose a boundary condition defining a constant mass flux from the bottom side of the FEM model

$$-\int_{\partial\Omega} \rho_w \left(\mathbf{v}\cdot\mathbf{n}\right) dA = \frac{dm_w}{dt} \tag{6}$$

and a zero stress condition at the opposite side

$$\left[-p\mathbf{I} + \eta_w \left(\nabla\mathbf{v} + \left(\nabla\mathbf{v}\right)^{\mathrm{T}}\right)\right]\mathbf{n} = 0 \tag{7}$$

The imposed mass flux was extracted from the MD system as described in 2.4.4. Although this approach results in a pressure gradient across the system which is not present in electroosmosis, the velocity profile of the fluid is quite similar, and more importantly, is closer by magnitude to the one in the MD system. As we are primarily testing the applicability of the PNP model to describe lipid pore conductance, we consider out of the scope of the present study to adapt the model of electroosmosis to accurately capture the fluid flow in the MD system, and consider a constant mass flow as a reasonable enough approximation. And indeed this is corroborated by results, as presented later.

For concentration and electric potential we use Dirichlet boundary conditions at the top and bottom of the electrolyte, the values of which are extracted from MD simulations (see section 2.4.2). The electric potential at the bottom is arbitrarily set to 0 V; consequently, the electric potential at the top has the value of the transmembrane voltage U_m (Fig. 1b).

At vertical sides of the electrolyte we use "zero flux" boundary conditions for ionic concentration and electric potential, and a "symmetry" condition for velocity

$$\mathbf{n}\cdot\mathbf{j_i} = 0 \qquad \mathbf{n}\cdot\nabla\Psi = 0 \qquad \mathbf{v}\cdot\mathbf{n} = 0 \tag{8}$$

Since the model geometry is left-right symmetrical, the zero flux and symmetry boundary conditions mimic the situation where the model would be replicated in the horizontal directions, which is similar to the implementation of periodic boundary conditions in MD simulations.

At the lipid-water interface the boundary conditions are the following:

$$\mathbf{n}\cdot\mathbf{j_i} = 0 \qquad \mathbf{n}\cdot\varepsilon_0\varepsilon_e\nabla\Psi = -q_{surf} \qquad \mathbf{v} = 0 \tag{9}$$

The zero flux for concentration simply implies that there is no flux of ions into the membrane. The boundary condition for electric potential describes the electric potential next to a surface with surface charge q_{surf} and imposes the requirement of electroneutrality. The no slip boundary condition for velocity implies that there is no fluid movement at the lipid-water interface. This is a typical boundary condition used for modeling electroosmotic flow and is argued by the fact that the interfacial water is immobilized next to a hydrophilic surface [80].

In simplified variants of the FEM model we omit the Navier-Stokes equation, set the fluid velocity to 0 m/s (model with surface charge only – FEM model 2), and neglect the surface charge by setting q_{surf} = 0 C/m^2 (model without surface charge and fluid flow – FEM model 1).

2.3.3 Calculation of pore conductance and selectivity

The electric current I_i through the pore due to Na and Cl ions is calculated integrating the electric current density $\mathbf{J_i}$ over the pore's horizontal cross-sectional area (Fig. 1b) (we verified that the calculated current is invariant to the plane of integration). $\mathbf{J_i}$ is directly related to the molar flux $\mathbf{j_i}$ from the Nernst-Planck equation by $\mathbf{J_i} = Fz_i\mathbf{j_i}$, hence

$$I_i = \iint_{A_{pore}} \mathbf{J_i} \cdot d\mathbf{A} = F\, z_i \iint_{A_{pore}} \mathbf{j_i} \cdot d\mathbf{A} \tag{10}$$

From the known electric current and transmembrane voltage U_m (which is imposed by boundary conditions), we can calculate the pore conductance for Na ions (G_{Na}), Cl ions (G_{Cl}), and the total pore conductance (G_{tot}), which is the sum of the former two.

$$G_{Na} = I_{Na}/U_m \qquad G_{Cl} = I_{Cl}/U_m \qquad G_{tot} = G_{Na} + G_{Cl} \tag{11}$$

The selectivity of the pore is then defined as the ratio

$$S = G_{Cl}/G_{Na} \tag{12}$$

2.4 Extraction of FEM model parameters from MD simulations

2.4.1 Membrane thickness, pore radius, and pore shape

The membrane thickness was extracted from the distance between the peaks in density distribution of phosphorus atoms in the system with $0q_e$ charge imbalance. The pore radius was calculated using HOLE [88]. The latter was developed to analyze inner dimensions of protein channels based on an algorithm, which moves a "flexible" sphere along the channel's vertical axis. The channel dimension at a given vertical position is determined as the radius of the largest possible sphere, which can be fitted into the channel without overlapping with van der Waals radii of any of the atoms which are specified beforehand. In our case, the specified atoms are phosphorous and nitrogen atoms of the lipid headgroups. The obtained pore dimensions along the vertical axis of the pore were averaged over 80 frames from each 20 ns part of trajectories, and the minimum radius of this average was used as the pore radius. The shape of the pore was always modeled as toroidal except in one set of calculations, where we investigated the effect of the pore shape on the calculated pore conductance.

2.4.2 Box size and boundary conditions

The size of the FEM model in x and y direction was taken as the corresponding size of the MD system, which was extracted from the GROMACS energy (.edr) file. The size of the model in the z direction was, however, defined differently. We namely "cut" the MD system at z planes where bulk properties are established (see also Fig. 1). A detailed image is presented in Fig. 3. We first search for the distance from the vacuum-water interface, where the water density reaches 99% of its bulk value. These z planes are indicated with vertical dotted lines.

Note that at these positions the interfacial water polarization at the vacuum-water interface is already negligible and the electric potential settles at its "bulk value" in the electrolyte. The ionic concentration, though, does not yet reach its bulk value. Bulk ionic concentration is established ~0.5 nm further towards the bilayer, though this value is not well determined due to the presence of a concentration gradient. Hence, we extracted the electric potential as an average between the "bulk water density boundary" and a plane shifted 1 nm further towards the bilayer, whereas we simply took the value of ionic concentration in between these planes (denoted with solid vertical lines). The values of ionic concentration and electric potential at these planes fully defined the boundary conditions of the FEM model and also determined the size of the FEM model in the *z* direction, as marked with arrows above the graph.

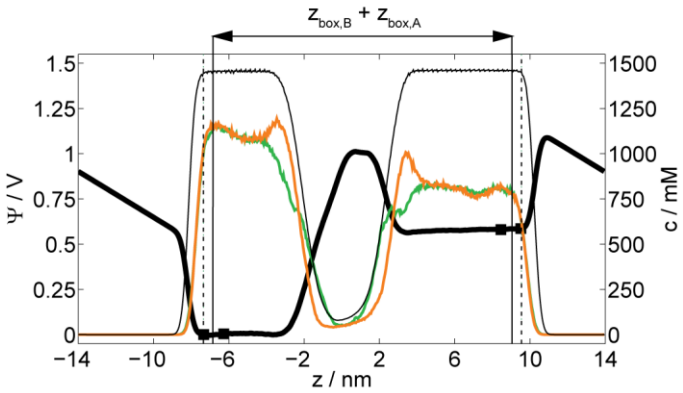

Fig. 3. Principle of extracting boundary conditions of the FEM model from MD simulations. Thin black solid line shows the density profile of water (not in scale); thick black solid line the electric potential; orange and green lines the concentration of Na and Cl ions, respectively. The *z*-planes, where water density reaches 99% of its bulk value are indicated by vertical dotted lines. The value of the electric potential was extracted as an average between this plane and a plane shifted 1 nm towards the bilayer (these *z* planes are also indicated with black squares in the electric potential profiles). The ionic concentration was taken at the *z* plane indicated by solid vertical line, which is shifted 0.5 nm from the "bulk density boundary". The FEM model represented the MD system between the solid vertical lines, as shown by arrows above the graph.

2.4.3 Surface charge

In certain calculations we considered that Na bound to lipid headgroups act as surface charge. The way how to extract the surface charge from MD system is though not so trivial, as there is no sharp transition between the lipid and water phase as in the FEM model, but a rather wide interfacial transitional region. An approach consistent with the Grahame equation, which derives from the Gouy-Chapman theory, was described in [81] where the surface charge is obtained by integrating the charge density of Na and Cl ions from the center of the bilayer up to the shear plane of the electric double layer, which lies close to the plane, where the water density drops to 50% of its bulk value [89]. Although integrating the ionic charge density along the direction normal to the bilayer is very simple in a planar bilayer, it would be rather difficult to perform such integration for the curved pore geometry. Since the most relevant for pore conductance is the surface charge inside the pore, we used a slightly different but related approach to estimate the surface charge inside the pore.

We first counted the average number of bound Na ions in the system with $0q_e$ charge imbalance. The Na ions were considered bound, if they were within a distance of 0.33 nm from any oxygen of the lipid headgroups [90].

(We verified that this cutoff distance is appropriate for our MD system by separately counting the bound ions using different cutoff distances for phosphate, carbonyl and ether oxygen atoms, which corresponded to the positions of the first minima in the radial distribution functions between Na ions and given oxygen atoms.) We then plotted the distribution of the ionic concentration at the interface (thick orange and green solid lines in Fig. 4) together with the cumulative increase in the number of ions as going from the center of the bilayer outwards. The latter is calculated as the cumulative integral of the number density of ions from the center of the bilayer towards the bulk phase, multiplied by the area of the box in the *x* and *y* direction (thin orange and green solid lines). We found that the average number of bound ions in one leaflet (104) found by the cutoff criterion almost directly corresponds to the *z* plane, where the Na and Cl concentration become equal (marked with thick black vertical solid line). This also overlaps with the *z* plane where we find the maximal difference between the cumulative number of Na and Cl ions (gray dotted line). Relating this result to the 2D profile of the difference in Cl and Na concentration presented in Fig. 2c, we can see that in a system with a pore this would correspond exactly to the thin region between the layer of excess Na ions and layer of excess Cl ions, where the Na and Cl concentration are equal. In addition, this plane lays close to the boundary, where the water density falls to 50% of bulk value (marked with arrow above the graph) and appears to be a reasonable dividing surface to separate bound and unbound ions, the former described by a surface charge and the latter described by concentration in the FEM model. The surface charge, which we obtained at this plane is 0.27 q_e/nm^2, which is in good agreement with [90], where the surface charge was found to be 0.26 q_e/nm^2 for a POPC bilayer in 0.5 M NaCl, though using a different force field.

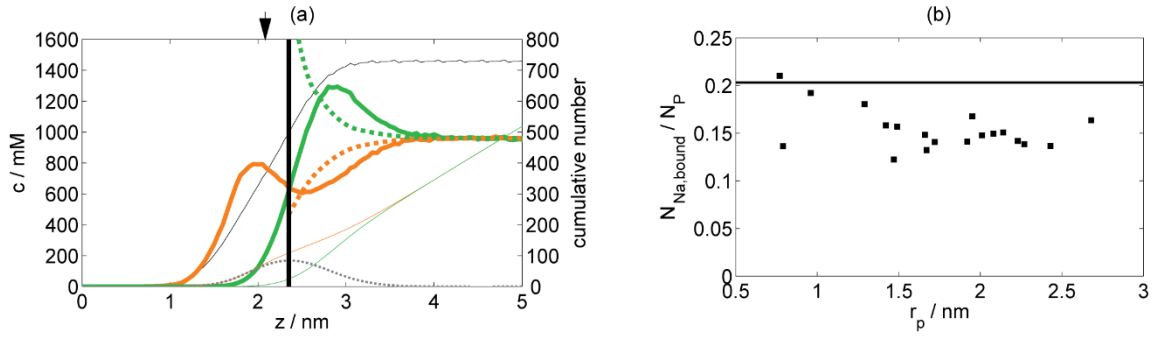

Fig. 4. (a) Extraction of surface charge at the lipid-water interface. Data are from the system with 0q_e charge imbalance. Position z = 0 nm corresponds to the center of the bilayer. Concentration profiles of Na and Cl ions are shown by orange and green thick solid lines, respectively. The cumulative increase in the number of Na and Cl ions from the center of the bilayer towards the bulk is shown in thin orange and green solid lines, respectively, and their difference in dotted gray line. The water density profile is shown as thin black solid line (not is scale) and the z plane where the water density falls to 50% of its bulk value is indicated with arrow above the graph. Solid black vertical line shows the z plane, up to which the charge from Na and Cl ions was integrated to obtain the surface charge. Orange and green thick dotted lines show the concentration profiles as predicted by the FEM model for surface charge 0.27 q_e/nm^2. (b) Number of bound Na ions per number of lipid phosphate atoms in the pore wall, extracted as an average over each 20 ns part of the trajectories.

Our approach suggests, that we can at least to a first approximation relate the number of bound Na ions directly to the surface charge. Therefore we also calculated the number of bound Na ions in a 2 nm high central region inside the pore along with the number of phosphate atoms in this region. Fig. 5b shows the ratio between the bound Na and P atoms for pores with different radii (black squares) together with the ratio determined in the

system with $0q_e$ charge imbalance (horizontal line). We found that the number of bound Na ions per lipid is reduced by ~25% in the pore region, which in fact corroborates with the concentration profile in Fig. 2c indicating that there are less bound Na ions along the pore wall than in the planar part of the bilayer. Using simple approximation that the surface charge is proportional to the number of bound Na ions, we can estimate that the surface charge inside the pore as ~0.20 q_e/nm^2. We are fully aware that the uncertainty of estimating the surface charge is rather high. However, the approximation of representing the bound Na with simple flat surface charge in the FEM model is already hardly applicable at molecular scale [53,91,92]. This can be directly seen from the prediction of the ionic concentration at the charged surface by the PNP model (Fig. 4, thick dotted lines). The discrepancy between the actual concentration profile results from neglecting the finite size of ions in the PNP model. Nevertheless, including surface charge into the FEM model can give an informative insight into the influence of the electric double layer on the pore conductance. Hence, we performed calculations for surface charges of 0.20 q_e/nm^2 and 0.27 q_e/nm^2 in addition to the calculations for 0 q_e/nm^2.

2.4.4 Mass flux

The total increase in the number of water molecules in the region above the bilayer was extracted for each 20 ns long part of the trajectory and plotted against the pore radius (Fig. 5). As we observed a weak correlation between the water flux and the pore radius, we fitted the data to a linear curve. The mass flux of water through the pore was then calculated using equation (1).

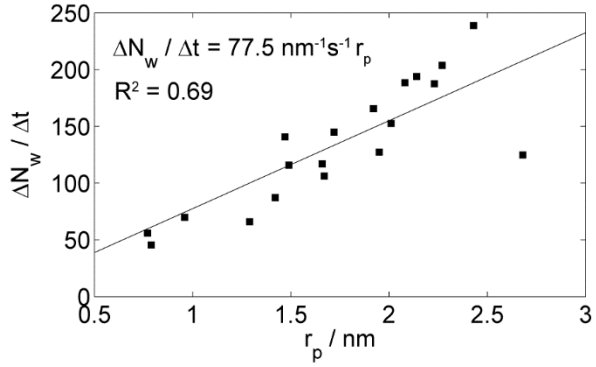

Fig. 5. Flux of water molecules through the pore. The flux was calculated as the total increase in the number of water molecules above the bilayer for each 20 ns part of the trajectories, divided by 20 ns. The data was fitted to a linear curve in the least square sense, by imposing the condition that the flux is 0 s^{-1} for r_p = 0 nm.

2.4.5 Diffusion coefficient of ions

The final parameter which we required to build the FEM model is the diffusion coefficient of Na and Cl ions. The diffusion coefficient depends on the ionic concentration, and since we observed that the ionic concentration in the MD system changes due to net water flux, we wanted to take into account the changes in diffusion coefficients due to changes in concentration. We therefore performed separate simulations, where we used a water box of 5 nm x 5 nm x 5 nm with varying concentration of NaCl. Simulations were ran for 21 ns under the same run options as the simulations for calculating the pore conductance, except that we used an isotropic Berendsen pressure coupling instead of surface tension coupling. The first ns was considered as equilibration, the

remaining 20 ns were used to calculate the mean square displacement (MSD) of ionic positions. We then extracted the diffusion coefficient using the Einstein relation

$$D = \lim_{t\to\infty} \frac{\partial}{\partial t} \frac{MSD}{6} \tag{13}$$

by fitting a linear slope to the MSD between 50 ps and 500 ps, where we found that the MSD is linear. The results of the calculated diffusion coefficients are shown in Fig. 6.

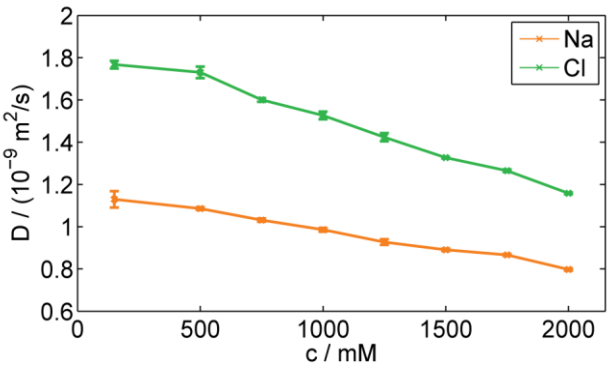

Fig. 6. Diffusion coefficient of Na and Cl depending on the NaCl concentration. The error bars (s.d.) were determined by dividing the time interval, where a linear slope was fitted to the MSD, into 5 subintervals and performing a separate fit to each of these subintervals.

3 Results and Discussion

The main intention of our study is to verify whether the Poisson-Nernst-Planck (PNP) theory can correctly predict the conductance of lipid pores. For this reason we developed three increasingly complex variants of our FEM model, the results of which are compared in the following sections with results from MD simulations.

3.1 Pore conductance

3.1.1 Basic PNP model

In the first stage of our FEM calculations of pore conductance we used the basic PNP model neglecting both the electric double layer and net fluid flow (FEM model 1). Results of the total pore conductance as obtained with the symmetric model (solid line) and asymmetric model (circles) are shown in Fig. 7 together with the results obtained from MD simulations (black squares in Fig. 7a). The agreement with the FEM model and MD results is quite remarkable considering that we are applying continuum theory on a few nm large system. The difference in the results obtained with the symmetric and asymmetric model are only minor, and arise from the different box dimensions and from accounting for the concentration difference across the bilayer, which results in higher ionic concentration inside the pore of the asymmetric model. However, the difference is not due to diffusive current, as the latter is three orders of magnitude lower than the electrophoretic current (up to 0.4% of the total current as predicted by the FEM model).

Since we approximated the pore as perfectly toroidal, we in addition probed the influence of the pore shape on the calculated pore conductance. We represented the pore edge with an ellipse (with semiaxes ratio of 0.5 or 2) instead of a circle. The considered pore shapes are shown in a schematic at the bottom right corner of Fig. 7a, and the corresponding results are presented using dotted lines (Figure 7a and 7b). The pore shape which resembles a cylindrical pore results in lower pore conductance; on the opposite, pore with more "egg-like" edges results in higher pore conductance. Notably, all data points from the MD system fall in between the results for different pore shapes and are indeed best represented by a toroidal shape, which also appears to be the best approximation according to ionic concentration profiles, later presented in Fig. 12.

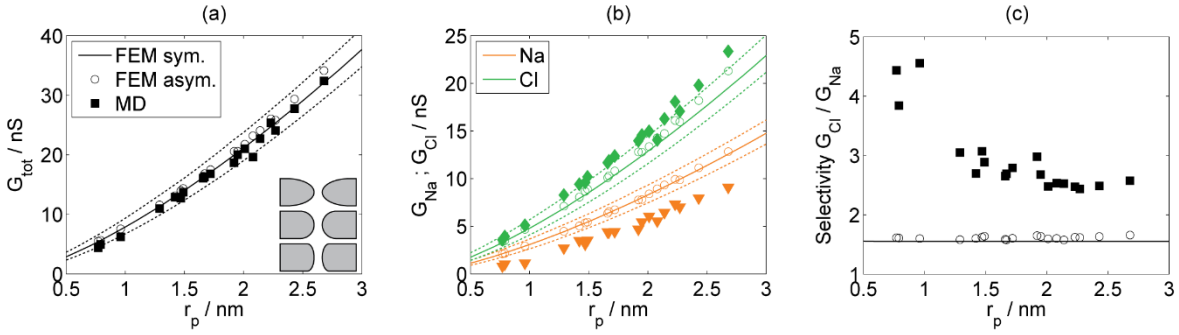

Fig. 7. Results obtained with the basic PNP model without surface charge and fluid flow (FEM model 1). Results from MD are shown in black squares (total pore conductance in (a) and selectivity in (b)), orange triangles (conductance for Na in (b)), and green diamonds (conductance for Cl in (b)). Results from symmetric model are represented by solid lines and the results from asymmetric model with open circles. The dotted lines show results considering different pore shapes, which are shown at the bottom right corner in (a). The upper and lower dotted curve correspond to the uppermost and lowermost pore shape, respectively.

Although the total pore conductance is very well described by the FEM model, the model does not predict correctly the conductance for Na and Cl ions separately, regardless of the pore shape considered (Fig. 7b). Consequently, the model is also not able to reproduce the selectivity of the pore for Cl ions, as was observed in MD simulations (Fig. 7c). The selectivity of 1.5 obtained with the FEM model is equal to the ratio of Cl and Na diffusion coefficients. Apart from the difference in the diffusion coefficients, there is nothing else incorporated in the FEM model that would invoke higher selectivity, and especially, not its dependence on the pore radius. Particularly interesting is that according to MD results, the selectivity for larger pores asymptotically approaches ~2.6 and not 1.5 as would be predicted by the FEM model. Obviously, there is something missing in the model to reproduce such result. Even more important is the question, how can the model reproduce the overall pore conductance, if it cannot properly describe the current of Na and Cl ions flowing through the pore? In the present case, the reason lies in the fact that the model underpredicts the conductance for Cl ions and overpredicts the conductance for Na ions in a similar way. However, at this stage we cannot be certain whether this is simply a coincidence, and whether the FEM model would completely fail to predict the total pore conductance in another situation.

According to the knowledge gained from ion channels and nanochannels, the selectivity for particular type of ions can be due to one or more of the following reasons:

- difference in ion mobilities (diffusion coefficients) inside the channel/pore,
- size exclusion (ions, which are too large and cannot enter the channel/pore) [53,54,57,59,93],
- electrostatic exclusion (channels/pores with charged inner surface will favor the presence of counterions and exclude coions) [53,54,56,59,93], and
- fluid motion, which enhances the current of ions with one charge and opposes the current of ions of the opposite charge (depending on the direction of the fluid movement) [78].

We already observed that there is a difference in the diffusion coefficient of Na and Cl ions in the bulk phase. To corroborate our calculation of the diffusion coefficients from MSD, we also independently calculated the diffusion coefficients from the autocorrelation functions of ion positions as described by Hummer [94] and applied by Vorobyov et al. [95], and obtained similar results (data not shown). Therefore we are confident that the estimates of diffusion coefficients in the bulk are robust. Nevertheless, there could be an additional reduction of the diffusion coefficient (for free ions) inside a confined pore [56,96]. However, it is not expected that the diffusion coefficient for Cl ions is increased, as would be required to reproduce the conductance for Cl ions in Fig. 7b. If there is a reduction in the diffusion coefficients, the FEM model should systematically overpredict the calculated pore conductance for both Na and Cl ions.

Size exclusion of Na ions in our MD system is unlikely, as the pores are larger (radius $\geq$ 0.8 nm) than the radius of Na ions imposed by the CHARMM36 force field used in the MD system (0.27 nm). We can also corroborate this by counting the number of ions inside the pore. Fig. 8 shows that inside the pore there is always a slightly higher number of Na than Cl ions. Size exclusion is hence not responsible for pore selectivity.

Fig. 8 also demonstrates that the higher number of Na ions in the pore is due Na ions bound to the lipid headgroups, which effectively acts as positive surface charge on the pore wall, as explained in section 2.4.3. Electrostatic exclusion should therefore contribute to the pore selectivity for mobile Cl ions, by making the environment energetically favorable for negative charges.

In addition, as we already explained in section 2.2, the net fluid movement observed in the MD simulations could notably contribute to the pore selectivity as it enhances the current of Cl ions and reduces the current of Na ions.

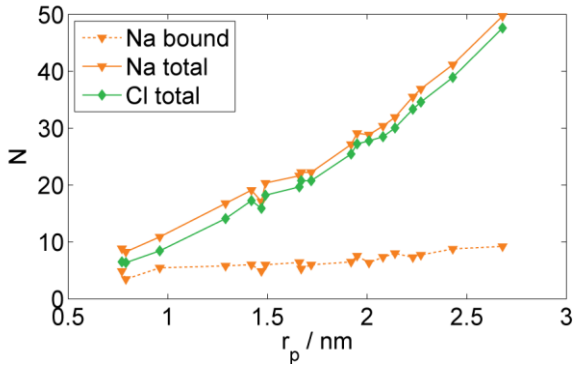

Fig. 8. Number of ions inside the pore. The number was extracted from each 20 ns long part of the trajectories by counting the number of ions in a 2 nm high central region of the pore.

Taking into account the above considerations, we upgraded the FEM model: in the first stage, we added a surface charge to the lipid-water interface representing bound Na ions (FEM model 2), and in the second stage we included in addition a description for the fluid flow (FEM model 3).

3.1.2 PNP model with surface charge and fluid flow

The results obtained with the model including surface charge are presented in Fig. 9. Similarly as we observed in Fig. 7, the results from the symmetric and asymmetric models yield comparable results, therefore we only present the results obtained with the symmetric model. Calculations were performed for two values of surface charge, namely 0.20 q_e/nm^2 and 0.27 q_e/nm^2, and we also present the results from FEM model 1 without surface charge (from Fig. 7) for comparison. Including surface charge into the model increases the conductance of the pore for Cl ions, whereas it reduces the conductance for Na ions, but to a lesser extent (Fig. 9b). Consequently, the total pore conductance is slightly higher than predicted by the model without surface charge, yet very close to the results obtained with the MD system (Fig. 9a). The predicted selectivity for Cl ions (Fig. 9c) is much better represented; the FEM model 2 with surface charge is able to recover the dependence of the selectivity on the pore radius as well as selectivity higher than predicted simply from the ratio of diffusion coefficients.

The agreement between the FEM model and the MD results is though not yet perfect. Particularly from Fig. 9b we can see that the FEM model still considerably overpredicts the conductance for Na ions. Moreover, further increase in the surface charge would not decrease the Na conductance as the results for both values of the surface charge practically overlap.

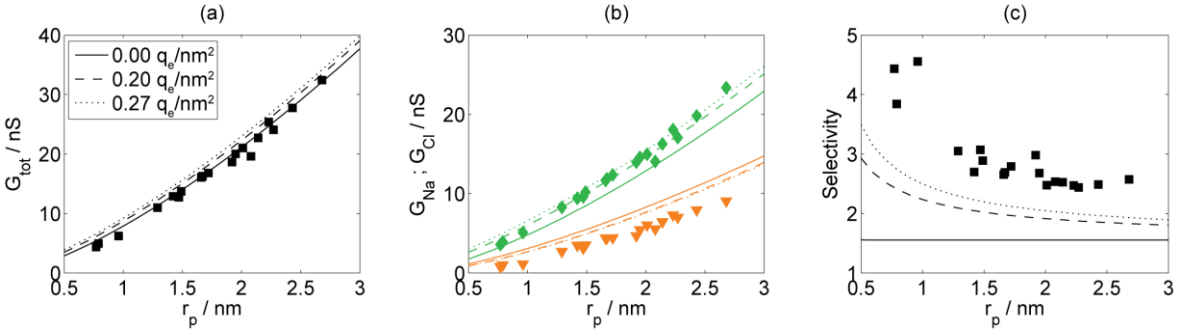

Fig. 9. Results obtained with PNP model with surface charge and without fluid flow (FEM model 2). Apart from results for different surface charge, which are presented with solid, dashed and dotted lines (see legend in (a)), the notation is the same as in Fig. 7.

An additional mechanism that reduces the Na conductance can be attributed to the net fluid flow, as is demonstrated in Fig. 10. Including both the surface charge and the fluid flow in the FEM model 3 (still) correctly predicts the total pore conductance, and in addition also reproduces the pore conductance for Na and Cl ions and the pore selectivity much better than the basic FEM model 1 (Fig. 7). Further argument that both surface charge and fluid flow need to be incorporated in the model to obtain such agreement is given by the results for selectivity in the case of zero surface charge (Fig. 10c, solid line). The fluid flow itself cannot correctly reproduce neither the dependence of the selectivity on the pore radius, nor the value of selectivity for the largest pores. In addition to the results obtained with the symmetric model, we show also the selectivity obtained with

the asymmetric model by circles in Fig. 10c, where the largest circles correspond to results with zero surface charge and the smallest circles to results obtained with the highest surface charge. In accordance with results shown in Fig. 7, the asymmetric model yields similar results as the symmetric model. This further confirms that the bound Na ions and the net fluid flow are the most important properties for reproducing the pore selectivity for Cl ions, whereas the concentration and volume changes on either side of the bilayer resulting from the net water flow and finite size of the system have a lesser effect on the pore conductance.

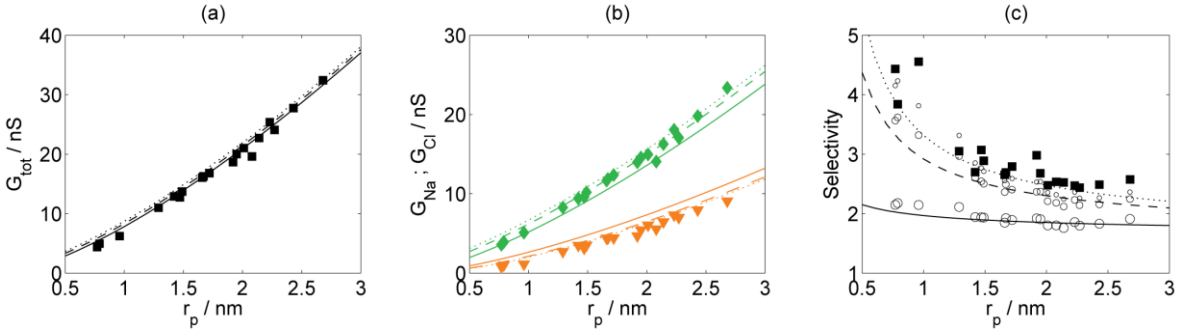

Fig. 10. Results obtained with PNP model with surface charge and fluid flow (FEM model 3). Notation is the same as in Fig. 9.

3.2 Electric potential and ionic concentration profiles

An additional way to verify whether the FEM model correctly presents the MD system is by comparing the profiles of the electric potential and ionic concentrations. We present results for pores with two sizes, namely 0.8 nm and 1.5 nm (Fig. 11). For the MD system, the profiles are shown for the region that was modeled with the FEM model. For the FEM model, the profiles are shown for the asymmetric model with surface charge and fluid flow. Similar profiles were also obtained with other models and are thus not presented. The agreement between the MD system and the FEM model is good, both implying that the highest electric potential gradient is present in the pore and hence most of the transmembrane voltage drops over the pore region. Note that the FEM model does not include the lipid bilayer, therefore the areas corresponding to it are white. The electric potential in the lipid region in the MD system is rather high due to the electric potential arising from the lipid dipoles, which is counterbalanced by the water dipoles, none included in the FEM model.

The profiles of ionic concentration are presented in Fig. 12, where only one half of the system is shown, with the center of the pore at coordinates (0, 0). Here we present both the results from the basic FEM model (FEM model 1), as well as the results from the model including the surface charge and fluid flow (FEM model 3). Note that the agreement is much better for FEM model 3, which can quite well reproduce the concentration of Na and Cl ions in the vicinity of the pore. This additionally confirms that FEM model 3 better represents the MD system than the basic FEM model, as was already argued by comparing the results for the pore selectivity.

Nonetheless, in all of the FEM models considered, the prediction of the total pore conductance is always very close to the one obtained from MD simulations. Including a description of the electric double layer and fluid flow has a counterbalancing effect on the electric current from Na and Cl ions. Both act to increase the current of

Cl ions, and at the same time decrease the current of Na ions. This keeps the overall pore conductance very similar in all models considered. Let us recall that our primary aim is to investigate the validity of using the basic PNP model (without surface charge and fluid flow) for description of pore conductance in electroporation models. In the latter, only the overall pore conductance is considered and not the conductance for each specific ionic species. In the limit of our results presented here, we can thus conclude that the basic model is indeed completely sufficient. Note, however, that our basic PNP model is still more complex than the models of lipid pore conductance considered in previous studies, in particular regarding the pore shape, which is most often approximated as cylindrical. In the next section we discuss the applicability of such approximation.

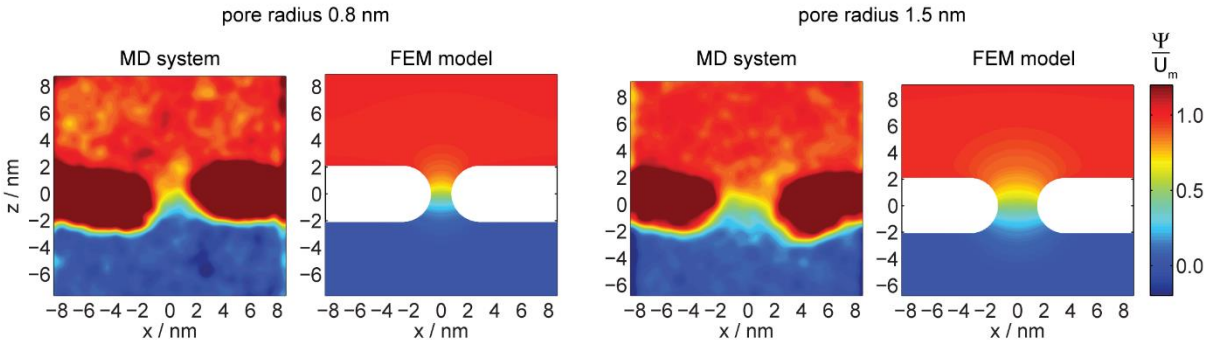

Fig. 11. Electric potential profiles from the MD system and the FEM model with surface charge and fluid flow (FEM model 3). The electric potential Ψ was normalized to the transmembrane voltage U_m. The profiles from the MD system were obtained based on an average over 20 ns long parts of the trajectory (see also the Supplementary Material).

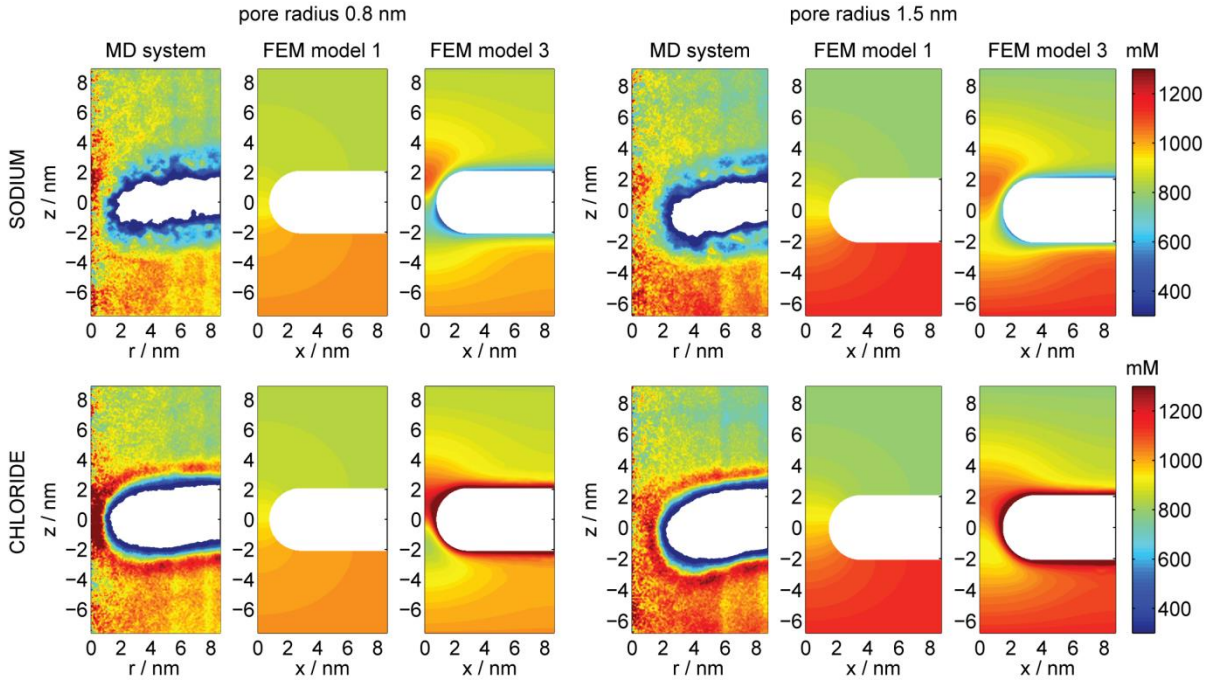

Fig. 12. Na and Cl concentration profiles from the MD system and the basic FEM model without surface charge and fluid flow (FEM model 1), and from the FEM model with surface charge and fluid flow (FEM model 3). The concentration profiles from MD system were obtained in the same way as in Fig. 2c (see also the Supplementary Material).

3.3 Applicability of simplified analytical derivations of pore conductance

Since analytical description is difficult or even impossible to obtain for complex pore shapes and complex electrolyte solutions, most derivations were performed by approximating the pore shape as cylindrical and considering a binary electrolyte (composed of only one cationic and one anionic species). Early derivations also assumed that the ions in the pore flow only in the direction parallel to the central axis of the pore, thereby deriving the current-voltage relationship based on one-dimensional equations. Indeed, the most recent derivation of pore conductance performed by Li and Lin [46] demonstrated that for cylindrical pores, such approximation is valid. The general analytical description for conductance of cylindrical pore is

$$G_p = \frac{I_p}{U_m} = \frac{1}{R_{spd} + R_{int}} = \frac{2\pi\sigma_e r_p^{\,2}}{\pi r_p + 2d_m} \tag{14a}$$

$$R_{spd} = \frac{1}{2\sigma_e r_p} \tag{14b}$$

$$R_{int} = \frac{d_m}{\sigma_e \pi r_p^{\,2}} \tag{14c}$$

where r_p is the pore radius, and σ_e is the conductance of the electrolyte inside the pore. When the conductivities of the electrolyte solutions on either side of the membrane are different, σ_e needs to be replaced by effective conductivity of the solution inside the pore [46]. R_{spd} is the spreading (also access or input) resistance and accounts for the voltage drop at the pore entrance, whereas R_{int} is the resistance of the pore interior region and accounts for the voltage drop across the central region of the pore.

3.3.1 Estimation of pore radius from experimental measurements of bilayer conductance

Analytical descriptions were also used for extraction of pore size based on conductance measurements on planar lipid bilayers. In certain experimental studies, the spreading resistance was neglected and only the resistance of the pore interior region was taken into account [67–70]. Fig. 13 compares different descriptions of pore conductance depending on the pore radius. Since the pore conductance depends linearly on the electrolyte conductivity σ_e, we normalized the total pore conductance by σ_e. On the left-hand side the normalized conductance is shown for pore radii up to 3 nm along with the results from MD simulations and the symmetric FEM model 1, already presented in previous sections. In addition we also show the conductance of a toroidal pore, assuming that the source of the electric potential in infinitely far away from the pore (black dotted line), which is related to the way how the conductance of cylindrical pores (gray solid line) was derived [46]. Note that the toroidal shape results in moderately higher pore conductance at small radii (Fig. 13, left), but basically overlaps with the conductance of cylindrical pores for large pore radii (Fig. 13, right), where the spreading resistance has the dominant contribution, as is also corroborated by experiment [97]. The description of pore conductance neglecting the spreading resistance (gray dotted line), however, results in different (purely quadratic) dependence on the pore radius, which is in disagreement with results from MD simulations. Moreover, when the spreading resistance is neglected, the pore conductance is considerably overestimated for larger pores. Hence, assuming that the pore conductance can simply be approximated as the conductance of its

interior region is an oversimplification for pores of practically any size. The studies, which reported estimates of pore size as calculated from conductance measurements and (14c), therefore underestimated the pore radii. This can be seen from Table 1, where we list selected data from studies measuring conductance of single pores along with the pore radii as reported in the studies, and corrected pore radii, which would be predicted by the PNP model considering a toroidal pore shape. The experimental data in Table 1 are primarily from conductance measurements on planar lipid bilayers, where the authors argued that, most likely, the measured conductance is due to single and not multiple pores. Measurements, where electric current, instead of transmembrane voltage, is enforced and controlled (constant current or linear rising current) are particularly suited for such purpose since the voltage, which controls the pore formation, reduces below pore creation threshold once a sufficiently large pore is formed. Table 1 furthermore shows, that the (normalized) conductance of pores observed in MD simulations is on the lower edge of the ones reported is the literature, but overall in agreement with experiment.

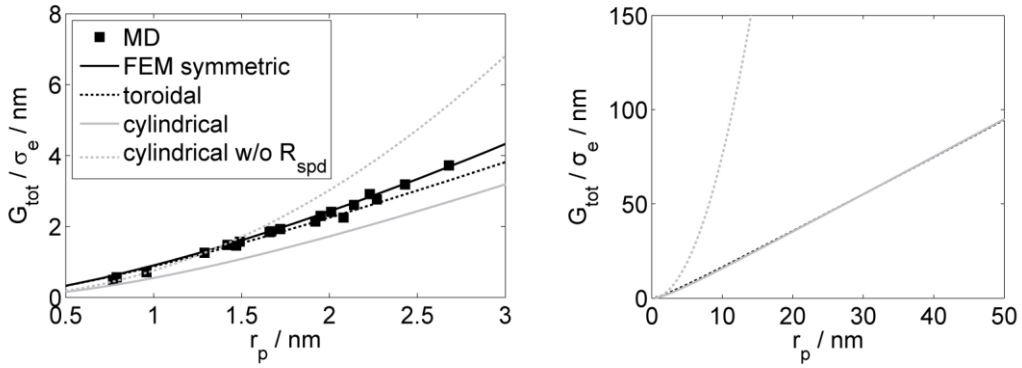

Fig. 13. Comparison of analytical descriptions of pore conductance. Pore conductance was normalized by the conductivity of electrolyte solution σ_e. Left graph shows the normalized pore conductance for pore radius up to 3 nm, and the right graph for pore radius up to 50 nm. "MD" and "FEM symmetric" are the results from MD simulations and the symmetric FEM model 1, as described in previous section. "Toroidal" shows our numerical result for a toroidal pore shape, but with the dimensions of the electrolyte region of the model much larger than the pore dimensions (as though the source of the electric potential was infinitely far away from the pore). "Cylindrical" and "cylindrical w/o R_{spd}" show normalized pore conductance as calculated by equations (14a) and (14c), respectively.

Table 1: Experimental measurements of the conductivity of (most probably) single pores

	Lipid	Electrolyte	Clamp conditions	Pore conductance (nS)	Normalized pore conductance†	Reported pore radius (nm)	Corrected pore radius‡ (nm)	Ref.
Current clamp (chronopotentiometry)			*Clamp current*					
a	egg PC bilayer area: 0.8 mm^2	0.1 M KCl + HEPES (pH 7.0) T = 25 ± 1ºC	0.2 nA 0.5 nA 1.0 nA	3.60–4.17 7.89–11.6 12.7–20.8	2.81–3.26 6.16–9.06 9.92–16.25	2.28–2.69 3.70–4.47 4.68–6.00	2.70–3.01 (2.48–2.77) 4.89–6.64 (4.56–6.23) 7.14–10.72 (6.72–10.19)	[67]
b	egg PC egg PC/Chol 1:1 egg PC/Chol 1:2 bilayer area: 0.8 mm^2	0.1 M KCl + HEPES (pH 7.0) T = 22 ± 1ºC	0.2–1.0 nA 0.2–2.0 nA 0.2–1.5 nA	2.10–8.10 1.90–13.10 1.10–7.98	1.64–6.33 1.48–10.23 0.86–6.23	1.90–3.75 1.65–4.35 1.25–3.40	1.82–5.00 (1.66–4.66) 1.61–7.09 (1.44–6.62) 1.09–4.56 (0.97–4.38)	[70]
c	egg PC bilayer area: 0.8 mm^2	NaCl + HEPES (pH 7.0) T = 20 ± 1ºC	0.19–0.23 nA	0.0032–0.0795 (metastable prepores)	–	–	–	[71]
Linearly rising current			*Current slopes*					
d	POPC bilayer area: 0.0108 mm^2	0.1 M KCl + HEPES + NaOH (pH 7.4)	0.03–8 μA/s	~100 (median) ~550 (max)	~78 (median) ~430 (max)	–	~33 (median) ~162 (max)	[72]
Voltage clamp (patch clamp measurement)			*Clamp voltage*					
e	DPhPC bilayer area: 10 μm^2	0.1 M KCl + HEPES (pH 7.0)	250–450 mV	~0.450 ± 0.250	~0.352 ± 0.195	~1	0.88	[66]
Current or voltage clamp (whole cell clamp technique)			*Clamp current / voltage*					
f	CHO-K1 cells bilayer area‡: ~470 μm^2	DMEM/F12+FCS+antibiotics (pH 8) σ_e = 1.52 S/m; T = 22ºC	between ± 300 nA between ± 1 V	2.4–63.7‡ 2.4–273.7‡	1.6–41.9 1.6–180.1	2.5–20 2.5–55	2.8–39.8 2.8–162.8	[98]
Data from present MD simulations			*Measured current*					
g	POPC bilayer area: 300 nm^2	1 M NaCl σ_e = 8.7 S/m; T = 27ºC	2.0–16.9 nA	4.4–32.4	0.5–3.7	0.8–2.7		[65]

Abbreviations: PC = phosphatidylcholine; POPC = pamitoyloleoylphosphatidylcholine; DPhPC = diphytanoylphosphatidylcholine; Chol = cholesterol. Solvents used for preparation of planar lipid bilayers: (a–c) n-decane; (d) hexane/ethanol 9:1, hexadecane/pentane 3:7 for torus formation; (e) squalene, decane/octane 1:1 for torus formation. The ambient temperature, at which the experiments were performed, the electrolyte conductivity and pH are given for studies, which reported these information.

† Pore conductance was normalized to the electrolyte conductivity. Since studies (a–e) did not report the electrolyte conductivity, we assumed a conductivity of 1.28 S/m, which is the conductivity of 0.1 KCl at 25ºC.

‡ The bilayer area for CHO-K1 cells was estimated as the area of spherical cells with mean radius of 6.1 μm [99]. Study [98] did not report the values of measured conductance, but rather the range of estimated pore radii. The conductance was therefore recalculated from the pore radii reported in [98] and their equation (9), relating the pore conductance to pore radius.

ǂ Corrected pore radii were calculated based on assumption that the basic PNP model is valid also for electrolytes with ionic strength 0.1 M. Corrected pore radii in (a,b) were obtained assuming electrolyte conductivity 1.28 S/m and membrane thickness 7 nm (5.0 nm) for egg PC and 5.9 nm (3.9 nm) for egg PC/Chol. The first thickness corresponds to the thickness used by the authors to calculate the pore radius, the thickness in brackets corresponds to hydrophobic thickness measured by authors [70]. Corrected pore radii in (d) and (e) were obtained assuming electrolyte conductivity 1.28 S/m and membrane thickness 4.0 nm and 3.6 nm, as measured for POPC and DPhPC at 20ºC, respectively [100]. Note that in [66] the radius was estimated based on reduction of pore conductance in the presence of $NMDG^+$/glutamate ions. Corrected pore radii in (f) were obtained assuming extracellular electrolyte conductivity 1.52 S/m, intracellular conductivity 0.5 S/m [33], and membrane thickness 10 nm, the latter assumed by authors [98].

3.3.2 Continuum electroporation models

As we already mentioned in Introduction, the description of the pore conductance plays an important role in electroporation models, where different variants of analytical derivations for the conductance of a cylindrical pore are most often used. For example, apart from derivation given in equation (14) [38,46,101,36], certain authors also assumed that the movement of ions through the pore is hindered because an ions has to overcome an energetic barrier arising from repulsive image forces in the low dielectric pore wall (the Born energy) [33,39,41,44,45,47,102,103], and/or that the pore walls exert a drag force on ions due to the finite size of ions (the steric hindrance) [104,103,39].

In this section we present an example of how different descriptions of pore conductance can affect the results of an electroporation model. Our intention is not to make an extensive analysis, but rather to make a statement that correct description of pore conductance will become increasingly important in further development of electroporation models with the aim of using the models for quantitative rather than qualitative predictions. The electroporation model we used was adapted from [103], the details of which are given in the Supplementary Material.

In the electroporation model we considered four descriptions of pore conductance: (i) numerically calculated conductance of a toroidal pore (this study); (ii) analytical derivation for conductance of a cylindrical pore based on the PNP theory (equation (14) [46]); (iii) analytical derivation for conductance of a cylindrical pore taking into account the Born energy and steric hindrance [103]; and (iv) analytical derivation for conductance of a cylindrical pore, neglecting the spreading resistance, but taking into account the Born energy of ions [33,47]. Fig. 14 shows the time evolution of the relative increase in the membrane conductance and the mean pore radius during and after application of a single electroporative 100 μs pulse. The results demonstrate that the descriptions of pore conductance including the Born energy (indicated with B in brackets in the legend of Fig. 14b) predict about an order of magnitude lower membrane conductance after the pulse, as well as lower mean pore radius during the pulse (Fig. 14b). The description of pore conductance also affects the calculated number of pores, and the fractional area of pores in the membrane, the latter sometimes used to describe the transport of molecules across the membrane [25,101] (data not shown). In addition, the influence of the description of the pore conductance is quantitatively and in certain cases qualitatively different for different pulse parameters (data not shown).

The Born energy of ions only needs to be taken into account in the case where only a single ion is found in the pore at a certain moment and the electrolytic shielding in the pore is not effective [55]. This is not the case in electroporation according to our MD simulations, where multiple ions are continuously present in the pore (Fig. 8). Furthermore, we observed no measurable influence of the transmembrane voltage on the conductance of pores with similar radius in MD simulations, which further confirms that the Born energy, which is reduced by the transmembrane voltage, does not affect the pore conductance in the MD system. The Born energy, however, may be important in the case of very low conductive electrolyte solutions, when much less ions are present in the electrolyte.

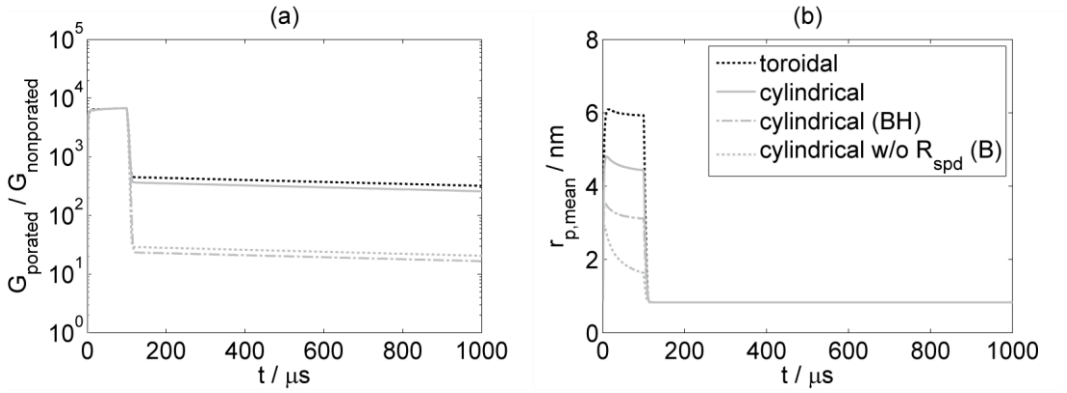

Fig. 14. Results obtained with electroporation model using four different descriptions of pore conductance: (i) numerically calculated conductance of a toroidal pore (black dotted line); (ii) analytical derivation for conductance of a cylindrical pore based on the PNP model (gray solid line); (iii) analytical derivation for conductance of a cylindrical pore taking into account the Born energy and steric hindrance (gray dash-dotted line); and (iv) analytical derivation for conductance of a cylindrical pore, neglecting the spreading resistance, but taking into account the Born energy of ions (gray dotted line). The graphs show the time evolution of the relative increase in the membrane conductance (a) and mean pore radius (b) during and after application of an electroporative 100 μs pulse.

Finally we need to stress that we tested the PNP theory for describing the pore conductance only in the case of 1 M NaCl solution, where the Debye length (~0.3 nm) is shorter than the smallest pore radius (~0.8 nm). In such case, the predictions of the PNP theory were already found comparable to Brownian dynamics simulations of ion conduction through ion channels [54]. Further research could therefore be performed by investigating the pore conductance at lower ionic concentrations, different ionic concentrations on each side of the bilayer, and in the presence of other ionic species, either using MD simulations as performed here, or less computationally demanding Brownian dynamics simulations [48,55,56].

4 Conclusions

In the present study we constructed a theoretical model of the pore conductance based on the continuum Poisson-Nernst-Planck (PNP) theory and compared the obtained results with results from molecular dynamics (MD) simulations. We developed an approach to relate the continuum model to the system in MD simulations by directly extracting all relevant model parameters from the MD system and by performing additional MD simulations when required. Our analysis demonstrates that the PNP theory correctly (quantitatively) predicts the dependence of the pore conductance on the pore radius at least for ionic concentrations in 1 M range, for which the MD simulations were performed. The basic PNP model, however, does not reproduce the selective (higher) conductance of the pore for Cl than to Na ions. We show that the selectivity can be described by taking into account the electric double layer next to the lipid-water interface, which results in electrostatic exclusion of Na ions from the pore; and by taking into account the electroosmotic flow which increases the current of Cl ions, and decreases the current of Na ions. We further demonstrate that correct description of the pore conductance is important when extracting the pore size from experimental measurements as well as when using continuum electroporation models. Among the existing analytical descriptions of the pore conductance the derivation for the

conductance of a cylindrical pore [46] seems to be the closest to the results obtained with MD simulations. However, approximating the pore shape as cylindrical underpredicts the pore conductance for pores with radii up to few nm, whereas modeling the pore shape as toroidal provides a better agreement with MD simulations. Overall we can conclude that the PNP theory is sufficient to describe conductance of lipid pores and can be used in continuum electroporation models with confidence. In addition, our study demonstrates that continuum modeling can be efficiently used as complementary method to molecular scale models for investigating lipid pores.

Acknowledgements

L.R. and D.M. acknowledge the support from the Slovenian Research Agency (ARRS) under program P2-0249 and funding for Junior Researchers R856. M.C. acknowledges the support of the "Istituto Italiano di Tecnologia" (IIT). M.T. acknowledges the support of the French Agence Nationale de la Recherche, under grant (ANR-10_BLAN-916-03-INTCELL). Part of the study was performed during the Short Term Scientific Mission (STSM-TD1104-270215-057439) of L.R., which was granted by COST action TD1104 (www.electroporation.net). The study was conducted in the scope of the European Associated Laboratory for Pulsed Electric Field Applications in Biology and Medicine (LEA EBAM).

References

[1] R. Cannon, S. Ellis, D. Hayes, G. Narayanan, R.C.G. Martin 2nd, Safety and early efficacy of irreversible electroporation for hepatic tumors in proximity to vital structures, J. Surg. Oncol. 107 (2013) 544–549.
[2] J. Teissie, Electrically Mediated Gene Delivery : Basic and translational concepts, (2013).
[3] M.L. Yarmush, A. Golberg, G. Serša, T. Kotnik, D. Miklavčič, Electroporation-based technologies for medicine: Principles, applications, and challenges, Annu. Rev. Biomed. Eng. 16 (2014) 295–320.
[4] R. Cadossi, M. Ronchetti, M. Cadossi, Locally enhanced chemotherapy by electroporation: clinical experiences and perspective of use of electrochemotherapy, Future Oncol. 10 (2014) 877–890.
[5] S. Lakshmanan, G.K. Gupta, P. Avci, R. Chandran, M. Sadasivam, A.E.S. Jorge, et al., Physical energy for drug delivery; poration, concentration and activation, Adv. Drug Deliv. Rev. 71 (2014) 98–114.
[6] G. Sersa, J. Teissie, M. Cemazar, E. Signori, U. Kamensek, G. Marshall, et al., Electrochemotherapy of tumors as in situ vaccination boosted by immunogene electrotransfer, Cancer Immunol. Immunother. CII. 64 (2015) 1315–1327.
[7] D. Miklavčič, B. Mali, B. Kos, R. Heller, G. Serša, Electrochemotherapy: from the drawing board into medical practice, Biomed. Eng. Online. 13 (2014) 29.
[8] S. Toepfl, V. Heinz, D. Knorr, High intensity pulsed electric fields applied for food preservation, Chem. Eng. Process. Process Intensif. 46 (2007) 537–546.
[9] P.Y. Phoon, F.G. Galindo, A. Vicente, P. Dejmek, Pulsed electric field in combination with vacuum impregnation with trehalose improves the freezing tolerance of spinach leaves, J. Food Eng. 88 (2008) 144–148.
[10] S. Shayanfar, O. Chauhan, S. Toepfl, V. Heinz, The interaction of pulsed electric fields and texturizing - antifreezing agents in quality retention of defrosted potato strips, Int. J. Food Sci. Technol. 48 (2013) 1289–1295.
[11] M. Sack, J. Sigler, S. Frenzel, C. Eing, J. Arnold, T. Michelberger, et al., Research on industrial-scale electroporation devices fostering the extraction of substances from biological tissue, Food Eng. Rev. 2 (2010) 147–156.
[12] S. Mahnič-Kalamiza, E. Vorobiev, D. Miklavčič, Electroporation in food processing and biorefinery, J. Membr. Biol. 247 (2014) 1279–1304.
[13] M.D.A. Zbinden, B.S.M. Sturm, R.D. Nord, W.J. Carey, D. Moore, H. Shinogle, et al., Pulsed electric field (PEF) as an intensification pretreatment for greener solvent lipid extraction from microalgae, Biotechnol. Bioeng. 110 (2013) 1605–1615.
[14] C. Gusbeth, W. Frey, H. Volkmann, T. Schwartz, H. Bluhm, Pulsed electric field treatment for bacteria reduction and its impact on hospital wastewater, Chemosphere. 75 (2009) 228–233.
[15] C. Liu, X. Xie, W. Zhao, N. Liu, P.A. Maraccini, L.M. Sassoubre, et al., Conducting nanosponge electroporation for affordable and high-efficiency disinfection of bacteria and viruses in water, Nano Lett. 13 (2013) 4288–4293.

[16] J. Teissie, M. Golzio, M.P. Rols, Mechanisms of cell membrane electropermeabilization: A minireview of our present (lack of ?) knowledge, Biochim. Biophys. Acta 1724 (2005) 270–280.
[17] P.T. Vernier, Z.. Levine, M.. Gundersen, Water bridges in electropermeabilized phospholipid bilayers, Proc. IEEE. 101 (2013) 494–504.
[18] Y. Hu, S.K. Sinha, S. Patel, Investigating hydrophilic pores in model lipid bilayers using molecular simulations: Correlating bilayer properties with pore-formation thermodynamics, Langmuir. 31 (2015) 6615–6631.
[19] I.G. Abidor, V.B. Arakelyan, L.V. Chernomordik, Y.A. Chizmadzhev, V.F. Pastushenko, M.P. Tarasevich, Electric breakdown of bilayer lipid membranes: I. The main experimental facts and their qualitative discussion, J. Electroanal. Chem. Interfacial Electrochem. 104 (1979) 37–52.
[20] E. Neumann, K. Toensing, S. Kakorin, P. Budde, J. Frey, Mechanism of electroporative dye uptake by mouse B cells, Biophys. J. 74 (1998) 98–108.
[21] J.C. Weaver, Y.A. Chizmadzhev, Theory of electroporation: A review, Bioelectrochem. Bioenerg. 41 (1996) 135–160.
[22] T.R. Gowrishankar, J.C. Weaver, Electrical behavior and pore accumulation in a multicellular model for conventional and supra-electroporation, Biochem. Biophys. Res. Commun. 349 (2006) 643–653.
[23] J.C. Neu, W. Krassowska, Asymptotic model of electroporation, Phys. Rev. E. 59 (1999) 3471–3482.
[24] J.C. Neu, W. Krassowska, Modeling postshock evolution of large electropores, Phys. Rev. E 67 (2003) 021915.
[25] D. Miklavcic, L. Towhidi, Numerical study of the electroporation pulse shape effect on molecular uptake of biological cells, Radiol. Oncol. 44 (2010) 34–41.
[26] R.P. Joshi, K.H. Schoenbach, Electroporation dynamics in biological cells subjected to ultrafast electrical pulses: a numerical simulation study, Phys. Rev. E 62 (2000) 1025–1033.
[27] J. Li, W. Tan, M. Yu, H. Lin, The effect of extracellular conductivity on electroporation-mediated molecular delivery, Biochim. Biophys. Acta. 1828 (2013) 461–470.
[28] M.E. Mezeme, G. Pucihar, M. Pavlin, C. Brosseau, D. Miklavčič, A numerical analysis of multicellular environment for modeling tissue electroporation, Appl. Phys. Lett. 100 (2012) 143701.
[29] A.A. Gurtovenko, J. Anwar, I. Vattulainen, Defect-mediated trafficking across cell membranes: Insights from in silico modeling, Chem. Rev. 110 (2010) 6077–6103.
[30] N.J. English, C.J. Waldron, Perspectives on external electric fields in molecular simulation: progress, prospects and challenges, Phys. Chem. Chem. Phys. 17 (2015) 12407–12440.
[31] H. Pera, J.M. Kleijn, F. a. M. Leermakers, On the edge energy of lipid membranes and the thermodynamic stability of pores, J. Chem. Phys. 142 (2015) 034101.
[32] J.C. Weaver, Y.A. Chizmadzhev, Theory of electroporation: A review, Bioelectrochem. Bioenerg. 41 (1996) 135–160.
[33] K.A. DeBruin, W. Krassowska, Modeling electroporation in a single cell. I. Effects Of field strength and rest potential., Biophys. J. 77 (1999) 1213–1224.
[34] T.R. Gowrishankar, A.T. Esser, Z. Vasilkoski, K.C. Smith, J.C. Weaver, Microdosimetry for conventional and supra-electroporation in cells with organelles, Biochem. Biophys. Res. Commun. 341 (2006) 1266–1276.
[35] T.R. Gowrishankar, J.C. Weaver, Electrical behavior and pore accumulation in a multicellular model for conventional and supra-electroporation, Biochem. Biophys. Res. Commun. 349 (2006) 643–653.
[36] J. Li, W. Tan, M. Yu, H. Lin, The effect of extracellular conductivity on electroporation-mediated molecular delivery, Biochim. Biophys. Acta. 1828 (2013) 461–470.
[37] G. Pucihar, D. Miklavcic, T. Kotnik, A time-dependent numerical model of transmembrane voltage inducement and electroporation of irregularly shaped cells, IEEE Trans. Biomed. Eng. 56 (2009) 1491–1501.
[38] W. Krassowska, P.D. Filev, Modeling electroporation in a single cell, Biophys. J. 92 (2007) 404–417.
[39] K.C. Smith, R.S. Son, T.R. Gowrishankar, J.C. Weaver, Emergence of a large pore subpopulation during electroporating pulses, Bioelectrochemistry. 100 (2014) 3–10.
[40] L. Rems, M. Ušaj, M. Kandušer, M. Reberšek, D. Miklavčič, G. Pucihar, Cell electrofusion using nanosecond electric pulses, Sci. Rep. 3 (2013) 3382.
[41] V.F. Pastushenko, Y.A. Chizmadzhev, Stabilization of conducting pores in BLM by electric current, Gen Physiol Biophys. 1 (1982) 43–52.
[42] J.C. Neu, K.C. Smith, W. Krassowska, Electrical energy required to form large conducting pores, Bioelectrochemistry. 60 (2003) 107–114.
[43] M. Hibino, M. Shigemori, H. Itoh, K. Nagayama, K. Kinosita, Membrane conductance of an electroporated cell analyzed by submicrosecond imaging of transmembrane potential., Biophys. J. 59 (1991) 209–220.
[44] A. Barnett, The current-voltage relation of an aqueous pore in a lipid bilayer membrane, Biochim. Biophys. Acta 1025 (1990) 10–14.
[45] S. Kakorin, E. Neumann, Ionic conductivity of electroporated lipid bilayer membranes, Bioelectrochemistry. 56 (2002) 163–166.
[46] J. Li, H. Lin, The current-voltage relation for electropores with conductivity gradients, Biomicrofluidics. 4 (2010) 013206.
[47] R.W. Glaser, S.L. Leikin, L.V. Chernomordik, V.F. Pastushenko, A.I. Sokirko, Reversible electrical breakdown of lipid bilayers: formation and evolution of pores, Biochim. Biophys. Acta. 940 (1988) 275–287.
[48] W. Im, B. Roux, Ion permeation and selectivity of OmpF porin: A theoretical study based on molecular dynamics, Brownian dynamics, and continuum electrodiffusion theory, J. Mol. Biol. 322 (2002) 851–869.
[49] B. Roux, T. Allen, S. Bernèche, W. Im, Theoretical and computational models of biological ion channels, Q. Rev. Biophys. 37 (2004) 15–103.

[50] Q. Zheng, G.-W. Wei, Poisson–Boltzmann–Nernst–Planck model, J. Chem. Phys. 134 (2011).
[51] H. Daiguji, P. Yang, A. Majumdar, Ion transport in nanofluidic channels, Nano Lett. 4 (2004) 137–142.
[52] S. Bhattacharyya, A.K. Nayak, Electroosmotic flow in micro/nanochannels with surface potential heterogeneity: An analysis through the Nernst–Planck model with convection effect, Colloids Surf. Physicochem. Eng. Asp. 339 (2009) 167–177.
[53] G. Moy, B. Corry, S. Kuyucak, S.H. Chung, Tests of continuum theories as models of ion channels. I. Poisson-Boltzmann theory versus Brownian dynamics., Biophys. J. 78 (2000) 2349–2363.
[54] B. Corry, S. Kuyucak, S.-H. Chung, Tests of continuum theories as models of ion channels. II. Poisson–Nernst–Planck theory versus Brownian dynamics, Biophys. J. 78 (2000) 2364–2381.
[55] B. Corry, S. Kuyucak, C. Shin-Ho, Dielectric self-energy in Poisson-Boltzmann and Poisson-Nernst-Planck models of ion channels, Biophys. J. 84 (2003) 3594–606.
[56] S.Y. Noskov, W. Im, B. Roux, Ion permeation through the α-hemolysin channel: Theoretical studies based on Brownian dynamics and Poisson-Nernst-Plank electrodiffusion theory, Biophys. J. 87 (2004) 2299–2309.
[57] D. Goulding, J.-P. Hansen, S. Melchionna, Size selectivity of narrow pores, Phys. Rev. Lett. 85 (2000) 1132–1135.
[58] D. Gillespie, M. Valiskó, D. Boda, Density functional theory of the electrical double layer: the RFD functional, J. Phys. Condens. Matter. 17 (2005) 6609.
[59] D. Gillespie, Energetics of divalent selectivity in a calcium channel: The ryanodine receptor case study, Biophys. J. 94 (2008) 1169–1184.
[60] Y. Hyon, B. Eisenberg, C. Liu, A mathematical model for the hard sphere repulsion in ionic solutions, Commun. Math. Sci. 9 (2011) 459–475.
[61] T.C. Lin, B. Eisenberg, A new approach to the Lennard-Jones potential and a new model: PNP-steric equations, Commun. Math. Sci. 12 (2014) 149–173. doi:10.4310/CMS.2014.v12.n1.a7.
[62] T.C. Lin, B. Eisenberg, Multiple solutions of steady-state Poisson–Nernst–Planck equations with steric effects, Nonlinearity. 28 (2015) 2053.
[63] M. Burger, B. Schlake, M.T. Wolfram, Nonlinear Poisson–Nernst–Planck equations for ion flux through confined geometries, Nonlinearity. 25 (2012) 961.
[64] J.L. Liu, B. Eisenberg, Numerical methods for a Poisson-Nernst-Planck-Fermi model of biological ion channels, Phys. Rev. E. 92 (2015) 012711.
[65] M. Casciola, M.A. Kasimova, L. Rems, S. Zullino, F. Apollonio, M. Tarek, Properties of lipid electropores I: Molecular dynamics simulations of stabilized pores by constant charge imbalance, Bioelectrochemistry. Submitted for Review.
[66] K.C. Melikov, V.A. Frolov, A. Shcherbakov, A.V. Samsonov, Y.A. Chizmadzhev, L.V. Chernomordik, Voltage-induced nonconductive pre-pores and metastable single pores in unmodified planar lipid bilayer, Biophys. J. 80 (2001) 1829–1836.
[67] S. Kalinowski, G. Ibron, K. Bryl, Z. Figaszewski, Chronopotentiometric studies of electroporation of bilayer lipid membranes, Biochim. Biophys. Acta 1369 (1998) 204–212.
[68] S. Koronkiewicz, S. Kalinowski, K. Bryl, Changes of structural and dynamic properties of model lipid membranes induced by α-tocopherol: implication to the membrane stabilization under external electric field, Biochim. Biophys. Acta 1510 (2001) 300–306.
[69] S. Koronkiewicz, S. Kalinowski, K. Bryl, Programmable chronopotentiometry as a tool for the study of electroporation and resealing of pores in bilayer lipid membranes, Biochim. Biophys. Acta 1561 (2002) 222–229.
[70] S. Koronkiewicz, S. Kalinowski, Influence of cholesterol on electroporation of bilayer lipid membranes: chronopotentiometric studies, Biochim. Biophys. Acta 1661 (2004) 196–203.
[71] M. Kotulska, J. Basalyga, M.B. Derylo, P. Sadowski, Metastable pores at the onset of constant-current electroporation, J. Membr. Biol. 236 (2010) 37–41.
[72] P. Kramar, L. Delemotte, A.M. Lebar, M. Kotulska, M. Tarek, D. Miklavčič, Molecular-level characterization of lipid membrane electroporation using linearly rising current, J. Membr. Biol. 245 (2012) 651–659.
[73] A.A. Gurtovenko, I. Vattulainen, Ion leakage through transient water pores in protein-free lipid membranes driven by transmembrane ionic charge imbalance, Biophys. J. 92 (2007) 1878–1890.
[74] H. Leontiadou, A.E. Mark, S.J. Marrink, Ion transport across transmembrane pores, Biophys. J. 92 (2007) 4209–4215.
[75] M.C. Ho, M. Casciola, Z.A. Levine, P.T. Vernier, Molecular dynamics simulations of ion conductance in field-stabilized nanoscale lipid electropores, J. Phys. Chem. B. 117 (2013) 11633–11640.
[76] M. Schmeer, T. Seipp, U. Pliquett, S. Kakorin, E. Neumann, Mechanism for the conductivity changes caused by membrane electroporation of CHO cell-pellets, Phys. Chem. Chem. Phys. 6 (2004) 5564–5574.
[77] P. Atkins, J. de Paula, Physical Chemistry, 9th edition, W. H. Freeman, New York, 2009.
[78] M. Yang, X. Yang, K. Wang, Q. Wang, X. Fan, W. Liu, et al., Tuning transport selectivity of ionic species by phosphoric acid gradient in positively charged nanochannel membranes, Anal. Chem. 87 (2015) 1544–1551.
[79] A.T. Conlis, S. Singer, Modeling electroosmotic flow in nanochannels, in: M. Ferrari, R. Bashir, S. Wereley (Eds.), BioMEMS Biomed. Nanotechnol., Springer US, 2006: pp. 301–330.
[80] R.H. Nilson, S.K. Griffiths, Influence of atomistic physics on electro-osmotic flow: An analysis based on density functional theory, J. Chem. Phys. 125 (2006) 164510.
[81] V. Knecht, B. Klasczyk, Specific binding of chloride ions to lipid vesicles and implications at molecular scale, Biophys. J. 104 (2013) 818–824.

[82] L. Yan, X. Ji, W. Lu, Molecular dynamics simulations of electroosmosis in perfluorosulfonic acid polymer, J. Phys. Chem. B. 112 (2008) 5602–5610.
[83] S.H. Lee, J.C. Rasaiah, Molecular dynamics simulation of ion mobility. 2. Alkali metal and halide ions using the SPC/E model for water at 25 °C, J. Phys. Chem. 100 (1996) 1420–1425.
[84] D. van der Spoel, P.J. van Maaren, H.J.C. Berendsen, A systematic study of water models for molecular simulation: Derivation of water models optimized for use with a reaction field, J. Chem. Phys. 108 (1998) 10220–10230.
[85] J.B. Hasted, D.M. Ritson, C.H. Collie, Dielectric properties of aqueous ionic solutions. Parts I and II, J. Chem. Phys. 16 (1948) 1–21.
[86] M.A. González, J.L.F. Abascal, The shear viscosity of rigid water models, J. Chem. Phys. 132 (2010) 096101.
[87] B. Kirby, Micro- and nanoscale fluid mechanics: transport in microfluidic devices, 1. paperback ed., reprint, Cambridge Univ. Press, Cambridge, 2013.
[88] O.S. Smart, J.M. Goodfellow, B.A. Wallace, The pore dimensions of gramicidin A., Biophys. J. 65 (1993) 2455–2460.
[89] V. Knecht, B. Klasczyk, R. Dimova, Macro- versus microscopic view on the electrokinetics of a water–membrane interface, Langmuir. 29 (2013) 7939–7948.
[90] A. Magarkar, V. Dhawan, P. Kallinteri, T. Viitala, M. Elmowafy, T. Róg, et al., Cholesterol level affects surface charge of lipid membranes in saline solution, Sci. Rep. 4 (2014).
[91] M.S. Kilic, M.Z. Bazant, A. Ajdari, Steric effects in the dynamics of electrolytes at large applied voltages. I. Double-layer charging, Phys. Rev. E. 75 (2007) 021502.
[92] A. Iglič, E. Gongadze, On the orientational ordering of water and finite size of molecules in the mean-field description of the electric double layer – a mini review, J. Phys. Conf. Ser. 398 (2012) 012004.
[93] W. Nonner, L. Catacuzzeno, B. Eisenberg, Binding and selectivity in L-type calcium channels: a mean spherical approximation., Biophys. J. 79 (2000) 1976–1992.
[94] G. Hummer, Position-dependent diffusion coefficients and free energies from Bayesian analysis of equilibrium and replica molecular dynamics simulations, New J. Phys. 7 (2005) 34.
[95] I. Vorobyov, T.E. Olson, J.H. Kim, R.E. Koeppe, O.S. Andersen, T.W. Allen, Ion-induced defect permeation of lipid membranes, Biophys. J. 106 (2014) 586–597.
[96] A.B. Mamonov, M.G. Kurnikova, R.D. Coalson, Diffusion constant of K^+ inside Gramicidin A: A comparative study of four computational methods, Biophys. Chem. 124 (2006) 268–278.
[97] C. Wilhelm, M. Winterhalter, U. Zimmermann, R. Benz, Kinetics of pore size during irreversible electrical breakdown of lipid bilayer membranes., Biophys. J. 64 (1993) 121–128.
[98] H. Krassen, U. Pliquett, E. Neumann, Nonlinear current–voltage relationship of the plasma membrane of single CHO cells, Bioelectrochemistry. 70 (2007) 71–77.
[99] M. Ušaj, K. Trontelj, D. Miklavčič, M. Kandušer, Cell–cell electrofusion: Optimization of electric field amplitude and hypotonic treatment for mouse melanoma (B16-F1) and Chinese hamster ovary (CHO) cells, J. Membr. Biol. 236 (2010) 107–116.
[100] N. Kučerka, M.-P. Nieh, J. Katsaras, Fluid phase lipid areas and bilayer thicknesses of commonly used phosphatidylcholines as a function of temperature, Biochim. Biophys. Acta 1808 (2011) 2761–2771.
[101] J. Li, H. Lin, Numerical simulation of molecular uptake via electroporation, Bioelectrochemistry. 82 (2011) 10–21.
[102] J.C. Weaver, R.A. Mintzer, H. Ling, S.R. Sloan, Conduction onset criteria for transient aqueous pores and reversible electrical breakdown in bilayer membranes, Bioelectrochem. Bioenerg. 15 (1986) 229–241.
[103] Z. Vasilkoski, A.T. Esser, T.R. Gowrishankar, J.C. Weaver, Membrane electroporation: The absolute rate equation and nanosecond time scale pore creation, Phys. Rev. E. 74 (2006) 021904.
[104] A. Barnett, J.C. Weaver, Electroporation: A unified, quantitative theory of reversible electrical breakdown and mechanical rupture in artificial planar bilayer membranes, Bioelectrochem. Bioenerg. 25 (1991) 163–182.

Supplementary material

Properties of lipid electropores II: Comparison of continuum-level modeling of pore conductance to molecular dynamics simulations

Lea Rems[a], Mounir Tarek[b,c,*], Maura Casciola[b,d,e], and Damijan Miklavčič[a]

[a] University of Ljubljana, Faculty of Electrical Engineering, Tržaška 25, SI-1000 Ljubljana, Slovenia
[b] Université de Lorraine, SRSMC, UMR 7565, Vandoeuvre-les-Nancy, F-54500, France
[c] CNRS, SRSMC, UMR 7565, Vandoeuvre-les-Nancy, F-54500, France
[d] Department of Information Engineering, Electronics and Telecommunications (D.I.E.T.), Sapienza University of Rome, 00184 Rome, Italy
[e] Center for Life Nano Science@Sapienza, Istituto Italiano di Tecnologia, 00161, Rome, Italy

*Corresponding author: mounir.tarek@univ-lorraine.fr

Finite element model (FEM)

Implementation of the FEM model into COMSOL Multiphysics

The equations describing the FEM model were solved in the following predefined COMSOL modules: Nernst-Planck equations were solved in *Transport of Diluted Species*, Poisson's equation in *Electrostatics*, and Navier-Stokes equation in *Laminar Flow*. The discretization of the finite elements in all modules was set to quadratic and the mesh size next to the pore wall was refined with maximum element size of 0.5 nm and maximum element growth rate of 1.1. The coupled equations were solved using the *Stationary* study and the direct solver *MUMPS*. The validity of the numerical calculations was verified in two stages. First we repeated the numerical calculations published in [1] and [2], which were based on models closely related to the one used in our study. We compared the published results to our results obtained with COMSOL Multiphysics and found complete agreement. With this we verified that we correctly implemented the model equations into the COMSOL software. Nevertheless, our FEM model which we used for comparison to the results from molecular dynamics (MD) simulations differs from the models described in [1,2] in few aspects: (i) the values of model parameters are different; (ii) we use 3D geometry instead of 2D axisymmetric geometry; (iii) our model also considers a surface charge on the membrane and a fluid flow through the pore. In order to test whether our numerical results are converged and not subject to significant errors resulting from finite discretization of the model, we in addition performed calculations in 2D axisymmetric geometry with refined mesh size around the pore edge. The maximum difference in the results for the total pore conductance, and the pore conductance to Na and Cl ions obtained with 3D and 2D axisymmetric geometry was always below 2.5%, with the highest difference observed for the largest pore. This difference can be partially attributed to numerical errors and partially to the difference in the geometry of the models: in our 3D model the electrolyte domain is represented by a cuboidal box, whereas in the 2D axisymmetric system the electrolyte domain is inherently modelled as cylinder.

According to the tests we performed we can conclude that our numerical results are valid and converged.

FEM model parameters

The numerical calculations reported in our study are performed for two different sets of FEM model parameters. In the first set we consider a simplified system, with the pore radius as the only variable, keeping the size of the system completely symmetric, with equal volumes and ionic concentrations below and above the bilayer, and using a constant transmembrane voltage for all pore radii. In this parameter set we also neglect the dependence of the diffusion coefficient of ions on ionic concentration. In the second set we adapt the size of the electrolyte volume and the ionic concentration below and above the bilayer, the transmembrane voltage, and the pore radius exactly as was extracted from each 20 ns part of the trajectories from MD simulations, taking into account that the diffusion coefficients of ions depend on the ionic concentration. We name a model with the first set of parameters as "symmetric", and a model with the second set as "asymmetric". Tables S1 and S2 list the values of the model parameters in detail. All the model parameters are directly extracted from MD simulations unless otherwise noted.

Table S1. Parameters of the symmetric model

Parameter	Label	Value	Reference
model size in *x*	x_{box}	17.5 nm	approximate average system size at the beginning of all performed MD simulations
model size in *y*	y_{box}	17.5 nm	
model size in *z* (region A)	$z_{box,A}$	8 nm	
model size in *z* (region B)	$z_{box,B}$	8 nm	
membrane thickness	d_m	4.15 nm	distance between peaks in the density profile of phosphorus atoms in the system without charge imbalance and without pore in the bilayer
pore radius	r_p	0.5–3.0 nm	arbitrary (in the range of MD simulations)
transmembrane voltage (V)	U_m	0.5 V	arbitrary (in the range of MD simulations)
concentration Na (region A)	$c_{Na,A}$	930 mM	average NaCl concentration on both sides of the bilayer in the system without charge imbalance and without pore in the bilayer
concentration Cl (region A)	$c_{Cl,A}$		
concentration Na (region B)	$c_{Na,B}$		
concentration Cl (region B)	$c_{Cl,B}$		
diffusion coefficient of Na	D_{Na}	$1.0 \cdot 10^{-9}$ m^2/s	calculated from MSD for 1 M NaCl as described in section 2.4.5 of the main manuscript
diffusion coefficient of Cl	D_{Cl}	$1.5 \cdot 10^{-9}$ m^2/s	
electrolyte permittivity	ε_e	80	TIP3P water model $\varepsilon_e \approx 86$ [3]. The calculations were also performed for $\varepsilon_e \approx 70$ and $\varepsilon_e \approx 60$ to verify that the actual value of ε_e does not considerably influence the results (for details see the main manuscript).
surface charge	q_{surf}	0.00 q_e/nm^2 0.20 q_e/nm^2 0.27 q_e/nm^2	estimated as described in section 2.4.3 of the main manuscript
water density	ρ_w	972 kg/m^3	bulk water density extracted from the system without charge imbalance and without pore in the bilayer
water dynamic viscosity	η_w	0.321 mPa·s	TIP3P water model [4]
mass flux of water	$\mathrm{d}m_w/\mathrm{d}t$	72.224 nm^{-1}·s^{-1} ·r_p	defined as described in section 2.4.4 of the main manuscript
temperature	T	300 K	temperature at which MD simulations were performed

Table S2. Parameters of the asymmetric model

Parameter	Label	Reference
model size in *x*	x_{box}	box size in *x* averaged over every 20 ns part of the trajectories
model size in *y*	y_{box}	box size in y averaged over every 20 ns part of the trajectories
model size in *z* (region A)	$z_{box,A}$	distance from the center of the bilayer to the *z* plane above the bilayer, which lies 0.5 nm below the *z* plane where the average water density reaches 99% of the bulk value
model size in *z* (region B)	$z_{box,B}$	distance from the center of the bilayer to the *z* plane below the bilayer, which lies 0.5 nm above the *z* plane where the average water density reaches 99% of the bulk value
membrane thickness	d_m	see Table S1
pore radius	r_p	minimum pore radius calculated with HOLE software, as described in section 2.4.1 of the main manuscript
transmembrane voltage (V)	U_m	transmembrane voltage averaged over every 20 ns part of the trajectories
concentration Na (region A)	$c_{Na,A}$	average of Na and Cl concentration at the *z* plane above the bilayer, which lies 0.5 nm below the *z* plane where the average water density reaches 99% of the bulk value
concentration Cl (region A)	$c_{Cl,A}$	
concentration Na (region B)	$c_{Na,B}$	average of Na and Cl concentration at the *z* plane below the bilayer, which lies 0.5 nm above the *z* plane where the average water density reaches 99% of the bulk value
concentration Cl (region B)	$c_{Cl,B}$	
diffusion coefficient of Na	D_{Na}	calculated from MSD for different NaCl concentration and using linear interpolation between the data points as shown in Fig. 6 of the main paper
diffusion coefficient of Cl	D_{Cl}	
electrolyte permittivity	ε_e	see Table S1
surface charge	q_{surf}	see Table S1
water density	ρ_w	see Table S1
water dynamic viscosity	η_w	see Table S1
mass flux of water	$\mathrm{d}m_w/\mathrm{d}t$	see Table S1
temperature	T	see Table S1

Extraction of data from MD simulations

Algorithm for selecting the pore center

Prior to analysis, all the trajectories from MD simulations were centered with respect to the center of the bilayer. The center of the pore was then determined by a custom script in Visual Molecular Dynamics (VMD) [5]. Although the algorithm is rather simple, it was sufficient for the purposes of our study.

The algorithm first searches for water molecules that are in between z planes, which lie ±0.5 nm from the center of the system (i.e. a layer of water inside the pore), and finds the center of mass of these water molecules. The selection of water in the narrow layer of ±0.5 nm ensures that only water inside the pore is selected and not the water outside the pore, which could fall into the selection due to bilayer undulations (the bilayer is not completely planar, at certain places it can become a bit wrinkled). This center of mass is then used to define the center of a cylindrical region, with cylinder radius of 3–5 nm (depending on the pore size) and cylinder height of 2 nm (approximately half of the membrane thickness). The algorithm afterwards finds all phosphorus atoms of the lipid headgroups in the cylindrical region and calculates their center of mass. The newly found center of mass better corresponds to the center of the pore in the z direction as the latter can deviate from the center of mass of the entire bilayer. In the end, the center of mass of phosphorus atoms is used to redefine the cylindrical region (with the same radius and height as before, but with its center corresponding to the found center of phosphorus atoms) and calculate the center of mass of all water molecules in the newly defined region. This center of mass is finally taken as the center of the pore.

The robustness of the algorithm was verified by randomly selecting certain frames of the trajectories and using the algorithm to calculate the pore center in the given frame. Two examples are shown in Fig. S1, where the center of the blue cylinder corresponds to the center of the pore as found by the algorithm.

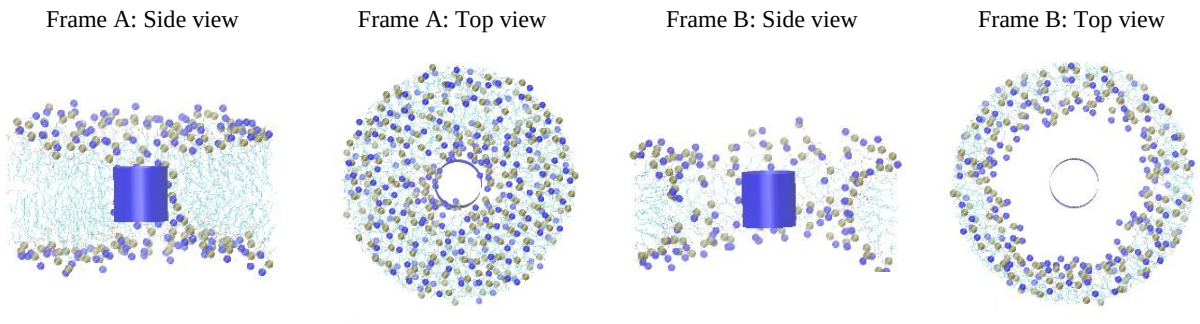

Fig. S1. Test of the robustness of the algorithm for selecting the center of the pore. Results are demonstrated for two randomly chosen frames from the trajectories, the first taken from the simulation which resulted in the smallest pore and the second from simulation which resulted in the largest pore. Only a cylindrical region of the lipid bilayer is presented with phosphorus and nitrogen atoms of the lipid headgroups shown as gold and dark blue spheres, respectively. The center of the small blue cylinder corresponds to the center of the pore as found by the algorithm.

Electric potential profiles

Electric potential profiles presented in Fig. 11 of the main manuscript were calculated in VMD using the PMEpot tool [6]. The positions of the atoms in the trajectories were first translated so that the center of the system corresponded to the average center of the pore as determines by the algorithm described above. The electric potential profiles were then obtained by averaging 100 frames of 20 ns long parts of the trajectories with Ewald factor set to 0.25 and the resolution of the grid set to 0.1 nm.

Ionic concentration profiles

Ionic concentration profiles presented in Fig. 12 were obtained with a custom script in MATLAB. First we calculated the position of the center of the pore at every frame of the trajectory as described above. Then we smoothed the time course of the *x*, *y*, and *z* position of the pore center with the Butterworth filter implemented in MATLAB (Fig. S2). Smoothing avoided taking into account fluctuations in the found positions of the pore center inherent to the algorithm we used, but allowed us to take into account any slow drift in the pore position in the bilayer with time. Then we extracted the positions of all ions at every 10 ps. We shifted the ion positions such that the smoothed position of the center of the pore was always in the center of the coordinate system. Afterwards we transformed the Cartesian coordinates of ions (*x*, *y*, *z*) into axisymmetric cylindrical coordinates (*r*, *z*), where $r = (x^2 + y^2)^{1/2}$. We divided the axisymmetric coordinate system into grid with resolution of 0.1 nm and calculated the number of ions between the grid points. The ionic concentration was then calculated as the number of ions between the grid points, averaged over 40 ns of a given trajectory, and normalized by the volume between the grid points $\pi(r_{i+1}^2 - r_i^2)\cdot(z_{j+1} - z_j)$ and the Avogadro constant.

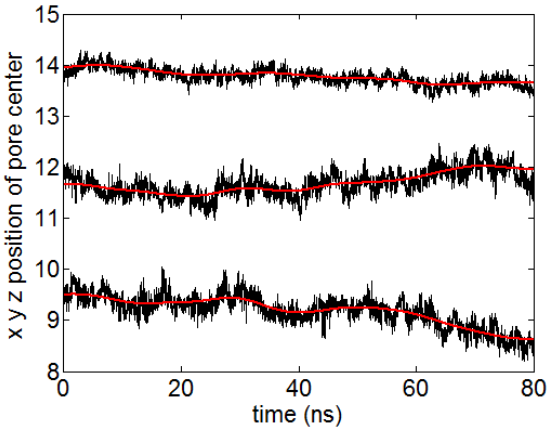

Fig. S2. Time evolution of the *x*, *y*, and *z* positions of the pore center. The black lines show the positions as determined by the algorithm for finding the pore center, whereas the red lines show the smoothed positions of the pore center.

Electroporation model

The model of electroporation is adapted from [7]. The membrane, surrounded by electrolyte solution, is represented by the equivalent circuit shown in Fig. S3, where R_e and C_e are the resistance and capacitance of the electrolyte, respectively, R_s and C_m are the static (passive) resistance and capacitance of the membrane, respectively, R_{ep} is the resistance of the electroporated areas of the membrane, U_{app} is the voltage of the applied electric pulse, and U_m is the transmembrane voltage.

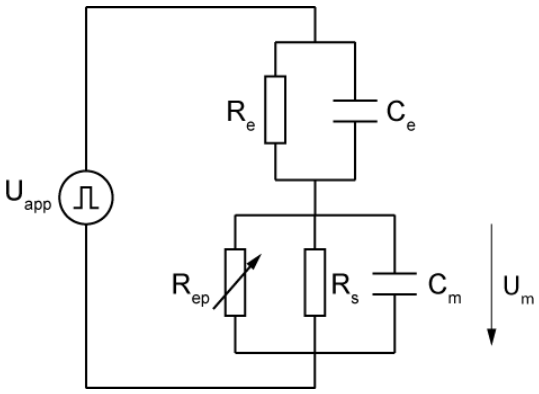

Fig. S3. Equivalent electrical circuit of the membrane model.

Using circuit analysis, the transmembrane voltage can be expressed in terms of an ordinary differential equation

$$\left(C_e + C_m\right)\frac{dU_m}{dt} = -\left(G_e + G_s + G_{ep}\right)U_m + C_e\frac{dU_{app}}{dt} + G_e U_{app} \tag{S1}$$

where the inverse of the resistance (the conductance) is denoted by G and the corresponding subscript.

The population of pores in the membrane is described by a distribution function n in the space of the pore radii such that ndr_p corresponds to the number of pores between radii r_p and $r_p + dr_p$. The size dynamics of the population of pores n is described by the Smoluchowski equation [8]

$$\frac{\partial n}{\partial t} = -\frac{\partial J_p}{\partial r_p} \qquad J_p = -D_p\frac{\partial n}{\partial r_p} - \frac{D_p}{kT}n\frac{\partial \Delta W}{\partial r_p} \tag{S2}$$

where J_p denotes the flux of pores in the space of their radii, D_p the pore diffusion coefficient, k the Boltzmann constant, and T the temperature. ΔW is the change in the pore energy when the pore changes its size, with the reference energy given to the energy of a pore with the minimum possible pore radius $r_{p,min}$ [7]. The pore energy has two contributions $\Delta W = \Delta W_m + \Delta W_e$. The first is the mechanical contribution [7]

$$\Delta W_m = 2\pi\gamma\left(r_p - r_{p,\min}\right) - \frac{\pi\Gamma}{2}\left(r_p^{\,2} - r_{p,\min}^{\,2}\right) \tag{S3}$$

where γ and Γ denote the pore edge tension and the membrane surface tension, respectively. The second is the electrical contribution, which derives from the Maxwell stress tensor at the lipid-water interface and is calculated as the integral of the radial force acting to expand the pore [2]. The latter was numerically calculated in [2] and fitted to analytical expression given in the rightmost side of (S4a).

$$\Delta W_e = -\int_{r_{p,\min}}^{r_{p,\max}} F_{radial}\, dr_p = -\int_{r_{p,\min}}^{r_{p,\max}} \frac{F_{\max} U_m^{\,2}}{1 + r_h / \left(r_p + r_t\right)} dr_p \tag{S4a}$$

$$\Delta W_e = -F_{\max} U_m^{\,2} \left[r_p - r_{p,\min} + r_h \ln\left(\frac{r_{p,\min} + r_t + r_h}{r_p + r_t + r_h} \right) \right] \tag{S4b}$$

The Smoluchowski equation is solved in the space of pore radii where we define the maximum allowed pore radius at $r_{p,max}$ = 50 nm. For boundary condition at $r_{p,max}$ we use zero flux of pores

$$J_p\left(r_{p,\max}\right) = 0 \tag{S5}$$

The model assumes that the hydrophilic pores are created from hydrophobic pores, where the minimum radius of a hydrophilic pore is $r_{p,min}$ = 0.8 nm (for details see [7]). The rate of creation and destruction of hydrophilic pores is described by Arrhenius-type rate equations [7]

$$J_p\left(r_{p,\min}\right) = A_0 \exp\left(\frac{-\delta_c + B U_m^{\,2}}{kT} \right) - n\left(r_{p,\min}\right) \chi \exp\left(\frac{-\delta_d}{kT} \right) \tag{S6}$$

where the first term on the right hand side of (S6) corresponds to the rate of pore creation and the second term to the rate of pore destruction. In equilibrium $J_p(r_{p,min}) = 0$, from which we can extract

$$n_{eq}\left(r_{p,\min}\right) = \frac{A_0}{\chi} \exp\left(\frac{-\delta_c + \delta_d}{kT} \right) \tag{S7}$$

and rewrite equation (S6) as

$$J_p\left(r_{p,\min}\right) = A_0 \exp\left(\frac{-\delta_c}{kT} \right) \left[\exp\left(\frac{B U_m^{\,2}}{kT} \right) - \frac{n\left(r_{p,\min}\right)}{n_{eq}\left(r_{p,\min}\right)} \right] \tag{S8}$$

which defines the boundary condition of Smoluchowski equation at $r_p = r_{p,min}$. The equilibrium distribution of pores at zero transmembrane voltage can also be obtained from

$$n_{eq}\left(r_p\right) = n_{eq}\left(r_{p,\min}\right) \exp\left(\frac{-\Delta W_m}{kT} \right) \tag{S9}$$

which yields the total number of pores in the membrane in equilibrium

$$N_{eq} = \int_{r_{p,\min}}^{r_{p,\max}} n_{eq}\left(r_{p,\min}\right) \exp\left(\frac{-\Delta W_m}{kT} \right) dr_p \tag{S10}$$

If we know the equilibrium number of pores N_{eq}, we can determine

$$n_{eq}\left(r_{p,\min}\right)=\frac{N_{eq}}{\int_{r_{p,\min}}^{r_{p,\max}}\exp\left(\frac{-\Delta W_m}{kT}\right)dr_p} \tag{S11}$$

which fully defines the boundary condition in (S8).

The changes in the distribution of the population of pores in the membrane influence the conductance of the membrane. In the equivalent circuit in Fig. S2, the change in membrane conductance due to pores is represented by $G_{ep} = R_{ep}^{-1}$. G_{ep} is obtained by integrating the product of the distribution n and the conductance of a single pore G_p, which varies with the pore radius.

$$G_{ep}=\int_{r_{p,\min}}^{r_{p,\max}} nG_p dr_p \tag{S12}$$

In our study we used four different descriptions of the conductance of a single pore, which are described below.

(i) We numerically calculated the conductance of a toroidal pore using parameters given in Table S3 and following the approach described in [1].

(ii) We used the analytical derivation for the conductance of a cylindrical pore based on the PNP theory [1], which is already given in equation (14) of the main manuscript and repeated here for completeness.

$$G_p=\frac{1}{R_{spd}+R_{int}}=\frac{2\pi\sigma_e r_p^{\,2}}{\pi r_p+2d_m} \tag{S13a}$$

$$R_{spd}=\frac{1}{2\sigma_e r_p} \tag{S13b}$$

$$R_{int}=\frac{d_m}{\sigma_e \pi r_p^{\,2}} \tag{S13c}$$

(iii) We used the analytical derivation for the conductance of a cylindrical pore taking into account the Born energy and steric hindrance [7]. The latter are taken into account by scaling the internal pore resistance given in (S13c) by factors K ($0 \le K \le 1$) and H ($0 \le H \le 1$)

$$R_{int}=\frac{d_m}{\sigma_e \pi r_p^{\,2} KH} \tag{S14a}$$

Factor K is given by [7,9,10]

$$K=\frac{\exp\left(\psi_m\right)-1}{\frac{w_0\exp\left(w_0-\eta\psi_m\right)-\eta\psi_m}{w_0-\eta\psi_m}\exp\left(\psi_m\right)-\frac{w_0\exp\left(w_0+\eta\psi_m\right)+\eta\psi_m}{w_0+\eta\psi_m}} \tag{S14b}$$

where $\psi_m = U_m q_e/(kT)$ is the nondimensional transmembrane voltage with q_e denoting the elementary charge, η the relative distance of the entrance region of the pore, and w_0 the non-dimensional Born energy of an ion in the center of the pore [7]

$$w_0(r_p) = \frac{1}{kT}\frac{(z_s q_e)^2}{4\pi\varepsilon_l r_p} P\left(\frac{\varepsilon_l}{\varepsilon_e}\right)\frac{4\exp\left(-0.98\,\mathrm{nm}^{-1} r_p\right)+1}{5} \tag{S14c}$$

Factor H is given by [7,11]

$$H = \left(1-\frac{r_s}{r_p}\right)^2\left[1-2.104\left(\frac{r_s}{r_p}\right)+2.09\left(\frac{r_s}{r_p}\right)^3-0.95\left(\frac{r_s}{r_p}\right)^5\right] \tag{S14d}$$

where r_s is the hydrated radius of an ion.

Apart from modification of the term describing the internal pore resistance R_{int}, the pore conductance is calculated in the same way as in (S13).

(iv) We used the analytical derivation for the conductance of a cylindrical pore, neglecting the spreading resistance, but taking into account the Born energy of ions [9,10].

$$G_p = \frac{1}{R_{int}} = \frac{\sigma_e \pi r_p^{\,2}}{d_m} K \tag{S15}$$

where factor K is already given in (S14b).

The presented equations were implemented and solved in COMSOL Multiphysics 5.0, with equation (S1) solved in the module *Global ODEs and DAEs*, and equation (S2) solved in the module *Coefficient Form PDE* with the domain representing the pore radius space defined as a line ranging from $r_{p,min}$ to $r_{p,max}$. The boundary conditions of (S2) are given in (S5) and (S8).

For the results presented in Fig. 14 of the main manuscript we calculated the relative increase in the membrane conductance as G_{ep}/G_s, and the mean pore radius $r_{p,\mathrm{mean}}$ as the first moment of the distribution function n

$$r_{p,\mathrm{mean}} = \int_{r_{p,\min}}^{r_{p,\max}} r_p n dr_p \tag{S16}$$

The values of all parameters of the electroporation model are given in Table S3.

Table S3. Parameters of the electroporation model

Parameter	Label	Value	Reference
Equivalent circuit			
Cell radius	R_{cell}	10 μm	[7]
Electrolyte conductivity	σ_e	1.2 S/m	[7]
Electrolyte permittivity	ε_e	80	[7]
Membrane area	A_m	10 μm^2	[7]
Membrane thickness	d_m	5 nm	[7]
Membrane conductivity	σ_m	10^{-7} S/m	[12]
Membrane permittivity	ε_m	5	[7]
Static membrane resistance	$R_s = \sigma_m A_m / d_m$	$5 \cdot 10^{9}$ Ω	
Membrane capacitance	$C_m = \varepsilon_m \varepsilon_0 A_m / d_m$	$8.8 \cdot 10^{-14}$ F	
Membrane charging time	$\tau_{chg} = R_{cell} C_m / A_m \cdot 1.5 / \sigma_e$	111 ns	
Electrolyte resistance	$R_e = \tau_{chg} / C_m$	$1.25 \cdot 10^{6}$ Ω	
Electrolyte capacitance	$C_e = (\varepsilon_e \varepsilon_0 / \sigma_e) / R_e$	$4.7 \cdot 10^{-16}$ F	
Electroporation model			
Minimum pore radius	$r_{p,min}$	0.8 nm	[7]
Pore diffusion coefficient	D_p	$5 \cdot 10^{-14}$ m^2/s	[7]
Membrane surface tension	Γ	10^{-5} N/m	[7]
Pore edge tension	γ	$2 \cdot 10^{-11}$ N	[7]
Constant in electric pore energy	F_{max}	$6.9 \cdot 10^{-10}$ N/V^2	[2]
Constant in electric pore energy	r_h	0.95 nm	[2]
Constant in electric pore energy	r_t	0.23 nm	[2]
Prefactor in pore creation rate	$A_0 = \nu_0 A_m d_m$	$1.5 \cdot 10^{17}$ s^{-1}	[7]
Attempt rate density	ν_0	$3 \cdot 10^{-36}$ $s^{-1}m^{-3}$	[7]
Energetic barrier for pore creation	δ_c	44 kT	[7]
Constant in pore creation rate	B	20 kT/V^2	[7]
Equilibrium number of pores	N_{eq}	$3.3 \cdot 10^{-5}$	[7]
Temperature	T	293 K	[7]

References

[1] J. Li, H. Lin, The current-voltage relation for electropores with conductivity gradients, Biomicrofluidics. 4 (2010) 013206.

[2] J.C. Neu, K.C. Smith, W. Krassowska, Electrical energy required to form large conducting pores, Bioelectrochemistry. 60 (2003) 107–114.

[3] D. van der Spoel, P.J. van Maaren, H.J.C. Berendsen, A systematic study of water models for molecular simulation: Derivation of water models optimized for use with a reaction field, J. Chem. Phys. 108 (1998) 10220–10230.

[4] M.A. González, J.L.F. Abascal, The shear viscosity of rigid water models, J. Chem. Phys. 132 (2010) 096101.

[5] W. Humphrey, A. Dalke, K. Schulten, VMD: Visual molecular dynamics, J. Mol. Graph. 14 (1996) 33–38.

[6] A. Aksimentiev, K. Schulten, Imaging α-hemolysin with molecular dynamics: Ionic conductance, osmotic permeability, and the electrostatic potential map, Biophys. J. 88 (2005) 3745–3761.

[7] Z. Vasilkoski, A.T. Esser, T.R. Gowrishankar, J.C. Weaver, Membrane electroporation: The absolute rate equation and nanosecond time scale pore creation, Phys. Rev. E. 74 (2006) 021904.

[8] J.C. Weaver, Y.A. Chizmadzhev, Theory of electroporation: A review, Bioelectrochem. Bioenerg. 41 (1996) 135–160.

[9] R.W. Glaser, S.L. Leikin, L.V. Chernomordik, V.F. Pastushenko, A.I. Sokirko, Reversible electrical breakdown of lipid bilayers: formation and evolution of pores, Biochim. Biophys. Acta. 940 (1988) 275–287.

[10] K.A. DeBruin, W. Krassowska, Modeling electroporation in a single cell. I. Effects Of field strength and rest potential., Biophys. J. 77 (1999) 1213–1224.

[11] E.M. Renkin, Filtration, diffusion, and molecular sieving through porous cellulose membranes, J. Gen. Physiol. 38 (1954) 225–243.

[12] T. Kotnik, D. Miklavcic, Theoretical evaluation of voltage inducement on internal membranes of biological cells exposed to electric fields, Biophys. J. 90 (2006) 480–491.

Conclusions

The present thesis demonstrated that numerical modeling can be efficiently applied as complementary method for studying different systems, from the molecular scale up to the tissue level. As all of the results were already thoroughly discussed in the papers, I will only comment on some points related to the performed studies and give the final concluding remarks.

In the study on electroporation of intracellular liposomes we concluded that the approach using nanosecond electric pulses to control the release of their content would be feasible. This study was in fact performed within the framework of a project, where we wanted to use this approach for electroporation of archaeosomes (i.e. artificial vesicles made from archaeal lipids). However, their electroporation was never detected experimentally.

In the theoretical study we assumed that the vesicles electroporate when the transmembrane voltage reaches roughly 1 V. More specifically, the maximum transmembrane voltage reached on a vesicle by the end of a pulse, which was considered as being able to induce electroporation, was ~1.4 V. I can compare this assumption with experimental results from Tekle *et al.*, who electroporated salt-filled and sucrose-filled DOPC vesicles with mean diameter of 103 nm (Tekle *et al.*, 2005). The vesicles were suspended in sucrose solution and exposed to a single 10 ns pulse resulting in 80, 160 or 240 kV/cm. They observed that none of the vesicles electroporated at 80 kV/cm, only salt-filled vesicles electroporated at 160 kV/cm, and both salt-filled and sucrose-filled vesicles electroporated at 240 kV/cm. When I theoretically replicated their experiments using our model and taking into account the conductivities of the salt and sucrose solutions, which they reported in their paper, I estimated that the vesicles were electroporated when the induced transmembrane voltage reached ~0.9 V (Rems and Miklavčič, 2015). This is lower than we assumed in our study, thereby the pulse amplitudes, which we predicted as being able to provoke vesicle electroporation, should be rather overestimated than underestimated.

Unfortunately, we did not know at that time the actual transmembrane voltage at which archaeal lipids electroporate. Later calculations with molecular dynamics simulations demonstrated that bilayers made from archaeal lipids and mixed bilayers made from archaeal and dipalmitoylphosphatidylcholine (DPPC) lipids in 50:50 molar ratio (both combinations were used to prepare the vesicles for experiments) require at least a factor of 2.0–2.6 higher transmembrane voltage for electroporation at room temperature as compared to pure DPPC bilayers (Polak *et al.*, 2014). Moreover, we later observed that archaeosomes enter the cells by means of endocytosis (Batista Napotnik *et al.*, 2013), which adds another envelope around the vesicles and would further increase the electric field required for their electroporation. Relating these observations to our numerical study and considering the electric fields that were imposed in the experiments (T. Batista Napotnik, private communication), I propose that these electric fields were probably too low to trigger archaeosome electroporation (the electric fields were at the limit achievable with our experimental setup). Another possible explanation for the absence of detectable archaeosome electroporation also comes from molecular dynamics

simulations, which showed that the pores formed in archaeal lipids are hydrophobic (i.e., not stabilized by lipid headgroups) (Polak *et al.*, 2014). This suggests that even if archaeosomes were electroporated, the formed pores closed very rapidly after each nanosecond pulse, preventing sufficient amount of calcein (used to detect archaeosome electroporation) to leak out from the vesicles in order to detect the leakage. The above experimental observations speak against the possibility of using nanosecond pulses as an approach to control the release of the archaeosome content. Nevertheless, if vesicles would be made from other lipids or lipid mixtures, which would allow them to electroporate at lower transmembrane voltage than archaeosomes, then the approach should still be feasible.

In order to test the validity of our model in yet another way, I can compare the model predictions with experiments performed by Batista Napotnik *et al.* (2010). They demonstrated that electroporation of endocytotic vesicles could be detected by release of Lucifer Yellow when ten 60 ns, 50 kV/cm pulses were applied. Though it is difficult to judge the exact size of the endocytotic vesicles in these experiments, the model suggests that any vesicle with radius larger than 100 nm could easily be electroporated using such pulses.

The study on cell electrofusion using nanosecond pulses demonstrated that the highest transmembrane voltage can be achieved at the contact zones between cells, if the pulses are sufficiently short. I need to stress that according to the model, this can only be observed, if the cells are exposed to pulses in medium with lower conductivity as compared to the conductivity of the cytoplasms. The less conductive the extracellular medium is, the more profound is the amplification of the transmembrane voltage at the contact zones. I only recently found two experimental studies, which further corroborate this prediction. Mehrle *et al.* (1989) exposed tobacco protoplasts in sucrose solution (conductivity <0.001 S/m) to 50 μs, 0.4 kV/cm pulse either as isolated cells or in pearl chains. They observed that when the cells were exposed to the pulse as isolated cells, only the anodic side of the membranes became permeable to the dye neutral red; but when the cells were exposed to the same type of a pulse in pearl chain aligned with the electric field, permeabilization occurred at both the anodic and cathodic sides of the membranes (the asymmetry in permeabilization is attributed to the effect of the resting potential, Paper 1). I estimated the charging time of the cell membranes under their experimental conditions according to (Kotnik *et al.*, 1997)

$$\tau_m = RC_m \frac{2\sigma_e + \sigma_i}{2\sigma_e\sigma_i} = 19\ \mu\text{m}^2 \cdot 1\frac{\mu\text{F}}{\text{cm}^2} \cdot \frac{2 \cdot 0.001\ \text{S/m} + 0.2\ \text{S/m}}{2 \cdot 0.001\ \text{S/m} \cdot 0.2\ \text{S/m}} \approx 19\ \mu\text{m}^2 \cdot 1\frac{\mu\text{F}}{\text{cm}^2} \cdot \frac{1}{2 \cdot 0.001\ \text{S/m}} = 95\ \mu\text{s}$$

where I used the cell radius R and extracellular conductivity σ_e, according to the reported values in their study, and assumed a typical membrane capacitance C_m of 1 μF/cm^2. I could neglect the intracellular conductivity σ_i due to the large difference between σ_e and σ_i. Note that the charging time is about two times longer than the applied pulse, which means that the amplification of the transmembrane voltage at the contact zones was definitely present (cf. Fig. 1 in Paper 3). In one of their earlier study, they made another, to my opinion ingenious, experiment based on dielectrophoresis (Mehrle *et al.*, 1988). Since in 1988 they did not have the numerical tools to calculate the electric field distribution, they "mapped" the electric field lines around plant

protoplasts in pearl chains by using smaller particles, namely bacteria and chloroplasts exhibiting positive dielectrophoresis (movement towards higher electric field), and polystyrene and glass beads exhibiting negative dielectrophoresis (movement towards lower electric field). Smaller particles require stronger dielectrophoretic signal to form pearl chains. Thereby, when they used a signal of low amplitude, only the protoplasts aligned with the electric field. But as they increased the amplitude of the signal, the smaller bacteria or chloroplasts started to move towards the regions, where the electric field was amplified around the protoplasts, and these regions were indeed around the contacts between cells. In contrast, polystyrene particles or glass beads moved to the regions, where the electric field was the lowest, which was at the "equators" of the protoplasts. The frequency of the dielectrophoretic signal was 1 MHz, which corresponds to a time constant of 1 μs, far below the charging time of the protoplast membranes in their experiments, which is where amplification of the electric field around the contact zones is also predicted by our model (Fig. S2 in Paper 3).

Numerical model of the spinach leaf demonstrated that most of the tissue electric properties are determined by the cuticular wax layer. As cuticular wax is highly nonconductive, most of the applied voltage drops over this layer. We may speculate that certain structural changes could be induced in this layer, similar as is observed in skin electroporation (Weaver *et al.*, 1999; Pavšelj and Miklavčič, 2011), and may deserve further investigation.

The main goal of electroporation in cryopreservation is to electroporate all cells in the tissue reversibly in order to bring the cryoprotectant inside the cells, but not damage the cells with the pulses. In the tissue model that we developed, we implemented a model of cell electroporation, thereby the model is able to (some extent) predict electroporation. But if we are to use this model, or any other similar cell-resolved tissue model, for optimizing pulse parameters such that we electroporate the cells but avoid cell death, we would need to find a phenomenological relation between some parameter in the model (e.g. magnitude of the local electric field or electric current density, number of created pores) and irreversible electroporation. Another point to consider is that when we mean "electroporate the cells" we more specifically mean "introduce cryopreservant into the cells". Consequently, we would need to upgrade the current model with a model of molecular transport. Experiments with protoplasts could give some insights into the kinetics of the transmembrane transport after electroporation.

Comparison of the molecular and continuum-level description of pore conductance was performed for ~1 M NaCl solution. Sodium and chloride ions are rather small, and it appears that the Poisson-Nernst-Planck (PNP) theory is able to adequately describe the passage of ions across the pore, albeit the theory inherently neglects the finite size of the ions. If the electrolyte contained considerably larger ions, the continuum description would hardly be applicable. The developed model should be considered valid only for small monovalent ions. Nevertheless, such ions are abundant in most physiological solutions. The question, which remains opened is whether we would obtain such good agreement also in the presence of physiological ~0.15 M salt solution. Namely, when PNP theory was compared to results from Brownian dynamics simulations of ionic conduction through ion channels, it was observed that the PNP theory performs inadequately particularly when

the ion channel has a radius of less than 2–3 Debye lengths (Corry *et al.*, 2000). In 1 M NaCl, the Debye length is roughly 0.3 nm, and the smallest pore in the simulations had a radius of ~0.8 nm, which is right at the border of validity. In 0.15 M salt solution, the Debye length is roughly a factor of 2.6 longer. Thereby it is possible that we would observe a disagreement between the results from simulations and continuum level description at this concentration. To answer this question, further simulations need to be carried out.

Finally, a comment on the predictive power of the numerical models. In all of our studies presented in this thesis we obtained good agreement between numerical predictions and experimental results, at least up to the point that could be tested. I attribute this in part to the robustness of electroporation and in part to the experience I gained on numerical modeling. Electroporation exhibits a threshold-like dependence on the transmembrane voltage, which is also embedded in the model of Neu and Krassowska, used in our studies (Neu and Krassowska, 1999). The model namely describes the pore creation rate with an Arrhenius factor that depends on the square of the transmembrane voltage. In our numerical calculations we always searched only for the "trigger" of electroporation, thereby this model was sufficient for our purpose. Moreover, since we modeled mostly the effects of nanosecond pulses, more complex models based on solving the full Smoluchowski equation would not give any additional information, as the pores are not expected to expand on such short time scale (Vasilkoski *et al.*, 2006). One may therefore ask, why is it necessary to theoretically describe electroporation in the model, if it would be possible to calculate the induced transmembrane voltage only, and consider that as long as the transmembrane voltage reaches the right threshold, electroporation occurs. I know from experience, though, that including a description of the increase in the membrane conductance does make a certain difference in the obtained results, thereby I find it as advantageous/required in the model.

With respect to the experience on modeling, I can give some examples. From the first study on electroporation of intracellular liposomes, where I made an extensive parametric study, I learned that I have to be very careful when choosing the parameters of the model, particularly when modeling exposure to nanosecond electric pulses. Thereby, in the next study on cell electrofusion, I spent quite some time searching for parameters that would describe the electric properties of cells incubated in low conductive hypoosmolar medium. To my fortune, electric properties of cells incubated in such media were extensively studied by Zimmermann *et al.* (Kiesel *et al.*, 2006; Sukhorukov *et al.*, 2005), thereby I was confident in the parameters I chose for the model. All other parameters of the model I measured myself. I also extensively studied the influence of how the contact areas between the cells are modeled. As I found that the length of the contact area should be considered, I estimated it from microscopic images of cells during dielectrophoresis as accurately as I could. After setting up the model, I simply performed the calculations that were published in Paper 3, and never made any fitting of the model to the final experimental results. I was not expecting such agreement when comparing the numerical results and results from experiments.

In the last study, where I compared the results on pore conductance from molecular dynamics simulations to the results from the PNP model, I first carefully thought through how I should extract the data from the simulations based on my knowledge of the PNP model. When plotting the results from the simulations with the results from

the PNP model on the same graph, I was also not expecting such agreement with respect to the overall pore conductance. I only later made adaptations to the numerical model in order to reproduce the difference between pore conductance for sodium and chloride ions.

Overall, the predictive power of the models can be very high provided that we know how the models behave and that we are aware of the limitations of the models in order to properly interpret the results that the models give. Apart from the predictive power of the models, perhaps the most important benefit of combining theoretical modeling with experiments is simply in enhancing our understanding of the systems that we study – providing us with ideas for improving the existing or developing new therapies and technologies.

Original contributions

Experimental protocol for fusing biological cells with different size using electric pulses with duration of up to few hundred nanoseconds

Electrofusion is an established technique for producing hybrid cells, and has the advantage of being a physical, rather then a chemical or a viral method, thereby it can be safely applied also in clinical treatments. The most important in electrofusion is that cells, which are to be fused, are not damaged by the electric pulses as to allow the fused cells to survive. In most applications of electrofusion, the aim is to fuse cells of different type. It is well known, that larger cells tend to electroporate at lower electric fields, in particular when electroporating them with conventional pulses with duration of tens or hundreds of microseconds. Using numerical modeling, we showed that pulses with duration in the nanosecond range can result in selective electroporation of the contact areas between cells, regardless of the cell size. Consequently, they could provide means to avoid problems when electrofusing cells of different size. We finally developed an experimental protocol for cell fusion using nanosecond pulses, and performed experiments which confirmed the predictions of the numerical model.

Numerical model of biological tissue with resolved cellular structure, which enables the design of electroporation treatment of this tissue

Numerical models of tissue electroporation generally treat the tissue as a homogeneous structure with bulk electrical properties. In tissues, which are highly heterogeneous, such treatment is an oversimplification, as the underlying cellular structure results in nonuniformity of the electric field distribution. Modeling heterogeneous tissue as a homogeneous structure can thereby give misleading conclusions. In electroporation protocols, where it is crucial that all cells are electroporated reversibly, it is highly important that we take the tissue heterogeneity into account in order to develop safe protocols which will not result in damage of valuable cells. Progressing towards developing tissue models with resolved cellular structure is consequently highly important. Cryopreservation is an example of an application of electroporation, where all cells need to be electroporated in order to allow the cryoprotectant to enter all of the cells and protect them from damage during freezing, yet the electric pulses should not induce irreversible electroporation leading to cell death. We successfully developed a model of the spinach leaf tissue taking into account its underlying cellular structure. The model vas validated by measurements of the leaf electrical properties in the frequency domain as well as by measuring the current through the leaf during application of electroporative electric pulses. This is the first numerical model of tissue electroporation, which takes into account the entire detailed tissue structure. Its development can guide further studies to develop such models for other tissue types.

Numerical model of ionic conduction through an aqueous pore in the lipid bilayer, validated by molecular dynamics simulations

Conductance of a single pore is one of the most important parameters bridging theoretical and experimental investigations on aqueous pores formed in the lipid bilayer under the influence of increased transmembrane voltage (i.e. electroporation). Namely, molecular dynamics simulations provide the means to theoretically study single pores in molecular detail, whereas experiments on planar lipid bilayers enable investigation of single pores through measurements of the pore conductance. A bridge between molecular scale investigations and experimental investigations can be given by theoretical models arising from continuum theories. We thereby developed a numerical Poisson-Nernst-Planck model of ionic conduction through a lipid pore directly based on a molecular system used to measure the pore conductance in molecular dynamics simulations. We quantitatively compared the results from the numerical model to the results extracted from molecular dynamics simulations and thereby validated our model. This is the first direct replication of a molecular system with a numerical model with respect to the ionic conduction through an aqueous pore in the lipid bilayer. We can expect this model will facilitate characterization of lipid pores based on experimental measurements as well as improve the predictions of models describing electroporation of cell membranes.

References

Abidor, I.G., Arakelyan, V.B., Chernomordik, L.V., Chizmadzhev, Y.A., Pastushenko, V.F., and Tarasevich, M.P. (1979). Electric breakdown of bilayer lipid membranes: I. The main experimental facts and their qualitative discussion. J. Electroanal. Chem. Interfacial Electrochem. *104*, 37–52.

Barnett, A. (1990). The current-voltage relation of an aqueous pore in a lipid bilayer membrane. Biochim. Biophys. Acta *1025*, 10–14.

Barnett, A., and Weaver, J.C. (1991). Electroporation: a unified, quantitative theory of reversible electrical breakdown and mechanical rupture in artificial planar bilayer membranes. J. Electroanal. Chem. Interfacial Electrochem. *320*, 163–182.

Batista Napotnik, T., Reberšek, M., Kotnik, T., Lebrasseur, E., Cabodevila, G., and Miklavčič, D. (2010). Electropermeabilization of endocytotic vesicles in B16 F1 mouse melanoma cells. Med. Biol. Eng. Comput. *48*, 407–413.

Batista Napotnik, T., Valant, J., Gmajner, D., Passamonti, S., Miklavčič, D., and Ulrih, N.P. (2013). Cytotoxicity and uptake of archaeosomes prepared from Aeropyrum pernix lipids. Hum. Exp. Toxicol. *32*, 950–959.

Beebe, S.J., Sain, N.M., and Ren, W. (2013). Induction of cell death mechanisms and apoptosis by nanosecond pulsed electric fields (nsPEFs). Cells *2*, 136–162.

Ben-David, E., Ahmed, M., Faroja, M., Moussa, M., Wandel, A., Sosna, J., Appelbaum, L., Nissenbaum, I., and Goldberg, S.N. (2013). Irreversible electroporation: treatment effect is susceptible to local environment and tissue properties. Radiology *269*, 738–747.

Ben-Dov, N., Rozman Grinberg, I., and Korenstein, R. (2012). Electroendocytosis is driven by the binding of electrochemically produced protons to the cell's surface. PLoS ONE *7*, e50299.

Benvegnu, T., Lemiegre, L., and Cammas-Marion, S. (2009). New generation of liposomes called archaeosomes based on natural or synthetic archaeal lipids as innovative formulations for drug delivery. Recent Pat. Drug Deliv. Formul. *3*, 206–220.

Benz, R., and Zimmermann, U. (1980). Relaxation studies on cell membranes and lipid bilayers in the high electric field range. Bioelectrochem. Bioenerg. *7*, 723–739.

Benz, R., and Zimmermann, U. (1981). The resealing process of lipid bilayers after reversible electrical breakdown. Biochim. Biophys. Acta *640*, 169–178.

Bhattacharyya, S., and Nayak, A.K. (2009). Electroosmotic flow in micro/nanochannels with surface potential heterogeneity: An analysis through the Nernst–Planck model with convection effect. Colloids Surf. Physicochem. Eng. Asp. *339*, 167–177.

Bockmann, R.A., de Groot, B.L., Kakorin, S., Neumann, E., and Grubmuller, H. (2008). Kinetics, statistics, and energetics of lipid membrane electroporation studied by molecular dynamics simulations. Biophys. J. *95*, 1837–1850.

Boukany, P.E., Morss, A., Liao, W., Henslee, B., Jung, H., Zhang, X., Yu, B., Wang, X., Wu, Y., Li, L., *et al.* (2011). Nanochannel electroporation delivers precise amounts of biomolecules into living cells. Nat. Nanotechnol. *6*, 747–754.

Bowman, A.M., Nesin, O.M., Pakhomova, O.N., and Pakhomov, A.G. (2010). Analysis of plasma membrane integrity by fluorescent detection of Tl^+ uptake. J. Membr. Biol. *236*, 15–26.

Breton, M., Delemotte, L., Silve, A., Mir, L.M., and Tarek, M. (2012). Transport of siRNA through lipid membranes driven by nanosecond electric pulses: An experimental and computational study. J. Am. Chem. Soc. *134*, 13938–13941.

Brianceau, S., Turk, M., Vitrac, X., and Vorobiev, E. (2015). Combined densification and pulsed electric field treatment for selective polyphenols recovery from fermented grape pomace. Innov. Food Sci. Emerg. Technol. *29*, 2–8.

Cadossi, R., Ronchetti, M., and Cadossi, M. (2014). Locally enhanced chemotherapy by electroporation: clinical experiences and perspective of use of electrochemotherapy. Future Oncol. *10*, 877–890.

Canatella, P.J., Karr, J.F., Petros, J.A., and Prausnitz, M.R. (2001). Quantitative study of electroporation-mediated molecular uptake and cell viability. Biophys. J. *80*, 755–764.

Canatella, P.J., Black, M.M., Bonnichsen, D.M., McKenna, C., and Prausnitz, M.R. (2004). Tissue electroporation: Quantification and analysis of heterogeneous transport in multicellular environments. Biophys. J. *86*, 3260–3268.

Cannon, R., Ellis, S., Hayes, D., Narayanan, G., and Martin, R.C.G., 2nd (2013). Safety and early efficacy of irreversible electroporation for hepatic tumors in proximity to vital structures. J. Surg. Oncol. *107*, 544–549.

Chang, W., Sretevan, D., and Kliot, M. (2009). A tribute to Dr. David Kline: a new approach to an old peripheral nerve problem–splicing instead of regenerating disrupted axons. Neurosurgery *65*, A52–A54.

Chen, X., Yin, S., Hu, C., Chen, X., Jiang, K., Ye, S., Feng, X., Fan, S., Xie, H., Zhou, L., *et al.* (2014). Comparative study of nanosecond electric fields *in vitro* and *in vivo* on hepatocellular carcinoma indicate macrophage infiltration contribute to tumor ablation *in vivo*. PLoS ONE *9*, e86421.

Chernomordik, L.V., Sukharev, S.I., Popov, S.V., Pastushenko, V.F., Sokirko, A.V., Abidor, I.G., and Chizmadzhev, Y.A. (1987). The electrical breakdown of cell and lipid membranes: the similarity of phenomenologies. Biochim. Biophys. Acta *902*, 360–373.

Chopinet, L., Wasungu, L., and Rols, M.P. (2012). First explanations for differences in electrotransfection efficiency *in vitro* and *in vivo* using spheroid model. Int. J. Pharm. *423*, 7–15.

Chopinet, L., Roduit, C., Rols, M.P., and Dague, E. (2013). Destabilization induced by electropermeabilization analyzed by atomic force microscopy. Biochim. Biophys. Acta *1828*, 2223–2229.

Coosemans, A., Vanderstraeten, A., Tuyaerts, S., Verschuere, T., Moerman, P., Berneman, Z.N., Vergote, I., Amant, F., and van Gool, S.W. (2013). Wilms' tumor gene 1 (WT1)-loaded dendritic cell immunotherapy in patients with uterine tumors: a phase I/II clinical trial. Anticancer Res. *33*, 5495–5500.

Corry, B., Kuyucak, S., and Chung, S.H. (2000). Tests of continuum theories as models of ion channels. II. Poisson–Nernst–Planck theory versus Brownian dynamics. Biophys. J. *78*, 2364–2381.

Corry, B., Kuyucak, S., and Shin-Ho, C. (2003). Dielectric self-energy in Poisson-Boltzmann and Poisson-Nernst-Planck models of ion channels. Biophys. J. *84*, 3594–3606.

Coster, H.G. (1965). A quantitative analysis of the voltage-current relationships of fixed charge membranes and the associated property of "punch-through." Biophys. J. *5*, 669–686.

Crowley, J.M. (1973). Electrical breakdown of bimolecular lipid membranes as an electromechanical instability. Biophys. J. *13*, 711–724.

Čemažar, M., Jarm, T., Miklavčič, D., Maček-Lebar, A., Ihan, A., Kopitar, N.A., and Serša, G. (1998). Effect of electric-field intensity on electropermeabilization and electrosensitivity of various tumor-cell lines *in vitro*. Electro-Magnetobiology *17*, 263–272.

Čorović, S., Lacković, I., Sustaric, P., Sustar, T., Rodic, T., and Miklavčič, D. (2013). Modeling of electric field distribution in tissues during electroporation. Biomed. Eng. OnLine *12*, 16.

Daiguji, H., Yang, P., and Majumdar, A. (2004). Ion transport in nanofluidic channels. Nano Lett. *4*, 137–142.

Danyluk, J., Perron, A., Houde, M., Limin, A., Fowler, B., Benhamou, N., and Sarhan, F. (1998). Accumulation of an acidic dehydrin in the vicinity of the plasma membrane during cold acclimation of wheat. Plant Cell *10*, 623–638.

DeBruin, K.A., and Krassowska, W. (1999). Modeling electroporation in a single cell. I. Effects of field strength and rest potential. Biophys. J. *77*, 1213–1224.

Dehez, F., Delemotte, L., Kramar, P., Miklavčič, D., and Tarek, M. (2014). Evidence of conducting hydrophobic nanopores across membranes in response to an electric field. J. Phys. Chem. C *118*, 6752–6757.

Delemotte, L., and Tarek, M. (2012). Molecular dynamics simulations of lipid membrane electroporation. J. Membr. Biol. *245*, 531–543.

Delemotte, L., Dehez, F., Treptow, W., and Tarek, M. (2008). Modeling membranes under a transmembrane potential. J. Phys. Chem. B *112*, 5547–5550.

Di Monta, G., Caracò, C., Benedetto, L., La Padula, S., Marone, U., Tornesello, M.L., Buonaguro, F.M., Simeone, E., Ascierto, P.A., and Mozzillo, N. (2014). Electrochemotherapy as "new standard of care" treatment for cutaneous Kaposi's sarcoma. Eur. J. Surg. Oncol. J. Eur. Soc. Surg. Oncol. Br. Assoc. Surg. Oncol. *40*, 61–66.

Dymek, K., Dejmek, P., Galindo, F.G., and Wisniewski, M. (2015a). Influence of vacuum impregnation and pulsed electric field on the freezing temperature and ice propagation rates of spinach leaves. LWT - Food Sci. Technol. *64*, 497–502.

Dymek, K., Rems, L., Zorec, B., Dejmek, P., Galindo, F.G., and Miklavčič, D. (2015b). Modeling electroporation of the non-treated and vacuum impregnated heterogeneous tissue of spinach leaves. Innov. Food Sci. Emerg. Technol. *29*, 55–64.

Escande-Géraud, M.L., Rols, M.P., Dupont, M.A., Gas, N., and Teissié, J. (1988). Reversible plasma membrane ultrastructural changes correlated with electropermeabilization in Chinese hamster ovary cells. Biochim. Biophys. Acta *939*, 247–259.

Esser, A.T., Smith, K.C., Gowrishankar, T.R., Vasilkoski, Z., and Weaver, J.C. (2010). Mechanisms for the intracellular manipulation of organelles by conventional electroporation. Biophys. J. *98*, 2506–2514.

Fernández, M.L., Marshall, G., Sagués, F., and Reigada, R. (2010). Structural and kinetic molecular dynamics study of electroporation in cholesterol-containing bilayers. J. Phys. Chem. B *114*, 6855–6865.

Fernández, M.L., Risk, M., Reigada, R., and Vernier, P.T. (2012). Size-controlled nanopores in lipid membranes with stabilizing electric fields. Biochem. Biophys. Res. Commun. *423*, 325–330.

Fošnarič, M., Kralj-Iglič, V., Bohinc, K., Iglič, A., and May, S. (2003). Stabilization of pores in lipid bilayers by anisotropic inclusions. J. Phys. Chem. B *107*, 12519–12526.

Freeman, S.A., Wang, M.A., and Weaver, J.C. (1994). Theory of electroporation of planar bilayer membranes: predictions of the aqueous area, change in capacitance, and pore-pore separation. Biophys. J. *67*, 42–56.

Frey, W., White, J.A., Price, R.O., Blackmore, P.F., Joshi, R.P., Nuccitelli, R., Beebe, S.J., Schoenbach, K.H., and Kolb, J.F. (2006). Plasma membrane voltage changes during nanosecond pulsed electric field exposure. Biophys. J. *90*, 3608–3615.

Gabriel, B., and Teissié, J. (1997). Direct observation in the millisecond time range of fluorescent molecule asymmetrical interaction with the electropermeabilized cell membrane. Biophys. J. *73*, 2630–2637.

Gabriel, B., and Teissié, J. (1998a). Mammalian cell electropermeabilization as revealed by millisecond imaging of fluorescence changes of ethidium bromide in interaction with the membrane. Bioelectrochem. Bioenerg. *47*, 113–118.

Gabriel, B., and Teissié, J. (1998b). Fluorescence imaging in the millisecond time range of membrane electropermeabilisation of single cells using a rapid ultra-low-light intensifying detection system. Eur. Biophys. J. *27*, 291–298.

Gabriel, B., and Teissié, J. (1999). Time courses of mammalian cell electropermeabilization observed by millisecond imaging of membrane property changes during the pulse. Biophys. J. *76*, 2158–2165.

Gabriel, S., Lau, R.W., and Gabriel, C. (1996). The dielectric properties of biological tissues: II. Measurements in the frequency range 10 Hz to 20 GHz. Phys. Med. Biol. *41*, 2251.

Garon, E.B., Sawcer, D., Vernier, P.T., Tang, T., Sun, Y., Marcu, L., Gundersen, M.A., and Koeffler, H.P. (2007). *In vitro* and *in vivo* evaluation and a case report of intense nanosecond pulsed electric field as a local therapy for human malignancies. Int. J. Cancer J. Int. Cancer *121*, 675–682.

Gibot, L., and Rols, M.P. (2013). 3D spheroids' sensitivity to electric field pulses depends on their size. J. Membr. Biol. *246*, 745–750.

Gibot, L., Wasungu, L., Teissié, J., and Rols, M.P. (2013). Antitumor drug delivery in multicellular spheroids by electropermeabilization. J. Controlled Release *167*, 138–147.

Glaser, R.W., Leikin, S.L., Chernomordik, L.V., Pastushenko, V.F., and Sokirko, A.I. (1988). Reversible electrical breakdown of lipid bilayers: formation and evolution of pores. Biochim. Biophys. Acta *940*, 275–287.

Golzio, M., Teissié, J., and Rols, M.P. (2002). Direct visualization at the single-cell level of electrically mediated gene delivery. Proc. Natl. Acad. Sci. *99*, 1292–1297.

Gómez Galindo, F., and Sjöholm, I. (2004). Applying biochemical and physiological principles in the industrial freezing of vegetables: a case study on carrots. Trends Food Sci. Technol. *15*, 39–43.

Gouaillier-Vulcain, F., Marchand, E., Martinez, R., Picquet, J., and Enon, B. (2015). Utility of electrofusion for the femoral approach in vascular surgery: A randomized prospective study. Ann. Vasc. Surg. *29*, 801–809.

Gowrishankar, T.R., and Weaver, J.C. (2006). Electrical behavior and pore accumulation in a multicellular model for conventional and supra-electroporation. Biochem. Biophys. Res. Commun. *349*, 643–653.

Gowrishankar, T.R., Esser, A.T., Vasilkoski, Z., Smith, K.C., and Weaver, J.C. (2006). Microdosimetry for conventional and supra-electroporation in cells with organelles. Biochem. Biophys. Res. Commun. *341*, 1266–1276.

Gregoriadis, G., and Ryman, B.E. (1971). Liposomes as carriers of enzymes or drugs: a new approach to the treatment of storage diseases. Biochem. J. *124*, 58P.

Greplová, M., Polzerová, H., and Vlastníková, H. (2008). Electrofusion of protoplasts from *Solanum tuberosum*, *S. bulbocastanum* and *S. pinnatisectum*. Acta Physiol. Plant. *30*, 787–796.

Gurtovenko, A.A., and Lyulina, A.S. (2014). Electroporation of asymmetric phospholipid membranes. J. Phys. Chem. B *118*, 9909–9918.

Gurtovenko, A.A., and Vattulainen, I. (2005). Pore formation coupled to ion transport through lipid membranes as induced by transmembrane ionic charge imbalance: Atomistic molecular dynamics study. J. Am. Chem. Soc. *127*, 17570–17571.

Gurtovenko, A.A., and Vattulainen, I. (2007). Ion leakage through transient water pores in protein-free lipid membranes driven by transmembrane ionic charge imbalance. Biophys. J. *92*, 1878–1890.

Gurtovenko, A.A., Anwar, J., and Vattulainen, I. (2010). Defect-mediated trafficking across cell membranes: insights from *in silico* modeling. Chem. Rev. *110*, 6077–6103.

Gusbeth, C., Frey, W., Volkmann, H., Schwartz, T., and Bluhm, H. (2009). Pulsed electric field treatment for bacteria reduction and its impact on hospital wastewater. Chemosphere *75*, 228–233.

Heller, L.C., and Heller, R. (2010). Electroporation gene therapy preclinical and clinical trials for melanoma. Curr. Gene Ther. *10*, 312–317.

Henslee, B.E., Morss, A., Hu, X., Lafyatis, G.P., and Lee, L.J. (2011). Electroporation dependence on cell size: Optical tweezers study. Anal. Chem. *83*, 3998–4003.

Henslee, B.E., Morss, A., Hu, X., Lafyatis, G.P., and Lee, L.J. (2014). Cell-cell proximity effects in multi-cell electroporation. Biomicrofluidics *8*, 052002.

Hibino, M., Shigemori, M., Itoh, H., Nagayama, K., and Kinosita, K. (1991). Membrane conductance of an electroporated cell analyzed by submicrosecond imaging of transmembrane potential. Biophys. J. *59*, 209–220.

Hibino, M., Itoh, H., and Kinosita, K. (1993). Time courses of cell electroporation as revealed by submicrosecond imaging of transmembrane potential. Biophys. J. *64*, 1789–1800.

Hillaireau, H., and Couvreur, P. (2009). Nanocarriers' entry into the cell: relevance to drug delivery. Cell. Mol. Life Sci. *66*, 2873–2896.

Ho, M.C., Casciola, M., Levine, Z.A., and Vernier, P.T. (2013). Molecular dynamics simulations of ion conductance in field-stabilized nanoscale lipid electropores. J. Phys. Chem. B *117*, 11633–11640.

Hooper, J.W., Moon, J.E., Paolino, K.M., Newcomer, R., McLain, D.E., Josleyn, M., Hannaman, D., and Schmaljohn, C. (2014). A Phase 1 clinical trial of Hantaan virus and Puumala virus M-segment DNA vaccines for haemorrhagic fever with renal syndrome delivered by intramuscular electroporation. Clin. Microbiol. Infect. *20*, 110–117.

Huang, S., Zu, Y., and Wang, S. (2014a). Gold nanoparticle-enhanced electroporation for leukemia cell transfection. In Electroporation Protocols, S. Li, J. Cutrera, R. Heller, and J. Teissié, eds. (Springer New York), pp. 69–77.

Huang, S., Deshmukh, H., Rajagopalan, K.K., and Wang, S. (2014b). Gold nanoparticles electroporation enhanced polyplex delivery to mammalian cells. Electrophoresis *35*, 1837–1845.

Huclova, S., Erni, D., and Fröhlich, J. (2010). Modelling effective dielectric properties of materials containing diverse types of biological cells. J. Phys. Appl. Phys. *43*, 365405.

Huclova, S., Baumann, D., Talary, M.S., and Fröhlich, J. (2011). Sensitivity and specificity analysis of fringing-field dielectric spectroscopy applied to a multi-layer system modelling the human skin. Phys. Med. Biol. *56*, 7777.

Huclova, S., Erni, D., and Fröhlich, J. (2012). Modelling and validation of dielectric properties of human skin in the MHz region focusing on skin layer morphology and material composition. J. Phys. Appl. Phys. *45*, 025301.

Huynh, C., Roth, D., Ward, D.M., Kaplan, J., and Andrews, N.W. (2004). Defective lysosomal exocytosis and plasma membrane repair in Chediak–Higashi/beige cells. Proc. Natl. Acad. Sci. U. S. A. *101*, 16795–16800.

Ibey, B.L., Pakhomov, A.G., Gregory, B.W., Khorokhorina, V.A., Roth, C.C., Rassokhin, M.A., Bernhard, J.A., Wilmink, G.J., and Pakhomova, O.N. (2010a). Selective cytotoxicity of intense nanosecond-duration electric pulses in mammalian cells. Biochim. Biophys. Acta *1800*, 1210–1219.

Ibey, B.L., Mixon, D.G., Payne, J.A., Bowman, A., Sickendick, K., Wilmink, G.J., Roach, W.P., and Pakhomov, A.G. (2010b). Plasma membrane permeabilization by trains of ultrashort electric pulses. Bioelectrochemistry *79*, 114–121.

Ibey, B.L., Roth, C.C., Pakhomov, A.G., Bernhard, J.A., Wilmink, G.J., and Pakhomova, O.N. (2011). Dose-dependent thresholds of 10-ns electric pulse induced plasma membrane disruption and cytotoxicity in multiple cell lines. PLoS ONE *6*, e15642.

Im, W., and Roux, B. (2002). Ion permeation and selectivity of ompf porin: A theoretical study based on molecular dynamics, brownian dynamics, and continuum electrodiffusion theory. J. Mol. Biol. *322*, 851–869.

Jiang, F.Y., Bouret, Y., and Kindt, J.T. (2004). Molecular dynamics simulations of the lipid bilayer edge. Biophys. J. *87*, 182–192.

Joshi, R.P., and Hu, Q. (2012). Evolution dynamics of pore sizes, cell volume, ionic concentrations following high-voltage pulsing. IEEE Trans. Plasma Sci. *40*, 2355–2359.

Joshi, R.P., and Schoenbach, K.H. (2000). Electroporation dynamics in biological cells subjected to ultrafast electrical pulses: a numerical simulation study. Phys. Rev. E *62*, 1025–1033.

Kakorin, S., and Neumann, E. (2002). Ionic conductivity of electroporated lipid bilayer membranes. Bioelectrochemistry *56*, 163–166.

Kakorin, S., Stoylov, S.P., and Neumann, E. (1996). Electro-optics of membrane electroporation in diphenylhexatriene-doped lipid bilayer vesicles. Biophys. Chem. *58*, 109–116.

Kalams, S.A., Parker, S.D., Elizaga, M., Metch, B., Edupuganti, S., Hural, J., De Rosa, S., Carter, D.K., Rybczyk, K., Frank, I., *et al.* (2013). Safety and comparative immunogenicity of an HIV-1 DNA vaccine in combination with plasmid interleukin 12 and impact of intramuscular electroporation for delivery. J. Infect. Dis. *208*, 818–829.

Kalinowski, S., Ibron, G., Bryl, K., and Figaszewski, Z. (1998). Chronopotentiometric studies of electroporation of bilayer lipid membranes. Biochim. Biophys. Acta *1369*, 204–212.

Kandasamy, S.K., and Larson, R.G. (2006). Cation and anion transport through hydrophilic pores in lipid bilayers. J. Chem. Phys. *125*, 074901.

Kandušer, M., Šentjurc, M., and Miklavčič, D. (2006). Cell membrane fluidity related to electroporation and resealing. Eur. Biophys. J. *35*, 196–204.

Kemna, E.W.M., Wolbers, F., Vermes, I., and van den Berg, A. (2011). On chip electrofusion of single human B cells and mouse myeloma cells for efficient hybridoma generation. Electrophoresis *32*, 3138–3146.

Kiesel, M., Reuss, R., Endter, J., Zimmermann, D., Zimmermann, H., Shirakashi, R., Bamberg, E., Zimmermann, U., and Sukhorukov, V.L. (2006). Swelling-activated pathways in human T-lymphocytes studied by cell volumetry and electrorotation. Biophys. J. *90*, 4720–4729.

Kinosita, K., and Tsong, T.T. (1977a). Hemolysis of human erythrocytes by transient electric field. Proc. Natl. Acad. Sci. U. S. A. *74*, 1923–1927.

Kinosita, K., and Tsong, T.Y. (1977b). Formation and resealing of pores of controlled sizes in human erythrocyte membrane. Nature *268*, 438–441.

Kinosita, K., Ashikawa, I., Saita, N., Yoshimura, H., Itoh, H., Nagayama, K., and Ikegami, A. (1988). Electroporation of cell membrane visualized under a pulsed-laser fluorescence microscope. Biophys. J. *53*, 1015–1019.

Kinosita, K., Itoh, H., Ishiwata, S., Hirano, K., Nishizaka, T., and Hayakawa, T. (1991). Dual-view microscopy with a single camera: real-time imaging of molecular orientations and calcium. J. Cell Biol. *115*, 67–73.

Kinosita, K., and Tsong, T.Y. (1979). Voltage-induced conductance in human erythrocyte membranes. Biochim. Biophys. Acta *554*, 479–497.

Koronkiewicz, S., Kalinowski, S., and Bryl, K. (2002). Programmable chronopotentiometry as a tool for the study of electroporation and resealing of pores in bilayer lipid membranes. Biochim. Biophys. Acta *1561*, 222–229.

Kos, B., Voigt, P., Miklavčič, D., and Moche, M. (2015). Careful treatment planning enables safe ablation of liver tumors adjacent to major blood vessels by percutaneous irreversible electroporation (IRE). Radiol. Oncol. *49*, 234–241.

Kotnik, T. (2013). Lightning-triggered electroporation and electrofusion as possible contributors to natural horizontal gene transfer. Phys. Life Rev. *10*, 351–370.

Kotnik, T., and Miklavčič, D. (2000). Second-order model of membrane electric field induced by alternating external electric fields. IEEE Trans. Biomed. Eng. *47*, 1074–1081.

Kotnik, T., and Miklavčič, D. (2006). Theoretical evaluation of voltage inducement on internal membranes of biological cells exposed to electric fields. Biophys. J. *90*, 480–491.

Kotnik, T., and Pucihar, G. (2010). Induced transmembrane voltage – theory, modeling, and experiments. In Advanced Electroporation Techniques in Biology and Medicine, A.G. Pakhomov, D. Miklavčič, and M.S. Markov, eds. (CRC Press, Boca Raton), pp. 51–70.

Kotnik, T., Bobanović, F., and Miklavc̆ic̆, D. (1997). Sensitivity of transmembrane voltage induced by applied electric fields—A theoretical analysis. Bioelectrochem. Bioenerg. *43*, 285–291.

Kotnik, T., Pucihar, G., Reberšek, M., Miklavčič, D., and Mir, L.M. (2003). Role of pulse shape in cell membrane electropermeabilization. Biochim. Biophys. Acta *1614*, 193–200.

Kotnik, T., Pucihar, G., and Miklavčič, D. (2010). Induced transmembrane voltage and its correlation with electroporation-mediated molecular transport. J. Membr. Biol. *236*, 3–13.

Kotnik, T., Pucihar, G., and Miklavčič, D. (2011). The cell in the electric field. In Clinical Aspects of Electroporation, S.T. Kee, J. Gehl, and E.W. Lee, eds. (Springer New York), pp. 19–29.

Kotnik, T., Kramar, P., Pucihar, G., Miklavčič, D., and Tarek, M. (2012). Cell membrane electroporation – Part 1: The phenomenon. IEEE Electr. Insul. Mag. *28*, 14–23.

Kotnik, T., Frey, W., Sack, M., Haberl Meglič, S., Peterka, M., and Miklavčič, D. (2015). Electroporation-based applications in biotechnology. Trends Biotechnol. *33*, 480–488.

Kotulska, M. (2007). Natural fluctuations of an electropore show fractional Lévy stable motion. Biophys. J. *92*, 2412–2421.

Kotulska, M., Basalyga, J., Derylo, M.B., and Sadowski, P. (2010). Metastable pores at the onset of constant-current electroporation. J. Membr. Biol. *236*, 37–41.

Kramar, P., Miklavčič, D., and Maček-Lebar, A. (2007). Determination of the lipid bilayer breakdown voltage by means of linear rising signal. Bioelectrochemistry *70*, 23–27.

Kramar, P., Delemotte, L., Maček-Lebar, A., Kotulska, M., Tarek, M., and Miklavčič, D. (2012). Molecular-level characterization of lipid membrane electroporation using linearly rising current. J. Membr. Biol. *245*, 651–659.

Kranjc, M., Markelc, B., Bajd, F., Čemažar, M., Serša, I., Blagus, T., and Miklavčič, D. (2014). In situ monitoring of electric field distribution in mouse tumor during electroporation. Radiology *274*, 115–123.

Krassowska, W., and Filev, P.D. (2007). Modeling electroporation in a single cell. Biophys. J. *92*, 404–417.

Kutzner, C., Grubmüller, H., de Groot, B.L., and Zachariae, U. (2011). Computational electrophysiology: The molecular dynamics of ion channel permeation and selectivity in atomistic detail. Biophys. J. *101*, 809–817.

Leguèbe, M., Silve, A., Mir, L.M., and Poignard, C. (2014). Conducting and permeable states of cell membrane submitted to high voltage pulses: Mathematical and numerical studies validated by the experiments. J. Theor. Biol. *360*, 83–94.

Leontiadou, H., Mark, A.E., and Marrink, S.J. (2004). Molecular dynamics simulations of hydrophilic pores in lipid bilayers. Biophys. J. *86*, 2156–2164.

Levine, Z.A., and Vernier, P.T. (2010). Life cycle of an electropore: field-dependent and field-independent steps in pore creation and annihilation. J. Membr. Biol. *236*, 27–36.

Levine, Z.A., and Vernier, P.T. (2012). Calcium and phosphatidylserine inhibit lipid electropore formation and reduce pore lifetime. J. Membr. Biol. *245*, 599–610.

Li, J., and Lin, H. (2010). The current-voltage relation for electropores with conductivity gradients. Biomicrofluidics *4*, 013206.

Li, J., and Lin, H. (2011). Numerical simulation of molecular uptake via electroporation. Bioelectrochemistry *82*, 10–21.

Li, J., Tan, W., Yu, M., and Lin, H. (2013). The effect of extracellular conductivity on electroporation-mediated molecular delivery. Biochim. Biophys. Acta *1828*, 461–470.

Lin, R., Chang, D.C., and Lee, Y.-K. (2011). Single-cell electroendocytosis on a micro chip using in situ fluorescence microscopy. Biomed. Microdevices *13*, 1063–1073.

Litster, J.D. (1975). Stability of lipid bilayers and red blood cell membranes. Phys. Lett. A *53*, 193–194.

Liu, C., Xie, X., Zhao, W., Liu, N., Maraccini, P.A., Sassoubre, L.M., Boehm, A.B., and Cui, Y. (2013). Conducting nanosponge electroporation for affordable and high-efficiency disinfection of bacteria and viruses in water. Nano Lett. *13*, 4288–4293.

Lojewska, Z., Farkas, D.L., Ehrenberg, B., and Loew, L.M. (1989). Analysis of the effect of medium and membrane conductance on the amplitude and kinetics of membrane potentials induced by externally applied electric fields. Biophys. J. *56*, 121–128.

Lopez, A., Rols, M.P., and Teissié, J. (1988). 31P NMR analysis of membrane phospholipid organization in viable, reversibly electropermeabilized Chinese hamster ovary cells. Biochemistry *27*, 1222–1228.

Maček-Lebar, A., and Miklavčič, D. (2001). Cell electropermeabilization to small molecules *in vitro*: control by pulse parameters. Radiol. Oncol. *35*.

Maček-Lebar, A., Troiano, G.C., Tung, L., and Miklavčič, D. (2002). Inter-pulse interval between rectangular voltage pulses affects electroporation threshold of artificial lipid bilayers. IEEE Trans. NanoBioscience *1*, 116–120.

Mahnič-Kalamiza, S., Vorobiev, E., and Miklavčič, D. (2014). Electroporation in food processing and biorefinery. J. Membr. Biol. *247*, 1279–1304.

Mali, B., Jarm, T., Snoj, M., Serša, G., and Miklavčič, D. (2013). Antitumor effectiveness of electrochemotherapy: a systematic review and meta-analysis. Eur. J. Surg. Oncol. J. Eur. Soc. Surg. Oncol. Br. Assoc. Surg. Oncol. *39*, 4–16.

Markelc, B., Skvarca, E., Dolinsek, T., Kloboves, V.P., Coer, A., Serša, G., and Čemažar, M. (2015). Inhibitor of endocytosis impairs gene electrotransfer to mouse muscle in vivo. Bioelectrochemistry *103*, 111–119.

Marrero, B., and Heller, R. (2012). The use of an *in vitro* 3D melanoma model to predict in vivo plasmid transfection using electroporation. Biomaterials *33*, 3036–3046.

Marrink, S.J., Lindahl, E., Edholm, O., and Mark, A.E. (2001). Simulation of the spontaneous aggregation of phospholipids into bilayers. J. Am. Chem. Soc. *123*, 8638–8639.

Marty, M., Serša, G., Garbay, J.R., Gehl, J., Collins, C.G., Snoj, M., Billard, V., Geertsen, P.F., Larkin, J.O., Miklavčič, D., *et al.* (2006). Electrochemotherapy – An easy, highly effective and safe treatment of cutaneous and subcutaneous metastases: Results of ESOPE (European Standard Operating Procedures of Electrochemotherapy) study. EJC Suppl. *4*, 3–13.

McCluskey, J.T., Hamid, M., Guo-Parke, H., McClenaghan, N.H., Gomis, R., and Flatt, P.R. (2011). Development and functional characterization of insulin-releasing human pancreatic beta cell lines produced by electrofusion. J. Biol. Chem. *286*, 21982–21992.

Mehrle, W., Zimmermann, U., and Hampp, R. (1985). Evidence for asymmetrical uptake of fluorescent dyes through electro-permeabilized membranes of Avena mesophyll protoplasts. FEBS Lett. *185*, 89–94.

Mehrle, W., Hampp, R., Zimmermann, U., and Schwan, H.P. (1988). Mapping of the field distribution around dielectrophoretically aligned cells by means of small particles as field probes. Biochim. Biophys. Acta *939*, 561–568.

Mehrle, W., Hampp, R., and Zimmermann, U. (1989). Electric pulse induced membrane permeabilisation. Spatial orientation and kinetics of solute efflux in freely suspended and dielectrophoretically aligned plant mesophyll protoplasts. Biochim. Biophys. Acta *978*, 267–275.

Melikov, K.C., Frolov, V.A., Shcherbakov, A., Samsonov, A.V., Chizmadzhev, Y.A., and Chernomordik, L.V. (2001). Voltage-induced nonconductive pre-pores and metastable single pores in unmodified planar lipid bilayer. Biophys. J. *80*, 1829–1836.

Mezeme, M.E., Pucihar, G., Pavlin, M., Brosseau, C., and Miklavčič, D. (2012a). A numerical analysis of multicellular environment for modeling tissue electroporation. Appl. Phys. Lett. *100*, 143701.

Mezeme, M.E., Kranjc, M., Bajd, F., Serša, I., Brosseau, C., and Miklavčič, D. (2012b). Assessing how electroporation affects the effective conductivity tensor of biological tissues. Appl. Phys. Lett. *101*, 213702.

Miklavčič, D., and Towhidi, L. (2010). Numerical study of the electroporation pulse shape effect on molecular uptake of biological cells. Radiol. Oncol. *44*, 34–41.

Miklavčič, D., Serša, G., Brecelj, E., Gehl, J., Soden, D., Bianchi, G., Ruggieri, P., Rossi, C.R., Campana, L.G., and Jarm, T. (2012). Electrochemotherapy: technological advancements for efficient electroporation-based treatment of internal tumors. Med. Biol. Eng. Comput. *50*, 1213–1225.

Mir, L.M. (2009). Nucleic acids electrotransfer-based gene therapy (electrogenetherapy): Past, current, and future. Mol. Biotechnol. *43*, 167–176.

Moy, G., Corry, B., Kuyucak, S., and Chung, S.H. (2000). Tests of continuum theories as models of ion channels. I. Poisson-Boltzmann theory versus Brownian dynamics. Biophys. J. *78*, 2349–2363.

Nesin, O.M., Pakhomova, O.N., Xiao, S., and Pakhomov, A.G. (2011). Manipulation of cell volume and membrane pore comparison following single cell permeabilization with 60- and 600-ns electric pulses. Biochim. Biophys. Acta *1808*, 792–801.

Neu, J.C., and Krassowska, W. (1999). Asymptotic model of electroporation. Phys. Rev. E *59*, 3471–3482.

Neu, J.C., and Krassowska, W. (2003). Modeling postshock evolution of large electropores. Phys. Rev. E *67*, 021915.

Neumann, E., and Rosenheck, K. (1972). Permeability changes induced by electric impulses in vesicular membranes. J. Membr. Biol. *10*, 279–290.

Neumann, E., Schaefer-Ridder, M., Wang, Y., and Hofschneider, P.H. (1982). Gene transfer into mouse lyoma cells by electroporation in high electric fields. EMBO J. *1*, 841–845.

Neumann, E., Toensing, K., Kakorin, S., Budde, P., and Frey, J. (1998). Mechanism of electroporative dye uptake by mouse B cells. Biophys. J. *74*, 98–108.

Nuccitelli, R., Wood, R., Kreis, M., Athos, B., Huynh, J., Lui, K., Nuccitelli, P., and Epstein, E.H., Jr (2014). First-in-human trial of nanoelectroablation therapy for basal cell carcinoma: proof of method. Exp. Dermatol. *23*, 135–137.

den Otter, W.K. (2009). Free energies of stable and metastable pores in lipid membranes under tension. J. Chem. Phys. *131*, 205101.

Paganin-Gioanni, A., Bellard, E., Escoffre, J.M., Rols, M.P., Teissié, J., and Golzio, M. (2011). Direct visualization at the single-cell level of siRNA electrotransfer into cancer cells. Proc. Natl. Acad. Sci. *108*, 10443–10447.

Pakhomov, A., Phinney, A., Ashmore, J., Walker, I., K., Kolb, J.F., Kono, S., Schoenbach, K.H., and Murphy, M.R. (2004). Characterization of the cytotoxic effect of high-intensity, 10-ns duration electrical pulses. IEEE Trans. Plasma Sci. *32*, 1579–1586.

Pakhomov, A.G., Kolb, J.F., White, J.A., Joshi, R.P., Xiao, S., and Schoenbach, K.H. (2007a). Long-lasting plasma membrane permeabilization in mammalian cells by nanosecond pulsed electric field (nsPEF). Bioelectromagnetics *28*, 655–663.

Pakhomov, A.G., Shevin, R., White, J.A., Kolb, J.F., Pakhomova, O.N., Joshi, R.P., and Schoenbach, K.H. (2007b). Membrane permeabilization and cell damage by ultrashort electric field shocks. Arch. Biochem. Biophys. *465*, 109–118.

Pakhomov, A.G., Gianulis, E., Vernier, P.T., Semenov, I., Xiao, S., and Pakhomova, O.N. (2015). Multiple nanosecond electric pulses increase the number but not the size of long-lived nanopores in the cell membrane. Biochim. Biophys. Acta *1848*, 958–966.

Panarese, V., Dejmek, P., Rocculi, P., and Gómez Galindo, F. (2013). Microscopic studies providing insight into the mechanisms of mass transfer in vacuum impregnation. Innov. Food Sci. Emerg. Technol. *18*, 169–176.

Pastushenko, V.F., Chizmadzhev, Y.A., and Arakelyan, V.B. (1979). Electric breakdown of bilayer lipid membranes II. Calculation of the membrane lifetime in the steady-state diffusion approximation. Bioelectrochem. Bioenerg. *6*, 53–62.

Pavlin, M., and Miklavčič, D. (2008). Theoretical and experimental analysis of conductivity, ion diffusion and molecular transport during cell electroporation — Relation between short-lived and long-lived pores. Bioelectrochemistry *74*, 38–46.

Pavlin, M., Pavšelj, N., and Miklavčič, D. (2002). Dependence of induced transmembrane potential on cell density, arrangement, and cell position inside a cell system. IEEE Trans. Biomed. Eng. *49*, 605–612.

Pavlin, M., Kandušer, M., Reberšek, M., Pucihar, G., Hart, F.X., Magjarević, R., and Miklavčič, D. (2005). Effect of cell electroporation on the conductivity of a cell suspension. Biophys. J. *88*, 4378–4390.

Pavlin, M., Leben, V., and Miklavčič, D. (2007). Electroporation in dense cell suspension—Theoretical and experimental analysis of ion diffusion and cell permeabilization. Biochim. Biophys. Acta *1770*, 12–23.

Pavšelj, N., and Miklavčič, D. (2011). Resistive heating and electropermeabilization of skin tissue during in vivo electroporation: A coupled nonlinear finite element model. Int. J. Heat Mass Transf. *54*, 2294–2302.

Phoon, P.Y., Galindo, F.G., Vicente, A., and Dejmek, P. (2008). Pulsed electric field in combination with vacuum impregnation with trehalose improves the freezing tolerance of spinach leaves. J. Food Eng. *88*, 144–148.

Polak, A., Mulej, B., and Kramar, P. (2012). System for measuring planar lipid bilayer properties. J. Membr. Biol. *245*, 625–632.

Polak, A., Tarek, M., Tomšič, M., Valant, J., Ulrih, N.P., Jamnik, A., Kramar, P., and Miklavčič, D. (2014). Electroporation of archaeal lipid membranes using MD simulations. Bioelectrochemistry *100*, 18–26.

Polak, A., Velikonja, A., Kramar, P., Tarek, M., and Miklavčič, D. (2015). Electroporation threshold of POPC lipid bilayers with incorporated polyoxyethylene glycol ($C_{12}E_8$). J. Phys. Chem. B *119*, 192–200.

Powell, K.T., and Weaver, J.C. (1986). Transient aqueous pores in bilayer membranes: A statistical theory. Bioelectrochem. Bioenerg. *15*, 211–227.

Prausnitz, M.R., Lau, B.S., Milano, C.D., Conner, S., Langer, R., and Weaver, J.C. (1993). A quantitative study of electroporation showing a plateau in net molecular transport. Biophys. J. *65*, 414–422.

Prausnitz, M.R., Corbett, J.D., Gimm, J.A., Golan, D.E., Langer, R., and Weaver, J.C. (1995). Millisecond measurement of transport during and after an electroporation pulse. Biophys. J. *68*, 1864–1870.

Puc, M., Kotnik, T., Mir, L.M., and Miklavčič, D. (2003). Quantitative model of small molecules uptake after *in vitro* cell electropermeabilization. Bioelectrochemistry *60*, 1–10.

Pucihar, G., Kotnik, T., Teissié, J., and Miklavčič, D. (2007). Electropermeabilization of dense cell suspensions. Eur. Biophys. J. *36*, 173–185.

Pucihar, G., Kotnik, T., Miklavčič, D., and Teissié, J. (2008). Kinetics of transmembrane transport of small molecules into electropermeabilized cells. Biophys. J. *95*, 2837–2848.

Ramos-Barrado, J., Benavente, J., and Heredia, A. (1993). Electrical conductivity of differently treated isolated cuticular membranes by impedance spectroscopy. Arch. Biochem. Biophys. *306*, 337–341.

Rems, L., and Miklavčič, D. (2015). Theoretical considerations for the potential of controlled drug release from lipid vesicles by means of electroporation or electrofusion. In 6th European Conference of the International Federation for Medical and Biological Engineering, MBEC 2014, 7-11 September 2014, Dubrovnik, Croatia, I. Lacković, and D. Vasić, eds. (Springer International Publishing), pp. 797–800.

Rems, L., Ušaj, M., Kandušer, M., Reberšek, M., Miklavčič, D., and Pucihar, G. (2013). Cell electrofusion using nanosecond electric pulses. Sci. Rep. *3*, 3382.

Retelj, L., Pucihar, G., and Miklavčič, D. (2013). Electroporation of intracellular liposomes using nanosecond electric pulses – A theoretical study. IEEE Trans. Biomed. Eng. *60*, 2624–2635.

Rols, M.P., and Teissié, J. (1989). Ionic-strength modulation of electrically induced permeabilization and associated fusion of mammalian cells. Eur. J. Biochem. *179*, 109–115.

Rols, M.P., and Teissié, J. (1990). Electropermeabilization of mammalian cells. Quantitative analysis of the phenomenon. Biophys. J. *58*, 1089–1098.

Rols, M.P., and Teissié, J. (1992). Experimental evidence for the involvement of the cytoskeleton in mammalian cell electropermeabilization. Biochim. Biophys. Acta *1111*, 45–50.

Rols, M.P., and Teissié, J. (1998). Electropermeabilization of mammalian cells to macromolecules: control by pulse duration. Biophys. J. *75*, 1415–1423.

Rosazza, C., Phez, E., Escoffre, J.-M., Cézanne, L., Zumbusch, A., and Rols, M.P. (2012). Cholesterol implications in plasmid DNA electrotransfer: Evidence for the involvement of endocytotic pathways. Int. J. Pharm. *423*, 134–143.

Rossmeisl, J.H., Jr, Garcia, P.A., Roberston, J.L., Ellis, T.L., and Davalos, R.V. (2013). Pathology of non-thermal irreversible electroporation (N-TIRE)-induced ablation of the canine brain. J. Vet. Sci. *14*, 433–440.

Roux, B., Allen, T., Bernèche, S., and Im, W. (2004). Theoretical and computational models of biological ion channels. Q. Rev. Biophys. *37*, 15–103.

Sack, M., Sigler, J., Frenzel, S., Eing, C., Arnold, J., Michelberger, T., Frey, W., Attmann, F., Stukenbrock, L., and Müller, G. (2010). Research on industrial-scale electroporation devices fostering the extraction of substances from biological tissue. Food Eng. Rev. *2*, 147–156.

Santini, M.T., Rainaldi, G., and Indovina, P.L. (2000). Apoptosis, cell adhesion and the extracellular matrix in the three-dimensional growth of multicellular tumor spheroids. Crit. Rev. Oncol. Hematol. *36*, 75–87.

Saulis, G., and Saulė, R. (2012). Size of the pores created by an electric pulse: Microsecond vs millisecond pulses. Biochim. Biophys. Acta *1818*, 3032–3039.

Saulis, G., Venslauskas, M.S., and Naktinis, J. (1991). Kinetics of pore resealing in cell membranes after electroporation. J. Electroanal. Chem. Interfacial Electrochem. *321*, 1–13.

Scheffer, H.J., Nielsen, K., de Jong, M.C., van Tilborg, A.A.J.M., Vieveen, J.M., Bouwman, A.R.A., Meijer, S., van Kuijk, C., van den Tol, P.M.P., and Meijerink, M.R. (2014). Irreversible electroporation for nonthermal tumor ablation in the clinical setting: a systematic review of safety and efficacy. J. Vasc. Interv. Radiol. JVIR *25*, 997–1011; quiz 1011.

Schmeer, M., Seipp, T., Pliquett, U., Kakorin, S., and Neumann, E. (2004). Mechanism for the conductivity changes caused by membrane electroporation of CHO cell-pellets. Phys. Chem. Chem. Phys. *6*, 5564–5574.

Schoellhammer, C.M., Blankschtein, D., and Langer, R. (2014). Skin permeabilization for transdermal drug delivery: recent advances and future prospects. Expert Opin. Drug Deliv. *11*, 393–407.

Schoenbach, K.H., and Joshi, R.P. (2010). Bioelectric effects of intense ultrashort pulses. Crit. Rev. Biomed. Eng. *38*, 255–304.

Schoenbach, K.H., Beebe, S.J., and Buescher, E.S. (2001). Intracellular effect of ultrashort electrical pulses. Bioelectromagnetics *22*, 440–448.

Shayanfar, S., Chauhan, O.P., Toepfl, S., and Heinz, V. (2014). Pulsed electric field treatment prior to freezing carrot discs significantly maintains their initial quality parameters after thawing. Int. J. Food Sci. Technol. *49*, 1224–1230.

Shirakashi, R., Sukhorukov, V.L., Tanasawa, I., and Zimmermann, U. (2004). Measurement of the permeability and resealing time constant of the electroporated mammalian cell membranes. Int. J. Heat Mass Transf. *47*, 4517–4524.

Siu, S.W.I., and Böckmann, R.A. (2007). Electric field effects on membranes: gramicidin A as a test ground. J. Struct. Biol. *157*, 545–556.

Sixou, S., and Teissié, J. (1990). Specific electropermeabilization of leucocytes in a blood sample and application to large volumes of cells. Biochim. Biophys. Acta *1028*, 154–160.

Smith, K.C., and Weaver, J.C. (2008). Active mechanisms are needed to describe cell responses to submicrosecond, megavolt-per-meter pulses: Cell models for ultrashort pulses. Biophys. J. *95*, 1547–1563.

Smith, K.C., Neu, J.C., and Krassowska, W. (2004). Model of creation and evolution of stable electropores for DNA delivery. Biophys. J. *86*, 2813–2826.

Sretavan, D.W.M.D., Chang, W., Hawkes, E., Keller, C., and Kliot, M. (2005). Microscale surgery on single axons. Neurosurg. Oct. 2005 *57*, 635–646.

Stacey, M., Fox, P., Buescher, S., and Kolb, J. (2011). Nanosecond pulsed electric field induced cytoskeleton, nuclear membrane and telomere damage adversely impact cell survival. Bioelectrochemistry *82*, 131–134.

Sukhorukov, V.L., Reuss, R., Zimmermann, D., Held, C., Müller, K.J., Kiesel, M., Geßner, P., Steinbach, A., Schenk, W.A., Bamberg, E., *et al.* (2005). Surviving high-intensity field pulses: Strategies for improving robustness and performance of electrotransfection and electrofusion. J. Membr. Biol. *206*, 187–201.

Susil, R., Šemrov, D., and Miklavčič, D. (1998). Electric field induced transmembrane potential depends on cell density and organization. Electro-Magnetobiology *17*, 391–399.

Sutherland, R.M. (1988). Cell and environment interactions in tumor microregions: the multicell spheroid model. Science *240*, 177–184.

Suzuki, D.O.H., Ramos, A., Ribeiro, M.C.M., Cazarolli, L.H., Silva, F.R.M.B., Leite, L.D., and Marques, J.L.B. (2011). Theoretical and experimental analysis of electroporated membrane conductance in cell suspension. IEEE Trans. Biomed. Eng. *58*, 3310–3318.

Szabo, M., and Wallace, M.I. (2015). Imaging potassium-flux through individual electropores in droplet interface bilayers. Biochim. Biophys. Acta. In press.

Šel, D., Cukjati, D., Batiuskaite, D., Slivnik, T., Mir, L.M., and Miklavčič, D. (2005). Sequential finite element model of tissue electropermeabilization. IEEE Trans. Biomed. Eng. *52*, 816–827.

Šemrov, D., and Miklavčič, D. (1998). Calculation of the electrical parameters in electrochemotherapy of solid tumors in mice. Comput. Biol. Med. *28*, 439–448.

Tan, C., Dannull, J., Nair, S.K., Ding, E., Tyler, D.S., Pruitt, S.K., and Lee, W.T. (2013). Local secretion of IL-12 augments the therapeutic impact of dendritic cell-tumor cell fusion vaccination. J. Surg. Res. *185*, 904–911.

Tarek, M. (2005). Membrane electroporation: a molecular dynamics simulation. Biophys. J. *88*, 4045–4053.

Taupin, C., Dvolaitzky, M., and Sauterey, C. (1975). Osmotic pressure-induced pores in phospholipid vesicles. Biochemistry *14*, 4771–4775.

Teissié, J., and Ramos, C. (1998). Correlation between electric field pulse induced long-lived permeabilization and fusogenicity in cell membranes. Biophys. J. *74*, 1889–1898.

Teissié, J., Golzio, M., and Rols, M.P. (2005). Mechanisms of cell membrane electropermeabilization: a minireview of our present (lack of ?) knowledge. Biochim. Biophys. Acta *1724*, 270–280.

Tekle, E., Astumian, R.D., and Chock, P.B. (1990). Electro-permeabilization of cell membranes: Effect of the resting membrane potential. Biochem. Biophys. Res. Commun. *172*, 282–287.

Tekle, E., Astumian, R.D., and Chock, P.B. (1994). Selective and asymmetric molecular transport across electroporated cell membranes. Proc. Natl. Acad. Sci. *91*, 11512–11516.

Tekle, E., Oubrahim, H., Dzekunov, S.M., Kolb, J.F., Schoenbach, K.H., and Chock, P.B. (2005). Selective field effects on intracellular vacuoles and vesicle membranes with nanosecond electric pulses. Biophys. J. *89*, 274–284.

Tieleman, D.P. (2004). The molecular basis of electroporation. BMC Biochem. *5*, 10.

Toepfl, S., Heinz, V., and Knorr, D. (2007). High intensity pulsed electric fields applied for food preservation. Chem. Eng. Process. Process Intensif. *46*, 537–546.

Tolpekina, T.V., den Otter, W.K., and Briels, W.J. (2004). Simulations of stable pores in membranes: System size dependence and line tension. J. Chem. Phys. *121*, 8014–8020.

Towhidi, L., Kotnik, T., Pucihar, G., Firoozabadi, S.M.P., Mozdarani, H., and Miklavčič, D. (2008). Variability of the minimal transmembrane voltage resulting in detectable membrane electroporation. Electromagn. Biol. Med. *27*, 372–385.

Trontelj, K., Reberšek, M., Kandušer, M., Serbec, V.C., Sprohar, M., and Miklavčič, D. (2008). Optimization of bulk cell electrofusion *in vitro* for production of human-mouse heterohybridoma cells. Bioelectrochemistry *74*, 124–129.

Tsong, T.Y. (1991). Electroporation of cell membranes. Biophys. J. *60*, 297–306.

Ušaj, M., and Kandušer, M. (2012). The systematic study of the electroporation and electrofusion of B16-F1 and CHO cells in isotonic and hypotonic buffer. J. Membr. Biol. *245*, 583–590.

Ušaj, M., Flisar, K., Miklavčič, D., and Kandušer, M. (2013). Electrofusion of B16-F1 and CHO cells: The comparison of the pulse first and contact first protocols. Bioelectrochemistry *89*, 34–41.

Valič, B., Golzio, M., Pavlin, M., Schatz, A., Faurie, C., Gabriel, B., Teissié, J., Rols, M.P., and Miklavčič, D. (2003). Effect of electric field induced transmembrane potential on spheroidal cells: theory and experiment. Eur. Biophys. J. *32*, 519–528.

Vasilkoski, Z., Esser, A., Gowrishankar, T., and Weaver, J. (2006). Membrane electroporation: The absolute rate equation and nanosecond time scale pore creation. Phys. Rev. E *74*.

Vernier, P.T., and Ziegler, M.J. (2007). Nanosecond field alignment of head group and water dipoles in electroporating phospholipid bilayers. J. Phys. Chem. B *111*, 12993–12996.

Vernier, P.T., Sun, Y., and Gundersen, M.A. (2006). Nanoelectropulse-driven membrane perturbation and small molecule permeabilization. BMC Cell Biol. *7*, 1–16.

Vernier, P.T., Levine, Z.A., and Gundersen, M.A. (2013). Water bridges in electropermeabilized phospholipid bilayers. Proc. IEEE *101*, 494–504.

Weaver, J.C., and Chizmadzhev, Y.A. (1996). Theory of electroporation: A review. Bioelectrochem. Bioenerg. *41*, 135–160.

Weaver, J.C., and Mintzer, R.A. (1981). Decreased bilayer stability due to transmembrane potentials. Phys. Lett. A *86*, 57–59.

Weaver, J.C., Vaughan, T.E., and Chizmadzhev, Y. (1999). Theory of electrical creation of aqueous pathways across skin transport barriers. Adv. Drug Deliv. Rev. *35*, 21–39.

Wegner, L.H., Frey, W., and Silve, A. (2015). Electroporation of DC-3F cells is a dual process. Biophys. J. *108*, 1660–1671.

Wohlert, J., den Otter, W.K., Edholm, O., and Briels, W.J. (2006). Free energy of a trans-membrane pore calculated from atomistic molecular dynamics simulations. J. Chem. Phys. *124*, 154905.

Xie, C., Lin, Z., Hanson, L., Cui, Y., and Cui, B. (2012). Intracellular recording of action potentials by nanopillar electroporation. Nat. Nanotechnol. *7*, 185–190.

Yanai, G., Hayashi, T., Zhi, Q., Yang, K.-C., Shirouzu, Y., Shimabukuro, T., Hiura, A., Inoue, K., and Sumi, S. (2013). Electrofusion of mesenchymal stem cells and islet cells for diabetes therapy: A rat model. PLoS ONE *8*, e64499.

Yarmush, M.L., Golberg, A., Serša, G., Kotnik, T., and Miklavčič, D. (2014). Electroporation-based technologies for medicine: Principles, applications, and challenges. Annu. Rev. Biomed. Eng. *16*, 295–320.

Yu, X., McGraw, P.A., House, F.S., and Crowe, J.E.J. (2008). An optimized electrofusion-based protocol for generating virus-specific human monoclonal antibodies. J. Immunol. Methods *336*, 142–151.

Yu, X., Bals, O., Grimi, N., and Vorobiev, E. (2015). A new way for the oil plant biomass valorization: Polyphenols and proteins extraction from rapeseed stems and leaves assisted by pulsed electric fields. Ind. Crops Prod. *74*, 309–318.

Zbinden, M.D.A., Sturm, B.S.M., Nord, R.D., Carey, W.J., Moore, D., Shinogle, H., and Stagg-Williams, S.M. (2013). Pulsed electric field (PEF) as an intensification pretreatment for greener solvent lipid extraction from microalgae. Biotechnol. Bioeng. *110*, 1605–1615.

Zheng, Q., and Wei, G.W. (2011). Poisson–Boltzmann–Nernst–Planck model. J. Chem. Phys. *134*.

Zheng, R., Cohen, P.A., Paustian, C.A., Johnson, T.D., Lee, W.T., Shu, S., and Koski, G.K. (2008). Paired toll-like receptor agonists enhance vaccine therapy through induction of interleukin-12. Cancer Res. *68*, 4045–4049.

Ziegler, M.J., and Vernier, P.T. (2008). Interface water dynamics and porating electric fields for phospholipid bilayers. J. Phys. Chem. B *112*, 13588–13596.

Zimmermann, U. (1982). Electric field-mediated fusion and related electrical phenomena. Biochim. Biophys. Acta *694*, 227–277.

Zimmermann, U., Pilwat, G., and Riemann, F. (1974). Dielectric breakdown of cell membranes. Biophys. J. *14*, 881–899.

Zimmermann, U., Pilwat, G., Holzapfel, C., and Rosenheck, K. (1976). Electrical hemolysis of human and bovine red blood cells. J. Membr. Biol. *30*, 135–152.

Zorec, B., Becker, S., Reberšek, M., Miklavčič, D., and Pavšelj, N. (2013). Skin electroporation for transdermal drug delivery: the influence of the order of different square wave electric pulses. Int. J. Pharm. *457*, 214–223.

Declaration

The author hereby declares that the content of the thesis is a result of her own research work supervised by Prof. Dr. Damijan Miklavčič and Dr. Mounir Tarek. The results, which were collected in collaboration with other colleagues, are published in the presented papers. The assistance from other colleagues is stated in the Acknowledgements. The published results of other authors are presented in the literature.

Lea Rems

Izjava

Izjavljam, da sem doktorsko disertacijo izdelala sama, pod mentorstvom prof. dr. Damijana Miklavčiča in dr. Mounirja Tareka. Rezultati, ki so nastali v sodelovanju z drugimi sodelavci, so bili objavljeni v predstavljenih člankih. Izkazano pomoč ostalih sodelavcev sem v celoti navedla v zahvali. Že objavljeni dosežki drugih avtorjev so navedeni v spisku literature.

Lea Rems